

**Multinucleon-Transfer Reactions
as a Gateway to Neutron-Rich Actinides
and Nuclei near the
 $N = 82$ and $Z = 50$ Shell Closures**

Inaugural-Dissertation

zur
Erlangung des Doktorgrades
der Mathematisch-Naturwissenschaftlichen Fakultät
der Universität zu Köln

vorgelegt von

Andreas Günter Heinz Vogt
aus Köln

Köln 2017

Berichterstatter:

Prof. Dr. Peter Reiter
Prof. Dr. Andreas Zilges
Prof. Dr. Rolf-Dietmar Herzberg

Tag der letzten mündlichen Prüfung:

10. Juli 2017

Abstract

Multinucleon-transfer reactions are a competitive and promising tool to provide access to hard-to-reach and exotic nuclei. In the present work, reaction products in the $^{136}\text{Xe} + ^{238}\text{U}$ multinucleon-transfer reaction at 1 GeV were investigated employing the high-resolution position-sensitive γ -ray tracking array AGATA coupled to the large-solid-angle mass spectrometer PRISMA at the Laboratori Nazionali di Legnaro (INFN, Italy). Beam-like reaction products were identified and selected by the PRISMA spectrometer. Recoils and fission fragments were tagged by DANTE micro-channel plate detectors installed within the scattering chamber. Fission and transfer events are discriminated by exploiting kinematic coincidences between the binary reaction products. Mass yields and relative cross-section distributions are extracted and compared with calculations based on the GRAZING model for multinucleon-transfer reactions. Furthermore, population yields for nuclei in the actinide region are obtained and compared to X-ray yields measured by AGATA. Perspectives and limitations for the production of the hard-to-reach neutron-rich isotopes are discussed. A Doppler correction for the target-like nuclei enables γ -ray spectroscopy of the heavy reaction partner. Nuclear structure information of neutron-rich actinide nuclei are a benchmark for theoretical models providing predictions for the heaviest nuclei. An extension of the ground-state rotational band in ^{240}U is achieved and evidence for an extended first negative-parity band in ^{240}U is found. The results are compared to recent mean-field and density-functional theory calculations. Furthermore, multinucleon-transfer reactions are a gateway to nuclei in the vicinity of the $Z = 50$ and $N = 82$ shell closures. Nuclei in this region serve as a benchmark for nuclear shell-model calculations based on modern effective interactions, but are difficult to populate due to a lack of suitable beam-target combinations. Excited reaction products were measured after multinucleon transfer in $^{136}\text{Xe} + ^{238}\text{U}$ at 1 GeV and $^{136}\text{Xe} + ^{208}\text{Pb}$ at 930 MeV with the AGATA tracking array coupled to PRISMA at LNL (INFN, Italy) as well as in the $^{136}\text{Xe} + ^{198}\text{Pt}$ multinucleon-transfer reaction employing the high-efficiency γ -ray spectrometer GAMMASPHERE in combination with the gas-detector array CHICO at LBNL. Moreover, Xe and Ba isotopes were populated in fusion-evaporation reactions using the HORUS γ -ray array at the University of Cologne. The high-spin level schemes of ^{132}Xe , ^{133}Xe , ^{134}Xe , ^{135}Xe and ^{137}Ba were considerably extended to higher energies. The 2058-keV state in ^{135}Xe is identified as a 9.0(9)-ns isomer, closing a gap in the systematics along the $N = 81$ isotones. Latest shell-model calculations reproduce the experimental findings. The experimentally-deduced reduced transition strengths of the isomer decays are compared to shell-model predictions. A detailed picture of the lower-mass $N \leq 82$, $Z \geq 50$ region of the Segrè chart is drawn. Another part of this thesis covers double-sided silicon strip detectors (DSSSD) which are employed for the detection of charged particles providing position and energy information. Intersecting areas of both p- and n-side strips form individual pixel segments resulting in a high detector granularity. However, due to limitations in fabrication and the response of the readout electronics, the performance of different channels may vary. Typically, charged particles do not illuminate homogeneously the detector surface during in-beam experiments. Consequently, radiation damages of the detector are distributed non-uniformly. Position-resolved charge-collection losses for front- and back-side segments were investigated for an in-beam experiment and by performing radioactive source measurements. A novel position-resolved calibration method for radiation-damaged DSSSDs, based on mutual consistency of p-side and n-side charges, was developed. It yields a significant enhancement of the energy resolution and the performance of radiation-damaged parts of the detector.

Zusammenfassung

Multinukleontransferreaktionen sind ein vielversprechender Zugang zur Produktion schwer zugänglicher und exotischer Atomkerne. Der erste Teil der Arbeit umfasst eine Reaktionsstudie zur Schwerionenkollision zwischen ^{136}Xe und ^{238}U bei einer Strahlenergie von 1 GeV, durchgeführt mit dem hochauflösenden und positionssensitiven Gamma-Tracking-Array AGATA am Laboratori Nazionali di Legnaro (INFN, Italien). Strahlähnliche Reaktionsprodukte wurden mit dem Massenspektrometer PRISMA identifiziert und selektiert. Targetähnliche Teilchen und Spaltfragmente wurden mittels DANTE-Mikrokanalplattendetektoren innerhalb der Strahlkammer detektiert. Kinematische Koinzidenzen zwischen den verschiedenen Reaktionsprodukten erlauben eine Diskriminierung zwischen Spaltung und erwünschtem Multinukleontransfer. Massenspektren und relative Wirkungsquerschnitte wurden aus den Daten extrahiert und mit Modellrechnungen des GRAZING-Codes verglichen. Die Ausbeute an überlebenden Aktinidenkernen wurde mit der von AGATA gemessenen Röntgenstrahlung, einem charakteristischen Fingerabdruck des jeweiligen Elements, verglichen. Die Diskussion der Ergebnisse zeigt Perspektiven und Limitierungen für die Produktion von schwer zugänglichen neutronenreichen Isotopen in der Aktinidenregion auf. Die Kernstruktur neutronenreicher Aktinide ist eine wichtige Richtgröße zur Bewertung theoretischer Modelle zur Beschreibung schwerster Transaktinide. Die Grundzustandsbande von ^{240}U konnte zu höheren Energien erweitert werden. Weiterhin gelang der Nachweis einer negativen Paritätsbande. Die Ergebnisse werden mit jüngst publizierten Mean-Field- und Funktionaldichtetheorie-Rechnungen verglichen. Multinukleontransferrreaktionen eignen sich ebenfalls als Zugang zu Kernen in der Region der magischen Schalenabschlüsse bei $Z = 50$ und $N = 82$. Kerne nordwestlich von ^{132}Sn sind wichtige Prüfmarken für moderne effektive Schalenmodellinteraktionen. Bedingt durch das Fehlen geeigneter Strahl-Target-Kombinationen ist die Produktion dieser Kerne jedoch oftmals sehr anspruchsvoll. Multinukleontransfer-Experimente an AGATA+PRISMA ($^{136}\text{Xe} + ^{238}\text{U}$ sowie $^{136}\text{Xe} + ^{208}\text{Pb}$), und an GAMMASPHERE+CHICO am LBNL ($^{136}\text{Xe} + ^{198}\text{Pt}$) erlauben eine detaillierte Spektroskopie von diversen schwer zugänglichen Isotopen in dieser Region der Nuklidkarte. Ferner wurden Xenon- und Bariumisotope mittels Fusionsverdampfungsreaktionen am HORUS-Aufbau an der Universität zu Köln spektroskopiert. Die Hochspin-Termschemata von ^{132}Xe , ^{133}Xe , ^{134}Xe , ^{135}Xe und ^{137}Ba wurden signifikant zu höheren Energien erweitert. Im Kern ^{135}Xe wurde der Zustand bei 2058 keV als Isomer mit einer Halbwertszeit von 9.0(9) ns identifiziert. Dieses Ergebnis schließt eine letzte verbliebene Lücke in der Systematik der Isotonenkette mit Neutronenzahl $N = 81$ und ergibt ein detaillierteres Bild der Isotopenregion. Die experimentell bestimmten reduzierten Übergangswahrscheinlichkeiten der isomeren Zustände werden mit Vorhersagen von Schalenmodellrechnungen konfrontiert. Ein weiterer Teil der Arbeit behandelt doppelseitig segmentierte Siliziumstreifen-Detektoren, welche in der Niederenergie-Kernphysik häufig zur Detektion geladener Teilchen eingesetzt werden. Diese Detektoren stellen nicht nur eine Energie-, sondern auch eine Ortsinformation mit hoher Detektorgranularität zur Verfügung. Überkreuzende Flächen von p- und n-dotierten Streifen formen hierbei einzelne Pixel. Bedingt durch Fabrikationsbeschränkungen und Limitierungen der Ausleseelektronik kann die Leistungsfähigkeit einzelner Kanäle drastisch variieren. Weiterhin illuminieren geladene Teilchen die Detektoroberfläche nicht gleichmäßig. Dies kann zu inhomogenen Strahlenschäden führen. Positionsabhängige Verluste bei der Ladungssammlung werden in einem In-Beam-Experiment sowie in einem dedizierten Testexperiment durch Bestrahlung mit einem radioaktiven Präparat untersucht. In diesem Zusammenhang wurde eine neuartige positionsabhängige Kalibrierungsmethode entwickelt, die auf der wechselseitigen Abhängigkeit der Ladungssammlung in der jeweils p- und n-dotierten Detektorseite beruht. Diese Kalibrierungsmethode erzielt eine signifikante Verbesserung der Energieauflösung und Messbefähigung von strahlengeschädigten Teilen des Detektorsystems.

Contents

1	Introduction	7
1.1	Nuclear reactions close and above the Coulomb barrier	7
1.1.1	Theory of multinucleon-transfer reactions	10
1.2	Nuclear structure northwest of ^{132}Sn	13
1.2.1	Reaction pathways for the study of high-spin states	13
1.2.2	Isomeric states northwest of ^{132}Sn	16
1.2.3	Existing experimental data in the $50 \leq Z, N \leq 82$ region	19
1.2.4	Shell-model interactions for the description of $50 \leq Z, N \leq 82$ nuclei . . .	21
1.3	Outline of this thesis	25
2	Light and heavy transfer products in the	
	$^{136}\text{Xe} + ^{238}\text{U}$ multinucleon transfer reaction	27
	Addendum: Simulation of the PRISMA spectrometer	41
3	Spectroscopy of the neutron-rich actinide nucleus ^{240}U	47
4	High-spin structure of ^{134}Xe	59
5	Isomers and high-spin structures	
	in the $N = 81$ isotones ^{135}Xe and ^{137}Ba	73
6	Characterization and calibration of radiation-damaged	
	double-sided silicon strip detectors	93
7	High-spin structures in ^{132}Xe and ^{133}Xe	
	and evidence for isomers along the $N = 79$ isotones	105
8	Summary and conclusions	121
	Bibliography	132
	List of figures	147
	Acknowledgments	153
	Curriculum vitae	157
	Erklärung zur Dissertation	158

Introduction

1.1 Nuclear reactions close and above the Coulomb barrier

Collisions between heavy ions close and above the Coulomb barrier yield a vast and diverse spectrum of reaction modes. Nuclear reactions can be classified by timescales, involved masses and kinetic energies, and by the impact parameter b . Simplified sketches of the different reaction mechanisms with varying penetration energy and impact parameter are given in Fig. 1 and in Fig. 2. Elastic Rutherford scattering and Coulomb excitation dominate for distant collisions, i.e. large impact parameters. If the energies of the colliding nuclei do not reach the *Coulomb barrier*, the trajectories are mostly governed by the electromagnetic interaction and are calculable with a high precision [1, 2].

At low impact parameters, a di-nuclear system is formed as a basic transitional stage between the entrance channel and the formation of reaction products [4]. At this initial phase of the reaction, the two fragments are linked by a neck [5]. In a head-on collision scenario at energies above the Coulomb barrier, fusion-evaporation reactions take place. The projectile is incorporated into the target nucleus and a hot compound nucleus, in which all degrees of freedom are populated, is formed. This highly-excited system reaches thermodynamic equilibrium in timescales of $t > 10^{-20}$ s and, subsequently, within 10^{-15} s, it evaporates nucleons and high-energy γ rays until the excitation energy is smaller than the particle-separation energy above the yrast line [6]. Depending on the number of emitted particles, various residual nuclei are populated which may further decay via γ -ray emission. Formation and decay of the compound nucleus are independent; the initial identities of projectile and target are lost. The excitation energy depends on the initial kinetic energy and the Q value

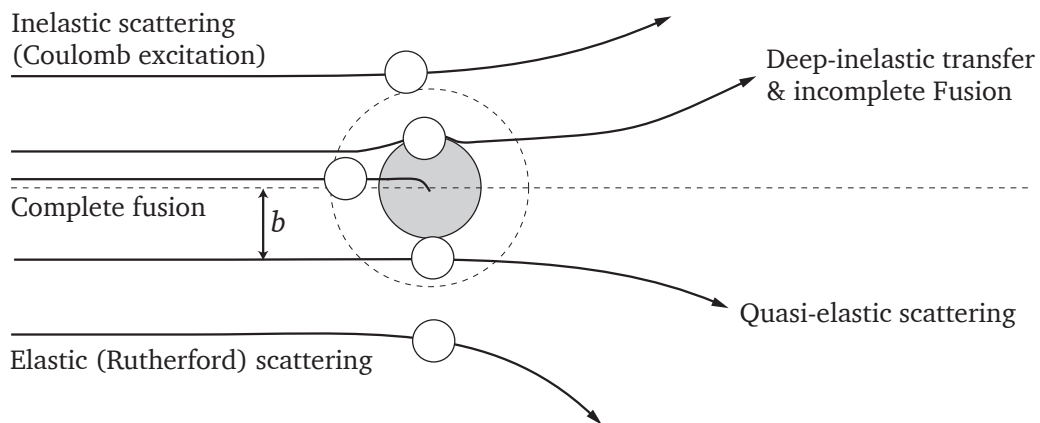


Figure 1: Reaction channels depending on the impact parameter. In the two regimes of multinucleon transfer, quasi-elastic and deep-inelastic transfer, beam- and target-like fragments retain a partial memory of the initial reaction channel. Production cross sections are maximized around a reaction-specific grazing angle. Adapted from Ref. [3].

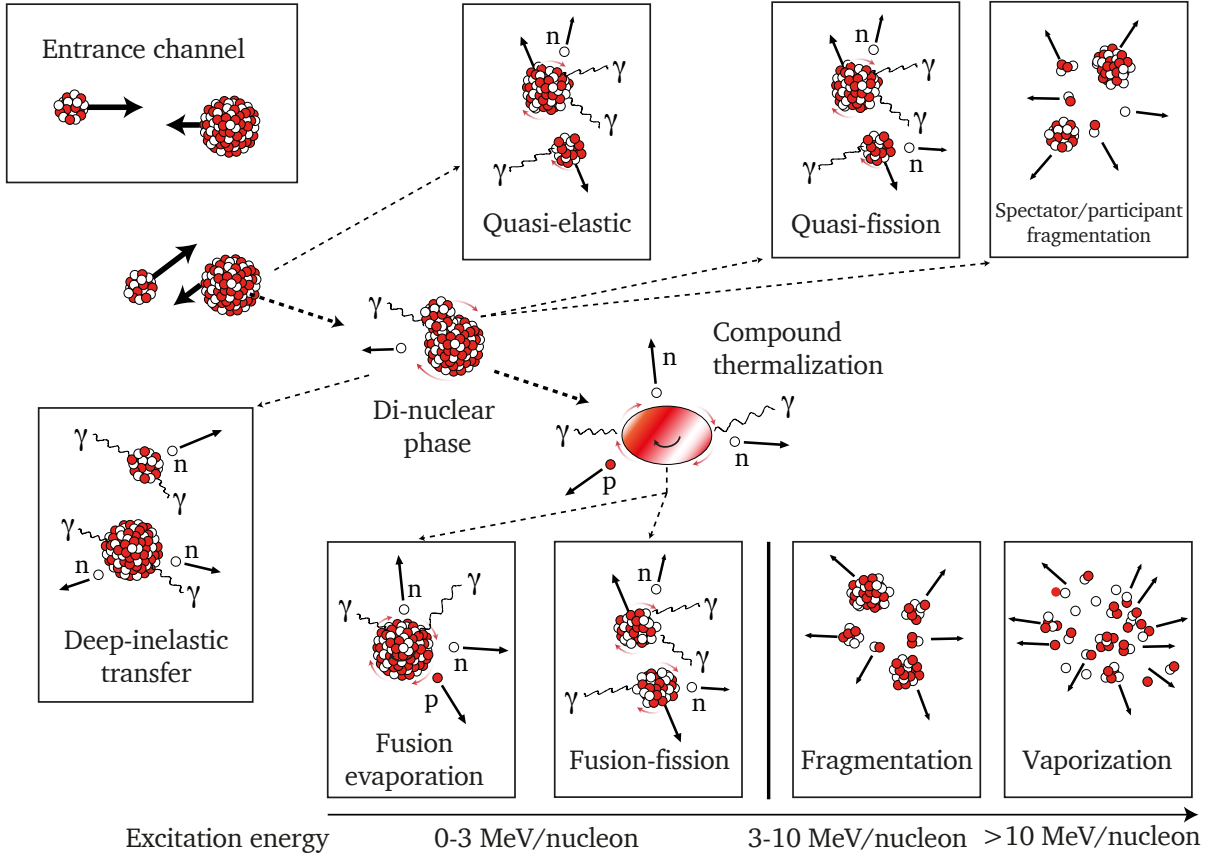


Figure 2: Regimes of nuclear reactions between heavy ions. Quasi-elastic reactions, deep-inelastic transfer and quasi-fission processes happen within small timescales in the early stages of the reaction, the so-called di-nuclear phase. Fusion-evaporation or fusion-fission reactions require the formation of a compound system. See text for details.

for the compound formation. If the transferred angular momentum is above a certain critical limit given by the mass of the compound nucleus, the compound system might also undergo fission. To be differentiated from this statistical fission is the so-called quasi-fission (QF) process [7] which occurs in the early di-nuclear stage of the collision in non-equilibrium before forming a compound nucleus: a nucleon transfer occurs from the heavy fragment toward the lighter one and the two fragments re-separate with a greater mass symmetry than in the initial entrance channel.

Between the two extremes of elastic scattering and fully-damped collisions leading to compound nuclei, there is a wealth of partially-damped inelastic collisions at intermediate impact parameters that are often referred to as multinucleon-transfer reactions [8]. Two regimes, nonetheless transitional in nature [9–12], can be distinguished: (i) quasi-elastic processes including inelastic scattering and the transfer of few nucleons, accompanied by small energy losses and (ii) deep-inelastic reactions with smaller impact parameters enabling larger-scale nucleon flow between the fragments. Latter is characterized by high values of total kinetic energy loss. Generally, essential features are the transfer of nucleons (from simple one-step transfers to complicated multistep reactions) and the partial conversion of kinetic energy of the projectile into internal excitation energy of the reaction residues.

The collisions keep the binary character of the system and the ejectiles retain some resemblance with the initial nuclei. Therefore, the reaction products are often called *beam-* and *target-like* fragments. There is a fast redistribution and rearrangement of nucleons among the colliding nuclei (N/Z equilibration), governed by strong driving forces associated with surface modes, single-particle degrees of freedom and tunneling probabilities in the di-nuclear complex. The reactions take place within approx. 10^{-22} s [6], similar to transfer reactions utilizing very light ions.

Since multinucleon-transfer reactions are peripheral collisions, the relative-motion angular momentum is dissipated into intrinsic spin of the reaction partners, although not as efficiently as in fusion-evaporation reactions. Experimentally, a precise knowledge of the grazing angle θ_{grazing} is crucial since it is the scattering angle at which the binary reaction cross section is maximized, rather than the ones of inelastic Coulomb or elastic interactions. Thus, to properly measure the highest production yields of reaction products, the solid-angle of a mass spectrometer measuring either of the reaction partners should cover a range around that specific angle. θ_{grazing} is approximated as the scattering angle that corresponds to the impact parameter when the two nuclei are just touching each other. There, the distance d is the sum of the radii of the nuclei participating in the reaction:

$$d = \left(\frac{Z_t Z_p e^2}{4\pi\epsilon_0 E_{\text{kin}}} \right) \left(1 + \csc \frac{\theta_{\text{grazing}}}{2} \right) \approx 1.2 (A_t^{1/3} + A_p^{1/3}) \text{ [fm]} \quad (1.1)$$

$Z_p e$ and $Z_t e$ correspond to the nuclear charges of the projectile and the target, A_p and A_t are their respective masses. E_{kin} is the kinetic energy of the impinging beam. The angular distributions of the reaction products are bell-shaped around the grazing angle [14, 15]. The evaporation of light particles from the primary fragments, especially neutrons, strongly influences the final isotopic yield distribution [8]. Figure 3 displays a typical production yield distribution of the $^{40}\text{Ca} + ^{208}\text{Pb}$ multinucleon-transfer reaction at $E_{\text{lab}} = 235$ MeV. Pure proton stripping and neutron pickup are

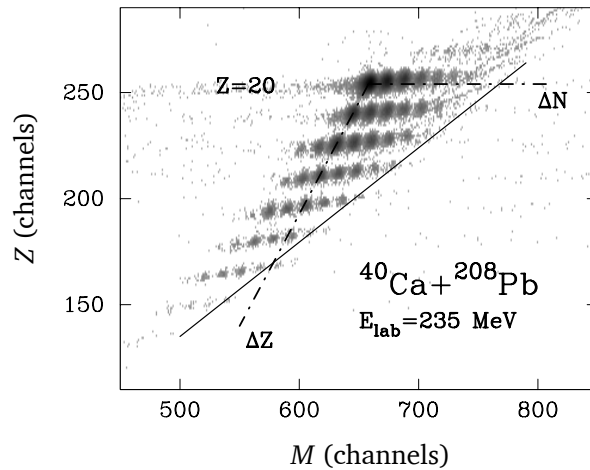


Figure 3: Distribution of mass and nuclear charge for the beam-like products of the $^{40}\text{Ca} + ^{208}\text{Pb}$ reaction at a beam energy of 235 MeV. The dashed lines label pure proton stripping and neutron pickup. The solid line depicts the N/Z charge equilibration. Reprinted figure with permission from Ref. [13]. Copyright by the American Physical Society.

labeled by dashed lines; the solid line depicts the confinement imposed by N/Z charge equilibration as well as by the optimum Q -value of the reaction. In this case, massive transfer of protons is accompanied by a drift towards lower masses, illustrating the role of particle (in this case neutron) evaporation. Thus, a specific reaction product may be accompanied by several binary partners. In the case of reaction systems involving heavier nuclei, especially actinide targets, the presence of fission may contaminate the genuine transfer channels [16].

For beam energies of 30 MeV/nucleon and above, so-called intermediate to relativistic energies, nuclear fragmentation is favored, populating a large range of exotic nuclei. These violent collisions can be described by the abrasion-ablation model in which the incoming projectile shears off the overlapping sector of the target nucleus (abrasion). The non-overlapping parts remain undisturbed in the collision and are often called spectators. The highly-excited, hot fragment of the overlap region (participant) decays via the emission of nucleons or further fragments; the spectator excess surface energy after the sudden abrasion is transformed into excitation energy [17]. Beam-like fragments carry on with a velocity similar to that of the initial beam. Projectile fragmentation is of interest in the production of radioactive ion beams employing large fragment separators [18] at in-flight fragmentation facilities like RIKEN, Japan [19], at the future facility FAIR in Darmstadt, Germany [20] or at its U.S. counterpart FRIB. Higher center-of-mass energies lead to even more violent reactions such as vaporization, leaving the area of low-energy nuclear-structure physics.

1.1.1 Theory of multinucleon-transfer reactions

The transfer of several nucleons between beam and target isotopes is a non-equilibrium quantum transport phenomenon which is not trivially computable. Several models aim for a description of partially-damped reactions in both the quasi-elastic and deep-inelastic regimes. Models with a reasonable predictive power should especially be able to predict how the total reaction cross section is shared among the different reaction channels. Multinucleon-transfer reactions have also been extensively analyzed by direct-reaction theories such as GRAZING and complex Wentzel-Kramers-Brillouin (CWKB) theory [21]. In these theories, the relative motion of the reaction partners is treated in a semi-classical approximation. The GRAZING model, based on the framework of direct reaction theory, is able to compute total reaction cross sections, angular distributions, excitation functions, and isotopic distributions for both pre- and post-neutron evaporation. The fundamentals of this model are briefly discussed in the following section.

Several models have been proposed for the description of deep-inelastic heavy-ion collisions, such as Fokker-Planck [22] equations, the so-called master equations [23], or the improved quantum molecular dynamics (ImQMD) model [24]. A successful description of mass transfer in multinucleon transfer was achieved within the time-dependent Hartree-Fock (TDHF) theory. This mean-field theory offers a microscopic framework yielding a full description of not only transfer, but all stages in the evolution of a nuclear collision. Recent developments were pursued by Sekizawa and Yabana [25, 26] employing the particle-number projection method [27, 28] for various reaction systems like $^{40}\text{Ca} + ^{208}\text{Pb}$, $^{58}\text{Ni} + ^{208}\text{Pb}$, $^{40,48}\text{Ca} + ^{124}\text{Sn}$, or $^{136}\text{Xe} + ^{198}\text{Pt}$. The colliding nuclei are treated as composite systems of individual neutrons and protons in their respective orbitals. Calculations are

performed in a three-dimensional grid with spatially separated projectile and target regions. While interacting, the two single-particle orbitals of the two nuclei extend to both spatial regions. Then, the probability distribution of the number of protons and neutrons in each region after the collision in the final wave function is calculated. By now, TDHF calculations yield not only encouraging quantitatively descriptions of multinucleon-transfer cross sections, but also insights into the time evolution and the reaction dynamics. Another recent macroscopic approach combines the two-center shell model and an unified adiabatic potential-energy surface with Langevin-type dynamical equations of motion for the description of the nucleon transport in low-energy multinucleon transfer. The potential energy surfaces depend on the distance, nuclear deformation, and the mass asymmetry of the colliding nuclei. A multitude of studies were published by Zagrebaev and Greiner [29, 30]; in particular, the prospects of multinucleon transfer for the production of superheavy nuclei using heavy beams and targets received much attention [31–35].

Grazing The GRAZING model, originally developed by A. Winther [36–38] is implemented in the computer code GRAZING maintained by G. Pollaro [39]. It uses a microscopic approach to multinucleon transfer, covering both the quasi-elastic and the deep-inelastic regimes. In the GRAZING model, colliding nuclei are assumed as ensembles of independent nucleons vibrating around their spherical equilibrium shapes. As the nuclei are many-body quantum systems, the wave functions are a superposition of a set of intrinsic states. The structure of the nucleus strongly affects the reaction dynamics and the evolution of the multinucleon-transfer reaction is an interplay between reaction mechanism and the intrinsic states of the colliding nuclei. Therefore, GRAZING calculates the evolution of the reaction in a coupled-channel formalism considering the orbits of the relative motion in a classical limit. This semi-classical treatment is justified as the reduced wavelength λ associated with the relative motion of two masses A_1 and A_2 and the incident center-of-mass energy E on top of the Coulomb barrier V_{CB} , approximated [40] as

$$\lambda \text{ [fm]} \approx \sqrt{\frac{A_1 + A_2}{A_1 A_2} \frac{20}{(E - V_{CB}) \text{ [MeV]}}} , \quad (1.2)$$

is much smaller than the interaction region, i.e., the distance d between two nuclei (cf. equation 1.1). The GRAZING model defines the total wave function as follows [41]:

$$\psi(t) = \sum_{\beta} c_{\beta}(t) \psi_{\beta} \exp\left(\frac{i}{\hbar} (E_{\beta} t + \delta_{\beta}(t))\right) . \quad (1.3)$$

The coefficients $c_{\beta}(t)$ are the amplitudes for the system in channel β at time t . E_{β} is the corresponding energy. The time-dependent phases δ_{α} and δ_{β} are defined as the integrals over the Lagrangian of the relative motion and describe the curved trajectory of the two ions: $\delta_{\beta} = \int^t \mathcal{L}_{\beta}(t) dt$. In the following, the reaction is labeled as $a + A \rightarrow b + B$. The channel wave functions ψ_{α} , expanded in terms of intrinsic states of the different involved mass partitions, here (A, a) , are given as

$$\psi_{\alpha}(t) = \psi^a(t) \psi^A(t) \exp(i\delta(\vec{R})) . \quad (1.4)$$

To consider non-linear motion in the Coulomb plus nuclear field, a semi-classical phase $\delta(\vec{R})$, \vec{R} being the distance between the center-of-mass of the two nuclei, is introduced. By inserting equation 1.3 into the time-dependent Schrödinger equation

$$i\hbar \frac{d}{dt} \psi(t) = i\hbar \dot{\psi}(t) = (H_0 + V) \psi(t) , \quad (1.5)$$

one obtains a system of semi-classical coupled equations describing the time evolution of the collision process [41, 42]:

$$i\hbar \dot{c}_\beta(t) = \sum_\alpha c_\alpha(t) \langle \beta | H_{\text{int}} | \alpha \rangle \exp\left(\frac{i}{\hbar} (E_\beta - E_\alpha)t + i(\delta_\beta - \delta_\alpha)\right) \quad (1.6)$$

The labels α and β denote the entrance and exit channels, respectively. All equations are solved under the condition that for $t = -\infty$ the system is in its entrance channel α (i.e. $c_\beta(t = -\infty) = \delta_{\alpha\beta}$). The intrinsic Hamiltonian and the interaction operator for the projectile (a) and the target (A) are defined as:

$$H_0 = H_a + H_A + V_{\text{int}} = \sum_{i \equiv (nljm)}^{(a)} \epsilon_i a_i^\dagger a_i + \sum_{\lambda\mu}^{(a)} \hbar\omega_\lambda a_{\lambda\mu}^\dagger a_{\lambda\mu} + (A) + V_{\text{transfer}} + V_{\text{inel.}} + \Delta U_{aA} \quad (1.7)$$

The operators a and a^\dagger are the fermion operators to annihilate or create a particle with energy ϵ_i and quantum number $i \equiv (nljm)$ on the single-particle level. The second term parametrizes the excitation of surface modes with multipolarity $\lambda\mu$. The interaction potential V_{int} contains three terms. V_{transfer} includes form factors for the single-nucleon stripping- and pick-up transfer reactions. $V_{\text{inel.}}$ holds the corresponding form-factors for inelastic excitation, thus, surface degrees of freedom such as the first quadrupole (2^+) and octupole (3^-) vibrations and higher-lying giant resonances. The colliding ions a and A interact via a Coulomb-plus-nuclear interaction [38]. Resulting modifications of the effective potential for the radial motion are parametrized in the term ΔU_{aA} . The Coulomb part is described by two point charges, while the nuclear potential is approximated by a Woods-Saxon potential in the so-called Akyüz-Winther parametrization [43].

Cross sections are obtained by evaluating with which probabilities $P_{\alpha\beta}$ the two ions exchange nucleons during the collision. Considering the trajectory of the Newtonian motion, the transition from channel α to β can be approximated as

$$P_{\beta\alpha} = \sqrt{\frac{1}{16\pi\hbar^2|\ddot{r}_0|\kappa}} |f_{\beta\alpha}(0, r_0)|^2 \exp\left(-\frac{(Q - Q_{\text{opt}})^2}{\hbar^2\ddot{r}_0\kappa}\right) \quad (1.8)$$

The optimum Q value, at which the maximum probability is reached, is defined as

$$Q_{\text{opt}} = \left(\frac{Z_d}{Z_A} - \frac{Z_d}{Z_b}\right) E_B + \left(\frac{m_d}{m_b} - \frac{m_d}{m_A}\right) (E - E_B) + \frac{m_d \ddot{r}}{m_a + m_A} (R_A m_b - R_a m_B) \quad (1.9)$$

with m_d and Z_d the mass and charge of the transferred particle and E_B the Coulomb barrier [38].

\ddot{r}_0 is the radial acceleration at the distance of closest approach r_0 between the two nuclei. The matrix element $f_{\beta\alpha}$ describes the overlap of initial and final states in the transfer, the coefficient κ contains the energy of the single-particle binding energy at the beginning of the channel transition. The transfer of more than one nucleon is estimated in a successive approximation [8]. Thus, for example, a two-neutron transfer is computed as a sequential transfer of two uncorrelated neutrons. The assumption of an independent particle transfer is supported by the experimental observation that neutron pick-up yields decrease by a constant factor for each transferred neutron. Predictions from the GRAZING model were successfully confronted with complex DWBA calculations [44] and a variety of experimental data (cf. Refs. [14, 45, 46]). Besides single-particle transfer modes, other degrees of freedom may also be of high importance. For instance, the role of pair-transfer modes or the exchange of clusters seem to be crucial and remain a current subject of research [16, 47, 48].

1.2 Nuclear structure northwest of ^{132}Sn

1.2.1 Reaction pathways for the study of high-spin states

Detailed nuclear-structure data of very neutron-deficient nuclei extends to nuclei at or even beyond the proton-drip lines [49–51]. It is possible to form very neutron-deficient compound systems at the extremes of angular momentum using fusion-evaporation reactions with stable beam-target combinations. Imparting the largest possible angular momentum into the nucleus of interest, fusion-evaporation reactions are the best way to produce high-spin states at high excitation energies with large production cross-sections. The Segrè chart plotted in Fig. 4 shows the compound nuclei (unfilled boxes) which are accessible via stable (black boxes) beam- and target combinations. It is recognizable that standard fusion-evaporation experiments indeed favor the production of more neutron-deficient systems in the nuclear landscape. Especially on the neutron-rich side, the pattern on the chart is not to be mistaken with the accessible yield of evaporation residues as the evaporation of neutrons dominates for compound nuclei with a large N/Z ratio along the valley of stability. Therefore, the observation of high-spin structures, e.g. yrast sequences up to energies at which interesting effects such as backbending occur [52], new features such as shape coexistence [53] or deformed collective bands [54, 55] is quite demanding for (even moderate) neutron-rich nuclei.

There is a considerable and not negligible number of only slightly neutron-rich nuclei near the valley of stability that cannot be easily populated up to high excitation energies since fusion-evaporation reactions are not applicable due to a lack of suitable stable beam-target combinations. Only for a few cases of β -stable nuclei and nuclei with a few nucleons to the neutron-rich side of the valley of stability, fusion-evaporation reactions are appropriate experimental techniques. Noticeable examples are reactions involving the exposed neutron-rich nucleus ^{48}Ca [58–63]. Further cases are nuclei northwest of ^{132}Sn in the Segrè chart, among them Xe and Ba isotopes like $^{131-134}\text{Xe}$ or $^{136,137}\text{Ba}$. There, the basic concept is to form a compound system with the largest neutron excess possible and to employ a charged-particle detector array to detect evaporated charged particles such as protons and α -particles. However, for neutron-rich compound systems, charged-particle evaporation

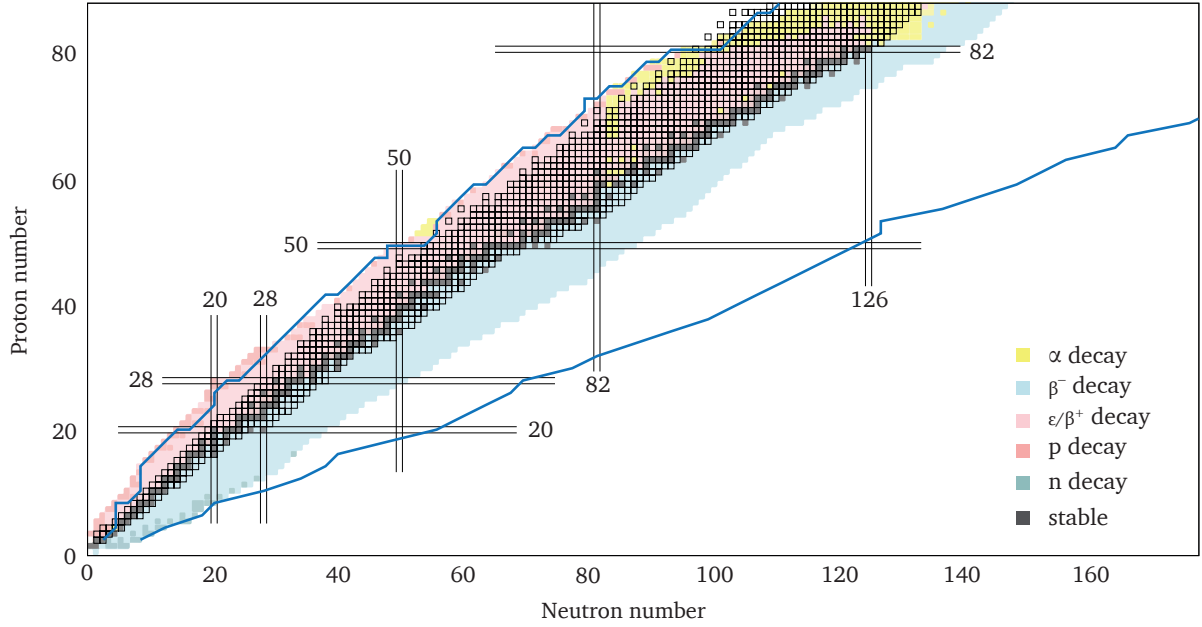


Figure 4: Segrè chart showing the compound nuclei [56] (open boxes) which can be formed in fusion-evaporation reactions using stable beam/target combinations. Fusion-evaporation reactions favor the production of neutron-deficient systems. The population of slightly neutron-rich nuclei beyond the valley of stability (filled black boxes) is very challenging employing compound reactions. The nuclear drip lines (blue lines) are taken from a covariant density-functional theory calculation using the NL3* functional by Agbemava *et al.* published in Ref. [57]. Magic shell closures are shown by solid black lines. The inset presents the color code of the different decay types present in the chart.

is hindered by the Coulomb barrier of the compound nucleus leading to integrated cross sections of a few mb. Therefore, a clean selection of the elusive reaction channels is crucial to overcome the larger neutron-evaporation cross sections and to perform spectroscopy studies.

In the region northwest of ^{132}Sn , the most neutron-rich stable targets are ^{124}Sn and ^{130}Te . Direct reactions with light ions (protons, deuterons, tritons, et cetera), which are well-suited to probe single-particle properties such as spectroscopic factors, are unfortunately highly selective regarding energy and angular momentum transfer. Alpha-induced fusion-evaporation reactions on ^{130}Te would not provide the required angular momentum and energy transfer. A beam of ^9Be impinging on Sn or Te targets would be well-suited to populate the neutron-rich Xe and Ba isotopes, yielding a pure neutron-evaporation channel with large production cross sections. Unfortunately, since inhaled beryllium dusts are highly toxic, ^9Be beams are often not provided in accelerator facilities. The isotope ^{134}Xe may be populated in a $^{130}\text{Te}(^7\text{Li}, p2n)$ fusion-evaporation reaction, however, the population cross section in the proton-evaporation channel yields only a few mb. ^{135}Xe would not be accessible by this reaction. Nonetheless, a higher mass of the projectile is preferred since it provides a higher angular momentum transfer and, therefore, leads to higher excitation energies in the residual nuclei. $^{10,11}\text{B}$ or even carbon beams would result in an adequate angular momentum transfer, nevertheless, the cross sections are again rather small. The advent of radioactive ion beam (RIB) facilities [18] opens

novel possibilities for studies employing fusion-evaporation reactions with low-energy radioactive nuclear beams. Recently, radioactive ^{17}N beams were successfully employed at the Research Center for Nuclear Physics (RCNP), Osaka to study the high-spin structure of ^{136}La [64]. However, these secondary beams are hard to produce, not yet widely accessible to the nuclear-physics community, and the beam intensities are still relatively small.

Another preferable way to study intermediate and high-spin features of neutron-rich nuclei in the vicinity of ^{132}Sn is to perform prompt γ -ray spectroscopy of fission fragments which are populated by (i) spontaneous fission sources, (ii) thermal neutron-induced fission of actinides or (iii) the exploitation of fusion-fission following fusion-evaporation reactions. Particularly successful experimental campaigns were undertaken employing ^{248}Cm and ^{252}Cf fission sources [65] at the GAMMASPHERE [66] array, the EUROBALL [67] setup at the Vivitron accelerator of IReS (Strasbourg) and the Tandem XTU accelerator in Legnaro or the EUROGAM [68] array at ILL. By exploiting triple- and higher-fold γ -coincidence events, the data enabled a plethora of new discoveries and have given great insight into the structure of very neutron-rich systems. One example is the observation of alternating-parity bands in various barium, lanthanum and cerium isotopes [69–71], confirming theoretical predictions of enhanced octupole collectivity in this region. However, slightly neutron-rich nuclei such as ^{136}Ba or ^{137}Ba are not accessible with sufficient yields [72, 73] employing spontaneous fission. Another efficient gateway to neutron-rich systems is fusion-fission after fusion evaporation reactions. For instance, various reaction products of $^{12}\text{C} + ^{238}\text{U}$ and $^{18}\text{O} + ^{208}\text{Pb}$ reactions were studied utilizing the EUROBALL γ -ray array [74] at the Legnaro XTU Tandem accelerator and at the Strasbourg Vivitron accelerator complex. Comprehensive results on high-spin structures were obtained for several nuclei in the $50 \leq Z, N \leq 82$ region, such as for five $N = 82$ nuclei ranging from ^{136}Xe to ^{140}Ce [75], for the odd-odd $N = 81$ isotones ^{136}Cs [76] and ^{138}La [77], and for the $^{119-126}\text{Sn}$ [78] and $^{124-131}\text{Te}$ [79] chains. Nevertheless, all of these approaches pose a certain common challenge: the experiments require very selective coincidences to individually identify the often elusive reaction channels from hundreds of populated channels. An unambiguous assignment of new γ rays requires coincidences between complementary fission fragments, thus, neutron evaporation has to be treated with great caution.

Multinucleon-transfer reactions involving heavy ions offer an efficient gateway for the synthesis of neutron-rich nuclei along the valley of stability and towards the neutron-rich side that cannot be produced by means of other production methods [8, 80]. In the last decades, multinucleon transfer was mainly employed in thick-target experiments with large arrays of germanium detectors. Pioneering work was performed by Broda *et al.* [81, 82] and Cocks *et al.* [83]. Nowadays, by employing high-resolution and large-acceptance mass spectrometers with trajectory reconstruction, sensitive experiments are also possible employing thin targets. Particle- γ coincidences enable a significant increase of the detection limits. Moreover, γ -ray transitions can be uniquely attributed to the specific isotopes by identifying both mass and charge. A very precise Doppler correction for γ rays emitted by both beam- and target-like fragments is achievable by state-of-the-art γ -ray tracking spectrometers like the European Advanced Gamma Tracking Array (AGATA) [84].

Several multinucleon-transfer experiments were carried out at the AGATA+PRISMA setup and the former CLARA+PRISMA setup at the Laboratori Nazionali di Legnaro (LNL, Italy), as well as at the VAMOS+EXOAM and VAMOS+AGATA setups at the Grand Accélérateur National d'Ions Lourds (GANIL, France). During the physics campaign at the LNL from 2010 to 2011, the AGATA spectrometer in the demonstrator configuration [85] consisted of five cluster detectors [86], each holding three high-purity germanium crystals. These large-volume crystals are electronically divided into 36 segments, yielding a total of 555 high-resolution spectroscopy channels. By using an online pulse-shape analysis and tracking algorithms, the segmentation enables a position determination of each γ -ray interaction within the crystal with a precision of few mm [87]. The AGATA demonstrator was installed around the target position and employed together with the magnetic mass spectrometer PRISMA [88] which is able to fully identify mass A , nuclear charge Z and atomic charge state q of the incoming ions. This detector combination is especially suited for the spectroscopy of exotic nuclei populated in multinucleon-transfer reactions since the selectivity of the reaction channel in a mass spectrometer is far superior to that of $\gamma\gamma$ or $\gamma\gamma\gamma$ coincidences in thick-target experiments if no γ -ray transitions are known for the nucleus of interest. Noticeable cases from the recent past are the challenging γ -ray spectroscopy study of neutron-rich ^{196}Os in the $-2p$ channel after $^{82}\text{Se} + ^{198}\text{Pt}$ multinucleon transfer [89] by John *et al.* and the yrast-band spectroscopy of $^{168,170}\text{Dy}$ in the $^{82}\text{Se} + ^{170}\text{Er}$ reaction by Söderström *et al.* [90].

1.2.2 Isomeric states northwest of ^{132}Sn

The $50 \leq Z, N \leq 82$ nuclei outside the doubly-magic nucleus ^{132}Sn can be described within the valence space made up by the major shells $0g_{7/2}$, $1d_{5/2}$, $1d_{3/2}$, $2s_{1/2}$, and $0h_{11/2}$. The corresponding orbital arrangement is depicted in Fig. 5. Excitations in nuclei near to ^{132}Sn are expected to exhibit predominantly single-particle characteristics. Metastable, long-lived nuclear excited states, i.e. isomers, are important signatures for sudden changes in the underlying nuclear structure [91]. Small overlap and large differences between the initial and final wave functions of the states involved in the decay cause a transition hindrance. Hence, it is of particular interest to study the evolution of isomers and states built on top as a function of the gradual filling of shell-model orbitals along shell closures. Isomers can be caused by various underlying mechanisms. Large changes in spin (spin trap) require higher-order multipole decays which are accompanied by lower transition rates and, hence, longer lifetimes. Other mechanisms involve drastic changes in the structure or shape (e.g. fission isomers), the underlying symmetry (K -isomers), or small transition energies between states as the electromagnetic transition rate depends on $E_\gamma^{(2\lambda+1)}$ favoring high-energy transitions and the lowest possible multipolarity λ . Latter cases can often be characterized as *seniority* isomers in the $50 \leq Z, N \leq 82$ region. The seniority quantum number ν is defined as the number of unpaired nucleons; a seniority isomer is a nuclear state with an electromagnetic decay that is hindered by selection rules related to the seniority quantum number.

A rather large energy gap between the $0g_{7/2}$ and $1d_{5/2}$ orbitals and the $1d_{3/2}$, $2s_{1/2}$, and $0h_{11/2}$ orbitals gives rise to a subshell-closure at $Z = 64$ and is reflected in the magicity of ^{146}Gd . However,

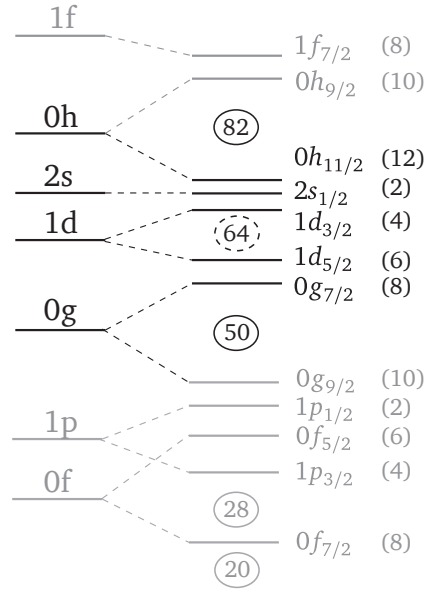


Figure 5: Excerpt of single-particle orbitals in the nuclear shell model. The $0g_{7/2}$, $1d_{5/2}$, $1d_{3/2}$, $2s_{1/2}$, and $0h_{11/2}$ orbitals lie between the $Z, N = 50$ and 82 magic numbers, $Z, N = 64$ is a sub-shell closure.

no discontinuity in the level structure is observed for the $N = 64$ counterpart nucleus along the $Z = 50$ chain, ^{114}Sn . Several typical isomeric states and level systematics are observed in the nuclei outside proton number 50 and neutron number 82. A compilation of all hitherto known $J^\pi = 6^+, 7^-, 10^+$, and $11/2^-$ isomers is displayed in a simplified Segrè chart in Fig. 6. The broad presence of $11/2^-$ isomers in the odd-mass nuclei with $64 < N < 82$ and $50 \leq Z < 64$ (cf. blue points in Fig. 6) demonstrates the essential role of the high- j , $h_{11/2}$ intruder orbital in this region. Predominantly, these isomers decay to the $3/2^+$ ground state by $M4$ γ -ray emission. Microsecond isomers of spin $J^\pi = 19/2^+$ were observed in $^{119-129}\text{Sn}$ isotopes. Here, the dominant single-particle configuration is $h_{11/2}^{-1} \otimes 5^-$; corresponding 5^- states are isomeric too, mostly with lifetimes in the ns regime, some in the μs range. Yrast isomers with spin $J^\pi = 23/2^+$ and $J^\pi = 27/2^-$ are present throughout the Sn chain [78, 92]. These multiplets of seniority $\nu = 3$ have dominant $\nu[d_{3/2}^{-1} h_{11/2}^{-n}]$ and $h_{11/2}^{-n}$ configurations, respectively. The decomposition of states in the Te and Xe isotopes is more complicated as the wave functions contain also proton- and not only neutron components; in addition, also proton-pair breaking has to be taken into account [79].

There is an increased occurrence of yrast isomeric 10^+ states in the even-even Sn and Te isotopes with $N < 82$, many of them with half-lives in the μs region. The energies of the transitions deexciting the isomers are generally very small and strongly converted. Likewise, 10^+ isomers accumulate in moderately neutron-rich Xe and Ba isotopes, as well throughout the $N = 78$, $N = 80$, and more proton-rich $N = 82$ isotones above the $Z = 50$ shell closure. Along the $N = 80$ isotones, between ^{130}Sn and ^{142}Sm , these isomers are predominantly of $\nu h_{11/2}^{-2}$ character and seniority $\nu = 2$. The $10^+ \rightarrow 8^+$ isomeric transitions of ^{132}Te and ^{134}Xe have very low energies of 22 and 28 keV, respectively [94]. A similar small level spacing of 18 keV was found in ^{130}Te [79]. In ^{132}Xe , the 8_1^+ level is still unknown.

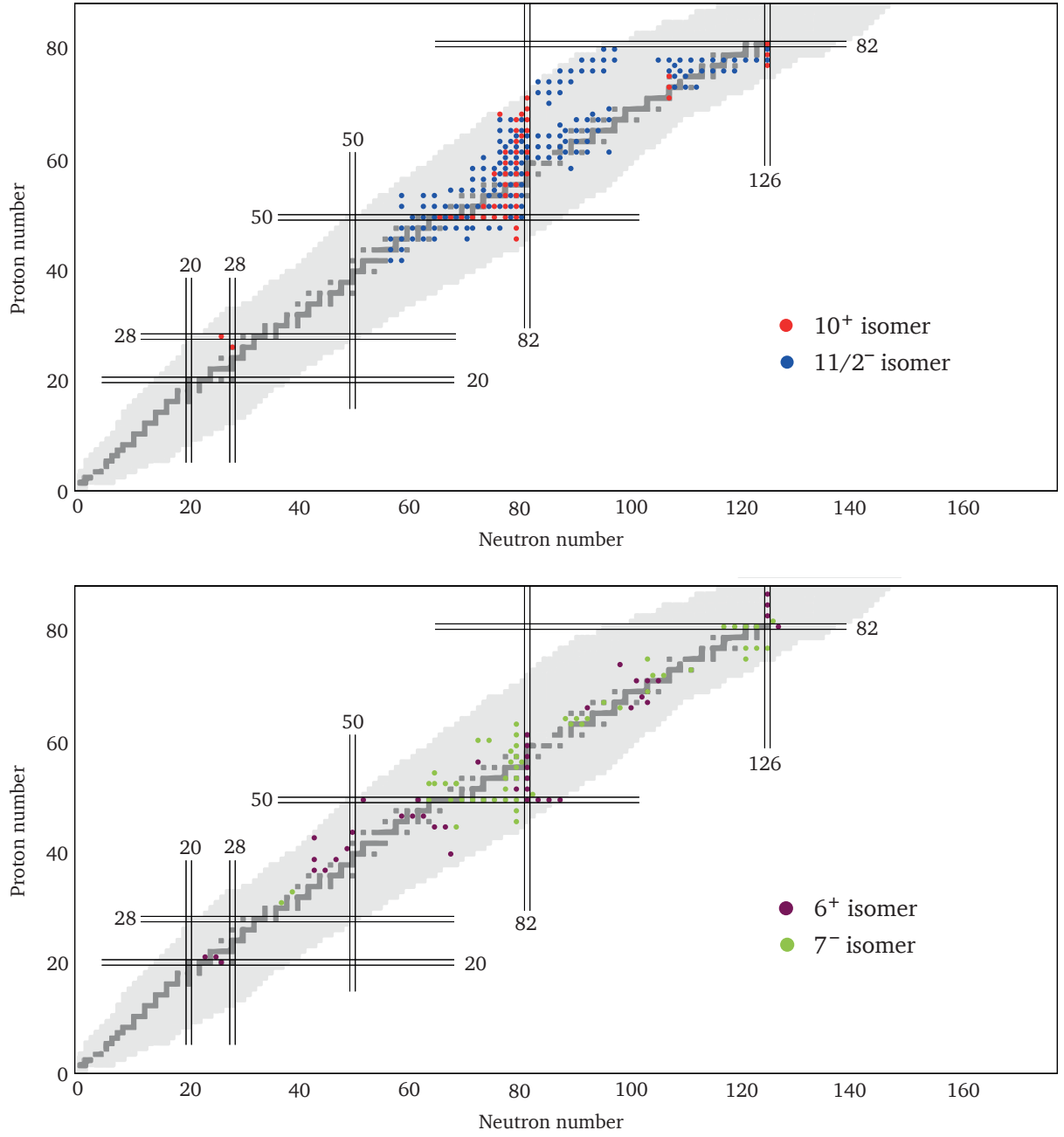


Figure 6: Simplified Segrè charts showing (top) all known 10^+ (red circles), $11/2^-$ (blue circles), (bottom) 6^+ (purple circles), and 7^- (green circles) isomers with half-lives longer than 10 ns. Solid black lines depict magic numbers. Isomer data extracted from Ref. [93].

The 10^+ isomers in the proton-rich $N = 82$ isotones above the sub-shell closure at $Z = 64$ can be attributed to $\pi h_{11/2}$ configurations and the presence of a pair excitation out of the $Z = 64$ core [95]. Furthermore, several even-even isotopes, especially along the $N = 80$ chain, exhibit mixed-orbital 7^- isomers (green points in Fig. 6) that are in many cases of $\nu(h_{11/2}^{-1} d_{3/2}^{-1})$ character. Along the even-even $^{118-126}\text{Sn}$ isotopes, the 7^- states decay via E2 transitions to the 5^- states with a dominant $\nu(s_{1/2}^{-1} h_{11/2}^{-1})$ quasi-particle configuration. In contrast, the 5^- state is above the 7^- state in the neutron-rich ^{128}Sn

and ^{130}Sn isotopes due to a reduced $s_{1/2}$ component in their wave functions. Here, the half-lives of the 7^- states exceed the μs range. In $^{120-132}\text{Te}$ and ^{134}Xe , the 7^- states predominantly decay to the yrast 6^+ states, whereas in ^{130}Xe and ^{132}Xe the decay to the 5^- state is favored again. It is worthwhile to mention that in both ^{132}Te and ^{132}Xe the 7^- state is fed by the decay of the 10^+ isomer via an $E3$ γ -ray transition [96]. Also, higher-seniority isomers with $\nu = 4$ and spin 15^- have been recently identified in several even-even Sn isotopes from $A = 120$ to 130 [97, 98].

The even-even $N = 82$ nuclei with fully-filled neutron orbitals exhibit typical yrast 6^+ isomers from ^{132}Sn up to ^{144}Sm . Lifetimes span from hundreds of ns to few μs . These isomers are explained by the breaking of one proton pair [75]. For example, in the simplest two-proton state of ^{132}Sn , ^{134}Te , the 6^+ state is predominantly of the $\pi g_{7/2}^2$ configuration and two protons are coupled to maximum angular momentum. For ^{137}Cs and ^{138}Ba it was pointed out, that also $\nu h_{11/2}^{-1} f_{7/2}^1$ neutron cross-shell excitations to the $N = 82$ -126 shells have to be considered for the description of intermediate-spin states [75, 99].

1.2.3 Existing experimental data in the $50 \leq Z, N \leq 82$ region

Precise and extensive experimental information is crucial to test nuclear models such as the nuclear shell model and to ascertain their ability to provide reliable predictions and to give insight into the shell evolution and its underlying driving forces. Detailed studies of nuclei in the vicinity of magic numbers are of utmost importance to establish single-particle energies and two-body matrix elements for shell-model residual interactions. The proximity of ^{132}Sn is a unique region around a heavy, neutron-rich nucleus with doubly-closed shells far-off stability that is experimentally accessible today. The other neutron-rich closed-shell nuclei are either stable (^{48}Ca and ^{208}Pb) or hardly accessible like ^{78}Ni which is much further away from the stability line.

Nuclei south ($Z < 50$) and (north)east ($N > 82$) of ^{132}Sn are of great importance for the description of the $A \approx 130$ peak in nucleosynthesis and solar r-process abundance calculations. Corresponding nuclei can be produced and separated at radioactive ion-beam facilities via in-flight fission. The exotic nuclei of interest are implanted into Si detector arrays. Thereafter, the γ radiation after β decay or β -delayed neutron emission is studied with HPGe detectors. Important results on neutron-rich Pd, Cd, In, Sn and Sb isotopes and the evolution of the $N = 82$ shell gap were recently obtained at RIKEN and GSI [100–105].

The $50 \leq Z, N \leq 82$ nuclei are not as exotic as their aforementioned counterparts around ^{132}Sn , nonetheless, the region provides a fertile study ground for the evolution of nuclear structure and the interplay between single-particle and collective degrees of freedom. Several nuclei, such as ^{130}Te or ^{136}Xe , attracted attention as candidates for the yet unobserved neutrino-less $0\nu 2\beta$ decay [106, 107]. Figure 7 presents a partial Segrè chart of the $50 \leq Z, N \leq 82$ nuclei northwest of ^{132}Sn . The color code shows the maximum excitation energy, affiliated with high spins, which were obtained in γ -ray spectroscopy experiments. A plethora of experimental information is available for nuclei with $Z > 54$ and $N < 78$. Detailed spectroscopy was performed up to highest spins and energies in

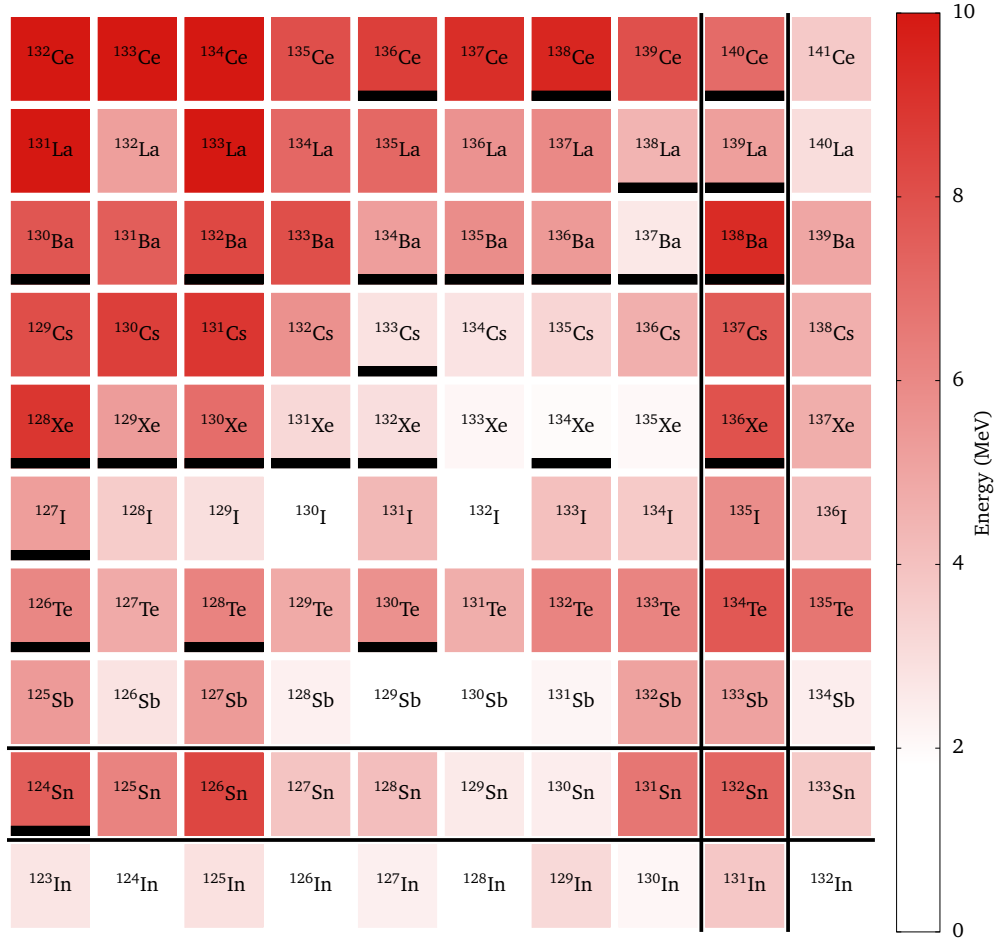


Figure 7: Partial Segrè chart of nuclei northwest of ^{132}Sn . The color code represents the maximum excitation energy which was observed in γ -ray spectroscopy experiments aiming at the measurement of high spins. High-lying low-spin excitations such as giant resonances are not taken into account. Black horizontal lines mark stable isotopes.

several transitional nuclei. For example, the maximum measured excitation energies are 17.3 MeV in ^{131}La [108] and $26.8 + x$ MeV in ^{132}Ce [109]. Various super-deformed bands have been observed in these nuclei. On the other hand, there is only scarce information on xenon isotopes with masses ranging from $A = 131$ to 135. Although stable, level schemes and high-spin data for ^{131}Xe , ^{132}Xe , and ^{134}Xe are only available for excitation energies up to approx. 3 MeV [110, 111]. In ^{133}Xe , excited states are only known up to 2.1 MeV [112]. Similarly, the level scheme of ^{137}Ba is measured up to 2.4 MeV [113]. Further “blank spots” visible in Fig. 7 are located along the antimony and iodine isotopic chains. Figure 8 shows the evolution of the yrast positive-parity states and the first 7^- states. Moving toward midshell, there are only minor changes in the excitation spectra, which are rotational in character, i.e. $E \propto J(J+1)$. Toward the $N = 82$ shell closure at ^{136}Xe , a characteristic transition to a vibrational character ($E \propto J$) is observed. Here, crucial information on high-spin states above the isomeric 10^+ states in ^{132}Xe and ^{134}Xe is missing.

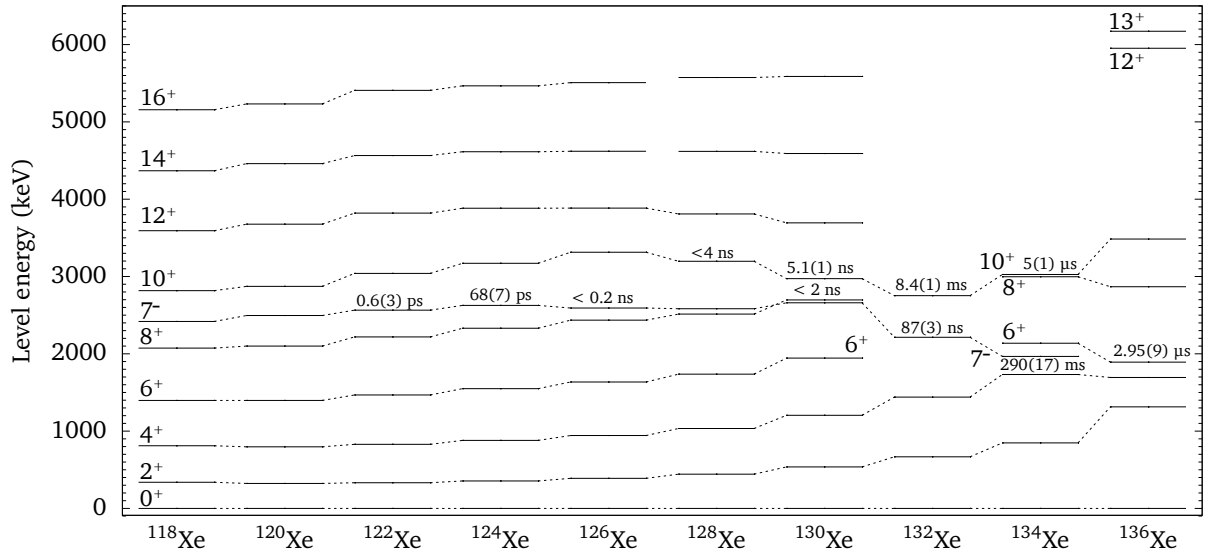


Figure 8: Evolution of yrast positive-parity states and the first 7^- states along the $Z = 54$ chain. Dashed lines connecting levels of same spin/parity are drawn to guide the eye. The 10^+ and 7^- states of xenon isotopes with $A > 130$ are isomeric in character. Half-lives are given by the labels above the states. Data extracted from ENSDF database [114].

1.2.4 Shell-model interactions for the description of $50 \leq Z, N \leq 82$ nuclei

The $50 \leq Z, N \leq 82$ nuclei are theoretically accessible by state-of-the-art large-scale shell model (LSSM) calculations with either ^{100}Sn or ^{132}Sn as inert cores. As x neutron particles with regard to ^{100}Sn are equivalent to $32-x$ neutron holes from the perspective of ^{132}Sn , calculations are manageable with existing shell-model codes and were performed within this work. Two different shell-model codes were used in this thesis: (i) NUSHELLX@MSU [115] based on the coupled jj scheme and, (ii), KSHELL [116] which is based on the uncoupled m scheme. The jj scheme has the advantage of yielding shell-model Hamiltonian matrices of relatively small dimensions. On the other hand, these matrices are very dense and have complex algebraic structures. Contrarily to NUSHELLX@MSU, the KSHELL does not provide detailed information on the shell-model configurations, spin decompositions, and couplings. However, the KSHELL code enables massive parallel computation employing an OpenMP-MPI (Message Passing Interface) hybrid with a speed advantage of up to a factor of 30 compared to NUSHELLX@MSU on the servers installed at IKP Cologne. The eigenvalues of the Hamiltonian matrix are solved “on-the-fly” by utilizing the Thick-Restart Lanczos method. The Lanczos vectors are stored in the random-access memory.

The m -scheme dimension, i.e. the number of Slater determinants to be solved, is a measure of calculability and expected computing time. Dimensions up to the order of 10^9 are computationally accessible today without truncations of the model space. The m -scheme dimensions in an untruncated shell-model calculation without core excitations are presented in Fig. 9 for nuclei with $N \geq 73$ and $Z \geq 50$. For all cases that are subject to this thesis – namely the xenon isotopes $^{132-135}\text{Xe}$ and ^{137}Ba – the number of valence nucleons does not necessitate a truncation of the full model space and calculations can be performed within a reasonable amount of computing time on parallel processors.

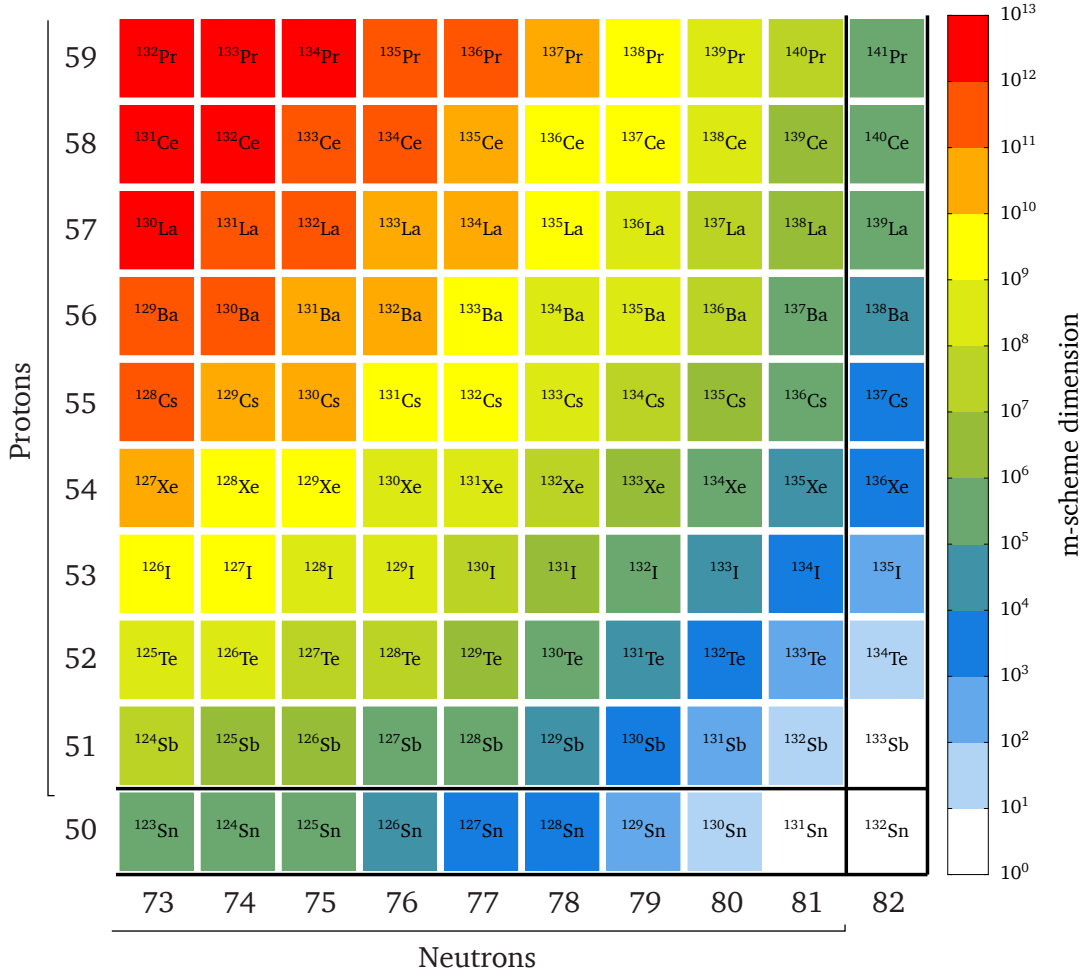


Figure 9: Partial Segrè chart of the $50 \leq Z, N \leq 82$ region. The color code indicates the magnitude of the m -scheme dimension in an untruncated shell-model calculation without core excitations employing the SN100PN interaction by Brown *et al.* [117].

Various realistic effective shell-model interactions derived from modern nucleon-nucleon potentials as well as phenomenological interactions are available for the description of the nuclear structure northwest of ^{132}Sn . At best, an interaction gives not only an accurate description of nuclear-structure features such as excitation energies, transition strengths and magnetic moments, but should also demonstrate predictive power for quantities which are not measured yet. Furthermore, a unified view on the nuclear structure requires as little as possible free parameters. The entanglement of single-particle and collective modes towards the midshell regime is another challenge. Early realistic interactions for the description of protons and neutrons in the valence space of the $0g_{7/2}$, $1d_{5/2}$, $1d_{3/2}$, $2s_{1/2}$, and $0h_{11/2}$ orbitals date back to the early 1980s. For example, the N82 interaction by Kruse and Wildenthal was derived from a least-squares fit to binding energies with a surface-delta interaction as a starting point and attempted to describe proton excitations along $N = 82$ isotones north of ^{132}Sn [118]. Recent progress and present-day realistic interactions are briefly described below.

SN100PN interaction

The SN100PN interaction is a realistic interaction by Brown *et al.* for the description of the $0g_{7/2}$, $1d_{5/2}$, $1d_{3/2}$, $2s_{1/2}$, and $0h_{11/2}$ orbitals in the valence space outside the ^{100}Sn core between the magic numbers 50 and 82. The interaction was originally developed to investigate magnetic moments of 2_1^+ states around ^{132}Sn [117] and consists of separate neutron-neutron, proton-proton, and proton-neutron effective interactions plus a Coulomb-repulsion part. The two-body residual interaction is based on a renormalized G matrix derived from the CD-Bonn nucleon-nucleon two-body potential [119]. Single-particle energies (SPE) are based on experimentally observed states in ^{133}Sb (proton SPEs) and ^{131}Sn (neutron SPEs). In particular, the predictive power of the neutron-neutron and the proton-proton part were thoroughly tested in experiments. The neutron-neutron part of the SN100PN effective interaction yields a good description of the excited states up to highest spins of the heavy Sn isotopes (cf. Ref. [78]). Detailed studies were also performed for the $N = 82$ chain [75]. For the heavy Te isotopes, the agreement between the calculated and experimental states is slightly reduced, but still reasonable [79, 120]. Despite some studies of odd-odd systems like ^{136}Cs [76] or ^{138}La [77], detailed and stringent tests of the proton-neutron part are still pending.

PQM130 interaction

Another independent approach is the *pair-truncated* shell model. Recent years have seen some promising developments and systematic studies for the description of nuclei around mass 130 within the shell comprising the five single-particle orbitals $0g_{7/2}$, $1d_{5/2}$, $1d_{3/2}$, $2s_{1/2}$, and $0h_{11/2}$ [121–123]. The approach of the pair-truncated shell model is very similar to the concept of the interacting boson model (IBM). However, to include Pauli effects, the bosons are replaced by correlated nucleon pairs. Odd-mass and doubly-odd nuclei are treated by coupling additional unpaired nucleons to the nuclear states calculated for the even-even nuclei. A plethora of results for nuclei ranging from Sn to Ba, including excitation energies, transition rates, and magnetic moments, were obtained by Teruya *et al.* [124] with a phenomenological interaction called PQM130 (Pairing+QQ+Multipole for mass region 130). Here, the effective Hamiltonian is given by $H = H_\nu + H_\pi + H_{\nu\pi}$ where H_ν , H_π , and $H_{\nu\pi}$ represent the neutron-neutron, proton-proton, and neutron-proton interactions, respectively. The interaction is constructed from a pairing-plus-quadrupole interaction that consists of spherical single-particle energies, the monopole-pairing (MP) interaction, the quadrupole-pairing (QP) interaction, as well as the quadrupole-quadrupole (QQ) interaction. It is combined with newly introduced higher multipole-pairing (HMP) interactions with multipolarities $L = 4, 6, 8, 10$. Valence neutrons and protons are treated as holes and particles relative to the closed shells. Single-particle energies are extracted from experimental excitation energies in ^{131}Sn (neutron SPEs) and ^{133}Sb (proton SPEs). Both neutron $0h_{11/2}$ SPE and the proton $0g_{7/2}$ SPE are scaled linearly with increasing numbers of valence neutrons and protons, respectively. Quadrupole-quadrupole strengths of two-body effective interactions are tuned to reproduce first excited states of positive parity in odd-mass isotopes. Other two-body effective-interaction strengths are fitted to several even-even Sn, Te, and Te isotopes to mirror experimental energy levels of yrast and other low-lying states. Hamiltonians of the proton

and neutron spaces, H_ν and H_π , are diagonalized separately; eigenenergies and wavefunctions are obtained for each of the proton and neutron systems; subsequently ordered by energy and coupled to proton-neutron basis states. Truncations are applied by restricting the number of levels from the lowest state in each of the proton and neutron spaces for the calculation of the proton-neutron basis. Finally, the total Hamiltonian of neutrons and protons is diagonalized in the truncated space.

GCN5082 interaction

The GCN5082 interaction is a new development by Gniady, Caurier, and Nowacki for the *gds* valence space for both protons and neutrons (unpublished, cf. Refs. [125–127]). Like the SN100PN interaction, the interaction is derived from a realistic G matrix based on the CD-Bonn potential. However, empirical corrections are added to the monopole part and certain pairing and other multipole matrix elements of the original G matrix by fitting different combinations of two-body matrix elements to sets of experimental data from the even-even and even-odd semi-magic nuclei, from all odd-even Sb isotopes and $N = 81$ isotones, and from some odd-odd nuclei around ^{132}Sn . In this way, a set of about 320 low-spin states in 87 nuclei within the $50 \leq Z, N \leq 82$ region was reproduced within a root-mean-square deviation of 110 keV [125, 127]. Among others, the interaction has been employed for shell-model studies of neutrinoless $\beta\beta$ decays in even-even Sn, Te and Xe isotopes [128], high-spin structures of ^{134}Xe [126], the analysis of electromagnetic transition rates for the understanding of mixed-symmetry states (MSS) along the $N = 80$ isotones [125], and even in studies of dark-matter scattering on xenon isotopes [129].

1.3 Outline of this thesis

The primary scope of this cumulative thesis is the population of neutron-rich actinide nuclei via multinucleon transfer and to utilize different reaction paths to study $50 \leq Z, N \leq 82$ nuclei in the vicinity of the doubly-magic nucleus ^{132}Sn . The thesis is structured as follows:

The first paper presents a dedicated study on the features of the $^{136}\text{Xe} + ^{238}\text{U}$ multinucleon-transfer reaction employing the large-solid-angle magnetic spectrometer PRISMA coupled to the high-resolution Advanced Gamma Tracking Array (AGATA). Mass yields, transformed into relative cross sections, are compared with calculations based on the GRAZING model. Contributions of multinucleon-transfer reaction products and fission fragments as well as the extent of neutron evaporation on the final yields are investigated. Additionally, limitations of this experimental technique are discussed, since no sizable yield of actinide nuclei beyond $Z = 93$ is found at the grazing angle.

The second publication focuses on the neutron-rich actinide ^{240}U . Besides an extension of the ground-state band, evidence for an extended first negative-parity band is found. Energy spectra and the upbend in moment of inertia are confronted with latest theoretical calculations.

Both the identification and characterization of isomers near magic numbers are important for establishing the two-body matrix elements for modern-day shell-model interactions. Two publications and one manuscript provide new insights and a detailed picture on transition probabilities of isomeric decays and high-spin excitations above long-lived isomers in ^{132}Xe , ^{133}Xe , ^{134}Xe , ^{135}Xe , and ^{137}Ba . Datasets from five different γ -ray spectroscopy studies, among them data from the next-generation γ -ray tracking array AGATA, the established “gold standard” high-performance array GAMMASPHERE and the smaller university-based HORUS array are exploited for this goal. Furthermore, the results reveal differences in the population patterns between the different reaction processes: fission and multinucleon transfer. The experimental findings are interpreted using state-of-the-art shell-model calculations.

Dedicated experiments in the $50 \leq Z, N \leq 82$ region require detector systems to track down elusive charged-particle channels in fusion-evaporation reactions. Preparatory tests of double-sided silicon-strip detectors yielded a novel calibration method which is presented in the last paper. Finally, the results of the six papers are briefly summarized before a synopsis of ongoing work and an outlook on possible future activities are given.

Publication I:

**Light and heavy transfer products
in the $^{136}\text{Xe} + ^{238}\text{U}$
multinucleon-transfer reaction**

Light and heavy transfer products in $^{136}\text{Xe} + ^{238}\text{U}$ multinucleon transfer reactions

A. Vogt,^{1,*} B. Birkenbach,¹ P. Reiter,¹ L. Corradi,² T. Mijatović,³ D. Montanari,^{4,5,†} S. Szilner,³ D. Bazzacco,⁵ M. Bowry,⁶ A. Bracco,⁷ B. Bruyneel,⁸ F. C. L. Crespi,⁷ G. de Angelis,² P. Désesquelles,⁹ J. Eberth,¹ E. Farnea,⁵ E. Fioretto,² A. Gadea,¹⁰ K. Geibel,¹ A. Gengelbach,¹¹ A. Giaz,⁷ A. Görgen,^{12,13} A. Gottardo,² J. Grebosz,¹⁴ H. Hess,¹ P. R. John,^{4,5} J. Jolie,¹ D. S. Judson,¹⁵ A. Jungclaus,¹⁶ W. Korten,¹³ S. Leoni,⁷ S. Lunardi,^{4,5} R. Menegazzo,⁵ D. Mengoni,^{17,4,5} C. Michelagnoli,^{4,5,‡} G. Montagnoli,^{4,5} D. Napoli,² L. Pellegri,⁷ G. Pollaro,¹⁸ A. Pullia,⁷ B. Quintana,¹⁹ F. Radeck,¹ F. Recchia,^{4,5} D. Rosso,² E. Şahin,^{2,§} M. D. Salsac,¹³ F. Scarlassara,^{4,5} P.-A. Söderström,^{20,||} A. M. Stefanini,² T. Steinbach,¹ O. Stezowski,²¹ B. Szpak,¹⁴ Ch. Theisen,¹³ C. Ur,⁵ J. J. Valiente-Dobón,² V. Vandone,⁷ and A. Wiens¹

¹*Institut für Kernphysik, Universität zu Köln, 50937 Köln, Germany*

²*Istituto Nazionale di Fisica Nucleare, Laboratori Nazionali di Legnaro, I-35020 Legnaro, Italy*

³*Ruđer Bošković Institute, HR-10 002 Zagreb, Croatia*

⁴*Dipartimento di Fisica e Astronomia, Università di Padova, I-35131 Padova, Italy*

⁵*Istituto Nazionale di Fisica Nucleare, Sezione di Padova, I-35131 Padova, Italy*

⁶*Department of Physics, University of Surrey, Guildford, Surrey GU2 7XH, United Kingdom*

⁷*Dipartimento di Fisica, Università di Milano and INFN Sezione di Milano, I-20133 Milano, Italy*

⁸*CEA Saclay, Service de Physique Nucleaire, F-91191 Gif-sur-Yvette, France*

⁹*Centre de Spectrométrie Nucléaire et de Spectrométrie de Masse—CSNSM, CNRS/IN2P3 and Univ. Paris-Sud, F-91405 Orsay Campus, France*

¹⁰*Instituto de Física Corpuscular, CSIC-Universidad de Valencia, E-46071 Valencia, Spain*

¹¹*Department of Physics and Astronomy, Uppsala University, SE-75121 Uppsala, Sweden*

¹²*Department of Physics, University of Oslo, P. O. Box 1048 Blindern, N-0316 Oslo, Norway*

¹³*Institut de Recherche sur les lois Fondamentales de l'Univers—IRFU, CEA/DSM, Centre CEA de Saclay, F-91191 Gif-sur-Yvette Cedex, France*

¹⁴*Henryk Niewodniczański Institute of Nuclear Physics PAN, PL-31342 Kraków, Poland*

¹⁵*Oliver Lodge Laboratory, The University of Liverpool, Liverpool L69 7ZE, United Kingdom*

¹⁶*Instituto de Estructura de la Materia, CSIC, Madrid, E-28006 Madrid, Spain*

¹⁷*Nuclear Physics Research Group, University of the West of Scotland, High Street, Paisley PA1 2BE, Scotland, United Kingdom*

¹⁸*Dipartimento di Fisica Teorica dell'Università di Torino and INFN, I-10125 Torino, Italy*

¹⁹*Laboratorio de Radiaciones Ionizantes, Universidad de Salamanca, E-37008 Salamanca, Spain*

²⁰*Department of Physics and Astronomy, Uppsala University, SE-75120 Uppsala, Sweden*

²¹*Université de Lyon, Université Lyon-1, CNRS/IN2P3, UMR5822, IPNL, F-69622 Villeurbanne Cedex, France*

(Received 10 June 2015; published 27 August 2015)

Background: Multinucleon transfer reactions (MNT) are a competitive tool to populate exotic neutron-rich nuclei in a wide region of nuclei, where other production methods have severe limitations or cannot be used at all.

Purpose: Experimental information on the yields of MNT reactions in comparison with theoretical calculations are necessary to make predictions for the production of neutron-rich heavy nuclei. It is crucial to determine the fraction of MNT reaction products which are surviving neutron emission or fission at the high excitation energy after the nucleon exchange.

Method: Multinucleon transfer reactions in $^{136}\text{Xe} + ^{238}\text{U}$ have been measured in a high-resolution γ -ray/particle coincidence experiment. The large solid-angle magnetic spectrometer PRISMA coupled to the high-resolution Advanced Gamma Tracking Array (AGATA) has been employed. Beamlike reaction products after multinucleon transfer in the Xe region were identified and selected with the PRISMA spectrometer. Coincident particles were tagged by multichannel plate detectors placed at the grazing angle of the targetlike recoils inside the scattering chamber.

Results: Mass yields have been extracted and compared with calculations based on the GRAZING model for MNT reactions. Kinematic coincidences between the binary reaction products, i.e., beamlike and targetlike nuclei, were exploited to obtain population yields for nuclei in the actinide region and compared to x-ray yields measured by AGATA.

Conclusions: No sizable yield of actinide nuclei beyond $Z = 93$ is found to perform nuclear structure investigations. In-beam γ -ray spectroscopy is feasible for few-neutron transfer channels in U and the $-2p$ channel populating Th isotopes.

DOI: 10.1103/PhysRevC.92.024619

PACS number(s): 24.10.-i, 25.70.Hi, 29.30.Aj, 29.40.Gx

I. INTRODUCTION

Recent studies of multinucleon transfer (MNT) reactions are based on the powerful combination of selective large solid angle magnetic spectrometers and highly efficient γ -ray spectrometers enabling simultaneously in-depth studies of the reaction mechanism and the nuclear structure of the involved reaction partners. Especially for the production of heavy and neutron-rich actinide nuclei, MNT reactions may provide a tool for population of these nuclei which cannot be synthesized by neutron capture or fusion reactions. The very first investigations of this type were based on transfer reactions employing actinide targets together with light and heavy projectiles. Identification of the reaction products relied on chemical separation of the actinide isotopes of interest [1–6]. These results showed production of neutron-rich actinide nuclei up to Fm and even one isotope of Md was identified. Cross-section values varied from a few micro- to millibarns [7].

Surprisingly, nuclear reactions between two ^{238}U nuclei and the U+Cm reaction at energies close to the Coulomb barrier showed enhanced cross sections for the production of very heavy actinide isotopes and even superheavy elements. The measured cross sections for surviving heavy actinides exceeded those in Ar+U, Kr+U, and Xe+U reactions by typically one order of magnitude [1,8,9]. Analyses of the survival probabilities of these highly fissionable nuclei revealed that their formation is associated with the low-energy tails of the excitation-energy distributions. To understand the different production yields for the highly fissile actinide nuclei, refined and exclusive experiments are needed. It is crucial to determine the fraction of MNT reaction products which are surviving the interplay between neutron emission and fission at the high excitation energy after the nucleon exchange.

The necessity to clarify the dynamics of dissipative collisions in very heavy nuclear systems at low excitation energies spurred different theoretical investigations implying a search for new ways for the production of neutron-rich superheavy nuclei [10]. Multinucleon transfer processes in heavy-ion reactions at energies slightly above the Coulomb barrier are investigated in a fully microscopic framework of the time-dependent Hartree-Fock (TDHF) theory in Ref. [11].

Another approach to multinucleon transfer processes is based on direct reaction theories, which incorporate important nuclear structure properties of the interacting nuclei. In particular, the GRAZING [12–14] code and complex Wentzel-Kramers-Brillouin (CWKB) [15] semiclassical theories have been extensively developed and successfully applied to

different sets of data [16]. In these models, MNT processes are described via a multistep mechanism.

Experimental results from reaction studies of MNT with ^{136}Xe beams and heavy targets from ^{208}Pb to ^{249}Cf are available for the following systems: the study of the $^{136}\text{Xe} + ^{208}\text{Pb}$ reaction allowed to investigate nuclear structure effects and their influence on the flow of nucleons in low-energy multinucleon transfer reactions towards both the $Z = 82$ and $N = 126$ closed shells. Mass-energy distributions of the $^{136}\text{Xe} + ^{208}\text{Pb}$ reaction have been measured [17,18]. The reaction $^{136}\text{Xe} + ^{244}\text{Pu}$ was used to produce and study the decay properties of the neutron-rich isotopes ^{243}Np and ^{244}Np [5]. The $^{136}\text{Xe} + ^{248}\text{Cm}$ reaction was employed to determine the formation cross sections of unknown actinide nuclei by chemical separation [4]. The $^{136}\text{Xe} + ^{249}\text{Cf}$ reaction was measured in order to study the feasibility of using low-energy multinucleon transfer reactions to produce new actinide and transactinide isotopes [7]. Prior to the new study presented in this paper, the system $^{136}\text{Xe} + ^{238}\text{U}$ was investigated by means of chemical separation in the 1970s and, for a small subgroup of individual isotopes, results were shown in comparison with yields from other reactions [1,8,9].

The experiment described here exploits the coupling of a magnetic and a γ -ray spectrometer, allowing for the first time the complete and detailed detection of all reaction products, separation of fission products, and determination of the total kinetic energy loss for the $^{136}\text{Xe} + ^{238}\text{U}$ reaction.

Additional motivation and interest in multinucleon transfer reactions is given by the possibility of producing neutron-rich heavy nuclei for studies using x-ray and nuclear spectroscopy. Recently, several γ -ray spectroscopy studies were based on transfer and multinucleon transfer reactions and managed to explore unknown actinide nuclei. One group of experiments is performed with thick actinide targets to produce the heavy reaction products. The target- and beamlike reaction products are stopped immediately, allowing spectroscopy of γ rays emitted at rest with the most efficient spectrometers available. The technique depends on available cross coincidences with known γ -ray transitions of the beamlike reaction partners in order to identify unknown transitions. The feasibility of these measurements was demonstrated in Rn and Ra nuclei which were produced in a series of experiments with different beams on thick ^{232}Th targets. The measured cross sections as a function of different beam-target combinations and the populated high spin range are described in Ref. [19]. In agreement with previous reaction studies [7], heavy projectiles allow for highest production yields. Excited states of MNT products with collective angular momentum up to $30\hbar$ were identified [20] in Rn and Ra isotopes.

Another group of measurements rely on few-nucleon transfer reactions with light oxygen beams and were successfully exploited to detect excited states, e.g., in neutron-rich ^{236}Th and $^{240,242}\text{U}$ isotopes. γ Rays were detected in coincidence with the outgoing transfer products. However, for the most neutron-rich cases the rotational ground-state band was detected up to lower spin values of 8 to $10\hbar$ [21,22].

The article reports on results from the multinucleon transfer reactions $^{136}\text{Xe} + ^{238}\text{U}$ at 1 GeV. The combination of the most neutron-rich stable U isotope as target material and the heavy

*Corresponding author: andreas.vogt@ikp.uni-koeln.de

[†]Present address: USIAS - Universite de Strasbourg, IPHC-CNRS, F-67037 Strasbourg Cedex 2, France.

[‡]Present address: GANIL, CEA/DSM-CNRS/IN2P3, F-14076, Caen, France.

[§]Present address: Department of Physics, University of Oslo, P. O. Box 1048 Blindern, N-0316 Oslo, Norway.

^{||}Present address: RIKEN Nishina Center, Wako, 351-0198 Saitama, Japan.

neutron-rich ^{136}Xe beam were employed, as multinucleon transfer reactions depend on optimum Q values. With neutron-deficient stable beams, only neutron pickup and proton-stripping channels are available. With neutron-rich beams, also neutron stripping and proton-pickup channels become available, leading to the possibility to populate neutron-rich heavy nuclei [23].

The combination of the PRISMA spectrometer [24–26] and the Advanced Gamma Tracking Array (AGATA) demonstrator array [27] provides an unprecedented sensitivity for these types of experiments. It allows the selection of the products of interest after multinucleon transfer reactions on an actinide target by identification of the beamlike reaction products in the PRISMA spectrometer. The corresponding targetlike reaction product is detected, in coincidence, by a position-sensitive multichannel plate detector of the Detector Array for multiNucleon Transfer Ejectiles (DANTE) array [28].

The experiment yielded results on mass distributions of lighter reaction products and on mass-integrated Z distributions for the heavy transfer products. Simultaneously, a spectroscopic study of the reaction products provides additional experimental information for the identification of individual isotopes via characteristic γ -ray transitions or chains of isotopes by x-ray detection.

II. EXPERIMENTAL SETUP AND DATA ANALYSIS

A beam of ^{136}Xe was accelerated onto ^{238}U targets by the PIAVE-ALPI accelerator complex at the INFN Laboratori Nazionali di Legnaro (LNL) with a bombarding energy of 1 GeV and an average intensity of $\simeq 2$ pnA. The ^{238}U targets had target thicknesses of 1 and 2 mg/cm² with a 0.8 mg/cm² Nb backing. The mean energy loss for the beam particles in the target is about 60 MeV [29]. Projectile-like reaction products were selected with the magnetic mass spectrometer PRISMA placed at the grazing angle of $\theta_{\text{lab}} = 50^\circ$.

γ Rays from excited states in both beam- and targetlike nuclei were measured employing the high-resolution position-sensitive γ -ray spectrometer AGATA [30] in its demonstrator configuration placed 23.5 cm from the target position. It consists of 15 large-volume electronically segmented high-purity Ge (HPGe) detectors in five triple cryostats [31]. The solid angle coverage of the AGATA demonstrator at its nominal position is $\approx 7\%$ of 4π and the full-energy efficiency is about 3% for 1 MeV and about 4% at 100 keV taking into account absorbing materials. The counting rate of the individual HPGe crystals was maintained between 20 and 30 kHz during the whole experiment.

Three 40×60 mm² large DANTE multichannel plate detectors were mounted in the reaction plane covering the angle range which corresponds to the grazing angle for the targetlike reaction product. The main purpose is to request a kinematical coincidence among the different reaction products. In this experimental setup (see Fig. 1), the focal-plane detector of PRISMA, a multiwire parallel-plate detector (MWPPAC) was taken as a trigger to start the data acquisition.

PRISMA covers a large solid angle of $\simeq 80$ msr with $\pm 6^\circ$ for θ and $\pm 11^\circ$ for ϕ . A two-dimensional position-sensitive microchannel plate (MCP) detector [32] is located at the

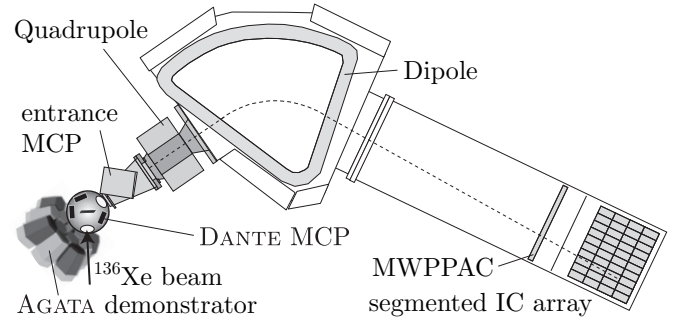


FIG. 1. The experimental setup comprised the γ -ray spectrometer AGATA, the ejectile-detecting heavy-ion mass spectrometer PRISMA, and the particle detector DANTE (not to scale). The DANTE MCP on a 58° ring [27] in the scattering chamber covers the grazing angles of the binary reaction products.

entrance of the spectrometer, 25 cm downstream the target ladder. It provides a delayed stop signal for the time-of-flight measurement along the spectrometer and a (x, y) position information with a ± 1 -mm resolution. The magnetic system consists of a magnetic quadrupole singlet and a magnetic dipole. After a total flight distance of $\simeq 6.5$ m from the start detector through the optical elements, the ions enter the position-sensitive focal-plane detector system consisting of a MWPPAC divided into 10 sections and an array of 10×4 segmented CH₄ gas-filled transverse-field multiparametric ionization chambers (IC) [33]. The MWPPAC is used as the start detector for the time-of-flight measurement. Each segment of the IC acts as a ΔE section and provides a signal proportional to the energy loss of the passing fragment. The detector system (see Fig. 1) gives all the necessary information for complete ion identification. An event-by-event trajectory reconstruction algorithm uses the entrance angle, the position on the focal plane, and the properties of the magnetic fields to calculate iteratively the trajectory length $L(\theta, \phi)$ of the ions and the curvature radius R inside the dipole magnet. The length $L(\theta, \phi)$ in combination with the time-of-flight measurements yields the velocity vector of reaction products entering PRISMA.

Different nuclear charges Z of the measured nuclei are selected by applying two different sets of graphical polygonal cuts in matrices of (i) the energy released in the first layer of the IC versus the total deposited energy and (ii) the energy deposited in the first two layers versus the total deposited energy. The latter energy loss matrix is shown in Fig. 2. The IC provides a resolution of $Z/\Delta Z = 52.7(1)$. The huge yield of beam like Xe isotopes did not allow an unambiguous selection of the neighboring $\pm 1p$ reaction channels Cs and I. A precise determination of the mass-over-charge ratio A/q requires a well-calibrated time-of-flight and a well-determined trajectory length [34]. Using the trajectory length $L(\theta, \phi)$, the time-of-flight t_{ToF} , and the dipole bending radius R inside the magnetic field B , we obtain

$$\frac{BR t_{\text{ToF}}}{L(\theta, \phi)} \propto \frac{A}{q}, \quad (1)$$

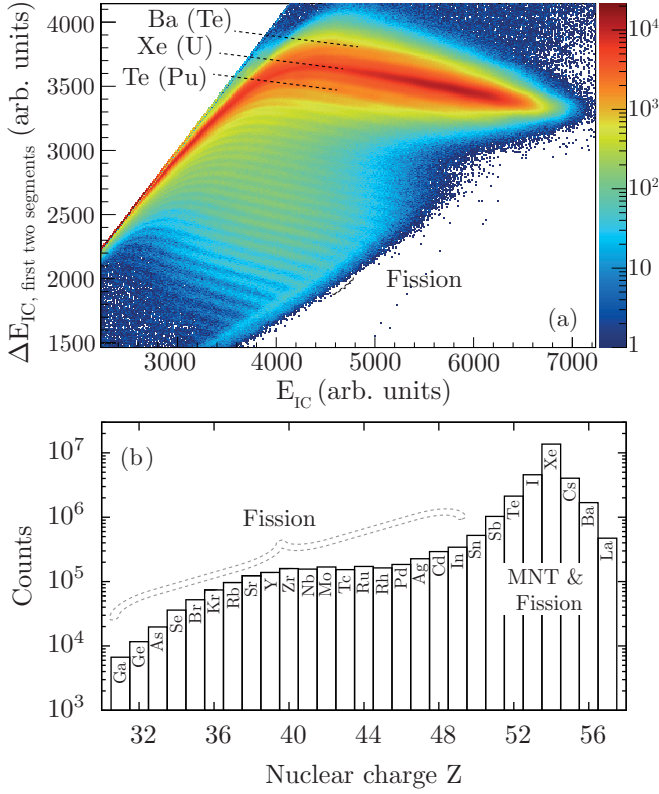


FIG. 2. (Color online) (a) IC energy loss matrix of the energy deposited in the first two layers versus the total deposited energy. (b) Yield distribution of nuclear charges from Ga ($Z = 31$) to La ($Z = 57$). The peak around $Z = 42$ results from asymmetric actinide fission residues. Corresponding fission partners in the Xe region overlap with the multinucleon transfer products in the vicinity of ^{136}Xe .

which is proportional to A/q . Nonlinearities and aberrations of the magnetic system, visible in systematic dependencies between A/q and the position coordinates of both the entrance MCP and the focal plane MWPPAC, need to be corrected. Effects of the magnetic fringe fields are partly reabsorbed by an effective quadrupole length. Remaining nonlinearities are corrected for by straightening deviations in the matrices of A/q against the MCP and MWPPAC coordinates using polynomial fit functions. Examples of pre- and postcorrected A/q spectra are presented in Fig. 3. The aberration correction improves the A/q spectra considerably and was crucial for the construction of high-resolution mass spectra.

The different atomic charge states were separated employing the relationship

$$\frac{Et_{\text{ToF}}}{BRL(\theta, \phi)} = \frac{E}{BR\beta} \propto q. \quad (2)$$

The two-dimensional plane of the total energy released in the IC, E_{IC} , versus $R\beta$ is plotted and charge states are selected by two-dimensional gates. The broad charge-state distribution ranges from $q \simeq 33$ to $\simeq 43$.

The different charge-state gated $A/q|_{q_i}$ distributions need to be aligned. Mass spectra are obtained by assigning correct mass values in terms of atomic mass units to the corresponding peaks in the various $A/q|_{q_i}$ spectra still given in arbitrary

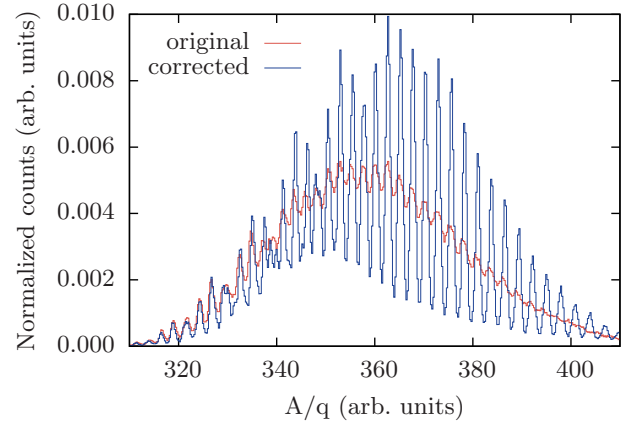


FIG. 3. (Color online) Results of the software-based aberration correction of nonlinear distortions of A/q as a function of the position information of PRISMA start and stop detectors.

units. The masses are finally determined by inspecting the characteristic γ rays in ejectile-like Doppler-corrected γ -ray spectra in coincidence with the separated masses. Calibrated $A/q|_{q_i}$ spectra are subsequently summed up. Masses are selected via graphical two-dimensional cuts in matrices of A plotted against the focal plane coordinate x .

Figure 4 shows the final projected mass distribution of all analyzed Z channels from Te to Ba. The final mass resolution accounts to $A/\Delta A = 298 \pm 1$ for the Ba channel and 262 ± 1 for the Te channel.

With the complete information on the kinematics of the lighter fragments, the velocity vector for the targetlike recoils is reconstructed event by event using relativistic two-body reaction kinematics assuming a pure binary reaction without any particle evaporation taking into account the energy loss of beam- and targetlike particles. The simultaneous measurement of both the momentum and the angle of the beamlike recoils with PRISMA enables a reconstruction of the total kinetic energy loss (TKEL) value of the reaction [35] (see Fig. 8). As the experiment was performed with a rather thick target, no angle-dependent yield distribution is deduced. The TKEL is broadened due to the integration over a range of effective bombarding energies.

The measured signals of the AGATA demonstrator were analyzed online and all relevant information was written to disk. The complete experiment was replayed offline with optimized calibrations of time and energy. The full width at half maximum of the prompt coincidence peak for the time difference between AGATA and PRISMA is about 16 ns for identified beamlike particles. Pulse-shape analysis of the fully digitized detector pulses was applied to determine the individual interaction points. This information is used by the Orsay forward-tracking algorithm [36] to reconstruct the individual emitted γ -ray energies, determine the first interaction point of the γ ray in the germanium and, thus, the emission angle. Combining this with the kinematic information from PRISMA, a precise Doppler correction for beam and targetlike nuclei was performed [34].

Direct detection and identification of actinide particles in PRISMA was not feasible due to their low kinetic energies. To

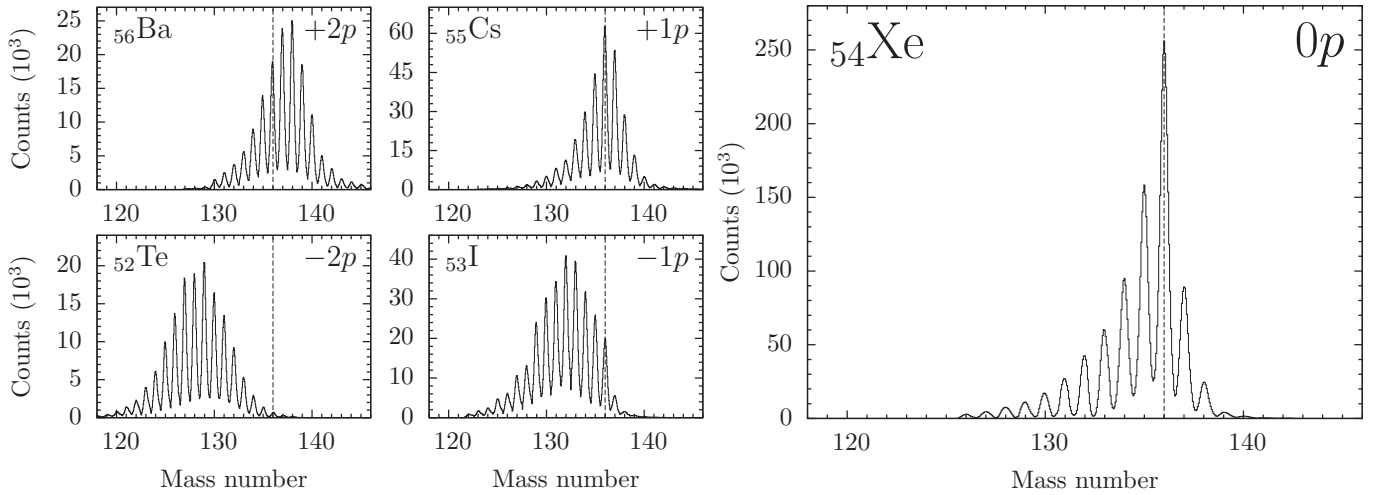


FIG. 4. Mass spectra for beamlike particles in the range from Te to Ba identified with PRISMA. The resolution in the Ba channel accounts to $A/\Delta A = 298 \pm 1$. Along the Xe channel, neutron pickup is not favored, whereas the $\pm xp$ channels are more evenly distributed. Dashed lines mark mass $A = 136$ to guide the eye.

select surviving actinides, kinematic coincidences between the binary reaction products, i.e., beamlike and targetlike nuclei, were exploited. The position information of the DANTE detectors could not be resolved. Information on the binary partner of the reaction was obtained with a time-amplitude converter (TAC) signal between the PRISMA entrance detector and the DANTE detector inside the scattering chamber (see Fig. 1). The total data set consists of 4.203×10^7 events with identified Z and A ; 59% of those events contain γ -ray interaction hits within AGATA, 9.17×10^6 events hold a coincidence between PRISMA and DANTE, and 5.30×10^6 of these events contain tracked γ rays.

III. EXPERIMENTAL RESULTS

The fast anode signals of the entrance MCP of PRISMA and the DANTE MCP allow us to measure the time-of-flight differences (ΔToF) between different coincident reaction products entering the PRISMA spectrometer. In case of fission of the targetlike nuclei, one of the two fission fragments causes a signal in the MCP detectors. A significant time difference is measurable due to the different kinetic energies and velocities of the fission products. The correlation of the nuclear charge Z versus the ΔToF information shows two different components which are separated in ΔToF as depicted in the left part of Fig. 5. The right component comprises a wide range of nuclear charges ranging from Ga up to La. These events are caused by fission products. The distribution resembles the expected yield distribution from asymmetric fission of actinide nuclei around ^{238}U . As magnetic fields and gas pressures of PRISMA were tuned to detect preferably multinucleon transfer products in the Xe region, the transmission and Z identification of lower nuclear charges in the fission yield distribution was not optimal.

In order to understand the difference between the two components of Fig. 5 the corresponding γ -ray transitions were inspected. Figure 6 shows a γ -ray spectrum of properly identified quasielastic ^{136}Xe events which are Doppler-corrected

for the binary partner ^{238}U . Two different gates are set on the two different regions in the PRISMA-DANTE ΔToF difference spectrum. By gating on the left peak the clear γ -ray spectrum of ^{238}U , i.e., signatures of the rotational band up

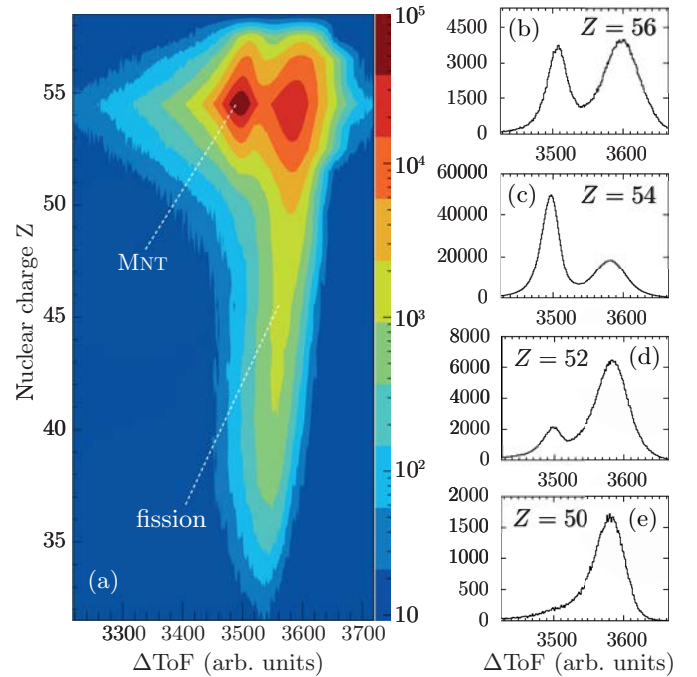


FIG. 5. (Color online) (a) Time-of-flight ΔToF difference spectrum between PRISMA and DANTE plotted against the nuclear charge Z . In the region near Xe the left maximum of the distribution is caused by multinucleon transfer products; these are marked by MNT. The left part of the distribution is caused by fission products and is clearly separated from transfer products. The fission fragments cover a broad Z range and show for lower Z values below $Z = 50$ one distinct ΔToF peak. Selected ΔToF projections for (b) Ba, (c) Xe, (d) Te, and (e) Sn are shown at the right side.

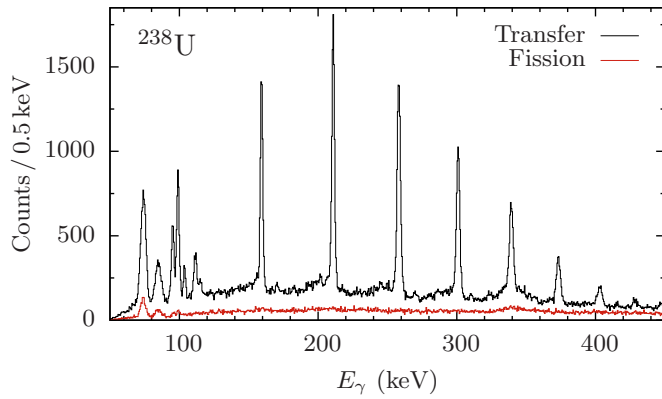


FIG. 6. (Color online) Recoil Doppler-corrected spectrum of ^{238}U with transfer and fissionlike ΔToF gates. A gate on the right fissionlike ΔToF peak yields a flat γ -ray background spectrum (red). The spectrum gated by the left part of the ΔToF distribution shows distinct known peaks from the ^{238}U rotational band up to spin $22\hbar$.

to spin $22\hbar$ is visible. A gate on the right ΔToF peak yields an unstructured, flat background spectrum originating from fission fragments produced in reactions like $^{238}\text{U}(^{136}\text{Xe}, F\gamma)$. Remaining uranium and lead x-ray peaks originate from abundant atomic excitation in the target and the beam dump which are slightly shifted in energy due to a false Doppler correction. Therefore, the ΔToF spectra of the binary partners allow us to successfully discriminate fission from multinucleon transfer reaction products.

The Z-gated ΔToF difference spectra are shown in the right part of Fig. 5. The corresponding intensities of the right fission peak and the left multinucleon transfer peaks give first indication for actinide production rates. For the Xe ejectile channel, the left peak is mainly associated with multinucleon transfer. For the $-2p$ channel $_{52}\text{Te}$ only a few multinucleon transfer events are present. In the $-4p$ channel $_{50}\text{Sn}$, which corresponds to Cm in the target, no distinct transferlike ΔToF peak is left. No sizable yield of actinide and transactinide nuclei beyond $Z = 93$ is found to perform nuclear structure investigations.

The relative contributions of multinucleon transfer reaction products and fission fragments are shown in Fig. 7 as a function of Xe isotope mass number. The area of the left multinucleon transferlike (red) and the right fissionlike (blue) ΔToF peak is divided by the absolute number of the different identified isotopes along the Xe chain. As expected, the left peak shows a maximum for nearly elastic and inelastic scattering where no neutrons are transferred to the actinide reaction partner. For the same isotope the relative area of the right peak shows a minimum. Already for $\pm 2n$ neutron transfer, the fission contribution is higher or comparable to multinucleon transfer. Hence, the discrimination of fission is mandatory to determine properties of multinucleon transfer reactions involving heavy reaction partners.

Figure 8 shows a matrix of the time difference between PRISMA and DANTE plotted against the total kinetic energy loss for ejectiles identified as Xe. Three different domains are distinguishable: transferlike, fissionlike, and elastically scattered events with $\text{TKEL} \approx 0$. The latter ones are located

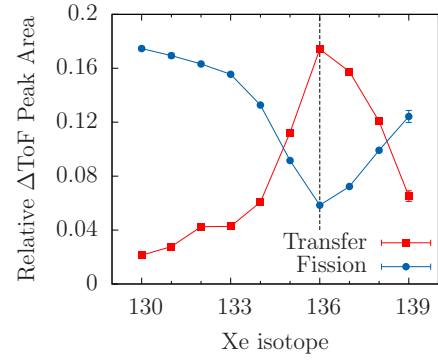


FIG. 7. (Color online) Area of the left (transferlike) and right (fissionlike) peak in the ΔToF spectrum between DANTE and PRISMA divided by the absolute number of the different identified Xe isotopes. A dashed line marks mass $A = 136$ to guide the eye.

around ΔToF channel 3500, right between the two main peaks in the projections, and can be rejected with this method to enhance the discriminability between transfer and fission events. The multinucleon transfer displays a tail towards large TKEL. The computed TKEL value in the fission channel is not meaningful since the TKEL calculation requires a binary-partner reaction system.

A detailed study of the mass-spectrometer transmission has to be performed to extract correct cross-section information from measured mass yields. For the determination of the PRISMA response function $f(E, \theta, \phi)$ [37], a Monte Carlo computer simulation is performed taking into account the kinematics of the reaction and the geometry of the magnetic system. The magnetic fields and the gas pressures in the focal plane detectors are carefully tuned in the same way like in the real experiment. An input event distribution uniform in E_{kin} , θ , and ϕ is created. Those events are then transported event by event with a simulation based on the ray-tracing code

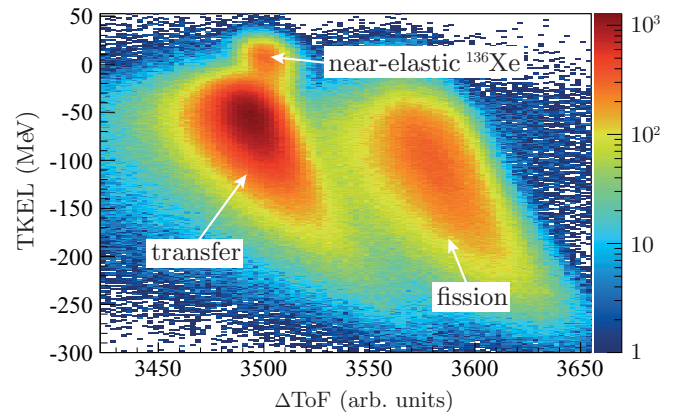


FIG. 8. (Color online) Matrix of the time difference between PRISMA and DANTE plotted against the total kinetic energy loss for Xe events. Transfer, fission, and elastically scattered ^{136}Xe particles with $\text{TKEL} \approx 0$ are distinguishable. The multinucleon transfer displays a tail towards large TKEL. For the fission channel, the computed TKEL is only qualitative since it is constructed assuming a binary reaction.

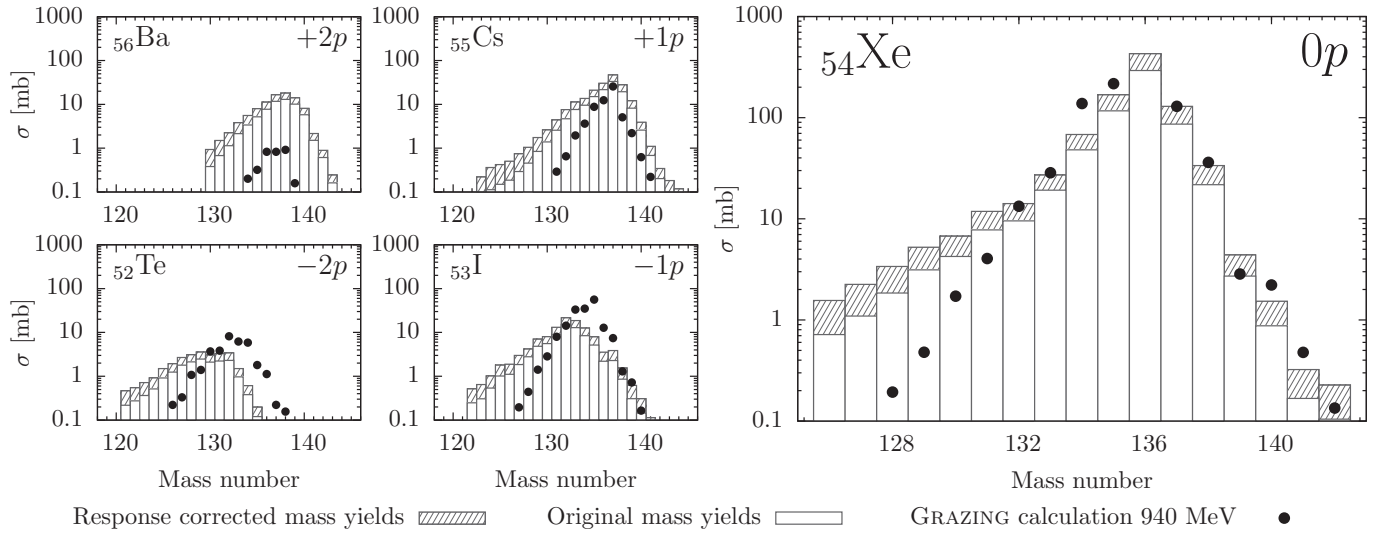


FIG. 9. Cross sections of a GRAZING calculation (points) and experimental yields (histogram bars) normalized to the calculated cross section of the $+1n$ channel ^{137}Xe . The mass yields are corrected for Xe contamination in the I and Cs channels. Fission events are excluded by a cut in the time-difference spectra between PRISMA and DANTE. Gray-shaded bars indicate the efficiency correction by applying the PRISMA response function to the experimental data.

provided by the PRISMA analysis software library. $f(E, \theta, \phi)$ is defined as the ratio between the output distribution of events $N_o(\theta_{\text{lab}}, E_{\text{kin}})$ detected at the focal plane and the uniform input distribution $N_i(\theta_{\text{lab}}, E_{\text{kin}})$ at the MCP. Applied to the mass yield $N(A)$, $f_A(E, \theta, \phi) \times N(A)$ gives a transmission-corrected event distribution as depicted in the Fig. 9.

As described before, the experimental data have been corrected for fission events by carefully applying two-dimensional gates on the transfer component in matrices of the ΔToF information plotted against the TKEL value. The extent of Xe contaminations in the $\pm 1p$ reaction channels I and Cs is identified and corrected by fitting characteristic Xe γ -ray signatures in the ejectile Doppler-corrected γ -ray spectra of isobaric mass channels. The 1313-keV and 812-keV transitions of the predominant ^{136}Xe channel and the 847-keV transition in ^{134}Xe are used as contamination probes. Contaminations are subtracted from the yield of each mass channel according to the measured Xe production yield. Even-mass isobars of ^{136}Xe are odd-odd nuclei with high level densities, so overlapping transitions in the region of 1313 keV [38] have to be taken into account in the fit model. The contamination of ^{136}Xe in ^{136}Cs accounts to 55.8(27)%, the one of ^{136}Xe in ^{136}I to 87.8(28)%.

Multinucleon transfer events were discriminated against fission fragments and subsequently selected by employing two-dimensional gates in matrices of the ΔToF between PRISMA and DANTE against the computed TKEL value as depicted in Fig. 8. The correction of the measured mass yields by applying response functions and subtracting Xe contaminations in the adjacent $\pm 1p$ channels results in final mass yields which can be compared to multinucleon transfer reaction theory.

IV. COMPARISON WITH REACTION THEORY

The semiclassical GRAZING code has been used to calculate the total cross sections for the multinucleon transfer channels

using standard parameters with both low-lying and high-lying collective nuclear excitation modes. This model calculates the evolution of the reaction by taking into account, besides the relative motion variables, the intrinsic degrees of freedom of projectile and target. These are the isoscalar surface modes and the single-nucleon transfer channels. The multinucleon transfer channels are described via a multistep mechanism. The relative motion of the system is calculated in a nuclear plus Coulomb field where for the nuclear part the empirical potential of Ref. [39] has been used. The excitation of the intrinsic degrees of freedom is obtained by employing the well-known form factors for the collective surface vibrations and the one-particle transfer channels [40,41]. The model takes into account in a simple way the effect of neutron evaporation.

The corrected experimental data have been normalized to the computed cross section of the $+1n$ channel, which is proven to be in good agreement to experimentally extracted cross sections in recent multinucleon transfer studies [25,26,42,43]. The same normalization constant has been kept for all other neutron-pickup and the proton-stripping channels. Figure 9 shows the results of the GRAZING calculation in comparison to the normalized experimental transferlike mass yields, with and without response correction.

The experimental yields agree well with the GRAZING results up to at least the $+5n$ and the $-4n$ Xe channels. The intensities of the neutron-pickup peaks in the Xe mass spectra drop rapidly. For ^{140}Xe , only a fraction of 0.4% with respect to ^{136}Xe was identified. In contrast, the $-8n$ channel ^{128}Xe still contains 5.6% of the ^{136}Xe yield. For the first picked-up neutron, the Xe mass yield drops by a factor of ~ 3 . The second neutron-pickup accounts for a further drop by a factor of ~ 4.4 . The distributions of the yields are not as symmetric as predicted by the calculation, especially in the lower masses. In the Cs channel, the highest populated isotope is ^{137}Cs in agreement with the prediction of the calculation, although the yield differs here by a factor of 2.3. The drop in the

cross section in the neutron-pickup as well as in the first four neutron-stripping channels is reproduced satisfactorily. As in the Xe isotopes, the channels with higher neutron stripping seem to be underestimated by the calculation. The GRAZING calculation underestimates considerably the $+2p$ channels, nonetheless the position of the maximum at ^{138}Ba agrees with the experimental distribution. The yields of neutron-rich species above ^{136}I of the $-1p$ are described well; however, the centroid of the experimental distribution is shifted by four mass units to the neutron-poor side. A similar shift can also be observed in the $-2p$ Te channel. This discrepancy between experiment and theory at large charge transfers was also observed in a recent $^{64}\text{Ni} + ^{238}\text{U}$ study [43].

The fission-corrected mass yields reveal typical characteristics of multinucleon transfer reactions [16]. For few-nucleon transfers in the Xe channel, the reaction cross sections are strongly determined by form factors and Q values. The mass-spectra envelopes of the $\pm 1, \pm 2p$ multinucleon transfer channels are distributed over more masses and are more Gaussian-like. The pure proton-transfer channels without neutron exchange become less favorable as more protons are transferred in the reaction. Concomitant neutron stripping is favored here. When more protons are stripped off the ejectile fragment in the multinucleon transfer reaction, the centroid of the mass distributions shifts to lower neutron numbers. This effect on the isotopic distribution may be mostly influenced by neutron evaporation from the primary reaction fragments, as the fragments are produced *hot* at quite high excitation energies.

The overall intensities of the Cs and Ba channels are higher compared to I and Te. The tendency to pick up neutrons in the $-1p$ and $-2p$ channels only occurs to a limited extent. The most neutron-rich produced Te isotope is ^{136}Te . The behavior of the experimental yields on the neutron-deficient side of the Xe, I, and Te distributions differ from what was observed in previously measured lighter systems [25].

V. ACTINIDE POPULATION

In order to investigate the population and the survival of actinide binary partners, different observables provided by the AGATA array were employed. The signatures of surviving actinide nuclei are the observation of the corresponding x rays, the detection of neutron-induced γ rays, and, finally, the direct detection of γ rays from the de-excitation of the actinide reaction products.

A. x-Ray detection

Characteristic x rays in the spectra are a clear signature for the presence of the nuclei of interest in the corresponding Z channels. x-Ray emission from the atomic shells depends mainly on the nuclear charge and not on nuclear structure properties. Figure 10 shows the low-energy parts of γ -ray spectra, Doppler-corrected for recoil fragments ranging from ^{89}Ac to ^{94}Pu . Here a gate on the transferlike ΔToF part is employed. The strongest lines in the spectra belong to the KL_{1-3} and KM_{1-5} lines of Pb which was used as a beam dump material.

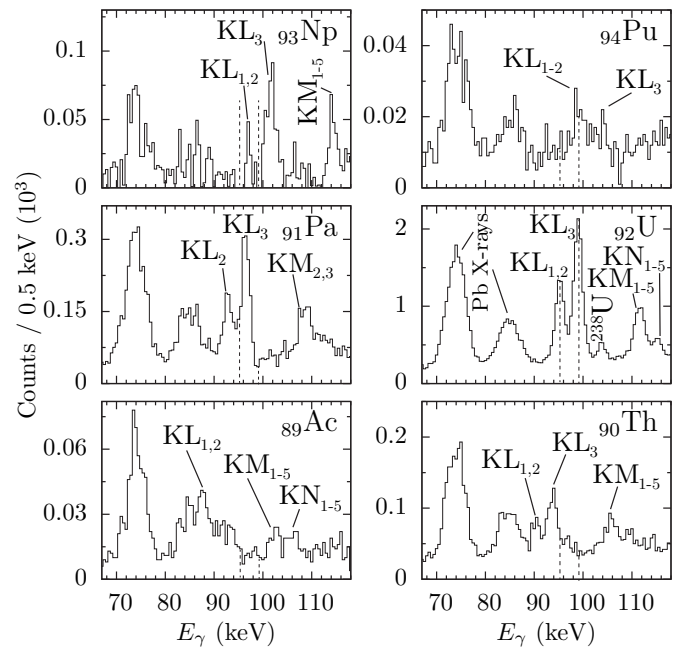


FIG. 10. Tracked singles γ -ray spectra with a gate on the transferlike ΔToF peak, Doppler-corrected for different actinide recoils ranging from Ac ($Z = 89$) to Pu ($Z = 94$) showing the x-ray energy region. ^{92}U KL x rays are indicated with dashed lines. The Pa (corresponding to $Z = 55$ Cs ejectiles) and Np (corresponding to $Z = 53$ I) channels are corrected for U contamination. The Pu channel corresponding to ^{52}Te ejectiles is only weakly populated.

Strong x-ray lines are visible in the uranium channel. The KL_{1-3} transitions at 93.8, 94.7, and 98.4 keV; KM_{1-5} transitions around 111 keV; and KN transitions around 114.5 keV are identified. Three peaks at 90.1(2), 93.3(1), and 105.3(2) keV are visible in the Th spectrum. They correspond to overlapping KL_{1-3} and KM_{1-5} x-ray transitions. The relative intensity of the Th x rays is substantially smaller than the ones in the U spectrum. Almost no Pu fragment candidates leaving the target were recorded with the DANTE detectors in coincidence with Te isotopes within PRISMA (see Fig. 5). There are only $\approx 5.0 \times 10^4$ Te events in the left PRISMA-DANTE ΔToF peak and 79(15) counts in the corresponding KL_3 x-ray peak. The Pa and Np x-ray spectra show contaminations of U arising from the broad Xe peak in the Z distribution. Both spectra show characteristic KL and KM x-ray peaks of Np and Pa, respectively. x-Ray yields are extracted by employing a multi-Gaussian fit model to the depicted spectra in Fig. 10. The prominent U KL_3 peak is used for comparison. The Pa and Np spectra are corrected for a uranium contamination by subtracting the appropriately scaled U γ -ray spectrum. Consequently, close-lying x-ray peaks of Pa and Np have to be disentangled by adequate fit procedures.

Figure 11 shows the x-ray yields (pink triangles), yields given by the before-mentioned PRISMA-DANTE transfer coincidence ΔToF (black points) and theoretical mass-integrated cross sections calculated by GRAZING (blue rhomboids). All values are normalized to the yield of the channel ^{94}Pu . The Th KL_3 x-ray peak contains 264(29) counts. Both x-ray and ΔToF distributions are in a good agreement for Th and Np.

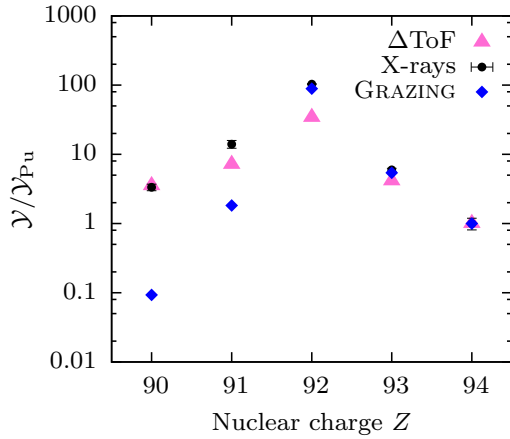


FIG. 11. (Color online) Mass-integrated yields of actinide nuclei Y from their x-ray yields in the recoil Doppler corrected γ -ray spectra (black points) and from the PRISMA-DANTE ΔToF yield scaled to the x-ray distribution (red triangles) together with theoretical cross sections calculated by GRAZING (blue rhomboids). All of the distributions are normalized to the Pu channel.

The values for the Pa channel agree within a factor of 2. This higher x-ray yield is due to more converted transitions in the odd- Z neighbors.

A normalization to uranium is not applicable since there is a considerable amount of secondary target x-ray excitation in the elastic and quasielastic channel which cannot be separated from the interesting x-ray yield from MNT reactions. Hence, the U x-ray yield is higher by a factor of ~ 3.1 than predicted by the PRISMA-DANTE particle coincidences. For the actinide binary partners, proton-stripping reactions are favored over proton pickup. Products in the $+1p$ channel Pa have about twice the survival probability as compared to the $-1p$ channel Np. Similar behavior for the survival rate is observed in the $\pm 2p$ Pu and Th channels. Pu is hardly accessible via this kind of reaction.

Despite those from the U channel, x-ray yields are consistent with the yield extracted on basis of the PRISMA-DANTE ΔToF , demonstrating that the technique of kinematic coincidences employing a recoil-tagging detector system is suitable to discriminate fission background successfully from true multinucleon-transfer events. The GRAZING calculations normalized to Pu reproduce the x-ray yields of Np and U, whereas they underestimate the population of Pa and Th significantly.

B. Neutron evaporation

Neutron evaporation strongly affects the final yield distribution of both binary partners and it hinders the production of very neutron-rich nuclei. Free neutrons are detected by the employed γ -ray detector array. Fast-neutron-induced delayed γ -ray lines originating from $(n, n'\gamma)$ scattering on ^{27}Al , ^{70}Ge , ^{72}Ge , and ^{74}Ge are visible in the AGATA energy spectra [44,45]. In the time spectrum, the hits are delayed due to the longer time-of-flight of the neutrons.

The fast-moving neutrons scatter and interact with the ^{74}Ge of the AGATA detector by exciting the first 2^+ state via the

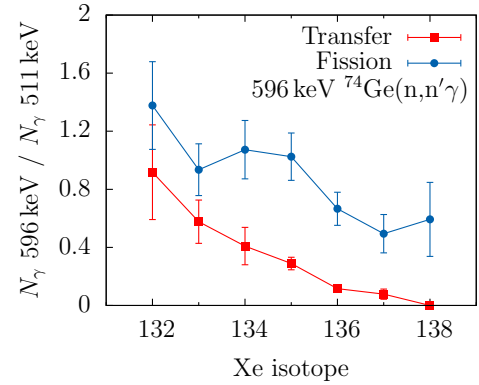


FIG. 12. (Color online) γ -ray intensities of neutron-induced background radiation with gates on the transfer- and fissionlike ΔToF peak. In the channels in which neutrons were stripped from the ejectile nucleus, more neutrons react with the surrounding HPGe detectors, hindering the production of actinide binary partners.

$^{74}\text{Ge}(n, n'\gamma)$ reaction. The corresponding $2_1^+ \rightarrow 0_1^+$ transition at 596 keV is clearly visible in the not-Doppler-corrected γ -ray spectra. The areas of the 596-keV line along the Xe isotopic chain divided by the area of the 511-keV line is depicted in Fig. 12. The 511-keV line was taken as a normalization factor as it does not depend on the amount of evaporated neutrons. Gates were applied on the individual isotopes, on the delayed part of the time signal, and on the fission- and transferlike ΔToF areas.

After neutron transfer, primary products may be highly excited due to the effects of large energy loss, in turn leading to particle (mainly neutron) evaporation. As expected, the transfer channels after neutron stripping show more neutron interactions in the germanium (red points in Fig. 12). With increasing number of neutrons which are transferred to the target nucleus, more evaporated neutrons are detected. Fission fragments (blue points) are related to much more neutron-induced background since several neutrons are produced in each fission process.

C. γ -Ray emission

γ -Ray spectra of actinide reaction channels are obtained by gating on the mass channel of the lighter binary partner and on the transferlike ΔToF region in two-dimensional matrices shown in Fig. 8. The Doppler correction for the actinide reaction partner is performed using the first interaction point of the γ ray within AGATA. The velocity vector of the targetlike nucleus is determined on an event-by-event basis using relativistic two-body reaction kinematics.

A Doppler-corrected γ -ray spectrum for the actinide partner ^{240}U is shown in Fig. 13 which corresponds to the identified ^{134}Xe fragments in PRISMA with a gate on the transferlike ΔToF events. In the top panel, neutron-evaporation channels to ^{239}U and ^{238}U are clearly visible in the spectrum. For example, in the region around 260 keV one observes three peaks belonging to ^{239}U , ^{238}U , and ^{240}U . The total excitation energy can be restricted by gating on the TKEL in the analysis. This yields for targetlike nuclei

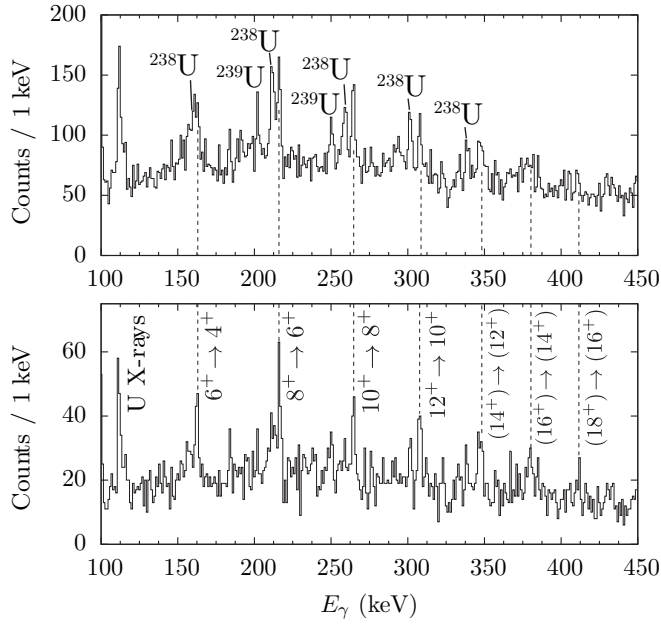


FIG. 13. Tracked singles γ -ray spectra of identified ^{134}Xe fragments in PRISMA with a gate on the transferlike ΔToF peak, Doppler-corrected for the actinide binary partner ^{240}U . (Top) Neutron evaporation to ^{239}U and ^{238}U dominate the spectrum. (Bottom) A cut on $\text{TKEL} > -65$ MeV yields a neutron-evaporation suppressed spectrum revealing the rotational band of ^{240}U .

a suppression of neutron-evaporation channels in the actinide spectra. Especially events with small TKEL values are related to reaction products with a lower excitation energy and therefore reduced neutron evaporation. As the TKEL is shared between the two reaction products, it is not distinguishable to which amount beam- and targetlike fragments are individually excited. After applying a cut on $\text{TKEL} > -65$ MeV and therefore suppressing neutron evaporation, the ^{238}U and ^{239}U contributions are less prominent in the γ -ray spectra, revealing the rotational band of ^{240}U with possible spins up to $18\hbar$. The rotational band was already observed up to the decay of the 12^+ state in a previous work [21], and the extension to higher-lying states and other results from discrete spectroscopy from this experiment are described in Refs. [34,46,47] and will be subject of a forthcoming publication [48].

Neutron evaporation becomes negligible for neutron-pickup channels in the actinide region, as already indicated in Fig. 12. Figure 14 shows the singles γ -ray spectrum of ^{236}U without cuts on particle coincidence or TKEL requirements. The spectrum does not exhibit lines from neighboring nuclei after neutron evaporation. The ground-state band is visible up to spin $14\hbar$. Channels corresponding to a higher number of transferred neutrons are not observed. In fact, in the spectrum corresponding to ^{242}U , there is no evidence of the de-excitation γ rays characteristic of this nucleus [22]. Cuts on TKEL and ΔToF particle coincidences do not improve the results.

VI. CONCLUSIONS

The present experiment and its results demonstrate the synergies of the high efficiency γ -ray tracking spectrometer

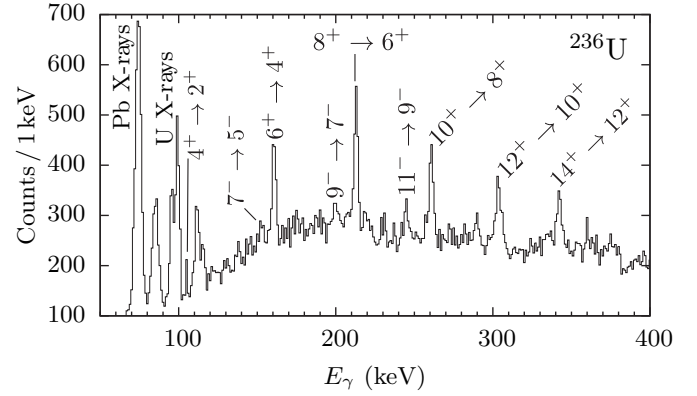


FIG. 14. Tracked singles γ -ray spectra of identified ^{138}Xe fragments, Doppler corrected for the binary actinide partner ^{236}U , no TKEL cut is applied. All observed transitions can be attributed to ^{236}U , and neutron evaporation channels are suppressed.

AGATA in combination with the mass spectrometer PRISMA and the ancillary multichannel-plate detector DANTE. It was shown that the setup is able to track down the elusive γ rays from weakly populated submillibarn reaction channels under demanding conditions caused by the high fission background from the employed actinide target.

The obtained results confirm that population of neutron-rich actinide nuclei without proton transfer is indeed favored, especially the $-2n$ channel leading to ^{240}U . Therefore, this type of reaction provides a promising tool to study the nuclear structure of heavier actinides used as target material. The results are in line with the measurement of Ishii *et al.* where the $-2n$ transfer channel was strongest for the $^{248}\text{Cm}(^{18}\text{O}, ^{16}\text{O})^{250}\text{Cm}$ reaction [49]. However, the transfer of two protons into the target nucleus is clearly much weaker and only few Pu isotopes were detected as transfer products via the corresponding x-ray yield. There was no measurable yield observed beyond Pu or the $-2p$ channel.

Comparison of experimental mass distributions after multinucleon-transfer with the GRAZING calculations yields a fair agreement for few-nucleon transfer channels. However, there are clear discrepancies, especially on the neutron-deficient side. The measured cross sections are off by more than a factor of 10 for the $+2p$ channel or the barium isotopes. The experimental cross-section values are considerably higher than GRAZING results. Neutron evaporation from excited actinide reaction products dominates the γ -ray spectra in the targetlike reaction channels and has to be treated carefully since it obstructs the correct assignment of γ -ray transition candidates to the corresponding targetlike nuclei.

Along the proton-transfer chains, GRAZING calculations underpredict proton pickup channels, fairly well reproduce the Xe isotopes, and overpredict channels involving proton stripping, though generally quite well reproducing the trend on the neutron-rich side of each isotopic distribution. First, an underprediction for the Cs isotopes is obtained in the $+1p$ channel. A fair reproduction of the Xe spectrum is obtained. An increasing overprediction by GRAZING from the $-1p$ to the $-2p$ channel is found. The last two channels deviate strongly in the overall distributions. Population of actinide nuclei with

higher Z is clearly disfavored for this reaction. GRAZING, with its coupled-channel semiclassical formalism, considers only surface degrees of freedom and single-particle transfer (stripping and pickup) channels. Other degrees of freedom such as pair transfer modes may be important yet very few data exist on those effects up to now.

Another obvious discrepancy is visible on the neutron-poor side for all the measured distributions. The experimental results were clearly improved by demanding particle coincidences of ejectile nuclei with surviving recoil fragments measured at the grazing angle. Hence, a rigorous fission suppression could be successfully obtained. Besides fission, the effect of neutron evaporation may be very strong which is not reproduced for these heavy systems by GRAZING. In the near future it will be very interesting to compare the observed production rates with the results of the extended GRAZING-F code [50].

However, with respect to fission probabilities, we note that in Ref. [42] the theoretical excitation energy and angular momenta provided by GRAZING for the light and heavy reaction products have been successfully used for comparison with the experimental multinucleon transfer cross sections and fission probability in the $^{58}\text{Ni} + ^{208}\text{Pb}$ system.

As Zagrebaev and Greiner [51] pointed out, high cross sections for the production of targetlike actinide nuclei are expected in the forward direction. In a recent study of multinucleon transfer reactions in $^{58,64}\text{Ni} + ^{207}\text{Pb}$ collisions at the velocity filter SHIP at GSI [52] transfers of up to seven

protons from the beam to the target nucleus were observed in the strong forward direction. The experimental geometry of our measurement did exclude the observation of large transfers in the narrow cone around zero degrees. Therefore, no similar experimental observation is expected from these results. Nevertheless, the refined detection capabilities and its new observables allow us to extract hard-to-reach nuclei in the low-statistics recoil channels for both few-neutron transfer and proton stripping. It will be of high interest to perform more detailed systematic investigations of this kind in the actinide region in the future.

ACKNOWLEDGMENTS

The research leading to these results has received funding from the German Bundesministerium für Bildung und Forschung (BMBF) under Contract No. 05P12PKFNE TP4, the European Union Seventh Framework Programme (FP7/2007-2013) under Grant No. 262010-ENSAR, and the Spanish Ministerio de Ciencia e Innovación under Contract No. FPA2011-29854-C04. A.V. thanks the Bonn-Cologne Graduate School of Physics and Astronomy (BCGS) for financial support. One of the authors (A. Gadea) was supported by MINECO, Spain, under Grants No. FPA2011-29854-C04 and No. FPA2014-57196-C5, Generalitat Valenciana, Spain, under Grant No. PROMETEOII/2014/019, and EU under the FEDER program.

-
- [1] M. Schädel, J. V. Kratz, H. Ahrens, W. Brüche, G. Franz, H. Gäggeler, I. Warnecke, G. Wirth, G. Herrmann, N. Trautmann, and M. Weis, *Phys. Rev. Lett.* **41**, 469 (1978).
 - [2] M. Schädel, W. Brüche, H. Gäggeler, J. V. Kratz, K. Sümmerer, G. Wirth, G. Herrmann, R. Stakemann, G. Tittel, N. Trautmann, J. M. Nitschke, E. K. Hulet, R. W. Loughheed, R. L. Hahn, and R. L. Ferguson, *Phys. Rev. Lett.* **48**, 852 (1982).
 - [3] D. Lee, H. von Gunten, B. Jacak, M. Nurmia, Y.-f. Liu, C. Luo, G. T. Seaborg, and D. C. Hoffman, *Phys. Rev. C* **25**, 286 (1982).
 - [4] K. J. Moody, D. Lee, R. B. Welch, K. E. Gregorich, G. T. Seaborg, R. W. Loughheed, and E. K. Hulet, *Phys. Rev. C* **33**, 1315 (1986).
 - [5] K. Moody, W. Brüche, M. Brägger, H. Gäggeler, B. Haefner, M. Schädel, K. Sümmerer, H. Tetzlaff, G. Herrmann, N. Kaffrell, J. Kratz, J. Rogowski, N. Trautmann, M. Skälberg, G. Skarnemark, J. Alstad, and M. Fowler, *Z. Phys. A* **328**, 417 (1987).
 - [6] R. B. Welch, K. J. Moody, K. E. Gregorich, D. Lee, and G. T. Seaborg, *Phys. Rev. C* **35**, 204 (1987).
 - [7] K. E. Gregorich, K. J. Moody, D. Lee, W. K. Kot, R. B. Welch, P. A. Wilmarth, and G. T. Seaborg, *Phys. Rev. C* **35**, 2117 (1987).
 - [8] H. Gäggeler, N. Trautmann, W. Brüche, G. Herrmann, J. V. Kratz, P. Peuser, M. Schädel, G. Tittel, G. Wirth, H. Ahrens, H. Folger, G. Franz, K. Sümmerer, and M. Zendel, *Phys. Rev. Lett.* **45**, 1824 (1980).
 - [9] J. V. Kratz, M. Schädel, and H. W. Gäggeler, *Phys. Rev. C* **88**, 054615 (2013).
 - [10] V. I. Zagrebaev and W. Greiner, *Phys. Rev. C* **87**, 034608 (2013).
 - [11] K. Sekizawa and K. Yabana, *Phys. Rev. C* **88**, 014614 (2013).
 - [12] A. Winther, *Nucl. Phys. A* **572**, 191 (1994).
 - [13] A. Winther, *Nucl. Phys. A* **594**, 203 (1995).
 - [14] A. Winther, Program grazing, <http://www.to.infn.it/~nanni/grazing> (2006).
 - [15] E. Vigezzi and A. Winther, *Ann. Phys. (N.Y.)* **192**, 432 (1989).
 - [16] L. Corradi, G. Pollaro, and S. Szilner, *J. Phys. G* **36**, 113101 (2009).
 - [17] E. M. Kozulin, E. Vardaci, G. N. Knyazheva, A. A. Bogachev, S. N. Dmitriev, I. M. Itkis, M. G. Itkis, A. G. Knyazev, T. A. Loktev, K. V. Novikov, E. A. Razinkov, O. V. Rudakov, S. V. Smirnov, W. Trzaska, and V. I. Zagrebaev, *Phys. Rev. C* **86**, 044611 (2012).
 - [18] J. S. Barrett, W. Loveland, R. Yanez, S. Zhu, A. D. Ayangeakaa, M. P. Carpenter, J. P. Greene, R. V. F. Janssens, T. Lauritsen, E. A. McCutchan, A. A. Sonzogni, C. J. Chiara, J. L. Harker, and W. B. Walters, *Phys. Rev. C* **91**, 064615 (2015).
 - [19] J. F. C. Cocks, P. A. Butler, K. J. Cann, P. T. Greenlees, G. D. Jones, J. F. Smith, P. M. Jones, R. Julin, S. Juutinen, D. Müller, M. Piiparinen, A. Savelius, R. Broda, B. Fornal, I. Ahmad, D. J. Blumenthal, M. P. Carpenter, B. Crowell, R. V. F. Janssens, T. L. Khoo, T. Lauritsen, D. Nisius, S. Asztalos, R. M. Clark, M. A. Deleplanque, R. M. Diamond, P. Fallon, I. Y. Lee, A. O. Macchiavelli, R. W. MacLeod, F. S. Stephens, P. Bhattacharyya, and C. T. Zhang, *J. Phys. G* **26**, 23 (2000).
 - [20] J. F. C. Cocks, P. A. Butler, K. J. Cann, P. T. Greenlees, G. D. Jones, S. Asztalos, P. Bhattacharyya, R. Broda, R. M. Clark, M. A. Deleplanque, R. M. Diamond, P. Fallon, B. Fornal,

- P. M. Jones, R. Julin, T. Lauritsen, I. Y. Lee, A. O. Macchiavelli, R. W. MacLeod, J. F. Smith, F. S. Stephens, and C. T. Zhang, *Phys. Rev. Lett.* **78**, 2920 (1997).
- [21] T. Ishii, S. Shigematsu, M. Asai, A. Makishima, M. Matsuda, J. Kaneko, I. Hossain, S. Ichikawa, T. Kohno, and M. Ogawa, *Phys. Rev. C* **72**, 021301 (2005).
- [22] T. Ishii, H. Makii, M. Asai, H. Koura, S. Shigematsu, K. Tsukada, A. Toyoshima, M. Matsuda, A. Makishima, J. Kaneko, H. Toume, I. Hossain, T. Shizuma, S. Ichikawa, T. Kohno, and M. Ogawa, *Phys. Rev. C* **76**, 011303 (2007).
- [23] C. H. Dasso, G. Pollaro, and A. Winther, *Phys. Rev. Lett.* **73**, 1907 (1994).
- [24] A. Stefanini, L. Corradi, G. Maron, A. Pisent, M. Trotta, A. Vinodkumar, S. Beghini, G. Montagnoli, F. Scarlassara, G. Segato, A. D. Rosa, G. Inglima, D. Pierrousakou, M. Romoli, M. Sandoli, G. Pollaro, and A. Latina, *Nucl. Phys. A* **701**, 217 (2002).
- [25] S. Szilner, C. A. Ur, L. Corradi, N. Marginean, G. Pollaro, A. M. Stefanini, S. Beghini, B. R. Behera, E. Fioretto, A. Gadea, B. Guiot, A. Latina, P. Mason, G. Montagnoli, F. Scarlassara, M. Trotta, G. de Angelis, F. Della Vedova, E. Farnea, F. Haas, S. Lenzi, S. Lunardi, R. Marginean, R. Menegazzo, D. R. Napoli, M. Nespola, I. V. Pokrovsky, F. Recchia, M. Romoli, M.-D. Salsac, N. Soić, and J. J. Valiente-Dobón, *Phys. Rev. C* **76**, 024604 (2007).
- [26] L. Corradi, S. Szilner, G. Pollaro, D. Montanari, E. Fioretto, A. Stefanini, J. Valiente-Dobón, E. Farnea, C. Michelagnoli, G. Montagnoli, F. Scarlassara, C. Ur, T. Mijatović, D. J. Malenica, N. Soić, and F. Haas, *Nucl. Instr. Meth. Phys. Res. B* **317** (Part B), 743 (2013).
- [27] A. Gadea, E. Farnea, J. Valiente-Dobón, B. Million, D. Mengoni, D. Bazzacco, F. Recchia, A. Dewald, T. Pissulla, W. Rother, G. de Angelis *et al.*, *Nucl. Instrum. Methods A* **654**, 88 (2011).
- [28] J. Valiente-Dobón, A. Gadea, S. Brambilla, N. A. Kondratiev, S. Beghini, L. Corradi, G. De Angelis, F. Della Vedova, E. Farnea, E. Fioretto, E. M. Kozulin, S. Lunardi, N. Marginean, G. Montagnoli, D. R. Napoli, R. Orlandi, I. Pokrovsky, E. Sahin, A. M. Stefanini, S. Szilner, M. Trotta, and C. A. Ur, *AIP Conf. Proc.* **853**, 202 (2006).
- [29] O. Tarasov and D. Bazin, *Nucl. Instrum. Methods B* **266**, 4657 (2008).
- [30] G. Duchene, E. Farnea, A. Gadea, A. Korichi, J. Nyberg, P. Reiter, J. Simpson *et al.*, *Nucl. Instrum. Methods A* **668**, 26 (2012).
- [31] A. Wiens, H. Hess, B. Birkenbach, B. Bruyneel, J. Eberth, D. Lersch, G. Pascovici, P. Reiter, and H.-G. Thomas, *Nucl. Instrum. Methods A* **618**, 223 (2010).
- [32] G. Montagnoli, A. Stefanini, M. Trotta, S. Beghini, M. Bettini, F. Scarlassara, V. Schiavon, L. Corradi, B. Behera, E. Fioretto, A. Gadea, A. Latina, S. Szilner, L. Donà, M. Rigato, N. Kondratiev, A. Y. Chizhov, G. Kniajeva, E. Kozulin, I. Pokrovskiy, V. Voskressensky, and D. Ackermann, *Nucl. Instrum. Methods A* **547**, 455 (2005).
- [33] S. Beghini, L. Corradi, E. Fioretto, A. Gadea, A. Latina, G. Montagnoli, F. Scarlassara, A. Stefanini, S. Szilner, M. Trotta, and A. Vinodkumar, *Nucl. Instrum. Methods A* **551**, 364 (2005).
- [34] B. Birkenbach, Ph.D. thesis, Universität zu Köln, 2014.
- [35] A. B. Brown, C. W. Snyder, W. A. Fowler, and C. C. Lauritsen, *Phys. Rev.* **82**, 159 (1951).
- [36] A. Lopez-Martens, K. Hauschild, A. Korichi, J. Roccas, and J.-P. Thibaud, *Nucl. Instrum. Methods A* **533**, 454 (2004).
- [37] D. Montanari, E. Farnea, S. Leoni, G. Pollaro, L. Corradi, G. Benzoni, A. Gadea, E. Fioretto, A. Latina, G. Montagnoli, F. Scarlassara, A. Stefanini, and S. Szilner, *Eur. Phys. J. A* **47**, 4 (2011).
- [38] A. Astier, M.-G. Porquet, G. Duchêne, F. Azaiez, D. Curien, I. Deloncle, O. Dorvaux, B. J. P. Gall, M. Houry, R. Lucas, P. C. Srivastava, N. Redon, M. Rousseau, O. Stézowski, and C. Theisen, *Phys. Rev. C* **87**, 054316 (2013).
- [39] R. Broglia and A. Winther, *Heavy Ion Reactions: The Elementary Processes*, Frontiers in Physics Lecture Note Series Vol. 84 (Addison-Wesley, Redwood City, CA, 1991).
- [40] R. Broglia, G. Pollaro, and A. Winther, *Nucl. Phys. A* **361**, 307 (1981).
- [41] G. Pollaro, R. Broglia, and A. Winther, *Nucl. Phys. A* **406**, 369 (1983).
- [42] L. Corradi, A. M. Vinodkumar, A. M. Stefanini, E. Fioretto, G. Prete, S. Beghini, G. Montagnoli, F. Scarlassara, G. Pollaro, F. Cerutti, and A. Winther, *Phys. Rev. C* **66**, 024606 (2002).
- [43] L. Corradi, A. M. Stefanini, C. J. Lin, S. Beghini, G. Montagnoli, F. Scarlassara, G. Pollaro, and A. Winther, *Phys. Rev. C* **59**, 261 (1999).
- [44] A. Ataç, A. Kaşkaş, S. Akkoyun, M. Şenyiğit, T. Hüyük, S. Kara, and J. Nyberg, *Nucl. Instr. Meth. Phys. Res. A* **607**, 554 (2009).
- [45] J. Ljungvall and J. Nyberg, *Nucl. Instrum. Methods A* **550**, 379 (2005).
- [46] K. Geibel, Ph.D. thesis, Universität zu Köln, 2012.
- [47] P. Reiter, B. Birkenbach, and T. Kotthaus, *Phys. Procedia* **59**, 119 (2014); GAMMA-2 Scientific Workshop on the Emission of Prompt Gamma-Rays in Fission and Related Topics.
- [48] B. Birkenbach, K. Geibel, P. Reiter, and A. Vogt (unpublished).
- [49] T. Ishii, S. Shigematsu, H. Makii, M. Asai, K. Tsukada, A. Toyoshima, M. Matsuda, A. Makishima, T. Shizuma, J. Kaneko, I. Hossain, H. Toume, M. Ohara, S. Ichikawa, T. Kohno, and M. Ogawa, *J. Phys. Soc. Jpn.* **75**, 043201 (2006).
- [50] R. Yanez and W. Loveland, *Phys. Rev. C* **91**, 044608 (2015).
- [51] V. I. Zagrebaev and W. Greiner, *Phys. Rev. C* **83**, 044618 (2011).
- [52] V. Comas, S. Heinz, S. Hofmann, D. Ackermann, J. Heredia, F. Heßberger, J. Khuyagbaatar, B. Kindler, B. Lommel, and R. Mann, *Eur. Phys. J. A* **49**, 112 (2013).

Addendum: Simulation of the PRISMA spectrometer

The identification of the individual reaction products in PRISMA is based on a software reconstruction of the ion trajectories. Incoming ions are transmitted and dispersed by their mass-over-charge ratio A/q from the MCP start detector down to the focal plane through the magneto-optical imaging system consisting of a quadrupole followed by a dipole magnet. The motion of a charged particle inside the quadrupole and the dipole is determined by the corresponding magnetic rigidities BR . Using precise measurements of position, time, and total energy signals both at the entrance and at the focal plane, the flight path $L(\theta, \phi)$ as well as the curvature bending radius $R(\theta, \phi)$ in the dipole magnet are reconstructed iteratively using a ray-tracing algorithm. Of course, unlike in an ideal instrument, non-linearities, inhomogeneous magnetization, and aberrations of any order due to misalignment and magnetic fringe fields may yield systematic dependencies between A/q and the position coordinates at the entrance and at the focal-plane detectors. Most of the magneto-optical aberration effects are compensated by the software trajectory reconstruction or reabsorbed with carefully chosen effective

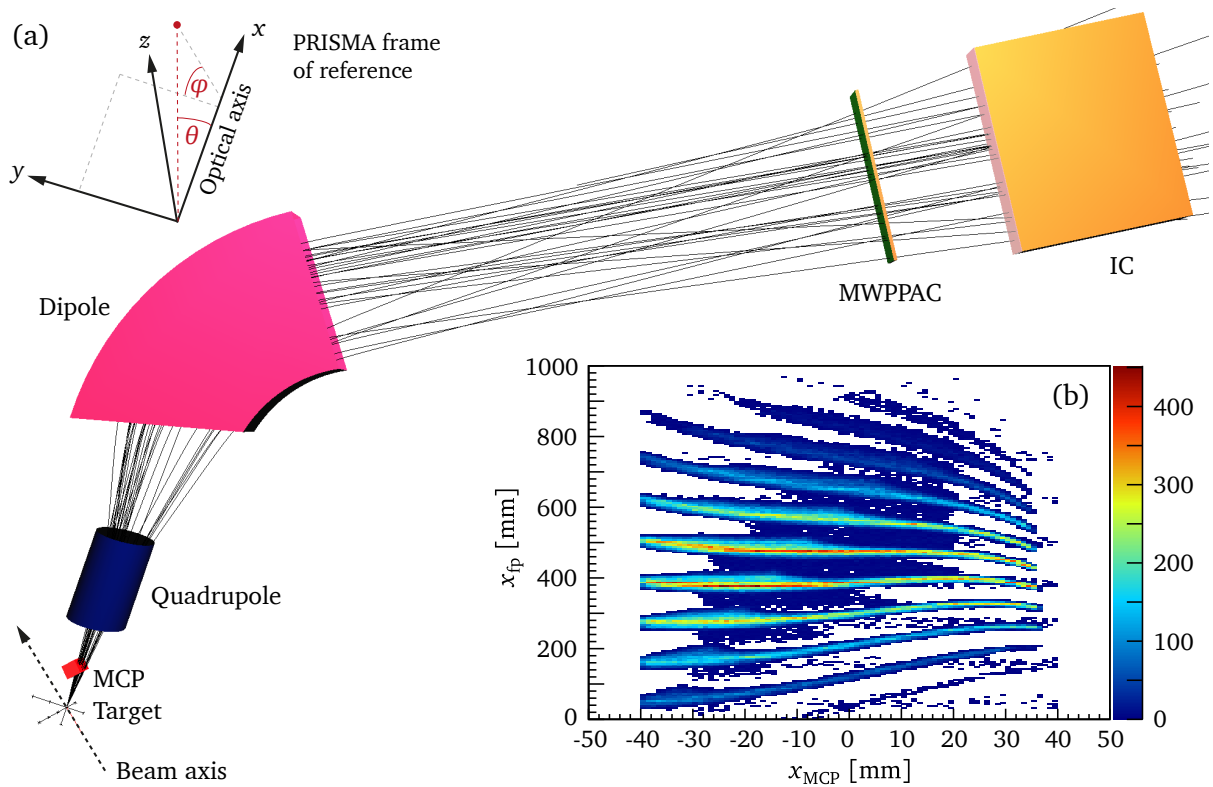


Figure 10: Simulation of the PRISMA mass spectrometer. (a) OpenGL visualization of the PRISMA detector setup with the first 100 virtual events transported through the magnetic system by the Monte-Carlo simulation. Further details on the detectors and magnets are available in Publication I of this thesis and Ref. [130]. A schematic view of the employed coordinate system in the PRISMA frame of reference is shown in the top-left inset. (b) Simulated charge-state distributions of ^{136}Xe with a kinetic energy of 519(3) MeV plotted in a matrix of the horizontal positions at the MCP entrance-detector and at the MWPPAC focal plane.

lengths between the different detector parts. Remaining aberration effects vanish after applying elaborate aberration-correction procedures. This procedure is thoroughly described in the preceding master thesis in Ref. [130]. In order to obtain relative cross sections, the mass yields also have to be corrected for the efficiency and the response of the PRISMA mass spectrometer. For this purpose, an isotropic event distribution uniform in energy is transported through the spectrometer employing a Monte-Carlo simulation as introduced in Refs. [131, 132].

The initial uniform input distribution is generated by the program `GENERALGENERATOR` with an energy in a range from 290 to 650 MeV, corresponding to the measured β^2 distribution or rather the device's momentum acceptance, and a (polar) angular range $\theta_{\text{lab}} = 50^\circ \pm 8^\circ$ around the reaction's grazing angle. Also slightly larger as in the experiment, the azimuthal angular range is chosen from -40° to $+40^\circ$. Each event contains the nuclear charge Z , mass A and a four-momentum vector (E, \vec{p}) . Subsequently, the program `EVENTGENERATOR` assigns an atomic charge state by evaluating a probability distribution which follows the semi-empirical formula by R.O. Sayer for heavy-ion stripping data [133, 134].

Finally, the program `PRISMA` transports each virtual ion event-by-event through PRISMA using the ray-tracing code of the PRISMA software library. Magnetic fields are set the same way as in the experimental analysis. Energy losses in Mylar[®] windows and gas volumes along the ion flight path are accounted for as well. The output is converted and stored in `ROOT` trees containing all PRISMA observables such as the time of flight, path length, curvature radius, deposited energies in the ionization chambers, and hit positions on entrance and focal-plane detectors. A simulated charge-state transmission of ^{136}Xe with a gate on $E_{\text{kin}} = 519(3)$ MeV is visible in Fig. 10(b). Horizontal positions of the MCP entrance-detector and MWPPAC focal plane are plotted in the bottom-right matrix.

Adjustment of the magnetic fields

The simulated charge-state transport and deflection must be consistent with experimental data. Therefore, both dipole and quadrupole fields are one by one adjusted to align the simulated event distributions with the experimental ones. The dipole field determines the ion trajectory along the optical axis. Accordingly, the trajectory off the optical axis is influenced by the quadrupole field. The tuning of the dipole field is performed by selecting a narrow gate around the horizontal and vertical centers of the MCP entrance detector. Distortions caused by the quadrupole are excluded in this way since the quadrupole field vanishes along the optical axis (cf. Fig. 10).

First, to compare the charge-state distributions, experimental absolute charge states are calculated from the ion velocity β , mass m and curvature radius R :

$$\frac{q}{e} = \frac{\beta c m}{\sqrt{1 - \beta^2} B R} \quad (2.1)$$

Spectra of charge-state distributions in dependence of the kinetic energy are shown in the right panels of Fig. 11. Generally, the employed semi-empirical expression reproduces the experimental

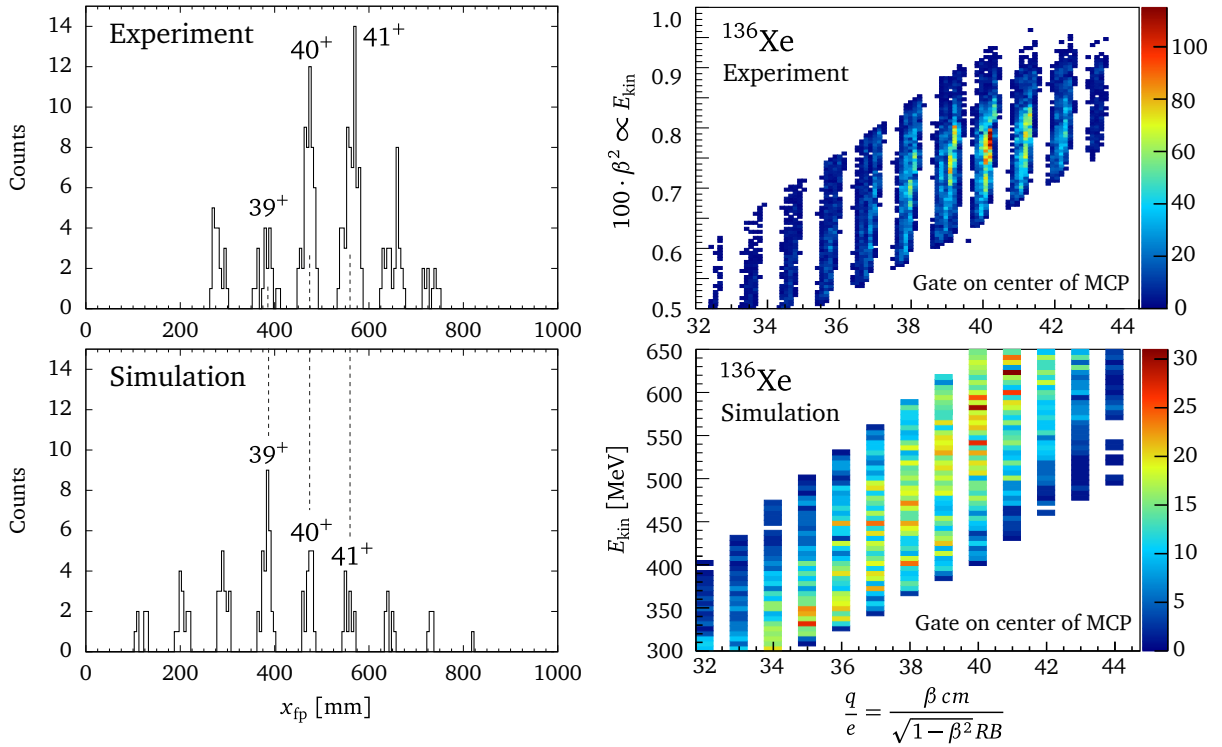


Figure 11: Tuning of the magnetic fields in the PRISMA simulation. Left: Projected experimental and simulated charge-state distributions detected at the focal plane of PRISMA. A gate is placed around $x_{\text{MCP}} \approx 0$ and $y_{\text{MCP}} \approx 0$. Right: Dependence of the charge state on the ejectile's kinetic energy (with a gate on the MCP center). The experimental absolute charge states have to be calculated from the kinetic energy, mass and curvature radius. The simulation reproduces the experimental behavior quite well.

behavior. The left panels show projected charge-state distributions as detected at the focal plane. After increasing the dipole field by 2.3% in the simulation, the simulated charge-state distribution matches the experimental one. Note that the peak intensities are mismatched in the order of $\Delta q \approx 2e$. Possible effects caused by the thick target or further electron stripping when passing the carbon foil at the entrance detector, which is not taken into account in the simulation, may be responsible for this shortcoming. Once the dipole field is set, the magnetic field of the quadrupole is tuned. To verify how the simulated event distributions are in comparison to the experimental ones, various small gates on the horizontal plane of the MCP (i.e. at $y = 0$ and at different x positions) are examined. The quadrupole field is reduced by 40% to match the experimental distribution.

Response function

The response function is defined as the ratio of transported events over the initial ones for each energy and angle. The corresponding correction factor reads as follows:

$$f(E_{\text{kin}}, \theta, \phi) = \frac{N_{\text{input, entrance detector}}(E_{\text{kin}}, \theta, \phi)}{N_{\text{output, focal plane}}(E_{\text{kin}}, \theta, \phi)} \quad (2.2)$$

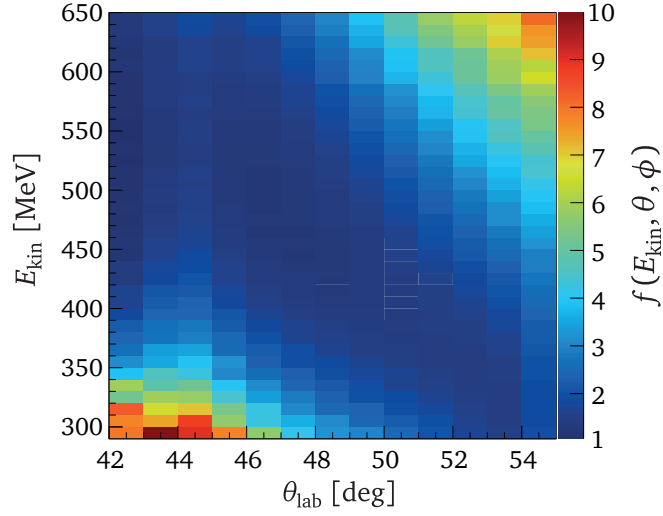


Figure 12: Response function for ^{135}Xe in a matrix of θ_{lab} plotted against the kinetic energy E_{kin} of the incoming ion. The color code parametrizes the correction factor $f(E_{\text{kin}}, \theta, \phi)$.

It is easily extracted from the simulation data by comparing the event distributions at the MCP entrance detector and the MWPPAC at the focal plane. The gating conditions are chosen as follows: the ion has to be successfully transported to the MWPPAC detector, there has to be a signal in the ionization chamber (IC), and no IC veto signal is allowed. An example response function of the ^{135}Xe channel is presented in Fig. 12. The correction factor is plotted in a matrix of θ_{lab} against the kinetic energy E_{kin} of the incoming ion. Applied to the measured mass yield \tilde{Y} , the resulting response function $f(E_{\text{kin}}, \theta, \phi)$ gives transmission-corrected yields Y :

$$Y = f(E_{\text{kin}}, \theta, \phi) \cdot \tilde{Y} \quad (2.3)$$

Contamination correction

The extent of Xe contamination in the $\pm 1p$ reaction channels I and Cs is identified and corrected by fitting characteristic Xe γ -ray signatures in the ejectile Doppler-corrected γ -ray spectra of isobaric mass channels. The 1313-keV and 812-keV transitions of the dominant ^{136}Xe channel and the 847-keV transition in ^{134}Xe are used as contamination probes. Each contamination is subtracted from the yield of the corresponding mass channel Y_A according to the measured Xe production yield. The percentage of the Xe contaminant κ is defined as follows:

$$\kappa = \frac{Y_{\text{cont.}}}{Y_A} = \frac{N_{\gamma}^{\text{cont.}}}{N_{\gamma}^{\text{Xe}}} \frac{Y_{\text{Xe}}}{Y_A} \quad (2.4)$$

where $Y_{\text{cont.}}$ is the contaminant yield, $N_{\gamma}^{\text{cont.}}$ the integral of the corresponding Xe γ -ray peaks in the γ -ray spectrum of the examined mass channel, Y_{Xe} the yield of ^{134}Xe or ^{136}Xe , and N_{γ}^{Xe} the integral of the peaks in the ^{134}Xe or ^{136}Xe γ -ray spectra. Next-neighbor even-mass isobars of ^{136}Xe are

odd-odd nuclei with high level densities, so that overlapping transitions in the region of 1313 keV have to be taken into account in the fit model. The contamination of ^{136}Xe in ^{136}Cs amounts to $\kappa = 55.8 \pm 2.7\%$, the one of ^{136}Xe in ^{136}I to $87.8 \pm 2.8\%$. Figure 13 presents xenon, iodine, and caesium mass distributions before and after the contamination correction. Especially the iodine channel is severely distorted by an overlapping distribution around mass $A = 136$; the corrected distribution shows the expected bell-shaped behavior. The xenon channel exhibits significant contamination in the $\pm 1n$, $-3n$, and in the $-4n$ channels due to repetitive characteristics in the magnetic system of the PRISMA mass spectrometer.

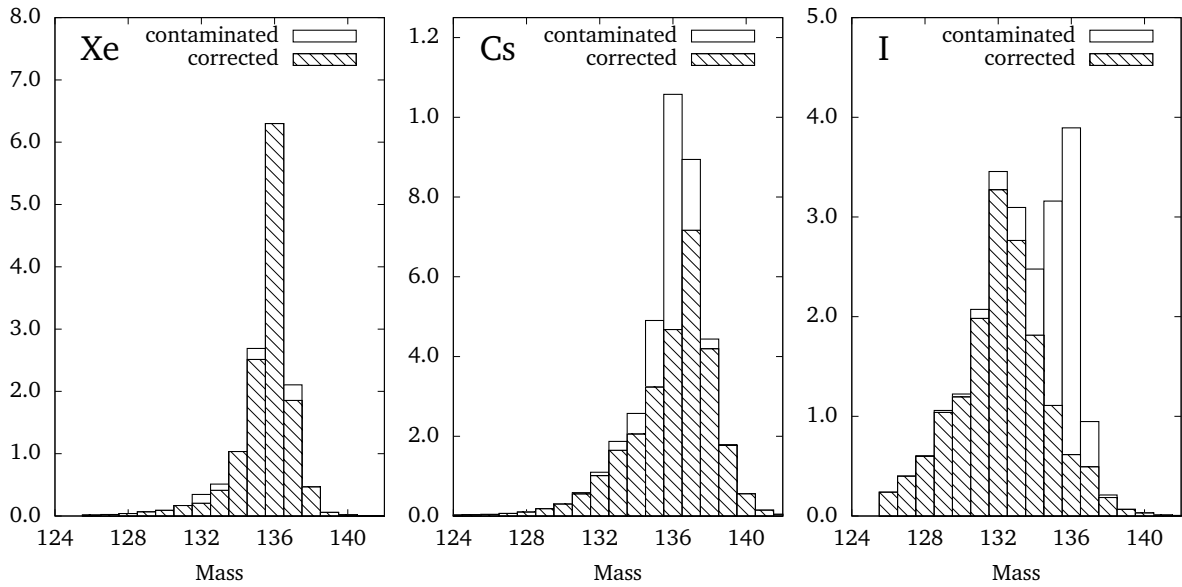


Figure 13: Xe, I, and Cs mass distributions before and after the contamination correction.

Publication II:

**Spectroscopy of the neutron-rich
actinide nucleus ^{240}U**

Spectroscopy of the neutron-rich actinide nucleus ^{240}U following multinucleon-transfer reactions

B. Birkenbach,^{1,*} A. Vogt,¹ K. Geibel,¹ F. Recchia,^{2,3} P. Reiter,¹ J. J. Valiente-Dobón,⁴ D. Bazzacco,³ M. Bowry,⁵ A. Bracco,⁶ B. Bruyneel,⁷ L. Corradi,⁴ F. C. L. Crespi,⁶ G. de Angelis,⁴ P. Désesquelles,⁸ J. Eberth,¹ E. Farnea,³ E. Fioretto,⁴ A. Gadea,⁹ A. Gengelbach,¹⁰ A. Giaz,⁶ A. Görgen,^{11,12} A. Gottardo,⁴ J. Grebosz,¹³ H. Hess,¹ P. R. John,^{2,3} J. Jolie,¹ D. S. Judson,¹⁴ A. Jungclaus,¹⁵ W. Korten,¹² S. Lenzi,² S. Leoni,⁶ S. Lunardi,^{2,3} R. Menegazzo,³ D. Mengoni,^{16,2,3} C. Michelagnoli,^{2,3,†} T. Mijatović,¹⁷ G. Montagnoli,^{2,3} D. Montanari,^{2,3,‡} D. Napoli,⁴ L. Pellegri,⁶ G. Pollarolo,¹⁸ A. Pullia,⁶ B. Quintana,¹⁹ F. Radeck,¹ D. Rosso,⁴ E. Şahin,^{4,§} M. D. Salsac,¹² F. Scarlassara,^{2,3} P.-A. Söderström,^{20,||} A. M. Stefanini,⁴ T. Steinbach,¹ O. Stezowski,²¹ S. Szilner,¹⁷ B. Szpak,¹³ Ch. Theisen,¹² C. Ur,³ V. Vandone,⁶ and A. Wiens¹

¹*Institut für Kernphysik, Universität zu Köln, 50937 Köln, Germany*

²*Dipartimento di Fisica e Astronomia, Università di Padova, I-35131 Padova, Italy*

³*Istituto Nazionale di Fisica Nucleare, Sezione di Padova, I-35131 Padova, Italy*

⁴*Istituto Nazionale di Fisica Nucleare, Laboratori Nazionali di Legnaro, I-35020 Legnaro, Italy*

⁵*Department of Physics, University of Surrey, Guildford, Surrey GU2 7XH, United Kingdom*

⁶*Dipartimento di Fisica, Università di Milano and INFN Sezione di Milano, I-20133 Milano, Italy*

⁷*CEA Saclay, Service de Physique Nucleaire, F-91191 Gif-sur-Yvette, France*

⁸*Centre de Spectrométrie Nucléaire et de Spectrométrie de Masse (CSNSM), CNRS/IN2P3 and Université Paris-Sud, F-91405 Orsay Campus, France*

⁹*Instituto de Física Corpuscular, CSIC-Universidad de Valencia, E-46071 Valencia, Spain*

¹⁰*Department of Physics and Astronomy, Uppsala University, SE-75121 Uppsala, Sweden*

¹¹*Department of Physics, University of Oslo, Post Office Box 1048 Blindern, N-0316 Oslo, Norway*

¹²*Institut de Recherche sur les lois Fondamentales de l'Univers (IRFU), CEA/DSM, Centre CEA de Saclay, F-91191 Gif-sur-Yvette Cedex, France*

¹³*Henryk Niewodniczański Institute of Nuclear Physics (PAN), PL-31342 Kraków, Poland*

¹⁴*Oliver Lodge Laboratory, University of Liverpool, Liverpool L69 7ZE, United Kingdom*

¹⁵*Instituto de Estructura de la Materia, CSIC, Madrid, E-28006 Madrid, Spain*

¹⁶*Nuclear Physics Research Group, University of the West of Scotland, High Street, Paisley PA1 2BE, Scotland, United Kingdom*

¹⁷*Ruđer Bošković Institute, HR-10 002 Zagreb, Croatia*

¹⁸*Dipartimento di Fisica Teorica dell'Università di Torino and INFN, I-10125 Torino, Italy*

¹⁹*Laboratorio de Radiaciones Ionizantes, Universidad de Salamanca, E-37008 Salamanca, Spain*

²⁰*Department of Physics and Astronomy, Uppsala University, SE-75120 Uppsala, Sweden*

²¹*Université de Lyon, Université Lyon-1, CNRS/IN2P3, UMR5822, IPNL, F-69622 Villeurbanne Cedex, France*

(Received 14 September 2015; published 21 October 2015)

Background: Nuclear structure information for the neutron-rich actinide nuclei is important since it is the benchmark for theoretical models that provide predictions for the heaviest nuclei.

Purpose: γ -ray spectroscopy of neutron-rich heavy nuclei in the actinide region.

Method: Multinucleon-transfer reactions in $^{70}\text{Zn} + ^{238}\text{U}$ and $^{136}\text{Xe} + ^{238}\text{U}$ have been measured in two experiments performed at the INFN Legnaro, Italy. In the ^{70}Zn experiment the high-resolution HPGe Clover Array (CLARA) coupled to the magnetic spectrometer PRISMA was employed. In the ^{136}Xe experiment the high-resolution Advanced Gamma Tracking Array (AGATA) was used in combination with PRISMA and the Detector Array for Multinucleon Transfer Ejectiles (DANTE).

Results: The ground-state band (g.s. band) of ^{240}U was measured up to the 20^+ level and a tentative assignment was made up to the (24^+) level. Results from $\gamma\gamma$ coincidence and from particle coincidence analyses are shown. Moments of inertia (MoI) show a clear upbend. Evidence for an extended first negative-parity band of ^{240}U is found.

Conclusions: A detailed comparison with latest calculations shows best agreement with cranked relativistic Hartree-Bogoliubov (CRHB) calculations for the g.s. band properties. The negative-parity band shows the characteristics of a $K^\pi = 0^-$ band based on an octupole vibration.

DOI: 10.1103/PhysRevC.92.044319

PACS number(s): 23.20.Lv, 25.70.Hi, 27.90.+b, 29.40.Gx

*Corresponding author: birkenbach@ikp.uni-koeln.de

[†]Present address: GANIL, CEA/DSM-CNRS/IN2P3, F-14076, Caen, France.

[‡]Present address: USIAS, Université de Strasbourg, IPHC-CNRS, F-67037 Strasbourg Cedex 2, France.

[§]Present address: Department of Physics, University of Oslo, P. O. Box 1048 Blindern, N-0316 Oslo, Norway.

^{||}Present address: RIKEN Nishina Center, Wako, 351-0198 Saitama, Japan.

I. INTRODUCTION

The heavy nuclei beyond the last doubly magic nucleus ^{208}Pb in the actinide region from radium to nobelium show a variety of shapes in their ground states and at higher excitation energies. Besides a pronounced ground-state deformation in the quadrupole degree of freedom, also higher multipole orders are relevant and necessary to understand the basic properties of these nuclei. This is especially relevant for the extrapolation into the region of the heaviest elements, where a reduced deformation beyond the midshell region is a clear indicator for the next magic number. At this point not only the deformation as a function of proton number but also its dependence on the neutron number are of highest interest for the understanding of the shell closures of super-heavy elements.

Several theoretical predictions based on different models are put forward to describe shapes and collective excitations and await experimental verification. The ground-state energies, first excited states, and deformation parameters of a wide range of heavy nuclei from Ra up to the superheavy region were calculated in a macroscopic-microscopic approach [1]. The Yukawa-plus-exponential model is taken for the macroscopic part of the energy and the Strutinsky shell correction is used for the microscopic part. Detailed predictions for the even isotope chains $^{226-236}\text{Th}$ and $^{226-242}\text{U}$ are given with a minimum of excitation energy of the first 2^+ state and a maximum of deformation energy at $N = 144, 146$ exactly at the border where experimental data are available.

A second macroscopic-microscopic model [2] is based on the Lublin-Strasbourg drop, the Strutinsky shell-correction method, and the Bardeen-Cooper-Schrieffer approach for pairing correlations used with the cranking model, taking into account a dynamical coupling of rotation with the pairing field. The results describe rotational bands in even-even Ra to Cn isotopes.

The g.s. band and low-lying alternative parity bands in the heaviest nuclei are also calculated within a cluster model [3]. The model is based on the assumption that reflection asymmetric shapes are produced by the motion of the nuclear system in the mass asymmetry coordinate. For the lightest $N = 148$ isotones including ^{240}U , detailed results on the levels of the ground-state rotational band and states of the alternative parity band are obtained. This includes transitional electric dipole, quadrupole, and octupole moments for the transitions from the ground state to the states of alternative parity band.

A very extensive theoretical study in the region from thorium to nobelium isotopes covered nearly all aspects of heavy actinide nuclei [4]. As part of the analysis, collective rotational excitations in the even-even nuclei $^{226-236}\text{Th}$ and $^{228-242}\text{U}$ were calculated employing the Gogny D1S force together with the constrained Hartree-Fock-Bogolyubov (HFB) mean-field method as well as the configuration mixing, blocking, and cranking HFB approaches. The experimental results from the present paper will be directly compared with the values for kinetic moments of inertia for the yrast normal deformed band of ^{240}U as a function of rotational frequency calculated in this theoretical work.

Recent theoretical results on sequences of heavy nuclei from Th to No are obtained within self-consistent

relativistic Hartree-Bogolyubov mean-field calculations which provide a unified description of particle-hole and particle-particle correlations on a mean-field level [5]. Predictions are made for unknown ground-state axial quadrupole and hexadecapole moments along the isotopic chains of various actinide nuclei.

Octupole deformation properties of even-even $^{220-240}\text{U}$ isotopes were also studied within the HFB mean-field framework employing realistic Gogny and Barcelona-Catania-Paris energy density functionals [6]. Here, an octupole collective Hamiltonian is used to obtain information on the evolution of excitation energies and $E1$ and $E3$ transition probabilities of the first negative-parity bandheads.

Afanasjev *et al.* [7,8] employed cranked relativistic Hartree-Bogoliubov (CRHB) calculations for a systematic study of pairing and normally deformed rotational bands of even-even and odd-mass actinides and transactinide nuclei within the relativistic (covariant) density functional theory (CDFT) framework. The calculations have been performed with the NL1 and NL3* parametrizations of the relativistic mean-field Lagrangian. Pairing correlations are taken into account by the Brink-Booker part of the finite-range Gogny D1S force. The stabilization of octupole deformation at high spin is suggested by an analysis of discrepancies between theory and existing experimental information in the band-crossing region of $A \approx 240$ nuclei.

The experimental results from in-beam γ -ray spectroscopy on excited states are either obtained in the vicinity of the few isotopes suited as target material in this mass region or have been measured after fusion evaporation reactions. In both cases mainly neutron-deficient actinide nuclei were investigated. Another approach is based on multinucleon-transfer (MNT) reactions as a tool for spectroscopy of heavy nuclei [9]. One type of experiments relies on the high resolving power and efficiency of a powerful γ -ray detector array to separate the γ rays from the multitude of reaction products and a tremendous background from fission [10]. A second group of measurements relies on few-nucleon transfer reactions with light oxygen beams and were successfully exploited to detect excited states, e.g., in neutron-rich ^{236}Th , $^{240,242}\text{U}$ isotopes [11,12]. γ rays were detected in coincidence with the outgoing transfer products. For the most neutron-rich cases the rotational g.s. band was detected up to spin 8 to 10 \hbar .

In this paper we report and discuss the results of two experiments based on different MNT reactions which were performed at the INFN Laboratori Nazionali di Legnaro (LNL) in order to study the structure of neutron-rich actinide nuclei. Experimental details and data analysis are described in the following two sections. Final results are deduced from γ -ray spectra in Sec. III. A detailed comparison with theoretical predictions and an interpretation of the new findings are given in Sec. IV before the paper closes with a summary and conclusions.

II. EXPERIMENTAL SETUP

In the first experiment, the tandem van de Graaff accelerator in combination with the postaccelerator ALPI delivered a ^{70}Zn beam with an energy of 460 MeV and a current of 2–2.5 pA.

TABLE I. Details of the experimental setups.

	Beam	
Particle	^{70}Zn	^{136}Xe
Energy	460 MeV	1000 MeV
Current	2–2.5 pA	2 pA
	Target	
Isotope	^{238}U	^{238}U
Backing		^{93}Nb
Target thickness	1 mg/cm ²	1/2 mg/cm ²
Backing thickness		0.8 mg/cm ²

The beam impinged onto a 1-mg ^{238}U target. The lighter beamlike reaction products were identified with the magnetic spectrometer PRISMA [13–15] and the γ rays were measured with the HPGe detector array CLARA [16]. The PRISMA spectrometer was placed at angles of 61° and 64° with respect to the beam axis that corresponds to the grazing angle for the multinucleon-transfer (MNT) reaction. The details of the targets and the beams are summarized in Table I. Details of the PRISMA analysis are reported in Ref. [17].

In the second experiment a beam of ^{136}Xe with an energy of 1 GeV, accelerated by the PIAVE-ALPI accelerator complex, impinged on a ^{238}U target. Again the PRISMA spectrometer was used to identify the beamlike particles following the MNT reaction. Experimental details are listed in Table I. γ Rays from excited states in both beam- and targetlike nuclei were measured, employing the high-resolution position-sensitive γ -ray spectrometer AGATA [18] in its demonstrator configuration [19] placed 23.5 cm from the target position. The array consisted of 15 large-volume electronically segmented high-purity Ge (HPGe) detectors in five triple cryostats [20]. The solid-angle coverage of the AGATA demonstrator was about 7% of 4π . During the experiment, the count rate of each individual HPGe crystals was maintained between 20 and 30 kHz. A $40 \times 60 \text{ mm}^2$ large DANTE (Detector Array for Multinucleon Transfer Ejectiles) microchannel plate detector [19] was mounted in the reaction plane covering the angle range which corresponds to the grazing angle for the targetlike reaction product in order to request a kinematic coincidence between the different reaction products.

III. DATA ANALYSIS

Details of the PRISMA analysis are reported in Ref. [17] for the CLARA experiment and in Refs. [21,22] for the AGATA experiment. The measured quantities allow univocal identification and determination of the velocity vector for the individual lighter MNT reaction products. This enables the calculation of the element, the mass number, and the velocity vector of the binary reaction partner prior to neutron evaporation or fission has occurred. Therefore, by gating on a particular isotope of the lighter beamlike reaction products, the actinide targetlike reaction products are identified. In addition, the total kinetic energy loss (TKEL) in the system after the reaction was determined [14]. The resolution of the TKEL value is limited by the target thickness and the position uncertainty of the beam spot on the target. Most of

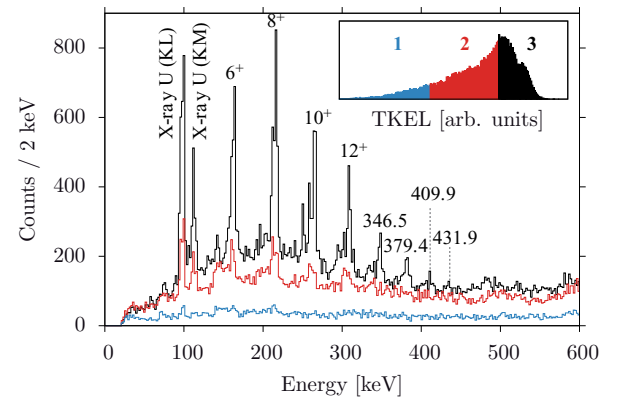


FIG. 1. (Color online) Single γ -ray spectra for ^{68}Zn identified in PRISMA. The corresponding binary partner of the reaction is ^{240}U . The spectra are Doppler corrected for the targetlike actinide nuclei. The inset shows the TKEL value in arbitrary units divided in three regions: 1, 2, and 3. The color code of the γ -ray spectra corresponds to the three different TKEL regions.

the produced actinide nuclei are excited up to an energy higher than the neutron-separation energy which enables neutron evaporation. Nonetheless, a gate on the TKEL value is helpful to constrain the excitation energy of the nuclei and to suppress fission events [21].

Results from the ^{70}Zn experiment are shown in Fig. 1. The selected nucleus after the identification with PRISMA is ^{68}Zn and the corresponding binary partner is ^{240}U . The γ -ray spectra are Doppler corrected for the targetlike actinide nuclei. The TKEL distribution is given in the inset. It is divided into three regions. The γ -ray spectrum corresponding to TKEL region 1 (blue [gray, bottom]) shows a constant structureless background caused by fission [21]. The γ -ray spectrum of region 2 (red [gray, middle]) shows high background contributions and indications of overlapping peaks. Events from fission and neutron evaporation are visible. In the γ -ray spectrum corresponding to the third TKEL cut (black [top]), distinct peaks of $^{238}\text{--}^{240}\text{U}$ can be identified. Known transitions from ^{240}U dominate and are indicated in the figure. Decays of the g.s. band up to the 12^+ state are visible, and the energies compare well with previous measurements [11]. In addition, unobserved lines of the rotational sequence can be identified.

To ensure that different γ -ray decays are part of the g.s. band, particle gated $\gamma\gamma$ coincidences are analyzed. The overall projection of the $\gamma\gamma$ matrix is shown in the top part of Fig. 2. Similar to the single spectrum (see Fig. 1) the γ rays from the transitions of the g.s. band in ^{240}U are clearly visible. In addition, candidates for the decay of the 14^+ up to the 20^+ levels are visible. By gating on the different energies up to 381 keV the expected coincidences show up; see Figs. 2(b)–2(g). In Fig. 2(h) the sum of all coincidence gates is shown. Up to an energy of 409.9 keV, intraband transitions are identified.

The second experiment employed the heavier ^{136}Xe beam with an energy of 1 GeV. The AGATA demonstrator was used for γ -ray detection and in addition to PRISMA the DANTE detector was mounted inside the scattering chamber. The trigger requested a signal from the focal plane detector of PRISMA. Data from all validated events including the

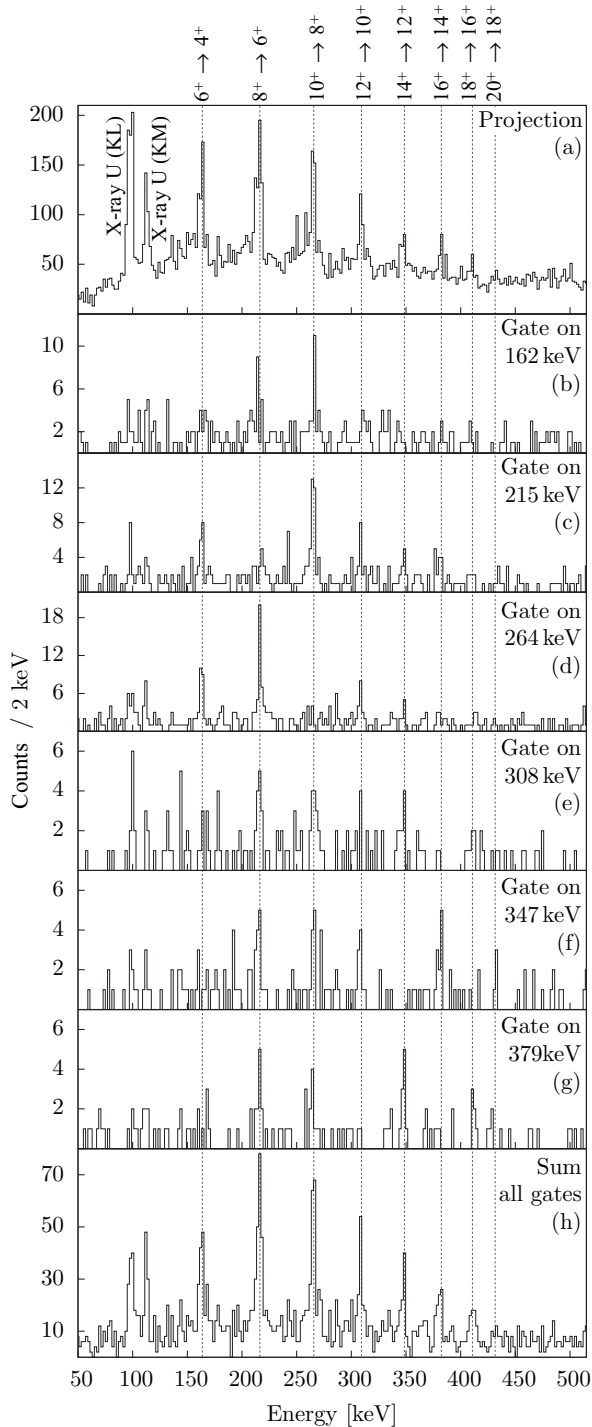


FIG. 2. Particle gated coincidence spectra for ^{240}U from the CLARA experiment. Projection on one axis of the $\gamma\gamma$ matrix (a), gate on 162 keV (b), gate on 215 keV (c), gate on 264 keV (d), gate on 307 keV (e), gate on 347 keV (f), gate on 381 keV (g), and the sum of all the shown gated spectra (h).

full information of the digitized preamplifier responses of all AGATA channels were acquired and stored. This opened the opportunity to optimize energy and timing settings by replaying the complete experiment. An improved Doppler correction, possible due to the position resolution and tracking

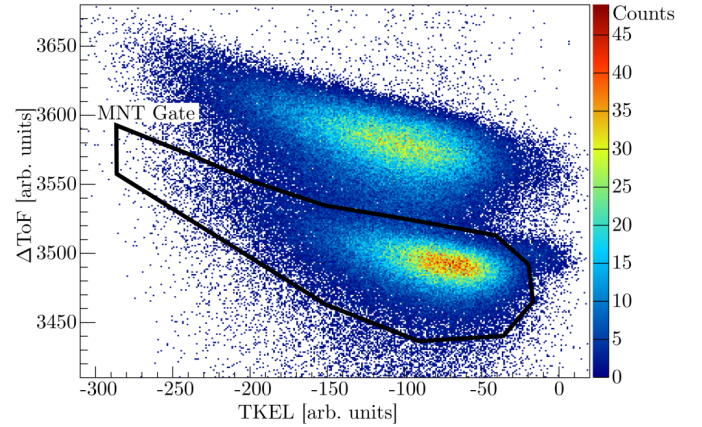


FIG. 3. (Color online) Two-dimensional (2D) histogram of ΔToF and TKEL values for all events with ^{134}Xe identified in PRISMA. The 2D gate selecting primarily MNT events is plotted as a solid black line.

capabilities of the AGATA spectrometer [23], was performed. By gating on the prompt time peak between AGATA and PRISMA, random background could be significantly suppressed. Similar to the Zn experiment, the targetlike actinide nuclei are selected by gating on the binary partner identified in PRISMA. As introduced in Ref. [21], the time-of-flight difference (ΔToF) between the two reaction products was measured at the entrance detector of PRISMA and the DANTE detector inside the scattering chamber. A 2D histogram in which ΔToF and the calculated TKEL are correlated is shown in Fig. 3 for ^{134}Xe . A gate is applied to select transfer events.

The resulting γ -ray spectra are presented in Ref. [21] (see Fig. 6 for ^{238}U and Fig. 13 for ^{240}U in Ref. [21]) in order to demonstrate the selectivity and quality of the MNT reaction; however, no results of the following detailed analysis were given. Different isotopes, namely $^{238-240}\text{U}$, contribute to the γ -ray spectrum of ^{240}U . An additional gate on the TKEL allows suppression of neutron evaporation.

The resulting spectra are shown in Fig. 4 for ^{238}U and in Fig. 5 for ^{240}U . The spectrum of ^{238}U shows γ rays from the de-excitation of states belonging to the g.s. band up to spin 22^+ . In addition, transitions from the first negative-parity band are observed up to spin 17^- , and the $(I \rightarrow I - 1)$ interband transitions are clearly visible.

In the γ -ray spectrum of ^{240}U the same transitions as in the $\gamma\gamma$ sum spectrum of Fig. 2 are seen up to the one with 431.9 keV. Additional weaker lines are visible in the spectrum which will be tentatively assigned to decays from higher spin states. Several peaks are candidates for the decay of states from the first negative-parity band, similar to the energies reported in Ref. [11]. Unfortunately, some of the observed lines are close in energy with decays of the first 2^+ and 4^+ states of the binary partner ^{134}Xe . Energies are shifted and their line width is broadened due to the Doppler correction made for ^{240}U . Two interband transitions from the 3^- state, the $I \rightarrow I \pm 1$ decays, are visible. For the decays from the 5^- , 7^- , and 9^- states only the $I \rightarrow I - 1$ transition could be identified. For none of the lines is the statistics sufficient to perform a $\gamma\gamma$ analysis and the proposed assignment is therefore tentative.

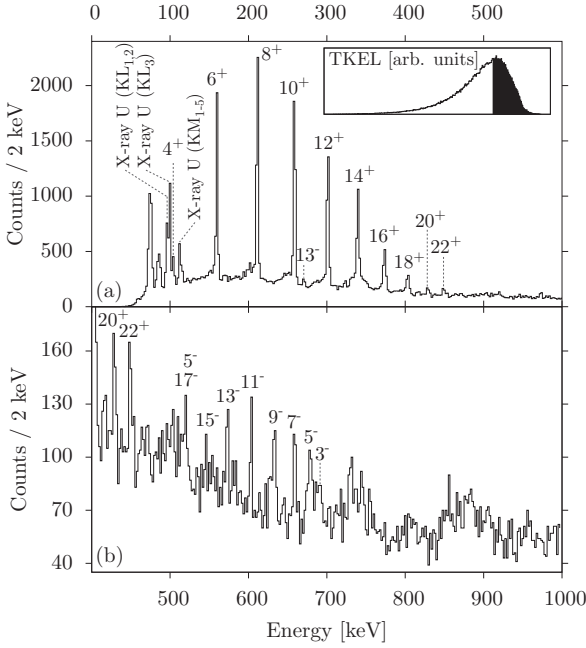


FIG. 4. Doppler-corrected single γ -ray spectrum for ^{238}U gated by ^{136}Xe identified in PRISMA. Beside the applied gate for MNT an additional cut on the TKEL value was performed (see black region in inset).

In summary, the spin assignment for the observed transitions of the ground-state rotational band up to spin 20^+ are based on the $\gamma\gamma$ coincidences relation (see Fig. 2). All transitions were clearly observed in the CLARA and AGATA

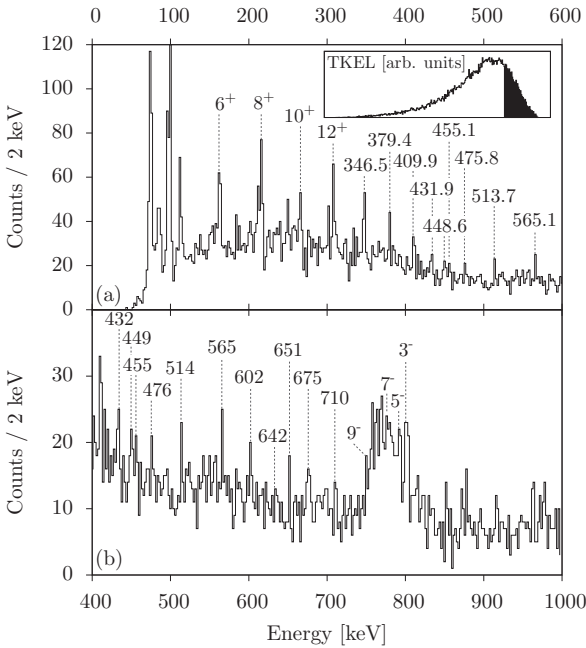


FIG. 5. Doppler-corrected single γ -ray spectrum for ^{240}U gated by ^{134}Xe identified in PRISMA. Beside the applied gate for MNT (see Fig. 3) an additional cut on the TKEL value was performed (see black region in inset).

TABLE II. γ -ray energies and spin assignments for ^{240}U . Relative intensities are determined from the $\gamma\gamma$ projection; see Fig. 2(a).

This work			Ishii <i>et al.</i> [11]	
E_γ [keV]	Rel. intensity	$I_i \rightarrow I_f$	E_γ [keV]	$I_i \rightarrow I_f$
161.9 (10)	0.630 (86)	$6^+ \rightarrow 4^+$	105.6 (1)	$4^+ \rightarrow 2^+$
215.4 (10)	1.00 (11)	$8^+ \rightarrow 6^+$	162.1 (1)	$6^+ \rightarrow 4^+$
263.9 (10)	0.84 (10)	$10^+ \rightarrow 8^+$	215.4 (1)	$8^+ \rightarrow 6^+$
307.5 (10)	0.495 (70)	$12^+ \rightarrow 10^+$	264.1 (2)	$10^+ \rightarrow 8^+$
346.5 (10)	0.289 (54)	$14^+ \rightarrow 12^+$	307.6 (3)	$12^+ \rightarrow 10^+$
379.4 (10)	0.228 (49)	$16^+ \rightarrow 14^+$		
409.9 (10)	0.138 (44)	$18^+ \rightarrow 16^+$		
431.9 (10)	0.068 (40)	$20^+ \rightarrow 18^+$		
448.6 (10)		$(22^+ \rightarrow 20^+)$		
(455.1) (10)		$(24^+ \rightarrow 22^+)$		
475.8 (10)				
513.7 (10)		$(21^- \rightarrow 20^+)$		
565.1 (10)		$(19^- \rightarrow 18^+)$		
601.6 (10)		$(17^- \rightarrow 16^+)$		
(642.0) (10)		$(15^- \rightarrow 14^+)$		
675.2 (10)		$(13^- \rightarrow 12^+)$		
697.2 (19)		$3^- \rightarrow 4^+$	696.4 (5)	$3^- \rightarrow 4^+$
710.0 (10)		$(11^- \rightarrow 10^+)$		
749.0 (20)		$9^- \rightarrow 8^+$	747.5 (3)	$9^- \rightarrow 8^+$
778.1 (32)		$7^- \rightarrow 6^+$	774.5 (3)	$7^- \rightarrow 6^+$
791.9 (35)		$5^- \rightarrow 4^+$	794.0 (3)	$5^- \rightarrow 4^+$
800.8 (20)		$3^- \rightarrow 2^+$	801.9 (5)	$3^- \rightarrow 2^+$

experiments. The two transitions at 449 and 455 keV most probably originate from the decay of the 22^+ and 24^+ states of the g.s. band. Level energies for the 3^- , 5^- , 7^- , and 9^- states are taken from Ref. [11] due to experimental difficulties explained above. All the measured γ -ray energies and the assignments are listed in Table II; included are also results reported in Ref. [11]. The corresponding level scheme is presented in Fig. 6.

IV. INTERPRETATION

In Fig. 7, a comparison between the energies of the g.s. band levels obtained in this experiment, the data obtained by Ishii *et al.* [11] and theoretical predictions are shown. The experimental data agree well with the level scheme calculated within the cluster model [3]. For the macroscopic-microscopic model two results are given [2]. The dynamical coupling of rotation and pairing mode agrees well with the experimental data. The level energies predicted by the $I(I+1)$ rule are increasingly too high as a function of spin underlining the necessary coupling as reported in Ref. [2].

A refined comparison between the experimental results and predictions from theory is based on the kinetic moment of inertia J_{kin} (MoI), which is deduced from the transition energies E_γ of the ground-state rotational band [24–26]:

$$J_{\text{kin}} = \frac{I}{\omega} = \frac{\hbar^2 (2I - 1)}{E_\gamma (I \rightarrow I - 2)}. \quad (1)$$

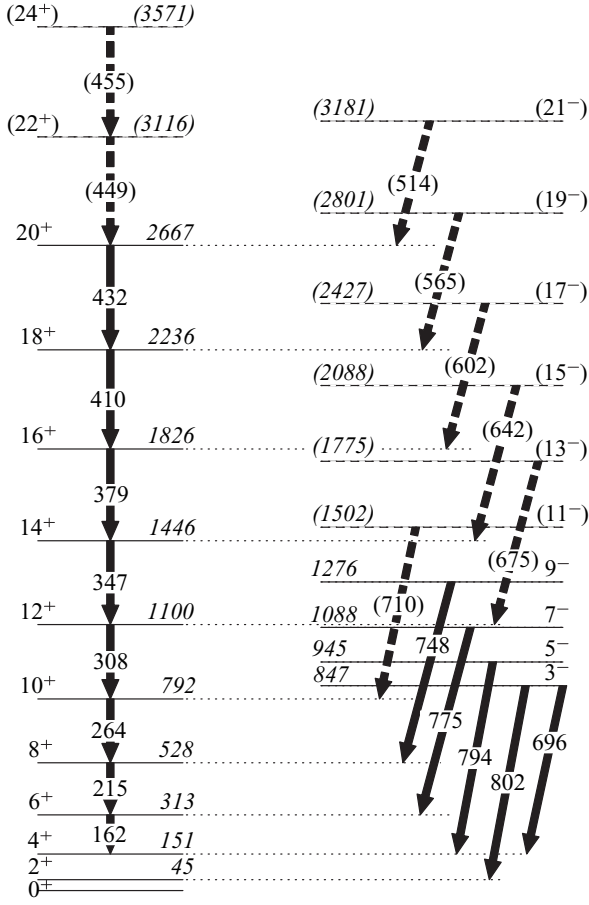


FIG. 6. Proposed extended level scheme for ^{240}U . Spin and parity assignments are taken from Ref. [11] or based on $\gamma\gamma$ -coincidence relationships. Tentative assignments are given in brackets.

The rotational frequencies are calculated using the expression

$$\hbar\omega_{\text{kin}} = \frac{E_{\gamma}}{\sqrt{I(I+1)} - \sqrt{(I-2)(I-1)}}. \quad (2)$$

The deviations in energy differences between the consecutive rotational transition energies are used as the basis to define a dynamic MoI J_{dyn} :

$$J_{\text{dyn}} = \frac{dI}{d\omega} \approx \frac{\hbar^2 \Delta I}{\Delta E_{\gamma}} = \frac{4\hbar^2}{E_{\gamma 1} - E_{\gamma 2}} \quad (3)$$

with $E_{\gamma 1} = E(I \rightarrow I-2)$ and $E_{\gamma 2} = E(I-2 \rightarrow I-4)$. The corresponding dynamic rotational frequencies are defined as

$$\hbar\omega_{\text{dyn}} = \frac{E_{\gamma 1} + E_{\gamma 2}}{4}. \quad (4)$$

With the following parametrization by Harris [27], the kinetic and dynamic MoI are found:

$$\begin{aligned} J_{\text{kin}} &= \mathcal{J}_1 + \mathcal{J}_2 \omega^2, \\ J_{\text{dyn}} &= \mathcal{J}_1 + 3 \mathcal{J}_2 \omega^2. \end{aligned} \quad (5)$$

The transitions below the 4^+ state are not visible in the γ -ray spectra due to decay by internal electron conversion. For the two lowest unobserved transitions, the energies and

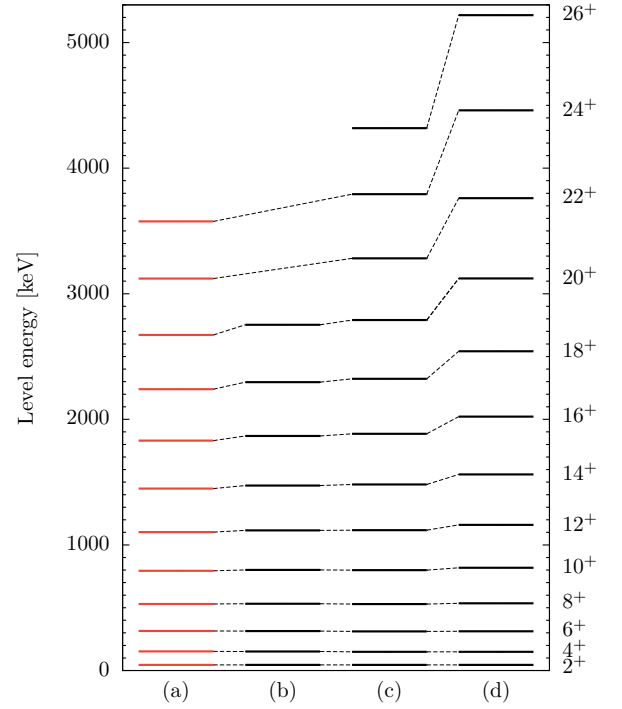


FIG. 7. (Color online) Comparison of experimentally determined level energies with theoretical predictions. (a) Data from this work. (b) Theoretical prediction from cluster model [3], and from a macroscopic-microscopic approach [2] with (c) dynamical coupling or (d) $I(I+1)$ sum rule.

spin-parity assignments from Ishii *et al.* [11] [$E_{\gamma}(4^+ \rightarrow 2^+) = 105.6 \text{ keV}$] and previous α -decay [28] and $^{238}\text{U}(t, p)$ [29] measurements [$E_{\gamma}(2^+ \rightarrow 0^+) = 45(1) \text{ keV}$] are taken.

The spins for the ground-state rotational band are linked to the rotational frequency and the Harris fit parameters [30]:

$$I = \mathcal{J}_1 \omega + \mathcal{J}_2 \omega^3 + \frac{1}{2}. \quad (6)$$

In this way the transition energies of the $2^+ \rightarrow 0^+$ and $4^+ \rightarrow 2^+$ states are determined to be 45.5(3) and 104.9(6) keV, respectively. These values agree well with the given literature values.

The Harris parametrization provides a good indicator for a comparison of the experimental MoI with the regular $I(I+1)$ behavior. Both MoI values, J_{kin} and J_{dyn} [see Eq. (5)], are fitted to the experimental data up to the 12^+ g.s. band state. The determined parameters are $\mathcal{J}_1 = (65.8 \pm 0.4) \hbar^2 \text{ MeV}^{-1}$ and $\mathcal{J}_2 = (369 \pm 27) \hbar^4 \text{ MeV}^{-3}$ for ^{240}U . The ground-state value of the MoI compares well with the value of $66.9 \hbar^2 \text{ MeV}^{-1}$ calculated by Sobczewski *et al.* [1].

The fits and the experimental data points are shown in Fig. 8. The evolution of the moments of inertia as a function of rotational frequency ω are also shown for the lighter even-even isotopes $^{236,238}\text{U}$ (experimental values for $^{236,238}\text{U}$ are taken from Ref. [31]). The \mathcal{J}_1 values are similar for all three isotopes; only the \mathcal{J}_2 value of ^{240}U is smaller than for $^{236,238}\text{U}$. For the higher transitions beyond the 12^+ state an increasing deviation to the fit, an upbend, is observed. The smooth upbend [32] in ^{240}U beyond the 18^+ g.s. band state is more pronounced

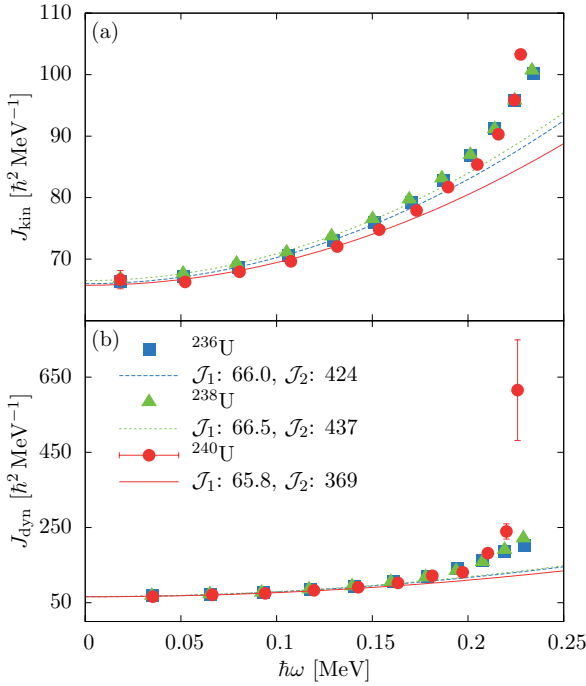


FIG. 8. (Color online) Fits employing the Harris parametrization of J_{kin} and J_{dyn} for the U isotopic chain from ^{236}U to ^{240}U . Data for $A = 236$ and 238 are taken from Ref. [31].

than in the corresponding neutron-deficient isotopes along the U isotopic chain. A similar behavior was also observed in neutron-rich Pu, Cm, and Cf isotopes [8,33].

The experimental kinetic MoI of ^{240}U is compared to kinetic MoIs from various theoretical calculations (red [gray] data points versus black lines in Fig. 9). For the model by Delaroche *et al.* [4] the absolute numbers of the kinetic MoI are consistently higher than the experimentally determined MoI. The slope of the upbend of the kinetic MoI around a rotational frequency of $0.2 \text{ MeV } \hbar^{-1}$ is in reasonable agreement with the experimental data. The macroscopic-microscopic model by Nerlo-Pomorska *et al.* [2] underestimates the beginning of the experimental upbend. The cluster model by Shneidman *et al.* [3] does not include predictions for the behavior at higher rotational frequencies. The behavior of the MoI is best reproduced by the relativistic CRHB approach by Afanasjev *et al.* [7,8]. Up to $18 \hbar$ the LN(NL3*) parametrization is in very good agreement with the data points, while at even higher spins the LN(NL1) parametrization provides the best agreement.

Both CRHB + LN(NL1) and CRHB + LN(NL3*) calculations suggest a sharp increase of the kinetic MoI above $\hbar\omega \approx 0.2 \text{ MeV}$. Indeed a change of slope is observed at this energy. This upbend is predominantly due to the alignment of $i_{13/2}$ protons and $j_{15/2}$ neutrons which take place at similar rotational frequencies [7].

Besides the extension of the g.s. band, the AGATA experiment also yielded results on the first negative-parity (octupole) band. The first states of the alternative-parity band of ^{240}U were reported in Ref. [11] at higher energies than in $^{236,238}\text{U}$.

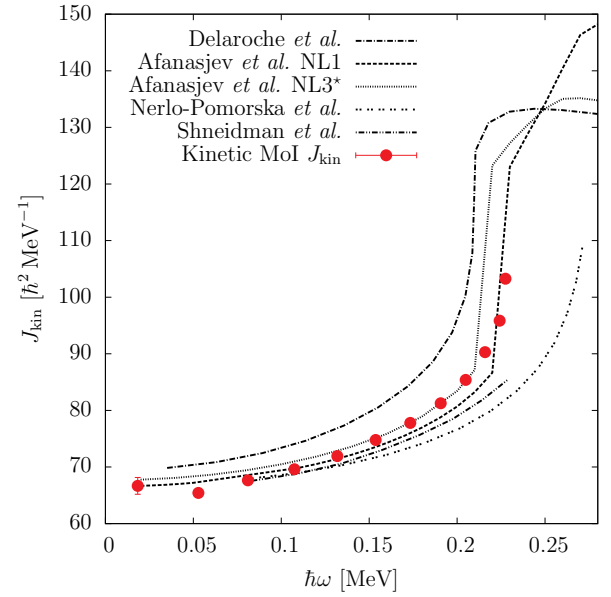


FIG. 9. (Color online) Kinetic MoI, J_{kin} , from this work (red [gray] points) in comparison to various theoretical predictions. The CRHB + LN(NL1) and CRHB + LN(NL3*) calculations by Afanasjev *et al.* best reproduce the experimental data. The experimental values for the decays of the 4^+ and 2^+ g.s. band states were taken from the literature [11,28,29].

To disentangle the octupole correlations or deformation from octupole vibration, properties of the negative-parity band were scrutinized. In the case of strong octupole correlations an alternating parity band occurs. Here, the odd-spin negative-parity states lie much lower in excitation energy and form an alternating parity band together with the adjacent positive-parity even-spin states. A characteristic feature of vibrational octupole motion is that the negative-parity states appear at higher excitation energies and are well separated from the positive-parity states [34]. In the top panel of Fig. 10, the energy staggering (or parity splitting) $S(I)$ between the odd-spin, negative-parity and even-spin, positive-parity bands of $^{236,238,240}\text{U}$ is presented.

$$S(I) = E(I) - \frac{E(I-1)(I+1) + E(I+1)I}{2I+1}. \quad (7)$$

$S(I)$ displays to which extent the odd spin I of the negative-parity band has an excitation energy located in between those of the two neighboring even-spin states with spins $I-1$ and $I+1$, therefore parameterizing to which extend the two bands of opposite parity can be regarded as a single, rotational octupole excitation [33,35]. The staggering observed in the three uranium isotopes is largest for ^{240}U at low spins as expected for a vibrational band. With increasing spin the $S(I)$ value comes down to values between ^{236}U and ^{238}U . A similar behavior is found at the even-even $^{242,244}\text{Pu}$ isotopes [33].

Another indicator is given by the ratio between the rotational frequencies of the positive- and the negative-parity bands:

$$\frac{\omega^-(I)}{\omega^+(I)} = 2 \frac{E^-(I+1) - E^-(I-1)}{E^+(I+2) - E^+(I-2)}. \quad (8)$$

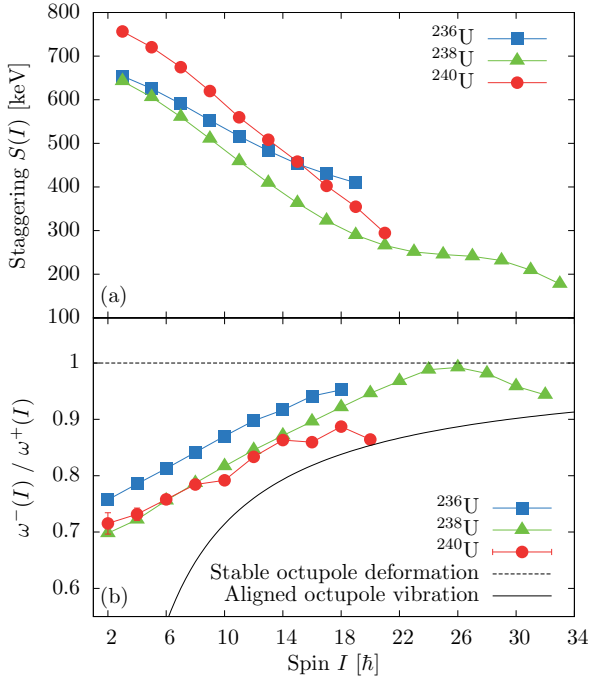


FIG. 10. (Color online) (a) Staggering $S(I)$ in the three uranium isotopes ^{236}U , ^{238}U , and ^{240}U . The staggering parameter for ^{240}U continues to decrease up to the highest spins while $S(I)$ saturates in the lighter U isotopes. (b) Ratio of rotational frequencies of the positive- and negative-parity bands as a function of spin. $^{236,238}\text{U}$ data taken from Ref. [31].

Values are presented in the bottom panel of Fig. 10. The ratio approaches 1 for a stable octupole deformation and is $(2I - 5)/(2I + 1)$ in the limit of an aligned octupole vibration [35].

Another approach to evaluate the behavior of the negative-parity band was introduced by Jolos and von Brentano [34]. The model suggests a formula for the angular momentum dependence of the parity splitting in alternating parity bands from a solution of the one-dimensional Schrödinger equation with a double-minimum potential. The normalized parity splitting is defined as $\Delta\epsilon(I) \equiv \Delta E(I)/\Delta E(2)$ with $\Delta E(I)$ being the parity splitting averaged over three neighboring values of I :

$$\Delta\epsilon(I) = \exp \left[-\frac{I(I+1)}{\mathcal{J}_0(\mathcal{J}_0+1)[1+aI(I+1)]} + \frac{6}{\mathcal{J}_0(\mathcal{J}_0+1)(1+6a)} \right]. \quad (9)$$

The deduced values of $-\ln[\Delta\epsilon(I)]$ for $^{236-240}\text{U}$ with two fits for $a = 0$ (dashed lines) and a as a free parameter (solid line) are plotted in Fig. 11. The general behavior for all three isotopes is comparable: Starting with a linear increase at low spins, for higher spin values a positive parameter a describes the data. This behavior is unambiguously assigned to octupole vibrational nuclei in Ref. [34]. Moreover, the good agreement of the fit and the data supports the validity of the experimental findings.

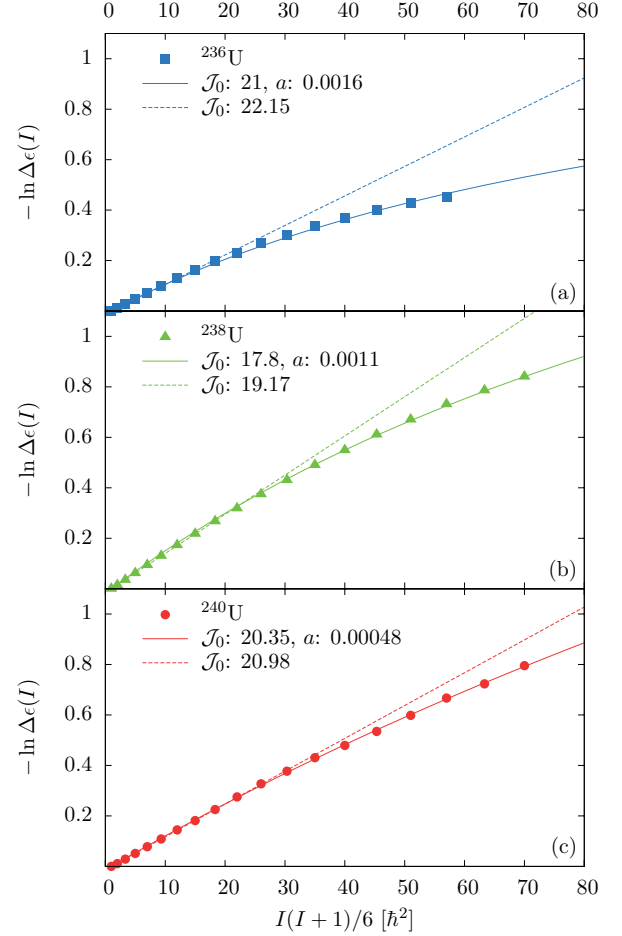


FIG. 11. (Color online) Experimental data, parametrized as $-\ln \Delta\epsilon(I)$ vs $I(I+1)/6$ for ^{236}U (a), ^{238}U (b), and ^{240}U (c). Fits with $a = 0$ are shown as dashed lines; solid curves include a as a free parameter. $^{236,238}\text{U}$ data taken from Ref. [31].

V. SUMMARY AND CONCLUSIONS

In summary, we have measured γ rays in ^{240}U following multinucleon transfer induced by $^{70}\text{Zn} + ^{238}\text{U}$ and $^{136}\text{Xe} + ^{238}\text{U}$ reactions. The magnetic spectrometer PRISMA was employed, in the first experiment coupled to the γ -ray detector CLARA and in the second one coupled to the γ -ray tracking detector AGATA together with the particle detector DANTE. Neutron-rich ^{240}U was selected by gating on the binary partner ^{134}Xe identified by PRISMA. Neutron-evaporation channels were suppressed by restrictions on the TKEL value. Conditions on particle-particle coincidences were employed to suppress the fission-induced background. The information on the beamlike reaction products from PRISMA was combined with a Doppler correction for the targetlike nuclei to study the structure of ^{240}U . Especially for the second experiment, the advanced opportunities of the novel γ -ray tracking technique yielded improved Doppler-corrected γ -ray spectra.

The heavy-ion-induced reactions involved higher angular momentum, allowing an extension of the g.s. band of ^{240}U up to the 20^+ state, and tentative assignments up to the (24^+) state were made. The kinetic and dynamic moments of inertia were

extracted and compared to theoretical predictions. The low-energy, low-spin part is well described by both cluster models and macroscopic-microscopic approaches. The population of high-spin states allowed for the first time the observation of an upbend at rotational frequencies around $0.2 \text{ MeV } \hbar^{-1}$. This behavior is best reproduced by recent relativistic mean-field calculations within the CDFT framework [7,8].

Despite experimental difficulties, there is convincing evidence for the $K^\pi = 0^-$ negative-parity band which was extended up to a tentatively assigned (21^-) state. Three different parametrizations such as energy staggering and parity splitting between the g.s. band and the negative-parity band yield consistent results. The experimental findings suggest that the newly observed band is interpreted best as a collective octupole vibrational excitation. This interpretation is supported by the similarities with the neighboring $^{236-240}\text{U}$ isotopes.

Our new experimental results are a further step in the understanding of more neutron-rich uranium isotopes and actinide nuclei in general. However, further experimental evidence is highly desirable and improved experiments with

higher statistics are needed to corroborate the results. For this endeavour high-efficiency detection devices are mandatory to overcome the reported low cross sections in the microbarn region for these type of reactions [21].

ACKNOWLEDGMENTS

The research leading to these results has received funding from the German Bundesministerium für Bildung und Forschung (BMBF) under Contract No. 05P12PKFNE TP4, the European Union Seventh Framework Programme (FP7/2007-2013) under Grant No. 262010-ENSAR, and the Spanish Ministerio de Ciencia e Innovación under Contract No. FPA2011-29854-C04. A.V. thanks the Bonn-Cologne Graduate School of Physics and Astronomy (BCGS) for financial support. One of the authors (A. Gadea) was supported by MINECO, Spain, under Grants No. FPA2011-29854-C04 759 and No. FPA2014-57196-C5; Generalitat Valenciana, Spain, under Grant No. PROMETEOII/2014/019; and EU under the FEDER program.

-
- [1] A. Sobiczewski, I. Muntian, and Z. Patyk, *Phys. Rev. C* **63**, 034306 (2001).
 - [2] B. Nerlo-Pomorska, K. Pomorski, and J. Bartel, *Phys. Rev. C* **84**, 044310 (2011).
 - [3] T. M. Shneidman, G. G. Adamian, N. V. Antonenko, and R. V. Jolos, *Phys. Rev. C* **74**, 034316 (2006).
 - [4] J.-P. Delaroche, M. Girod, H. Goutte, and J. Libert, *Nucl. Phys. A* **771**, 103 (2006).
 - [5] D. Vretenar, T. Niksic, and P. Ring, *Int. J. Mod. Phys. E* **19**, 548 (2010).
 - [6] L. M. Robledo and R. R. Rodríguez-Guzmán, *J. Phys. G: Nucl. Part. Phys.* **39**, 105103 (2012).
 - [7] A. V. Afanasjev and O. Abdurazakov, *Phys. Rev. C* **88**, 014320 (2013).
 - [8] A. V. Afanasjev, *Phys. Scr.* **89**, 054001 (2014).
 - [9] L. Corradi, G. Pollaro, and S. Szilner, *J. Phys. G: Nucl. Part. Phys.* **36**, 113101 (2009).
 - [10] J. F. C. Cocks *et al.*, *J. Phys. G: Nucl. Part. Phys.* **26**, 23 (2000).
 - [11] T. Ishii, S. Shigematsu, M. Asai, A. Makishima, M. Matsuda, J. Kaneko, I. Hossain, S. Ichikawa, T. Kohn, and M. Ogawa, *Phys. Rev. C* **72**, 021301 (2005).
 - [12] T. Ishii *et al.*, *Phys. Rev. C* **76**, 011303 (2007).
 - [13] A. Stefanini *et al.*, *Nucl. Phys. A* **701**, 217 (2002).
 - [14] S. Szilner *et al.*, *Phys. Rev. C* **76**, 024604 (2007).
 - [15] L. Corradi *et al.*, *Nucl. Instrum. Methods Phys. Res., Sect. B* **317**, 743 (2013).
 - [16] A. Gadea *et al.*, *J. Phys. G: Nucl. Part. Phys.* **31**, S1443 (2005).
 - [17] K. Geibel, Ph.D. thesis, Universität zu Köln, 2012.
 - [18] S. Akkoyun *et al.*, *Nucl. Instrum. Methods Phys. Res., Sect. A* **668**, 26 (2012).
 - [19] A. Gadea *et al.*, *Nucl. Instrum. Methods Phys. Res., Sect. A* **654**, 88 (2011).
 - [20] A. Wiens, H. Hess, B. Birkenbach, B. Bruyneel, J. Eberth, D. Lersch, G. Pascovici, P. Reiter, and H.-G. Thomas, *Nucl. Instrum. Methods Phys. Res., Sect. A* **618**, 223 (2010).
 - [21] A. Vogt *et al.*, *Phys. Rev. C* **92**, 024619 (2015).
 - [22] B. Birkenbach, Ph.D. thesis, Universität zu Köln, 2014.
 - [23] A. Lopez-Martens, K. Hauschild, A. Korichi, J. Roccas, and J.-P. Thibaud, *Nucl. Instrum. Methods Phys. Res., Sect. A* **533**, 454 (2004).
 - [24] J. E. Draper, F. S. Stephens, M. A. Deleplanque, W. Korten, R. M. Diamond, W. H. Kelly, F. Azaiez, A. O. Macchiavelli, C. W. Beausang, E. C. Rubel, J. A. Becker, N. Roy, E. A. Henry, M. J. Brinkman, A. Kuhnert, and S. W. Yates, *Phys. Rev. C* **42**, R1791 (1990).
 - [25] J. A. Becker, E. A. Henry, A. Kuhnert, T. F. Wang, S. W. Yates, R. M. Diamond, F. S. Stephens, J. E. Draper, W. Korten, M. A. Deleplanque, A. O. Macchiavelli, F. Azaiez, W. H. Kelly, J. A. Cizewski, and M. J. Brinkman, *Phys. Rev. C* **46**, 889 (1992).
 - [26] G. Hackman, T. L. Khoo, M. P. Carpenter, T. Lauritsen, A. Lopez-Martens, I. J. Calderin, R. V. F. Janssens, D. Ackermann, I. Ahmad, S. Agarwala, D. J. Blumenthal, S. M. Fischer, D. Nisius, P. Reiter, J. Young, H. Amro, E. F. Moore, F. Hannachi, A. Korichi, I. Y. Lee, A. O. Macchiavelli, T. Døssing, and T. Nakatsukasa, *Phys. Rev. Lett.* **79**, 4100 (1997).
 - [27] S. M. Harris, *Phys. Rev.* **138**, B509 (1965).
 - [28] B. Back, E. Flynn, O. Hansen, R. Casten, and J. Garrett, *Nucl. Phys. A* **217**, 116 (1973).
 - [29] C. E. Bemis Jr., J. Halperin, and R. Eby, *J. Inorg. Nucl. Chem.* **31**, 599 (1969).
 - [30] P. Reiter *et al.*, *Phys. Rev. Lett.* **82**, 509 (1999).
 - [31] Evaluated Nuclear Structure Data File (ENSDF) [<http://www.nndc.bnl.gov/ensdf/>].
 - [32] W. Spreng, F. Azgui, H. Emling, E. Grosse, R. Kulesa, C. Michel, D. Schwalm, R. S. Simon, H. J. Wollersheim, M. Mütterer, J. P. Theobald, M. S. Moore, N. Trautmann, J. L. Egido, and P. Ring, *Phys. Rev. Lett.* **51**, 1522 (1983).
 - [33] I. Wiedenhöver *et al.*, *Phys. Rev. Lett.* **83**, 2143 (1999).
 - [34] R. V. Jolos and P. von Brentano, *Phys. Rev. C* **49**, R2301 (1994).
 - [35] W. Nazarewicz and P. Olanders, *Nucl. Phys. A* **441**, 420 (1985).

Publication III:
High-spin structure of ^{134}Xe

High-spin structure of ^{134}Xe

A. Vogt,^{1,*} B. Birkenbach,¹ P. Reiter,¹ A. Blazhev,¹ M. Siciliano,^{2,3} J. J. Valiente-Dobón,³ C. Wheldon,⁴ D. Bazzacco,⁵ M. Bowry,⁶ A. Bracco,⁷ B. Bruyneel,⁸ R. S. Chakrawarthy,⁹ R. Chapman,¹⁰ D. Cline,¹¹ L. Corradi,³ F. C. L. Crespi,⁷ M. Cromaz,¹² G. de Angelis,³ J. Eberth,¹ P. Fallon,¹² E. Farnea,^{5,†} E. Fioretto,³ S. J. Freeman,⁹ A. Gadea,¹³ K. Geibel,¹ W. Gelletly,⁶ A. Gengelbach,¹⁴ A. Giaz,⁷ A. Görgen,^{15,16,12} A. Gottardo,³ A. B. Hayes,¹¹ H. Hess,¹ H. Hua,¹¹ P. R. John,^{2,5} J. Jolie,¹ A. Jungclaus,¹⁷ W. Korten,¹⁶ I. Y. Lee,¹² S. Leoni,⁷ X. Liang,¹⁸ S. Lunardi,^{2,5} A. O. Macchiavelli,¹² R. Menegazzo,⁵ D. Mengoni,^{18,2,5} C. Michelagnoli,^{2,5,‡} T. Mijatović,¹⁹ G. Montagnoli,^{2,5} D. Montanari,^{2,5,§} D. Napoli,³ C. J. Pearson,^{6,||} L. Pellegri,⁷ Zs. Podolyák,⁶ G. Pollaro,²⁰ A. Pullia,⁷ F. Radeck,¹ F. Recchia,^{2,5} P. H. Regan,^{6,21} E. Şahin,^{3,¶} F. Scarlassara,^{2,5} G. Sletten,²² J. F. Smith,¹⁸ P.-A. Söderström,^{14,#} A. M. Stefanini,³ T. Steinbach,¹ O. Stezowski,²³ S. Szilner,¹⁹ B. Szpak,²⁴ R. Teng,¹¹ C. Ur,⁵ V. Vandone,⁷ D. Ward,¹² D. D. Warner,^{25,†} A. Wiens,¹ and C. Y. Wu^{11,**}

¹*Institut für Kernphysik, Universität zu Köln, D-50937 Köln, Germany*

²*Dipartimento di Fisica e Astronomia, Università di Padova, I-35131 Padova, Italy*

³*Istituto Nazionale di Fisica Nucleare, Laboratori Nazionali di Legnaro, I-35020 Legnaro, Italy*

⁴*School of Physics and Astronomy, University of Birmingham, Birmingham B15 2TT, United Kingdom*

⁵*Istituto Nazionale di Fisica Nucleare, Sezione di Padova, I-35131 Padova, Italy*

⁶*Department of Physics, University of Surrey, Guildford, Surrey GU2 7XH, United Kingdom*

⁷*Dipartimento di Fisica, Università di Milano and INFN Sezione di Milano, I-20133 Milano, Italy*

⁸*CEA Saclay, Service de Physique Nucleaire, F-91191 Gif-sur-Yvette, France*

⁹*Department of Physics and Astronomy, Schuster Laboratory, University of Manchester, Manchester M13 9PL, United Kingdom*

¹⁰*SUPA, School of Engineering and Computing, University of the West of Scotland, Paisley PA1 2BE, United Kingdom*

¹¹*Department of Physics, University of Rochester, Rochester, New York 14627, USA*

¹²*Lawrence Berkeley National Laboratory, Berkeley, California 94720, USA*

¹³*Instituto de Física Corpuscular, CSIC-Universidad de Valencia, E-46071 Valencia, Spain*

¹⁴*Department of Physics and Astronomy, Uppsala University, SE-75121 Uppsala, Sweden*

¹⁵*Department of Physics, University of Oslo, Post Office Box 1048 Blindern, N-0316 Oslo, Norway*

¹⁶*Institut de Recherche sur les lois Fondamentales de l'Univers (IRFU), CEA/DSM, Centre CEA de Saclay, F-91191 Gif-sur-Yvette Cedex, France*

¹⁷*Instituto de Estructura de la Materia, CSIC, Madrid, E-28006 Madrid, Spain*

¹⁸*Nuclear Physics Research Group, University of the West of Scotland, High Street, Paisley PA1 2BE, Scotland, United Kingdom*

¹⁹*Ruđer Bošković Institute, HR-10 002 Zagreb, Croatia*

²⁰*Dipartimento di Fisica Teorica dell'Università di Torino and INFN, I-10125 Torino, Italy*

²¹*Radioactivity Group, National Physical Laboratory, Teddington, Middlesex, TW11 0LW, United Kingdom*

²²*Niels Bohr Institute, University of Copenhagen, Blegdamsvej 17, 2100 Copenhagen, Denmark*

²³*Université de Lyon, Université Lyon-1, CNRS/IN2P3, UMR5822, IPNL, F-69622 Villeurbanne Cedex, France*

²⁴*Henryk Niewodniczański Institute of Nuclear Physics PAN, PL-31342 Kraków, Poland*

²⁵*CCLRC Daresbury Laboratory, Warrington WA4 4AD, United Kingdom*

(Received 2 March 2016; published 25 May 2016)

Detailed spectroscopic information on the $N \sim 82$ nuclei is necessary to benchmark shell-model calculations in the region. The nuclear structure above long-lived isomers in ^{134}Xe is investigated after multinucleon transfer (MNT) and actinide fission. Xenon-134 was populated as (i) a transfer product in $^{136}\text{Xe} + ^{238}\text{U}$ and $^{136}\text{Xe} + ^{208}\text{Pb}$ MNT reactions and (ii) as a fission product in the $^{136}\text{Xe} + ^{238}\text{U}$ reaction employing the high-resolution Advanced Gamma Tracking Array (AGATA). Trajectory reconstruction has been applied for the complete identification of beamlike transfer products with the magnetic spectrometer PRISMA. The $^{136}\text{Xe} + ^{198}\text{Pt}$ MNT reaction was studied with the γ -ray spectrometer GAMMASPHERE in combination with the gas detector array Compact Heavy Ion Counter (CHICO). Several high-spin states in ^{134}Xe on top of the two long-lived isomers are discovered based on $\gamma\gamma$ -coincidence relationships and information on the γ -ray angular distributions as well as excitation energies from the total kinetic energy loss and fission fragments. The revised level scheme of ^{134}Xe is extended up to an

*Corresponding author: andreas.vogt@ikp.uni-koeln.de

†Deceased.

‡Present address: GANIL, CEA/DSM-CNRS/IN2P3, F-14076, Caen, France.

§Present address: USIAS - Université de Strasbourg, IPHC-CNRS, F-67037 Strasbourg Cedex 2, France.

||Present address: TRIUMF, 4004 Wesbrook Mall, Vancouver, British Columbia V6T 2A3, Canada.

¶Present address: Department of Physics, University of Oslo, P. O. Box 1048 Blindern, N-0316 Oslo, Norway.

#Present address: RIKEN Nishina Center, Wako, 351-0198 Saitama, Japan.

**Present address: Lawrence Livermore National Laboratory, Livermore, California 94551, USA.

excitation energy of 5.832 MeV with tentative spin-parity assignments up to 16^+ . Previous assignments of states above the 7^- isomer are revised. Latest shell-model calculations employing two different effective interactions reproduce the experimental findings and support the new spin and parity assignments.

DOI: 10.1103/PhysRevC.93.054325

I. INTRODUCTION

The nuclear structure of high-spin states in the vicinity of the $N = 82$ magic number is of high interest to benchmark nuclear shell-model calculations. Isomeric yrast $I^\pi = 10^+$ states of $\nu h_{11/2}^{-2}$ character have been reported in all the even-mass $N = 80$ isotones ranging from ^{130}Sn to ^{142}Sm [1–8]. Comprehensive shell-model (SM) calculations and detailed predictions for these nuclei are the subject of several recent studies, which are either based on the jj coupled scheme or on the uncoupled m scheme. The jj scheme is adopted by the codes NATHAN [9,10] and NUSHELLX [11]. It has the advantage of yielding shell-model Hamiltonian matrices of relatively small dimensions. On the other hand, these matrices are very dense and have complex algebraic structures. The Xe isotopes with four valence protons and increasing deformation have come within reach of these types of advanced shell-model calculations. With respect to the Sn isotopes, the number of neutron holes is increased and the deformation is driven by the proton-neutron force, which acts efficiently in Xe isotopes. Therefore, the Xe isotopes provide an intriguing and important test case for new shell-model developments. In summary, the following theoretical studies were performed employing pair-truncated shell-model calculations [12], large scale shell-model calculations [13], and shell-model frameworks with the monopole and quadrupole pairing plus quadrupole-quadrupole interaction employed as an effective interaction [14].

This work focuses on the $N = 80$ isotope $^{134}_{54}\text{Xe}$, located in the proton midshell between the $Z = 50$ shell closure and the $Z = 64$ subshell one. The data on low-spin states in ^{134}Xe originate from earlier work employing β decay [15–18] and Coulomb excitation [19,20]. The most recent study was performed by Ahn *et al.* [21]. The authors obtained absolute $E2$ and $M1$ transition strengths in ^{134}Xe in an inverse kinematics $^{12}\text{C}(^{134}\text{Xe}, ^{134}\text{Xe}') \text{ Coulomb excitation experiment}$ employing the GAMMASPHERE array at the superconducting Argonne Tandem Linac Accelerator System (ATLAS) accelerator. The 1100-keV transition was validated to connect the mixed-symmetry 2_3^+ state with the first excited 2_1^+ state.

Excited states above the yrast $I^\pi = 10^+$ isomeric state were identified only recently. The first relevant results were obtained by Fotiades *et al.* [22], measuring a variety of fusion-fission fragments from the ^{226}Th compound nucleus via triple- γ coincidences using the GAMMASPHERE array at the Lawrence Berkeley National Laboratory (LBNL) in 2007. A cascade based on a 1323-keV γ -ray transition was attributed to ^{135}Xe by means of $\gamma\gamma$ coincidences. However, the same sequence of γ rays with energies of 218, 320, and 1323 keV was found in an experiment by Shrivastava *et al.* [23] in 2009. The reaction products of the fusion-fission reaction $^{12}\text{C}(^{238}\text{U}, ^{134}\text{Xe})\text{Ru}$ were unambiguously identified with the magnetic mass spectrometer VArIable MOde high acceptance Spec-

trometer (VAMOS). γ -ray decays of excited states in ^{134}Xe were measured with two EXOGAM Compton-suppressed segmented clover detectors at the Grand Accélérateur National d'Ions Lourds. The γ rays with energies of 218, 320, and 1323 keV and additional lines at 612 and 1100 keV were observed in coincidence with ^{134}Xe , correcting the assignment by Fotiades *et al.* Shrivastava *et al.* argue that all observed lines feed the long-lived 10^+ [$T_{1/2} = 5(1)\mu\text{s}$] [2] and 7^- [$T_{1/2} = 290(17)\text{ms}$] isomers [24]. The authors claim that the transitions below those isomeric states are not observed, although a clear indication for the 847-keV $2_1^+ \rightarrow 0^+$ transition below the isomeric states is visible in the corresponding γ -ray spectrum. The observed γ -ray transitions were ordered into cascades above the aforementioned isomers. Due to low statistics, no $\gamma\gamma$ coincidences were analyzed [23]. The placement of the excited states and spin/parity assignments were guided and suggested by the results of a large-scale shell model (LSSM) calculation.

These findings, together with recent theoretical advances, motivated a refined investigation of the nuclear structure in ^{134}Xe , especially regarding high-spin states above the two long-lived isomers. In this article, we report and discuss new results for the nucleus ^{134}Xe obtained in three different experiments, which are based on direct identification of ^{134}Xe and coincident prompt γ -ray spectroscopy. The combination of the high-resolution position-sensitive Advanced Gamma Tracking Array (AGATA) [25] and the PRISMA magnetic mass spectrometer [26–28] was employed to study ^{134}Xe after $^{136}\text{Xe} + ^{208}\text{Pb}$ multinucleon transfer (MNT) and $^{136}\text{Xe} + ^{238}\text{U}$ MNT and fission reactions, respectively. Further, ^{134}Xe was measured after a $^{136}\text{Xe} + ^{198}\text{Pt}$ MNT reaction using the GAMMASPHERE+CHICO setup [29,30] at LBNL.

This paper is organized as follows: the experimental setup, data analysis, and the results of the three experiments are described in Sec. II. A detailed comparison with two modern shell-model calculations is presented in Sec. III, before the paper closes with a summary and conclusions.

II. EXPERIMENTAL PROCEDURE AND RESULTS

A. $^{136}\text{Xe} + ^{238}\text{U}$

In this experiment, the PIAVE+ALPI accelerator complex provided a ^{136}Xe beam with an energy of 1 GeV and a beam current of 2 pA, impinging onto ^{238}U targets. The ^{238}U targets had thicknesses of 1 and 2 mg/cm², respectively, with a 0.8-mg/cm² Nb backing facing the beam. Projectile-like reaction fragments in the Xe region were identified with the magnetic mass spectrometer PRISMA placed at the grazing angle of $\theta_{\text{lab}} = 50^\circ$. The measured quantities allowed unequivocal determination of the atomic and mass numbers and the velocity vector for the individual lighter reaction products. A $40 \times 60 \text{ mm}^2$ microchannel plate detector DANTE (Detector

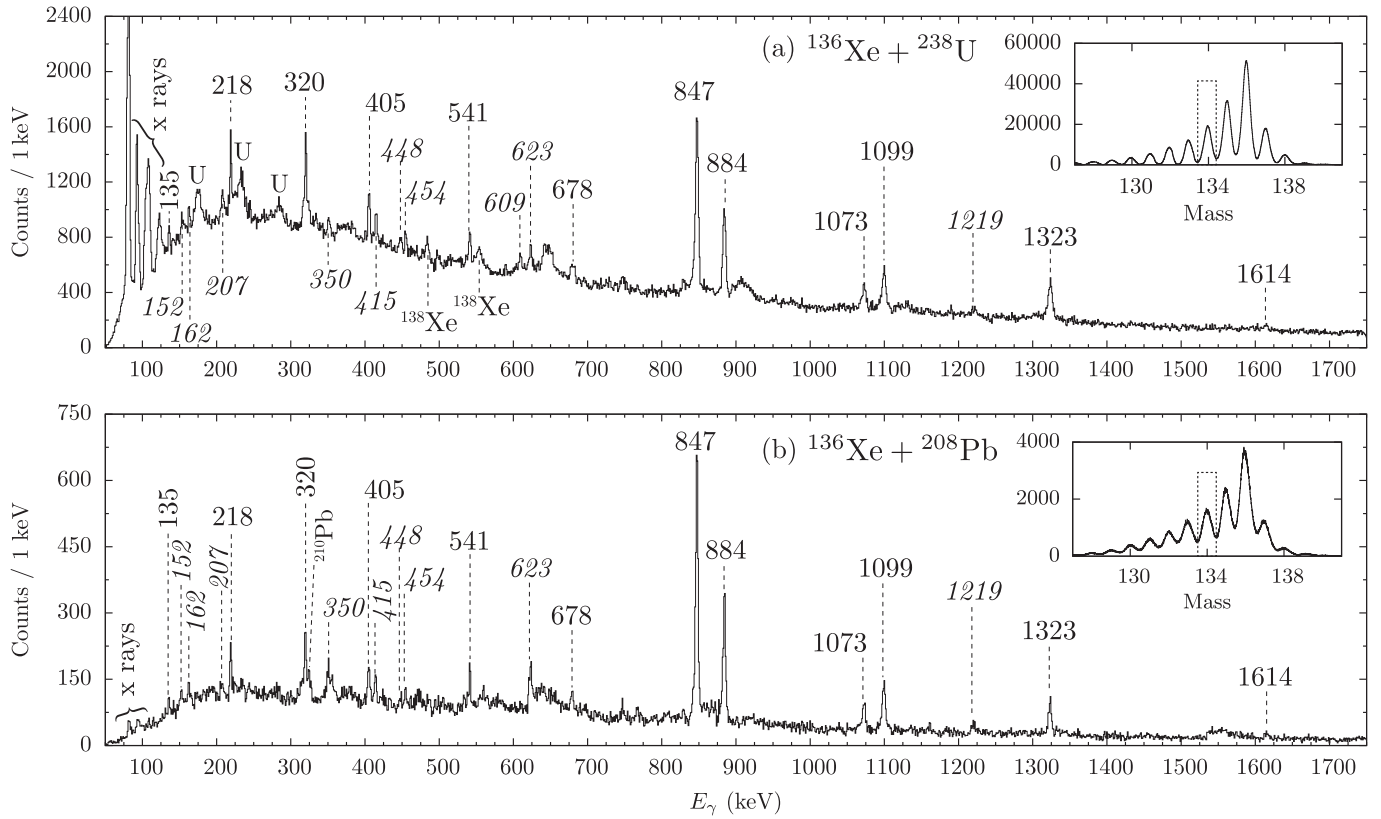


FIG. 1. Doppler-corrected γ -ray spectra gated on ^{134}Xe identified in PRISMA (a) in the $^{136}\text{Xe} + ^{238}\text{U}$ experiment and (b) in the $^{136}\text{Xe} + ^{208}\text{Pb}$ experiment with indicated γ -ray energies in keV. The spectra are obtained with a cut on the prompt time peak between AGATA and PRISMA. Remaining contaminations of the U and Pb binary reaction partners are marked in the spectra. Italic numbers label newly observed γ -ray transitions.

Array for Multinucleon Transfer Ejectiles) [31,32] covered the angular range which corresponds to the grazing angle for the targetlike reaction product in order to request a kinematic coincidence between the different reaction products. γ rays from excited states in both beam- and targetlike nuclei were detected with the AGATA array [25] in the demonstrator configuration [31] placed 23.5 cm from the target position. The array consisted of 15 large-volume electronically segmented high-purity Ge (HPGe) detectors in five triple cryostats [33]. An event registered by the PRISMA focal-plane detector in coincidence with an AGATA event was taken as a trigger for the data acquisition. Pulse-shape analysis of the fully digitized detector signals was applied to determine the individual interaction points. This information is used by the Orsay forward-tracking algorithm [34] to reconstruct the individual emitted γ -ray energies and determine the first interaction point of the γ ray in the germanium and, thus, the emission angle. Combining this information with the kinematic information of PRISMA, a precise Doppler correction for beam- and targetlike nuclei was performed. Details and results of the analysis procedure are reported in Refs. [35,36].

The Xe Doppler-corrected singles γ -ray spectrum of ^{134}Xe is shown in Fig. 1(a). The corresponding mass spectrum of the Xe isotopes is depicted in the inset. Random background is significantly suppressed by gating on the prompt time-difference peak between AGATA and PRISMA. The full

width at half maximum (FWHM) of the prompt coincidence peak is approximately 16 ns for identified beamlike particles. Transitions belonging to both primary binary partners are present in the γ -ray spectra. Results on the heavy binary partner ^{240}U are presented in Ref. [37].

The ground-state band of ^{134}Xe is visible up to the 6_1^+ state at an excitation energy of 2272.0 keV. The corresponding $6_1^+ \rightarrow 4_1^+$, $4_1^+ \rightarrow 2_1^+$, and $2_1^+ \rightarrow 0_1^+$ decays at 405, 884, and 847 keV, respectively, can be seen in the singles spectrum. Furthermore, a peak at 1073 keV can be identified as the $3^+ \rightarrow 2_1^+$ transition, de-exciting the 1920-keV level. A smaller peak at 1614 keV was expected as the decay of the 2_2^+ state to the stable ground state [24]. Transitions with energies of 135, 162, 541, and 678 keV were already observed in studies of the β decay of ^{134}I [18].

As reported in Ref. [23], we also unambiguously identify the 218-, 320-, 1099-, and 1323-keV γ rays to be transitions of ^{134}Xe . However, the peak intensities in our experiment exceed the previous work by three orders of magnitude. The broad peak at 320 keV in the singles spectrum consists of two peaks with energies of 320 and 323 keV. New peaks well above the background level are observed at 152, 207, 350, 415, 448, 454, 623, and 1219 keV. Peaks at 207, 415, and 448 keV were also visible in the γ -ray spectrum by Shrivastava *et al.*, but were neither marked nor listed as transitions belonging to ^{134}Xe . However, transitions with energies of 152 and 350 keV were

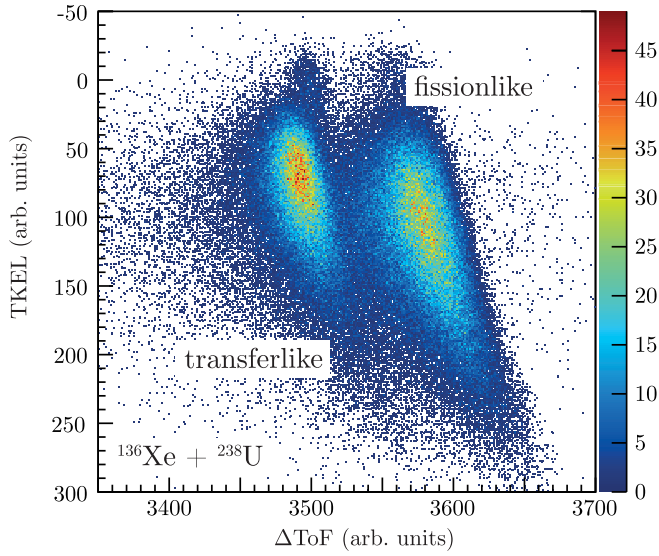


FIG. 2. Matrix of the time difference ΔToF between PRISMA and DANTE plotted against the total kinetic energy loss for ^{134}Xe events in the $^{136}\text{Xe} + ^{238}\text{U}$ experiment. Transfer and fission are clearly separated. Note that for the fission channel, the computed TKEL is only qualitative since a binary reaction is assumed.

previously reported and tentatively assigned to low-spin states in an preliminary published level scheme of a $^{\text{nat}}\text{Xe}(n,n'\gamma)$ experiment [38].

The $^{136}\text{Xe} + ^{238}\text{U}$ experiment allows to distinguish the two production modes of ^{134}Xe , which is populated both as a

fission fragment and as a two-neutron transfer product via particle-particle coincidences. The population of ^{134}Xe in the multinucleon transfer is observed with a cross section of ~ 70 mb [35]. Simultaneously, ^{134}Xe is populated as a highly excited actinide fission fragment of the $^{238}\text{U}(^{136}\text{Xe}, F\gamma)$ reaction. In this way, the separation between highly excited fission fragments and preferentially colder transfer products gives valuable additional information related to the population modes of excited states in the identified ejectile nuclei and their level scheme.

In the $^{136}\text{Xe} + ^{238}\text{U}$ experiment the fast anode signals of the entrance detector of PRISMA and the DANTE MCP enabled the measurement of time-of-flight differences (ΔToF) between different coincident reaction products entering the PRISMA spectrometer. A significant time difference is observed due to the different kinetic energies and velocities of the fission products compared to the transfer products. The simultaneous measurement of both the momentum and the angle of the beamlike recoils with PRISMA enables a reconstruction of the total kinetic energy loss (TKEL) value of the reaction [39]. As presented in Fig. 2, transferlike and fissionlike fragments are separated as two different domains in a matrix of ΔToF plotted against the TKEL for ejectiles identified as Xe. The computed TKEL value for the fission fragment is not complete and correct since the TKEL calculation is based on the binary-partner reaction system.

The ejectile Doppler-corrected γ -ray spectrum is shown in Fig. 3(a) for transferlike events while γ rays originating from ^{134}Xe fission fragments are sorted into Fig. 3(b). The ground-state $2_1^+ \rightarrow 0_1^+$ transition at 847 keV and the $4_1^+ \rightarrow 2_1^+$

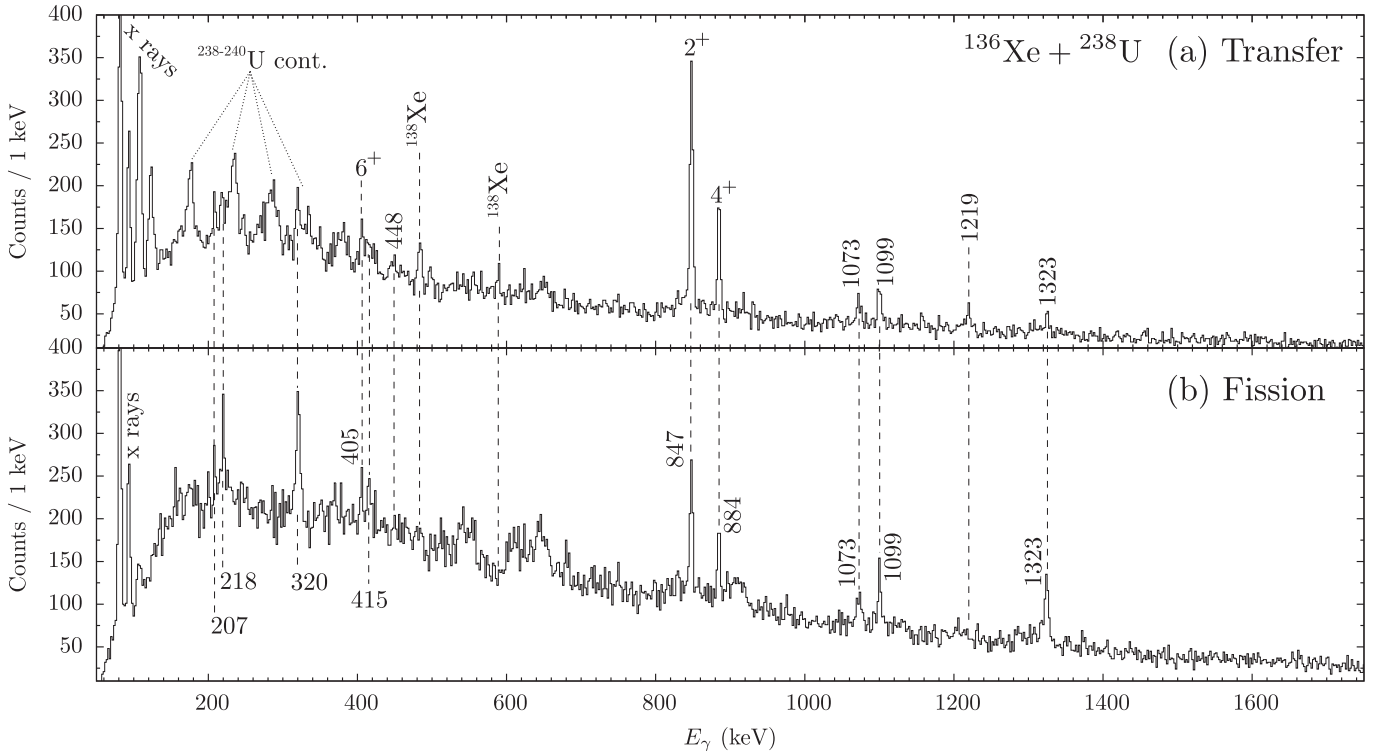


FIG. 3. Doppler-corrected ^{134}Xe γ -ray spectra from the $^{136}\text{Xe} + ^{238}\text{U}$ experiment with (a) a gate on transferlike events and (b) events originating from actinide fission.

transition at 884 keV are visible in both spectra, but dominate in the transferlike spectrum. In the transfer case the integral of the 847-keV peak is ten times larger than the integral of the 1323-keV line. For the fission case this factor is reduced to ~ 1.4 . The fission spectrum shows prominent peaks from 207-, 218-, 320-, 415-, and 1323-keV transitions, which are clearly suppressed in the transfer spectrum. Hence, those decaying states are mainly populated in highly excited fission residues. The peak at 1099 keV is visible in both transfer- and fissionlike spectra. In contrast, the 448- and 1219-keV transitions prevail in the transferlike spectrum.

By exploiting the position sensitivity for γ -ray interaction points in AGATA and for ejectile nuclei in the PRISMA entrance detector, it is possible to investigate γ -ray angular distributions of the measured γ rays with respect to the momentum of ^{134}Xe nuclei. In this way, the multiplicities of observed γ -ray transitions are compared and constrained in comparison with well-known and documented γ -ray decays.

The spin alignment is perpendicular to the reaction plane and defined by the magnetic spectrometer itself. In contrast to fusion-evaporation reactions, the spin alignment after multinucleon-transfer reactions is reduced, yet it is large enough to perform detailed angular distributions [40]. However, multinucleon-transfer shows an asymmetry of the spin alignment with respect to the azimuthal angle [41]. Contrarily to traditional detector arrays with single detectors, the AGATA demonstrator can be considered as an extended and continuous HPGe detector. Examples of such continuous distributions are given in Ref. [42]. For each γ ray the first interaction point within AGATA and the reconstructed momentum vector by PRISMA are used to calculate the corresponding angles $\theta_{\gamma,\text{Xe}}$ between the ejectile fragments and the emitted γ rays. The isotropic angular distributions of 1408-keV γ rays from a ^{152}Eu source placed at the target position serve as a geometrical efficiency correction for the detector setup. Moreover, background contributions are carefully selected and subsequently subtracted from the measured angular distributions. The degree of spin orientation with respect to the beam axis strongly depends on the initial formation process and the reaction mechanism. Thus, the angular distributions yield qualitative and tentative results on the γ -ray multiplicities.

The five AGATA triple cluster detectors were placed at backward angles with respect to the PRISMA entrance window. Figure 4 shows the ratio $W(\theta_{\gamma,\text{Xe}})$ between the number of counts in the angular range from 161° to 180° over the number of counts in the 150° to 161° angular range for various strong transitions of known multipolarity ℓ in $^{134,135,136,138}\text{Xe}$. The horizontal dashed line depicts the mean value $\overline{W}_{\ell=2}$ of the measured ratios for evaluated $E2$, $\ell = 2$ transitions [24,43–45] that are also labeled in the figure. As anticipated, the 1073-keV $3^+ \rightarrow 2^+_1$ $M1 + E2$ transition in ^{134}Xe with a mixing ratio of $\delta = +0.16(2)$ [24] exhibits a considerable deviation from the mean $\ell = 2$ value. Similarly, $W(\theta_{\gamma,\text{Xe}})$ of the 320-keV transition in ^{134}Xe is more than 2σ off with respect to $\overline{W}_{\ell=2}$, corroborating the assumption that this transition is of $\ell = 1$ dipole character. The angular-distribution ratio of the 1323-keV transition is consistent with an $E2$ multipolarity of $\ell = 2$.

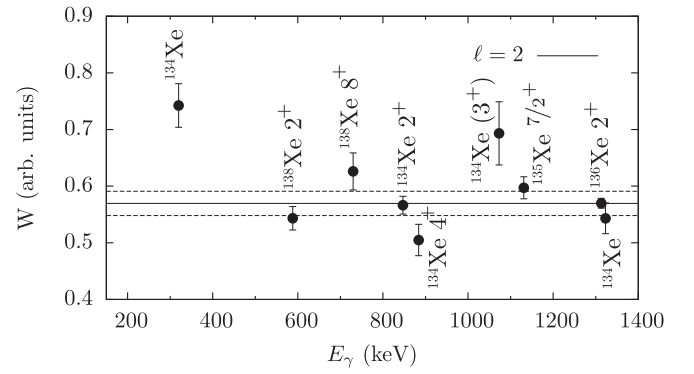


FIG. 4. Ratio $W(\theta_{\gamma,\text{Xe}})$ from γ -ray angular distributions between the number of counts in the angular range from 161° to 180° over the number of counts in the 150° to 161° angular range, measured with AGATA in the $^{136}\text{Xe} + ^{238}\text{U}$ experiment for various transitions in Xe isotopes (see labels). The horizontal line depicts the weighted mean ratio for evaluated $I \rightarrow I - 2$ transitions. Dashed lines mark the corresponding standard deviation.

Events with γ -ray multiplicities $M_\gamma \geq 2$ are sorted into a $\gamma\gamma$ -coincidence matrix. Coincidence spectra are created by projecting the matrix onto one of its axes. A corresponding gate on the 1323-keV peak is shown in Fig. 5; it demonstrates that the 1323-keV transition is coincident with the 218-, 320-, and 207-keV γ rays. Extended results on an improved $\gamma\gamma$ -coincidence analysis are the subject of the paragraph related to the $^{136}\text{Xe} + ^{198}\text{Pt}$ experiment.

To summarize, the $^{136}\text{Xe} + ^{238}\text{U}$ experiment yields results on two different population paths, multinucleon transfer and fission. By means of particle identification, several previously reported transitions as well as new transitions are unambiguously assigned to ^{134}Xe . In the fission-gated γ -ray spectra, six transitions are enhanced with respect to the transfer-gated spectra, suggesting that states with larger excitation energies as well as higher angular momentum are populated.

B. $^{136}\text{Xe} + ^{208}\text{Pb}$

In this experiment, a ^{136}Xe beam provided by the PIAVE+ALPI accelerator complex at an energy of 930 MeV impinged onto a 1 mg/cm² thick ^{208}Pb target. PRISMA was placed at the grazing angle of $\theta_{\text{lab}} = 42^\circ$. γ rays were measured

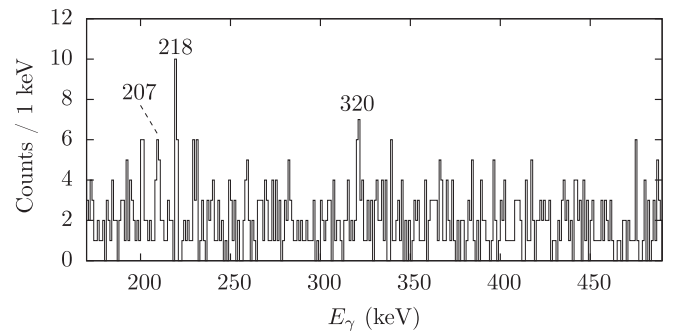


FIG. 5. $\gamma\gamma$ -coincidence spectrum of the $^{136}\text{Xe} + ^{238}\text{U}$ experiment with a gate around $E_\gamma = 1323$ keV (shown in the inset panel).

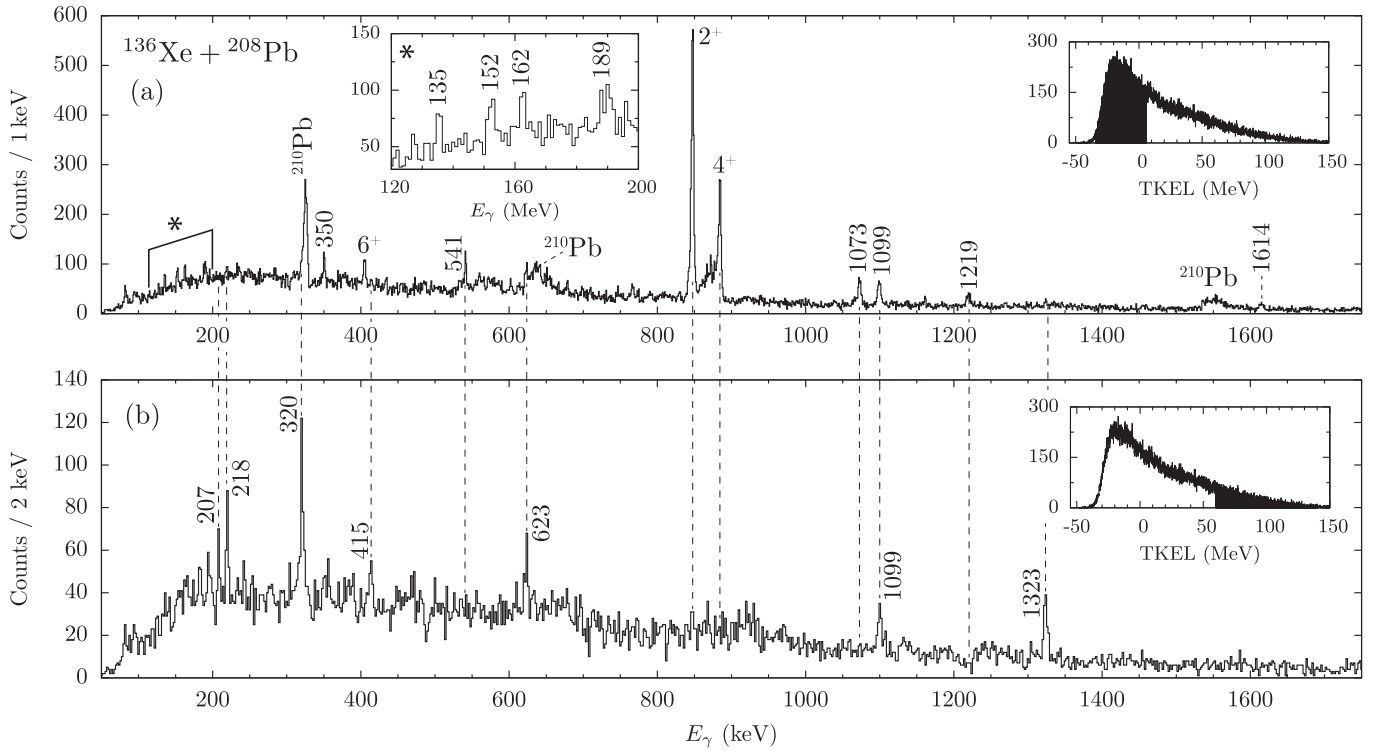


FIG. 6. Doppler-corrected ^{134}Xe γ -ray spectra with gates on low and large TKEL values from the $^{136}\text{Xe} + ^{208}\text{Pb}$ experiment: (a) gate on low TKEL and (b) gate on large TKEL corresponding to higher excitation energies after the deep-inelastic MNT reaction. The applied gates on the TKEL distributions are shown in the insets. Both spectra are obtained with a cut on the prompt time peak between AGATA and PRISMA.

by the AGATA demonstrator in an earlier configuration in which only three triple clusters were available. The experimental configuration, trigger conditions, as well as the data analysis resemble those described in Sec. II A. The singles γ -ray spectrum depicted in Fig. 1(b) exhibits the same lines as in the $^{136}\text{Xe} + ^{238}\text{U}$ experiment, yet there is much less random background from fission present in the spectrum. Further details of the analysis are presented in Refs. [46,47].

Multinucleon transfer reactions populate excitation energies and spins differing substantially from the ones reached by fusion-evaporation reactions or fission residues [27,48]. The total excitation energy can be restricted by gating on the TKEL, which was calculated in a similar way to that described in Sec. II A. In particular, events with small TKEL values are related to reaction products with a lower excitation energy. We remind the reader that as the TKEL is shared between the two reaction products, the excitation energy of both light and heavy reaction products is included in the TKEL distribution. Due to the presence of the two long-lived isomers in the level scheme of ^{134}Xe , the TKEL-gated prompt in-beam γ -ray spectra are excellent tools to discriminate between γ -ray transitions below and above the isomeric states. Thus, TKEL spectra are correlated with coincident γ rays of AGATA. By gating on different TKEL regions, γ -ray transitions between states with different excitation energies and angular momenta can be suppressed or enhanced [27,28]. Figure 6 shows γ -ray spectra for ^{134}Xe obtained with different conditions on the TKEL. The TKEL spectra are presented in the top right insets.

By gating on the low-TKEL region (a), the three lowest $6_1^+ \rightarrow 4_1^+$, $4_1^+ \rightarrow 2_1^+$, and $2_1^+ \rightarrow 0_1^+$ yrast transitions are

clearly enhanced in the spectrum. As expected, the 1073-keV transition connecting the low-lying 1920-keV 3^+ state with the 2_1^+ state is only visible in panel (a). Transitions of other low-lying non-yrast states such as the $(5^+) \rightarrow 4_1^+$ at 541 keV, the $(5^+) \rightarrow 6_1^+$ at 135 keV γ rays, and a new peak at 1219 keV are visible as well. The gate also reveals transitions with a small branching ratio such as the 189 keV γ ray connecting the 1920 keV 3^+ state with the 4_1^+ yrast state. All these lower-energy transitions, including the yrast γ -ray transitions below the 10^+ isomer vanish for gates on large TKEL values in Fig. 6(b). The peaks at 207, 218, 415, 623, and 1323 keV and a broad peak at 320 keV only appear at large TKEL. The 1099-keV line is visible for both TKEL domains in Fig. 6. In conclusion, due to the presence of two long-lived isomers, gates on large TKEL can indeed entirely suppress de-excitations of states below the isomeric states. Hence, there is strong evidence that the above-mentioned transitions (207, 218, 320, 415, 623, and 1323 keV) are in fact located at higher excitation energies in the level scheme. The singles spectra of both AGATA experiments exhibit a high-statistics peak at 1099 keV.

C. $^{136}\text{Xe} + ^{198}\text{Pt}$

In this experiment, a 850-MeV ^{136}Xe beam provided by the 88-inch cyclotron at LBNL impinged onto a 92% isotopically enriched self-supporting $420\text{-}\mu\text{g}/\text{cm}^2$ ^{198}Pt target. γ rays were detected by the GAMMASPHERE array, which consisted of 103 Compton-suppressed HPGe detectors in this experiment [29]. Both polar and azimuthal angles and the time-of-flight difference ΔToF between the detection of

the 218- and 320-keV γ rays, verifying these transitions to be members of a cascade above the 10^+ isomer. In this measurement the 1323-keV gate exhibits contamination due to the nearby 1313-keV $2^+ \rightarrow 0^+$ transition in ^{136}Xe . A broad accumulation of counts around 400 keV is subsequently caused by falsely Doppler-corrected targetlike ^{198}Pt γ rays. The 6.3(1)-keV FWHM of the 320-keV peak is broader than that of the neighboring peaks (e.g., $\text{FWHM}_{218\text{ keV}} = 3.54(9)$ keV). A gate on the left part of the 320-keV peak reveals a second peak at 323 keV, as depicted in Fig 8(c). Coincidences with 623-keV γ rays are present in all gated spectra; a coincidence with the 207-keV line is observed except for the 218-keV gate.

The construction of the level scheme which is built on top of the 10^+ isomeric state is based on the prompt $\gamma\gamma$ coincidences and the efficiency-corrected γ -ray intensities from the GAMMASPHERE experiment. The extended and modified level scheme is presented in Fig. 7. Intensities of the yrast cascade below the isomer are extracted from the out-of-beam delayed $\gamma\gamma$ matrix and normalized to the 2_1^+ decay; intensities above the isomer are normalized to the intensity of the 1323-keV transition. The intensity balance between the ground-state sequence and the high-spin structure is extracted from the $^{136}\text{Xe} + ^{208}\text{Pb}$ dataset.

The intensity relations affirm the placement of the 1323-keV transition on top of the isomer, fed by the 320- and 218-keV transitions. Fotiadis *et al.* reported two more lines to be in coincidence with the 1323-keV line: 323 and 541 keV [22]. The intensity of the 323-keV line corroborates a placement directly above the 4886-keV state. The 541-keV transition expected to be in coincidence with the 320- and the 1323-keV transition is neither observed in the prompt spectra nor in the large-TKEL gated AGATA data. The 541-keV line visible in the low-TKEL gated γ -ray spectrum in Fig. 6(a) can be attributed to the low-spin structure below the isomer [24]. However, a line at 538 keV is visible in the delayed-prompt coincidence spectrum in Fig. 8(a) and, consequently, it is part of a cascade above the isomer. Indeed, the sum of the 320- and 218-keV transitions suggests that the transition of 538 keV bypasses the 320- and 218-keV γ rays. The 623-keV transition is coincident with all transitions of the cascade and, thus,

placed on top of the 5209-keV state based on its low intensity. The line at 207 keV coincides with the 320- and 1323-keV γ rays, but not with the 218-keV transition or other decays from higher-lying states. It is assumed to feed the 4668-keV state.

Shrivastava *et al.* tentatively assigned a 1100-keV line to be a $(9^-) \rightarrow 7^-$ transition feeding the 290-ms $E_x = 1965$ keV 7^- isomer [23]. This assignment was based on a comparison with results of a LSSM calculation. A 1100-keV transition was also found to connect the mixed-symmetry 2_3^+ state with the 2_1^+ yrast state in a later experiment [21]. As shown in Sec. II B, the 1099-keV transition appears in both TKEL-gated γ -ray spectra of the $^{136}\text{Xe} + ^{208}\text{Pb}$ experiment in Fig. 6. Consequently, it is interpreted as a doublet. The gate on low TKEL in the $^{136}\text{Xe} + ^{208}\text{Pb}$ experiment predominantly selects the $2_3^+ \rightarrow 2_1^+$ transition. On the other hand, the decay of the 2_1^+ state to the ground state is not present in the γ -ray spectrum gated on large TKEL. Subsequently, the 1099-keV transition visible in Fig. 6(b) is not connected to the yrast band and has to be placed on top of an isomeric state. Due to missing coincidences with any known or newly observed transitions above the 10^+ isomer, it is placed on top of the second isomer feeding directly the 7^- isomer at 1965 keV. A 612-keV $(11^-) \rightarrow (9^-)$ transition, which was suggested in Ref. [23] to sit on top of the 1099-keV transition is not observed in either AGATA or GAMMASPHERE spectra. It was shown before that the 415-keV γ ray was found in the $^{136}\text{Xe} + ^{238}\text{U}$ fission γ -ray spectrum as well as in the γ -ray spectrum of the $^{136}\text{Xe} + ^{238}\text{U}$ experiment gated on large TKEL. Since the 415-keV transition is also not observed in coincidence with any transitions above the 10^+ isomer, the transition is placed above the long-lived 7^- isomer feeding the 3064-keV state. The newly found 454-keV transition also does not show any γ -ray coincidences with members of the band above the 10^+ isomer. The 454-keV transition is placed directly above the 10^+ isomer decaying from the (already introduced) excited (11^-) state at 3479 keV into the 10^+ isomer. The energy differences between the 3479-keV state and the 3025-keV 10^+ state match nicely. In this way, a decay branch connects the negative-parity states above the 7^- isomer with the 10^+ excited state. The 448-keV transition present in the AGATA

TABLE I. Energies, assignments, and relative in-beam intensities for transitions observed in ^{134}Xe above the 10^+ and 7^- isomers. The energies are fitted in the AGATA datasets; intensities are taken from the GAMMASPHERE measurement. The uncertainties in the transition energies are ± 0.5 keV. Possible spin-parity assignments are discussed in Sec. III.

E_γ (keV)	E_i	E_f	I_i^π	I_f^π	I_γ
Transitions feeding the 10^+ isomer					
207	4875	4668		(13 ⁺)	2.3(2)
218	4886	5290	(14 ⁺)	(13 ⁺)	10.4(2)
320	4668	4348	(13 ⁺)	(12 ⁺)	16.1(25)
323	5209	4886	(15 ⁺)	(14 ⁺)	7.2(24)
454	3479	3025	(11 ⁻)	10 ⁺	4.7(3)
538	5209	4668	(14 ⁺)	(12 ⁺)	2.7(3)
623	5290	4668	(16 ⁺)	(15 ⁺)	5.9(2)
1323	4348	3025	(12 ⁺)	10 ⁺	27.6(7)
Transitions feeding the 7^- isomer					
415	3479	3064	(11 ⁻)	(9 ⁻)	
1099	3064	1965	(9 ⁺)	7 ⁻	

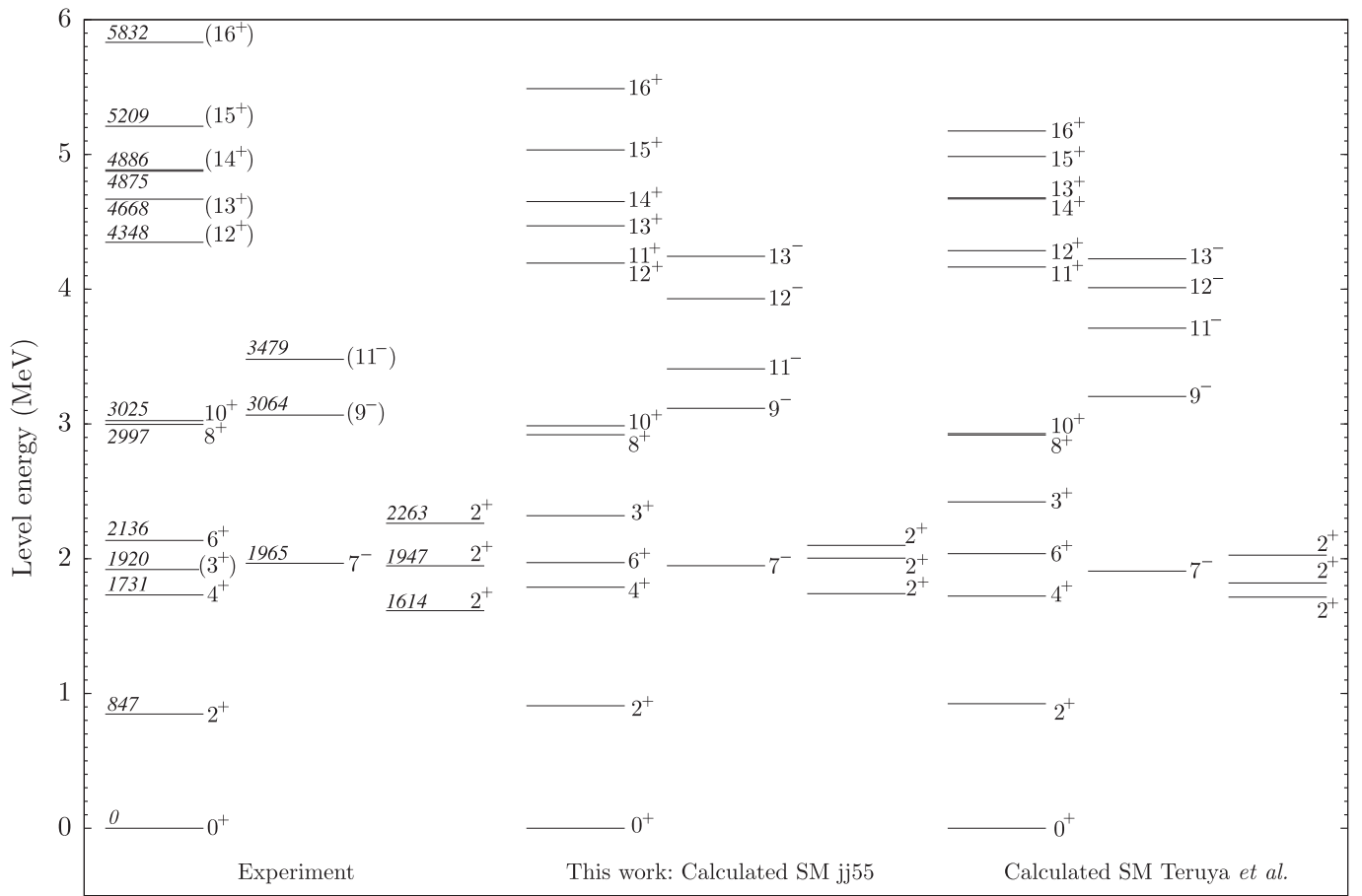


FIG. 9. Comparison of the experimental energy spectra (left panel) with the results of the shell-model calculations within the $jj55$ effective interaction (middle panel) and by Teruya *et al.* [51] (right panel). Note that in all panels the states are separated into three columns for the positive-parity, negative-parity, and higher-lying 2^+ states.

spectra is not visible in any coincidence spectra and could not be included in the level scheme. The γ -ray transitions above the isomeric states and their corresponding intensities are summarized in Table I. Possible spin-parity assignments are discussed in Sec. III. In brief, the $^{136}\text{Xe} + ^{198}\text{Pt}$ data yields crucial results on the extended and revised level structure above the two isomers by exploiting delayed-prompt and prompt $\gamma\gamma$ coincidences.

III. SHELL MODEL CALCULATION

The extended level scheme was compared to results of two different shell-model calculations for ^{134}Xe . The first calculations were carried out in the proton-neutron formalism without any truncations for positive- and negative-parity states in the full $gdsh$ valence space outside the ^{100}Sn core between the magic numbers 50 and 82, including the $0g_{7/2}$, $1d_{5/2}$, $1d_{3/2}$, $2s_{1/2}$, and $0h_{11/2}$ orbitals for both protons and neutrons. The shell-model code NUSHELLX@MSU [11] was employed using the $jj55$ effective interaction obtained by Brown *et al.* [49] based on a renormalized G matrix derived from the CD-Bonn nucleon-nucleon interaction [50] considering ^{132}Sn as the core nucleus.

An independent extensive theoretical study of nuclei around mass 130 was published by Teruya *et al.* [51]. The

results include excited states and electromagnetic transition probabilities for Xe isotopes within the shell model in the $gdsh$ model space including the $0g_{7/2}$, $1d_{5/2}$, $1d_{3/2}$, $2s_{1/2}$, and $0h_{11/2}$ orbitals. The effective interaction consists of spherical single-particle energies and phenomenological two-body effective interactions consisting of monopole-pairing, quadrupole-pairing, and quadrupole-quadrupole terms. Further newly introduced higher-order pairing interactions are also taken into account. Single-particle energies (SPE) were adopted from the experimental excited states of ^{133}Sb (proton SPEs) and ^{131}Sn (neutron SPEs) [51].

In Fig. 9 the results of both shell-model calculations (middle and right panels) have been compared to the experimental levels (left panel). Note that in all panels the states are separated into three columns for (i) positive-parity and (ii) negative-parity states visible in the experiments from this work and (iii) $2^+_{2,3,4}$ states from the literature as a further benchmark for the validity of the shell-model calculations. Good agreement is obtained for the even-spin states of the yrast band up to spin 10^+ . In particular, both calculations reproduce the small energy spacing between the 8^+ and the 10^+ state. Only the 3^+_1 state with a 61% $\pi g^3_{7/2} d^1_{5/2}$ configuration is placed in both theoretical results too high in energy above the 6^+_1 state with respect to the experimentally obtained sequence. The spin of the (3^+_1) state was only assigned tentatively in the

literature [18]. The position of the experimental 7^- isomer state with regard to the even-spin yrast cascade is also mirrored with high precision in the calculations. Both calculations reproduce the three low-lying $2_{2,3,4}^+$ states.

Above the 10^+ isomeric state, both shell-model approaches predict 11^+ and 12^+ states more than 1200-keV higher-lying in energy. Within the *jj55* interaction, the 12^+ state is located below the 11^+ state with nearly degenerate excitation energy. The 1323-keV γ ray, de-exciting the 4348-keV state, is inferred to be a stretched $E2$ transition (see Sec. II A). This would be a consistent scenario and the two shell-model calculations suggest the 4348-keV state to be tentatively assigned a spin-parity value of 12^+ . In the *jj55* calculation, states on top of the 12^+ and 11^+ pair are predicted to have positive parity with consecutive spin differences of $\Delta I = 1$, giving the corresponding transitions $M1$ character. This calculation also adequately reproduces the experimental energy spacings of states in the energy range from 4.3 up to 5.8 MeV, besides the yet unresolved 4875-keV state that de-excites via a weak 207-keV γ ray. From this point of view, the states on top of the 4348-keV state up to spin 16^+ are of positive parity, connected by magnetic dipole transitions.

The calculation performed by Teruya *et al.* suggests that the 14^+ state lies, nearly degenerate in energy, below the 13^+ state. According to the tentative (12^+) assignment for the 4348-keV state and the measured multipolarity $\Delta l = 1$ of the feeding 320-keV transition, the spin parity of the 4668-keV state is possibly 13^+ .

Moreover, the SM results provide insight into the structure of the isomeric states and the levels built on top. The 10^+ state is calculated to be of $\nu h_{11/2}^{-2}$ character with a configuration of 68% $\nu_{10^+} \otimes \pi_{0^+}$ and 23% $\nu_{10^+} \otimes \pi_{2^+}$ by the *jj55* shell-model calculation. Up to spin 16^+ , the first high-spin states above the 10^+ state consist of a neutron 10^+ configuration coupled to even-spin proton configurations. The 7^- isomer is dominated by the $\nu d_{3/2}^{-1} h_{11/2}^{-1}$ neutron configuration. According to the calculated level schemes there is strong evidence to interpret the 1099-keV transition, placed above the 7^- isomer, as the decay of the 9^- state. Teruya *et al.* as well as the *jj55* calculation describe the negative-parity states above the 7^- isomer with a stretched angular momentum of $7\hbar$ coupled to

the proton quadrupole excited states ($0^+, 2^+, 4^+$). Further on, a sequence of 12^- and 13^- states is predicted at higher excitation energies.

IV. CONCLUSIONS

In summary, new high-spin states in ^{134}Xe on top of the two long-lived isomers have been discovered. The results are based on γ -ray spectroscopy after MNT reactions and fission fragment spectroscopy. $\gamma\gamma$ coincidence relations, γ -ray angular distributions, and excitation energies from the total kinetic energy loss and fission fragments are used to construct an extended decay scheme including several newly observed states and γ -ray transitions. The high-spin structure above the 10^+ isomer could be unambiguously identified for the first time by delayed-prompt $\gamma\gamma$ coincidences. The extended and revised level scheme of ^{134}Xe is constructed up to an excitation energy of 5.832 MeV with tentative spin-parity assignments up to 16^+ . Previous assignments of states above the 7^- isomer, with the exception of the 3064-keV level, have been revised by introducing two newly observed γ rays in two decay branches. Recent shell-model calculations reproduce the experimental findings remarkably well and corroborate most of the suggested assignments.

ACKNOWLEDGMENTS

The research leading to these results has received funding from the German BMBF under Contract No. 05P12PKFNE TP4, from the European Union Seventh Framework Programme FP7/2007–2013 under Grant Agreement No. 262010-ENSAR, from the Spanish Ministerio de Ciencia e Innovación under Contract No. FPA2011-29854-C04, from the Spanish Ministerio de Economía y Competitividad under Contract No. FPA2014-57196-C5, from the Bonn-Cologne Graduate School of Physics and Astronomy (BCGS), from the UK Science and Technology Facilities Council (STFC), and from the US National Science Foundation (NSF). One of the authors (A. Gadea) has been supported by the Generalitat Valenciana, Spain, under Grant No. PROMETEOII/2014/019 and EU under the FEDER program.

-
- [1] B. Fogelberg, K. Heyde, and J. Sau, Nucl. Phys. A **352**, 157 (1981).
 - [2] J. Genevey, J. A. Pinston, C. Foin, M. Rejmund, R. F. Casten, H. Faust, and S. Oberstedt, Phys. Rev. C **63**, 054315 (2001).
 - [3] J. J. Valiente-Dobón, P. H. Regan, C. Wheldon, C. Y. Wu, N. Yoshinaga, K. Higashiyama, J. F. Smith, D. Cline, R. S. Chakrawarthy, R. Chapman, M. Cromaz, P. Fallon, S. J. Freeman, A. Görgen, W. Gelletly, A. Hayes, H. Hua, S. D. Langdown, I. Y. Lee, X. Liang, A. O. Macchiavelli, C. J. Pearson, Z. Podolyák, G. Sletten, R. Teng, D. Ward, D. D. Warner, and A. D. Yamamoto, Phys. Rev. C **69**, 024316 (2004).
 - [4] T. Shizuma, Z. G. Gan, K. Ogawa, H. Nakada, M. Oshima, Y. Toh, T. Hayakawa, Y. Hatsukawa, M. Sugawara, Y. Utsuno, and Z. Liu, EPJ A **20**, 207 (2004).
 - [5] M. Müller-Veggian, Y. Gono, R. M. Lieder, A. Neskakis, and C. Mayer-Böricke, Nucl. Phys. A **304**, 1 (1978).
 - [6] J. C. Merdinger, F. A. Beck, E. Bozek, T. Byrski, C. Gehringer, Y. Schutz, and J. P. Vivien, Nucl. Phys. A **346**, 281 (1980).
 - [7] M. Ferraton, R. Bourgain, C. M. Petrache, D. Verney, F. Ibrahim, N. de Séréville, S. Franchoo, M. Lebois, C. Phan Viet, L. Sagui, I. Stefan, J. Clavelin, and M. Vilnay, EPJ A **35**, 167 (2008).
 - [8] M. Lach, J. Styczen, R. Julin, M. Piiparinen, H. Beuscher, P. Kleinheinz, and J. Blomqvist, Z. Phys. A **319**, 235 (1984).
 - [9] E. Caurier, G. Martínez-Pinedo, F. Nowacki, A. Poves, J. Retamosa, and A. P. Zuker, Phys. Rev. C **59**, 2033 (1999).
 - [10] E. Caurier and G. Martínez-Pinedo, Nucl. Phys. A **704**, 60 (2002).
 - [11] B. A. Brown and W. D. M. Rae, Nucl. Data Sheets **120**, 115 (2014).

- [12] K. Higashiyama and N. Yoshinaga, *Phys. Rev. C* **83**, 034321 (2011).
- [13] K. Sieja, G. Martínez-Pinedo, L. Coquard, and N. Pietralla, *Phys. Rev. C* **80**, 054311 (2009).
- [14] K. Higashiyama, N. Yoshinaga, and K. Tanabe, *Phys. Rev. C* **65**, 054317 (2002).
- [15] W. G. Winn and D. G. Sarantites, *Phys. Rev.* **184**, 1188 (1969).
- [16] E. Achterberg, E. Y. de Aisenberg, F. C. Iglesias, A. E. Jech, J. A. Moragues, D. Otero, M. L. Pérez, A. N. Proto, J. J. Rossi, W. Scheuer, and J. F. Suárez, *Phys. Rev. C* **4**, 188 (1971).
- [17] C. D. Coryell, H. N. Erten, P. K. Hopke, W. B. Walters, R. Dams, and H. C. Griffin, *Nucl. Phys. A* **179**, 689 (1972).
- [18] J. M. Gualda, R. N. Saxena, and F. C. Zawislak, *Nucl. Phys. A* **234**, 357 (1974).
- [19] G. Jakob, N. Benczer-Koller, G. Kumbartzki, J. Holden, T. J. Mertzimekis, K.-H. Speidel, R. Ernst, A. E. Stuchbery, A. Pakou, P. Maier-Komor, A. Macchiavelli, M. McMahan, L. Phair, and I. Y. Lee, *Phys. Rev. C* **65**, 024316 (2002).
- [20] K. H. Speidel, H. Busch, S. Kremeyer, U. Knopp, J. Cub, M. Bussas, W. Karle, K. Freitag, U. Grabowy, and J. Gerber, *Nucl. Phys. A* **552**, 140 (1993).
- [21] T. Ahn, L. Coquard, N. Pietralla, G. Rainovski, A. Costin, R. V. F. Janssens, C. J. Lister, M. Carpenter, S. Zhu, and K. Heyde, *Phys. Lett. B* **679**, 19 (2009).
- [22] N. Fotiades, R. O. Nelson, M. Devlin, J. A. Cizewski, J. A. Becker, W. Younes, R. Krücken, R. M. Clark, P. Fallon, I. Y. Lee, A. O. Macchiavelli, T. Ethvignot, and T. Granier, *Phys. Rev. C* **75**, 054322 (2007).
- [23] A. Shrivastava, M. Caamaño, M. Rejmund, A. Navin, F. Rejmund, K. H. Schmidt, A. Lemasson, C. Schmitt, L. Gaudefroy, K. Sieja, L. Audouin, C. O. Bacri, G. Barreau, J. Benlliure, E. Casarejos, X. Derkx, B. Fernández-Domínguez, C. Golabek, B. Jurado, T. Roger, and J. Taieb, *Phys. Rev. C* **80**, 051305 (2009).
- [24] A. A. Sonzogni, *Nucl. Data Sheets* **103**, 1 (2004).
- [25] S. Akkoyun *et al.*, *Nucl. Instr. Meth. Phys. Res. A* **668**, 26 (2012).
- [26] A. Stefanini, L. Corradi, G. Maron, A. Pisent, M. Trotta, A. Vinodkumar, S. Beghini, G. Montagnoli, F. Scarlassara, G. Segato, A. D. Rosa, G. Inglima, D. Pierrousakou, M. Romoli, M. Sandoli, G. Pollarolo, and A. Latina, *Nucl. Phys. A* **701**, 217 (2002).
- [27] S. Szilner, C. A. Ur, L. Corradi, N. Marginean, G. Pollarolo, A. M. Stefanini, S. Beghini, B. R. Behera, E. Fioretto, A. Gadea, B. Guiot, A. Latina, P. Mason, G. Montagnoli, F. Scarlassara, M. Trotta, G. de Angelis, F. Della Vedova, E. Farnea, F. Haas, S. Lenzi, S. Lunardi, R. Marginean, R. Menegazzo, D. R. Napoli, M. Nespola, I. V. Pokrovsky, F. Recchia, M. Romoli, M.-D. Salsac, N. Soić, and J. J. Valiente-Dobón, *Phys. Rev. C* **76**, 024604 (2007).
- [28] L. Corradi, S. Szilner, G. Pollarolo, D. Montanari, E. Fioretto, A. Stefanini, J. Valiente-Dobón, E. Farnea, C. Michelagnoli, G. Montagnoli, F. Scarlassara, C. Ur, T. Mijatović, D. J. Malenica, N. Soić, and F. Haas, *Nucl. Instr. Meth. Phys. Res. B* **317**, 743 (2013).
- [29] I.-Y. Lee, *Nucl. Phys. A* **520**, c641 (1990).
- [30] M. W. Simon, D. Cline, C. Y. Wu, R. W. Gray, R. Teng, and C. Long, *Nucl. Instr. Methods Phys. Res. Sec. A* **452**, 205 (2000).
- [31] A. Gadea, E. Farnea, J. J. Valiente-Dobón, B. Million, D. Mengoni, D. Bazzacco, F. Recchia, A. Dewald, T. Pissulla, W. Rother, G. de Angelis *et al.*, *Nucl. Instr. Meth. Phys. Res. A* **654**, 88 (2011).
- [32] J. J. Valiente-Dobón *et al.*, *Acta. Phys. Pol. B* **37**, 225 (2006).
- [33] A. Wiens, H. Hess, B. Birkenbach, B. Bruyneel, J. Eberth, D. Lersch, G. Pascovici, P. Reiter, and H.-G. Thomas, *Nucl. Instr. Meth. Phys. Res. A* **618**, 223 (2010).
- [34] A. Lopez-Martens, K. Hauschild, A. Korichi, J. Roccas, and J.-P. Thibaud, *Nucl. Instr. Meth. Phys. Res. A* **533**, 454 (2004).
- [35] A. Vogt, B. Birkenbach, P. Reiter, L. Corradi, T. Mijatović, D. Montanari, S. Szilner, D. Bazzacco, M. Bowry, A. Bracco, B. Bruyneel, F. C. L. Crespi, G. de Angelis, P. Désesquelles, J. Eberth, E. Farnea, E. Fioretto, A. Gadea, K. Geibel, A. Gengelbach, A. Giaz, A. Görgen, A. Gottardo, J. Grebosz, H. Hess, P. R. John, J. Jolie, D. S. Judson, A. Jungclaus, W. Korten, S. Leoni, S. Lunardi, R. Menegazzo, D. Mengoni, C. Michelagnoli, G. Montagnoli, D. Napoli, L. Pellegri, G. Pollarolo, A. Pullia, B. Quintana, F. Radeck, F. Recchia, D. Rosso, E. Şahin, M. D. Salsac, F. Scarlassara, P.-A. Söderström, A. M. Stefanini, T. Steinbach, O. Stezowski, B. Szpak, C. Theisen, C. Ur, J. J. Valiente-Dobón, V. Vandone, and A. Wiens, *Phys. Rev. C* **92**, 024619 (2015).
- [36] B. Birkenbach, Ph.D. thesis, Universität zu Köln, 2014, <http://kups.ub.uni-koeln.de/5648/>.
- [37] B. Birkenbach, A. Vogt, K. Geibel, F. Recchia, P. Reiter, J. J. Valiente-Dobón, D. Bazzacco, M. Bowry, A. Bracco, B. Bruyneel, L. Corradi, F. C. L. Crespi, G. de Angelis, P. Désesquelles, J. Eberth, E. Farnea, E. Fioretto, A. Gadea, A. Gengelbach, A. Giaz, A. Görgen, A. Gottardo, J. Grebosz, H. Hess, P. R. John, J. Jolie, D. S. Judson, A. Jungclaus, W. Korten, S. Lenzi, S. Leoni, S. Lunardi, R. Menegazzo, D. Mengoni, C. Michelagnoli, T. Mijatović, G. Montagnoli, D. Montanari, D. Napoli, L. Pellegri, G. Pollarolo, A. Pullia, B. Quintana, F. Radeck, D. Rosso, E. Şahin, M. D. Salsac, F. Scarlassara, P.-A. Söderström, A. M. Stefanini, T. Steinbach, O. Stezowski, S. Szilner, B. Szpak, C. Theisen, C. Ur, V. Vandone, and A. Wiens, *Phys. Rev. C* **92**, 044319 (2015).
- [38] C. A. McGrath, M. F. Villaniand, D. P. Diprete, P. E. Garrett, M. Yeh, S. W. Yates, and Z. Revay (eds.), *Proceedings of the 9th International Symposium on Capture Gamma-Ray Spectroscopy and Related Topics, Budapest, Hungary, October 1996* (Springer, Budapest, Hungary, 1997), Vol. 1, p. 299.
- [39] A. B. Brown, C. W. Snyder, W. A. Fowler, and C. C. Lauritsen, *Phys. Rev.* **82**, 159 (1951).
- [40] P. Aguer, R. P. Schmitt, G. J. Wozniak, D. Habs, R. M. Diamond, C. Ellegaard, D. L. Hillis, C. C. Hsu, G. J. Mathews, L. G. Moretto, G. U. Rattazzi, C. P. Roulet, and F. S. Stephens, *Phys. Rev. Lett.* **43**, 1778 (1979).
- [41] D. Montanari, S. Leoni, D. Mengoni, J. J. Valiente-Dobon, G. Benzoni, N. Blasi, G. Bocchi, P. F. Bortignon, S. Bottoni, A. Bracco, F. Camera, P. Casati, G. Colò, A. Corsi, F. C. L. Crespi, B. Million, R. Nicolini, O. Wieland, D. Bazzacco, E. Farnea, G. Germogli, A. Gottardo, S. M. Lenzi, S. Lunardi, R. Menegazzo, G. Montagnoli, F. Recchia, F. Scarlassara, C. Ur, L. Corradi, G. de Angelis, E. Fioretto, D. R. Napoli, R. Orlandi, E. Sahin, A. M. Stefanini, R. P. Singh, A. Gadea, S. Szilner, M. Kmiecik, A. Maj, W. Meczynski, A. Dewald, T. Pissulla, and G. Pollarolo, *Phys. Rev. C* **85**, 044301 (2012).
- [42] L. Pellegri, A. Bracco, F. Crespi, S. Leoni, F. Camera, E. Lanza, M. Kmiecik, A. Maj, R. Avigo, G. Benzoni, N. Blasi,

- C. Boiano, S. Bottoni, S. Brambilla, S. Ceruti, A. Giaz, B. Million, A. Morales, R. Nicolini, V. Vandone, O. Wieland, D. Bazzacco, P. Bednarczyk, M. Bellato, B. Birkenbach, D. Bortolato, B. Cederwall, L. Charles, M. Ciemala, G. D. Angelis, P. Désesquelles, J. Eberth, E. Farnea, A. Gadea, R. Gernhäuser, A. Görgen, A. Gottardo, J. Grebosz, H. Hess, R. Isocrate, J. Jolie, D. Judson, A. Jungclaus, N. Karkour, M. Krzysiek, E. Litvinova, S. Lunardi, K. Mazurek, D. Mengoni, C. Michelagnoli, R. Menegazzo, P. Molini, D. Napoli, A. Pullia, B. Quintana, F. Recchia, P. Reiter, M. Salsac, B. Siebeck, S. Siem, J. Simpson, P.-A. Söderström, O. Stezowski, C. Theisen, C. Ur, J. V. Dobon, and M. Zieblinski, *Phys. Lett. B* **738**, 519 (2014).
- [43] B. Singh, A. Rodionov, and Y. Khazov, *Nucl. Data Sheets* **109**, 517 (2008).
- [44] A. A. Sonzogni, *Nucl. Data Sheets* **95**, 837 (2002).
- [45] A. A. Sonzogni, *Nucl. Data Sheets* **98**, 515 (2003).
- [46] R. Kempley *et al.*, *Acta. Phys. Pol. B* **42**, 717 (2011).
- [47] M. Siciliano *et al.*, LNL Annual Report 2014, **241**, 63, 2015, http://www.lnl.infn.it/~annrep/read_ar/2014/contributions/pdfs/063_B_127_B122.pdf.
- [48] L. Corradi, G. Pollarolo, and S. Szilner, *J. Phys. G* **36**, 113101 (2009).
- [49] B. A. Brown, N. J. Stone, J. R. Stone, I. S. Towner, and M. Hjorth-Jensen, *Phys. Rev. C* **71**, 044317 (2005).
- [50] R. Machleidt, F. Sammarruca, and Y. Song, *Phys. Rev. C* **53**, R1483 (1996).
- [51] E. Teruya, N. Yoshinaga, K. Higashiyama, and A. Odahara, *Phys. Rev. C* **92**, 034320 (2015).

Publication IV:

**Isomers and high-spin structures
in the $N = 81$ isotones ^{135}Xe and ^{137}Ba**

Isomers and high-spin structures in the $N = 81$ isotones ^{135}Xe and ^{137}Ba

A. Vogt,^{1,*} B. Birkenbach,¹ P. Reiter,¹ A. Blazhev,¹ M. Siciliano,^{2,3} K. Hadyńska-Kłęk,³ J. J. Valiente-Dobón,³ C. Wheldon,⁴ E. Teruya,⁵ N. Yoshinaga,⁵ K. Arnsward,¹ D. Bazzacco,⁶ M. Bowry,⁷ A. Bracco,⁸ B. Bruyneel,⁹ R. S. Chakrawarthy,¹⁰ R. Chapman,¹¹ D. Cline,¹² L. Corradi,³ F. C. L. Crespi,⁸ M. Cromaz,¹³ G. de Angelis,³ J. Eberth,¹ P. Fallon,¹³ E. Farnea,^{6,†} E. Fioretto,³ S. J. Freeman,¹⁰ B. Fu,¹ A. Gadea,¹⁴ K. Geibel,¹ W. Gelletly,⁷ A. Gengelbach,¹⁵ A. Giaz,⁸ A. Görgen,^{16,17,13} A. Gottardo,³ A. B. Hayes,¹² H. Hess,¹ R. Hirsch,¹ H. Hua,¹² P. R. John,^{2,6} J. Jolie,¹ A. Jungclaus,¹⁸ L. Kaya,¹ W. Korten,¹⁷ I. Y. Lee,¹³ S. Leoni,⁸ L. Lewandowski,¹ X. Liang,¹¹ S. Lunardi,^{2,6} A. O. Macchiavelli,¹³ R. Menegazzo,⁶ D. Mengoni,^{19,2,6} C. Michelagnoli,^{2,6,‡} T. Mijatović,²⁰ G. Montagnoli,^{2,6} D. Montanari,^{2,6,§} C. Müller-Gattermann,¹ D. Napoli,³ C. J. Pearson,^{7,||} L. Pellegri,⁸ Zs. Podolyák,⁷ G. Pollarolo,²¹ A. Pullia,⁸ M. Queiser,¹ F. Radeck,¹ F. Recchia,^{2,6} P. H. Regan,^{7,22} D. Rosiak,¹ N. Saed-Samii,¹ E. Şahin,^{3,¶} F. Scarlassara,^{2,6} D. Schneiders,¹ M. Seidlitz,¹ B. Siebeck,¹ G. Sletten,²³ J. F. Smith,¹¹ P.-A. Söderström,^{15,#} A. M. Stefanini,³ T. Steinbach,¹ O. Stezowski,²⁴ S. Szilner,²⁰ B. Szpak,²⁵ R. Teng,¹² C. Ur,⁶ V. Vandone,⁸ D. D. Warner,^{26,†} A. Wiens,¹ C. Y. Wu,^{12,**} and K. O. Zell¹

¹*Institut für Kernphysik, Universität zu Köln, D-50937 Köln, Germany*

²*Dipartimento di Fisica e Astronomia, Università di Padova, I-35131 Padova, Italy*

³*Istituto Nazionale di Fisica Nucleare, Laboratori Nazionali di Legnaro, I-35020 Legnaro, Italy*

⁴*School of Physics and Astronomy, University of Birmingham, Birmingham B15 2TT, United Kingdom*

⁵*Department of Physics, Saitama University, Saitama City 338-8570, Japan*

⁶*Istituto Nazionale di Fisica Nucleare, Sezione di Padova, I-35131 Padova, Italy*

⁷*Department of Physics, University of Surrey, Guildford, Surrey GU2 7XH, United Kingdom*

⁸*Dipartimento di Fisica, Università di Milano and INFN Sezione di Milano, I-20133 Milano, Italy*

⁹*CEA Saclay, Service de Physique Nucleaire, F-91191 Gif-sur-Yvette, France*

¹⁰*Department of Physics and Astronomy, Schuster Laboratory, University of Manchester, Manchester M13 9PL, United Kingdom*

¹¹*SUPA, School of Engineering and Computing, University of the West of Scotland, Paisley PA1 2BE, United Kingdom*

¹²*Department of Physics, University of Rochester, Rochester, New York 14627, USA*

¹³*Lawrence Berkeley National Laboratory, Berkeley, California 94720, USA*

¹⁴*Instituto de Física Corpuscular, CSIC-Universidad de Valencia, E-46071 Valencia, Spain*

¹⁵*Department of Physics and Astronomy, Uppsala University, SE-75121 Uppsala, Sweden*

¹⁶*Department of Physics, University of Oslo, P.O. Box 1048 Blindern, N-0316 Oslo, Norway*

¹⁷*Institut de Recherche sur les lois Fondamentales de l'Univers - IRFU, CEA, Université Paris-Saclay, F-91191 Gif-sur-Yvette Cedex, France*

¹⁸*Instituto de Estructura de la Materia, CSIC, Madrid, E-28006 Madrid, Spain*

¹⁹*Nuclear Physics Research Group, University of the West of Scotland, High Street, Paisley PA1 2BE, Scotland, United Kingdom*

²⁰*Ruđer Bošković Institute, HR-10 002 Zagreb, Croatia*

²¹*Dipartimento di Fisica Teorica dell'Università di Torino and INFN, I-10125 Torino, Italy*

²²*Radioactivity Group, National Physical Laboratory, Teddington, Middlesex, TW11 0LW, United Kingdom*

²³*The Niels Bohr Institute, University of Copenhagen, Blegdamsvej 17, 2100 Copenhagen, Denmark*

²⁴*Université de Lyon, Université Lyon-1, CNRS/IN2P3, UMR5822, IPNL, F-69622 Villeurbanne Cedex, France*

²⁵*Henryk Niewodniczański Institute of Nuclear Physics PAN, PL-31342 Kraków, Poland*

²⁶*CCLRC Daresbury Laboratory, Warrington WA4 4AD, United Kingdom*

(Received 22 December 2016; published 15 February 2017)

The high-spin structures and isomers of the $N = 81$ isotones ^{135}Xe and ^{137}Ba are investigated after multinucleon-transfer (MNT) and fusion-evaporation reactions. Both nuclei are populated (i) in $^{136}\text{Xe} + ^{238}\text{U}$ and (ii) $^{136}\text{Xe} + ^{208}\text{Pb}$ MNT reactions employing the high-resolution Advanced Gamma Tracking Array (AGATA) coupled to the magnetic spectrometer PRISMA, (iii) in the $^{136}\text{Xe} + ^{198}\text{Pt}$ MNT reaction employing the γ -ray array GAMMASPHERE in combination with the gas-detector array CHICO, and (iv) via a $^{11}\text{B} + ^{130}\text{Te}$ fusion-evaporation reaction with the HORUS γ -ray array at the University of Cologne. The high-spin level schemes

*Corresponding author: andreas.vogt@ikp.uni-koeln.de

†Deceased.

‡Institut Laue-Langevin (ILL), 38042 Grenoble Cedex 9, France.

§USIAS – Université de Strasbourg, IPHC-CNRS, F-67037 Strasbourg Cedex 2, France.

||TRIUMF, 4004 Wesbrook Mall, Vancouver, British Columbia, V6T 2A3 Canada.

¶Department of Physics, University of Oslo, P.O. Box 1048 Blindern, N-0316 Oslo, Norway.

#RIKEN Nishina Center, Wako, 351-0198 Saitama, Japan.

**Lawrence Livermore National Laboratory, Livermore, California 94551, USA.

of ^{135}Xe and ^{137}Ba are considerably extended to higher energies. The 2058-keV ($19/2^-$) state in ^{135}Xe is identified as an isomer, closing a gap in the systematics along the $N = 81$ isotones. Its half-life is measured to be 9.0(9) ns, corresponding to a reduced transition probability of $B(E2, 19/2^- \rightarrow 15/2^-) = 0.52(6)$ W.u. The experimentally deduced reduced transition probabilities of the isomeric states are compared to shell-model predictions. Latest shell-model calculations reproduce the experimental findings generally well and provide guidance to the interpretation of the new levels.

DOI: 10.1103/PhysRevC.95.024316

I. INTRODUCTION

The nuclear structure of high-spin states in the vicinity of the $N = 82$ magic number is a benchmark for nuclear shell-model (SM) calculations based on modern effective interactions in the region above the doubly magic nucleus ^{132}Sn . $N = 81$ nuclei with one neutron hole with respect to the closed neutron shell offer an especially fertile study ground for the ingredients of nucleon-nucleon effective interactions and nucleon-nucleon correlations in the shell-model framework. The $N = 81$ chain is accessible by advanced large-scale shell-model calculations. Several effective interactions have been developed recently [1–5], heading toward a unified description of the $50 \leq N, Z \leq 82$ region. Particularly, neutron-neutron and proton-proton correlations up to highest spins were thoroughly investigated along the semimagic $Z = 50$ isotopes [6,7] as well as the semimagic $N = 82$ [8,9] isotones. However, the evolution of the proton-neutron force remains an ongoing subject of discussion in this region. Tests of all components of effective interactions, including the proton-neutron correlations as a function of isospin and spin, have to be performed, either in nuclei having several neutron holes in the presence of a few proton particles, or vice versa with few neutron holes and a larger number of protons. Comprehensive studies were carried out, for example, along the Te isotopes [10–12].

This work focuses on the $N = 81$ isotones ^{135}Xe and ^{137}Ba with one neutron hole, and four and six valence protons outside the $Z = 50$ closed shell, respectively. Detailed data on the low-spin states in ^{135}Xe were obtained in β -decay studies of ^{135}I [13,14]. The $11/2^-$ neutron-hole isomer at 526.551(13) keV with a half-life of 15.29(5) min [15] has been known since the 1940s [16,17]. First results on the high-spin structure were obtained by Fotiadis *et al.* [18] in 2007, who measured ^{135}Xe as a fusion-fission fragment from the ^{226}Th compound nucleus via triple- γ coincidences using the GAMMASPHERE array at Lawrence Berkeley National Laboratory (LBNL). The level scheme was extended up to 3.17 MeV in energy. Tentative spin-parity assignments were given up to the 2058-keV level. High-spin isomers were not subjects of the experiment.

The data on low-spin states of the stable isotope ^{137}Ba originate from earlier work utilizing β decay [19,20], neutron-induced reactions [21], and Coulomb excitation [22]. The spins and parities of the ground state and the $11/2^-$ isomer at 661.659(3) keV with a half-life of 2.552(1) min are well established [23]; the 661.657(3)-keV $M4$ γ -ray transition is even one of the best-known energy calibration standards in nuclear physics. The decay of this $\nu h_{11/2}^{-1}$ state attracted renewed attention with the recent observation of both a competitive $E5$ decay [24] and double- γ decay [25]. A pioneering

work on medium-spin states was performed by Kerek *et al.* in 1973 [26]. The authors irradiated a ^{136}Xe -enriched gas target with 20–29 MeV α particles to populate ^{137}Ba . Excited states were observed up to excitation energies of approx. 3 MeV, among them the $T_{1/2} = 590(10)$ ns isomeric state at 2349.1 keV with possible spin assignments $J^\pi = (15/2, 17/2, 19/2)$. This state was found to decay via a cascade of 120.2- and 1567.3-keV γ rays, finally populating the long-lived $11/2^-$ isomer. A 274.7-keV γ -ray decay was observed to connect another higher-lying nonisomeric 2623.8-keV state with the 2349.1-keV isomeric state. The half-life of this 2623.8-keV state was constrained to be smaller than 70 ps.

Low-lying $J^\pi = 11/2^-$ yrast-trap isomers are a common and unifying feature of even-odd nuclei along the $N = 81$ isotone chain ranging from ^{131}Sn up to ^{151}Yb . These states correspond to one-neutron hole in the $h_{11/2}$ orbital and decay predominantly via $M4$ γ -ray transitions to the positive-parity $d_{3/2}$ ground states or the first excited $3/2^+$ states [35,36]. Another characteristic nuclear-structure feature along the lower-mass $N = 81$ isotones are shorter-lived high-spin isomers above the $11/2^-$ states. A compilation of several partial level schemes is shown in Fig. 1. Besides the aforementioned $J = (15/2, 17/2, 19/2)$ 0.6- μs isomer at 2.349 MeV in ^{137}Ba , high-spin isomers were also found in ^{133}Te and ^{139}Ce . The level scheme of ^{133}Te was extended up to 6.2 MeV with tentative spin assignments up to $J^\pi = (31/2^-)$ [30]. A $J^\pi = (19/2^-)$ state at 1.610 MeV was found to be isomeric with an adopted half-life of $T_{1/2} = 100(5)$ ns [37]. The level scheme of ^{139}Ce is known up to 8.0 MeV in excitation energy and $43/2^-$ in spin [31,38]. The half-life of the first $J^\pi = 19/2^-$ state at 2.632 MeV was observed to be $T_{1/2} = 70(5)$ ns [39]. A $[\nu h_{11/2}^{-1} \otimes 4^+; ^{140}\text{Ce}]$ configuration was assigned via g -factor measurements [40]. The most elaborate nuclear structure information along the $N = 81$ isotone chain is available for ^{141}Nd . Recently, the level scheme was extended up to an excitation energy of 18.9 MeV and spin $(81/2)\hbar$ [32,41]. Several dipole and quadrupole bands above 4.4 MeV were discovered. The dipole bands were interpreted as magnetic rotational bands, with transition probabilities that show the characteristic decrease with angular momentum caused by the shears mechanism. Furthermore, they exhibit a shape evolution from low-deformation triaxial to spherical shape. In an earlier ($\alpha, 5n\gamma$) experiment, delayed time distributions were measured for the 349-keV $17/2^- \rightarrow 15/2^-$ and the 1781-keV $15/2^- \rightarrow 11/2^-$ transitions depopulating the 2886-keV level. An isomeric state with $T_{1/2} = 26(5)$ ns was deduced to be located at an energy of $2886 + x$ keV [33]. However, this isomer was not confirmed by the later studies in Refs. [32,41]. Thus, the typical feature of $J^\pi = 19/2^-$ isomers is first discontinued in ^{141}Nd . In ^{143}Sm (cf. Fig. 1) a $J^\pi = 23/2^{(-)}$

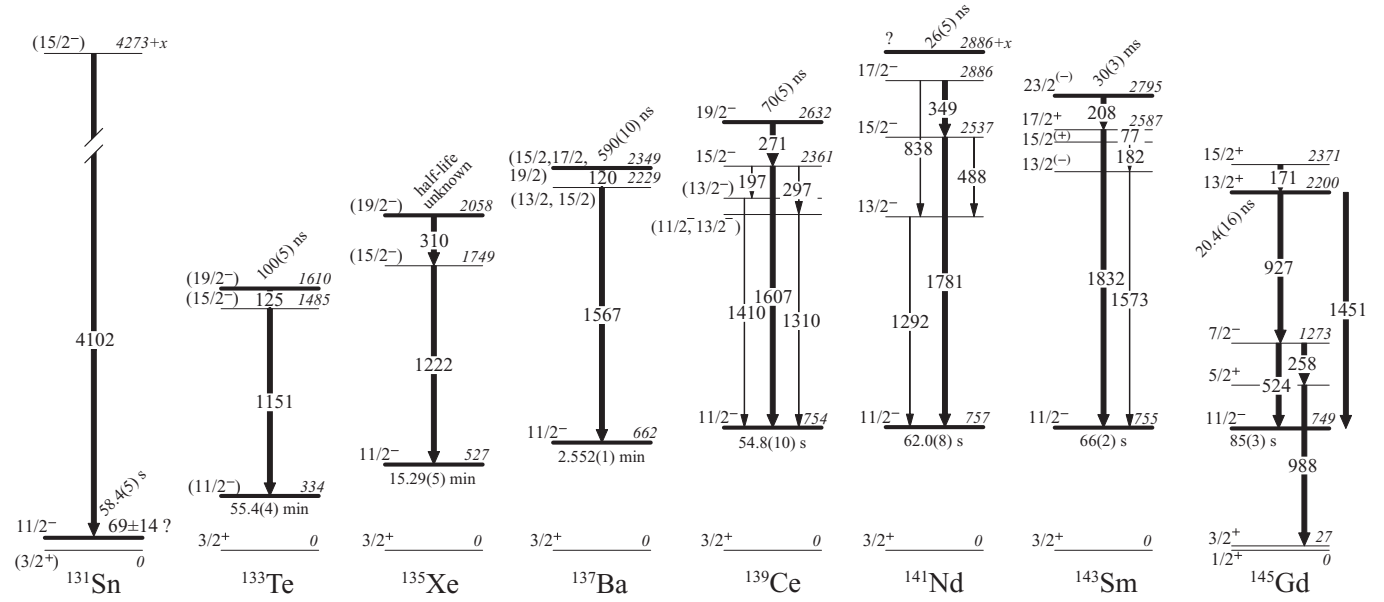


FIG. 1. Comparison of high-spin states and isomer half-lives along the $N = 81$ isotones; data taken from Refs. [18,26–34]. A sequence of $J^\pi = 19/2^-$ isomers is found in the isotones ranging from ^{133}Te to ^{139}Ce . Tentative assignments are written in parentheses.

isomer with a half-life of 30(3) ms is located at 2795 keV [42]. The level scheme is known up to 12 MeV with spin $(57/2)^-$. The 2795-keV isomer is explained as a three-quasiparticle $[\nu h_{11/2}^{-1} \otimes \pi(g_{7/2}^{-1} d_{5/2}^{-1})_6^+]$ configuration [43]. Again, the high-spin structure evolves by adding two more protons with respect to the ^{143}Sm nucleus. In ^{145}Gd , a 2200-keV $13/2^+$ isomer with a half-life of 20.4(16) ns decays predominantly by a strongly collective $E3$ transition to the $7/2^-$ state. The $13/2^+$ state is proposed to be a mixing of the one-phonon $[\nu 1 f_{7/2} \otimes |3^-; ^{146}\text{Gd}]$ and the $\nu 0 i_{13/2}$ configurations [34,42].

A significant piece of experimental information is missing for two nuclei along the presented $N = 81$ isotonic chain, namely ^{135}Xe and ^{137}Ba . The available data concern either low-spin levels observed in single-nucleon transfer reactions or levels with spin values limited by the β^- -decay selection rules. The existing data on the states above the $11/2^-$ isomers in ^{135}Xe and ^{137}Ba are rather scarce and the spin-parity assignments of the known levels are only tentative. The lifetime of the expected $J^\pi = (19/2^-)$ isomer in ^{135}Xe is unknown. The limited experimental data, together with recent theoretical advances, motivate a refined investigation of nuclear-structure features in both nuclei and a test of the predictive power of modern shell-model calculations.

In this article, we report and discuss new results for ^{135}Xe and ^{137}Ba obtained in four different experiments. Two of these experiments were based on direct identification of the nuclei of interest and coincident prompt γ -ray spectroscopy. The combination of the high-resolution position-sensitive Advanced Gamma Tracking Array (AGATA) [44] and the PRISMA magnetic mass spectrometer [45–47] was employed to study the nuclei after $^{136}\text{Xe} + ^{208}\text{Pb}$ multinucleon-transfer (MNT) and $^{136}\text{Xe} + ^{238}\text{U}$ MNT and fission reactions, respectively. Another experiment to study both nuclei of interest was conducted at the GAMMASPHERE+CHICO setup [48,49] at Lawrence Berkeley National Lab (LBNL), using a $^{136}\text{Xe} + ^{198}\text{Pt}$ MNT reaction. In addition, ^{137}Ba was

populated via the fusion-evaporation reaction $^{130}\text{Te}(^{11}\text{B}, p3n)$ employing the High-efficiency Observatory for γ -Ray Unique Spectroscopy (HORUS) [50] at the Institute of Nuclear Physics, University of Cologne.

This paper is organized as follows: the experimental setup and data analysis of the four experiments are described in Sec. II, followed by the experimental results in Sec. III. A detailed comparison with shell-model calculations is presented in Sec. IV before the paper closes with a summary and conclusions.

II. EXPERIMENTAL PROCEDURE AND DATA ANALYSIS

The $^{136}\text{Xe} + ^{238}\text{U}$ and $^{136}\text{Xe} + ^{208}\text{Pb}$ MNT experiments, performed at the Laboratori Nazionali di Legnaro at beam energies of 7.35 and 6.84 MeV/nucleon, respectively, delivered an isotopic identification of the nuclei of interest. Correlations between prompt γ -ray transitions populating isomers and delayed deexciting γ -ray transitions were enabled by the pulsed-beam $^{136}\text{Xe} + ^{198}\text{Pt}$ experiment employing the GAMMASPHERE+CHICO setup at LBNL. Furthermore, ^{137}Ba was populated via the fusion-evaporation reaction $^{130}\text{Te}(^{11}\text{B}, p3n)$ with a beam energy of 54 MeV at the FN Tandem accelerator of the Institute of Nuclear Physics, University of Cologne, providing detailed $\gamma\gamma$ -coincidence data. Details of the four complementary experiments are described below.

A. $^{136}\text{Xe} + ^{238}\text{U}$

The PIAVE+ALPI accelerator complex at the Laboratori Nazionali di Legnaro provided a ^{136}Xe beam with an energy of 1 GeV and a beam current of 2 pA. The beam was used to subsequently bombard two different ^{238}U targets with thicknesses of 1 and 2 mg/cm². A 0.8-mg/cm² Nb backing faced the beam. The light projectile-like reaction fragments were identified

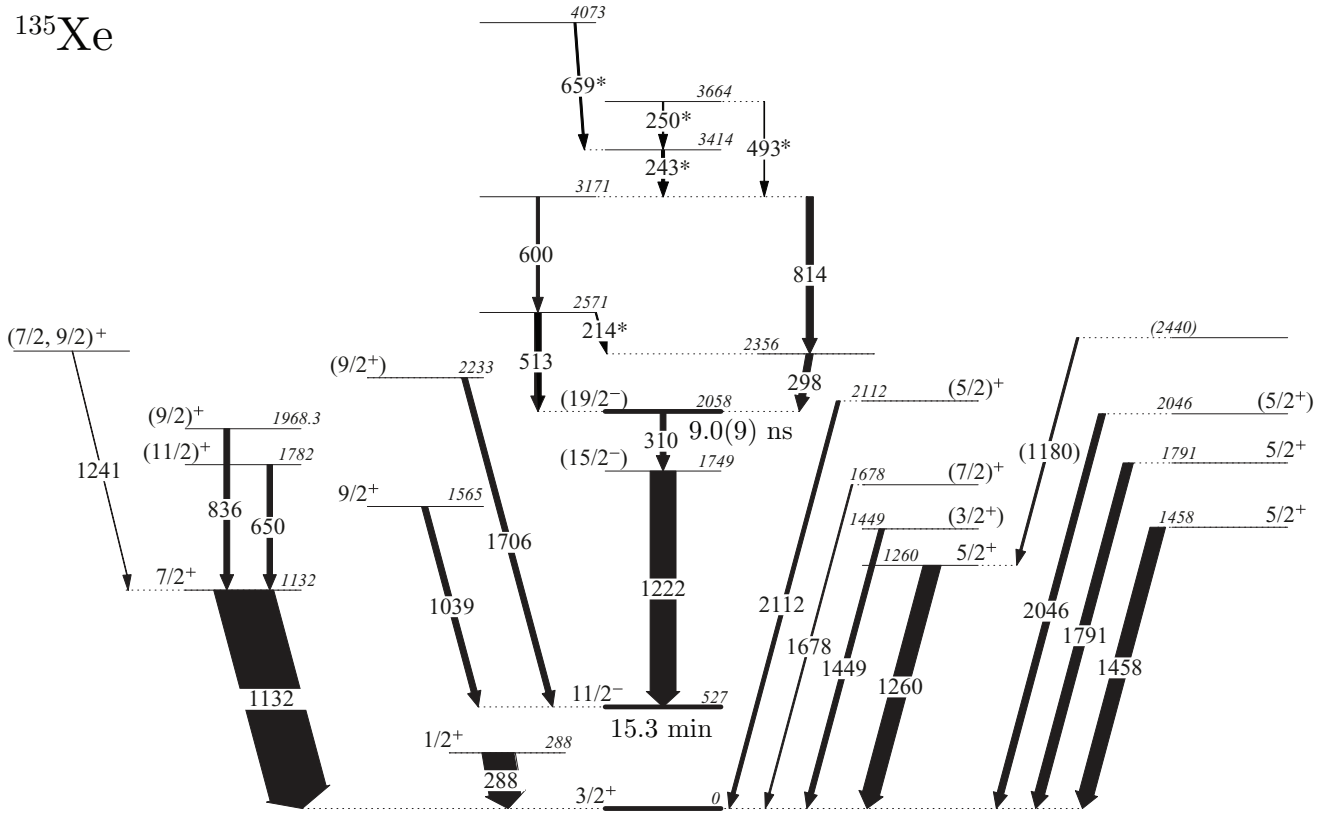


FIG. 2. Level scheme of ^{135}Xe with the newly observed 214-, 243-, 250-, 493-, and 659-keV γ -ray transitions marked with an asterisk. Spins and parities of the states below 2.3 MeV are taken from Refs. [13,15,18]. Intensities are extracted from the $^{136}\text{Xe} + ^{208}\text{Pb}$ experiment and normalized to the 1132-keV γ -ray transition. See text for details.

with the magnetic mass spectrometer PRISMA [45–47] placed at the grazing angle of $\theta_{\text{lab}} = 50^\circ$. Nuclear charge, mass and the velocity vector for the individual lighter reaction products were determined via an event-by-event trajectory reconstruction within the magnetic system. γ rays from excited states in both beam- and target-like nuclei were detected with AGATA [44] in the demonstrator configuration [51] placed 23.5 cm from the target position. The array consisted of 15 large-volume electronically segmented high-purity Ge (HPGe) detectors in five triple cryostats [52]. An event registered by the PRISMA focal-plane detector in coincidence with an AGATA event was taken as a trigger for the data acquisition. Pulse-shape analysis of the digitized detector signals was applied to determine the individual interaction points [53]. This information is used by the Orsay forward-tracking algorithm [54] to reconstruct the individual emitted γ -ray energies, to determine the first interaction point of the γ ray in the germanium and, thus, the emission angle. Combining this information with the kinematic information of PRISMA, a precise Doppler correction for beam- and target-like nuclei was performed. Further details on the analysis are available in Ref. [55].

B. $^{136}\text{Xe} + ^{208}\text{Pb}$

In this experiment, a ^{136}Xe beam from the PIAVE+ALPI accelerator complex at an energy of 930 MeV impinged onto a 1-mg/cm²-thick ^{208}Pb target. PRISMA was placed at the grazing angle of $\theta_{\text{lab}} = 42^\circ$. γ rays were measured by the AGATA

Demonstrator in a configuration of three triple clusters. The further setup, trigger conditions, and the data analysis are similar to those described in Sec. II A. The measurement of the momentum vector of beam-like recoils with PRISMA enabled a reconstruction of the total kinetic energy loss (TKEL) value of the reaction which is defined as the energy transferred to internal degrees of freedom and corresponds to the reaction's Q value with an opposite sign [46,56]. Further details on the analysis can be found in Refs. [57,58].

C. $^{136}\text{Xe} + ^{198}\text{Pt}$

A 850-MeV ^{136}Xe beam provided by the 88-Inch Cyclotron impinged onto a self-supporting 420- $\mu\text{g}/\text{cm}^2$ ^{198}Pt target, isotopically enriched to >92%. γ rays were detected by the GAMMASPHERE array, which in this experiment consisted of 103 Compton-suppressed HPGe detectors [48]. Both polar and azimuthal angles and the time-of-flight difference Δt_{TOF} between the detection of beam-like and target-like reaction products were measured with the gas-filled parallel-plate avalanche detector array CHICO, allowing for an event-by-event Doppler-shift correction for emitted γ rays. The experimental trigger required two CHICO elements and at least three germanium detectors to fire. Further details are given in Ref. [59]. The data from the experiment were sorted into four two-dimensional matrices gated on beam-like fragments: (i) an in-beam Doppler-corrected prompt $\gamma\gamma$ matrix, (ii) an out-of-beam delayed-delayed $\gamma\gamma$ matrix, (iii) a

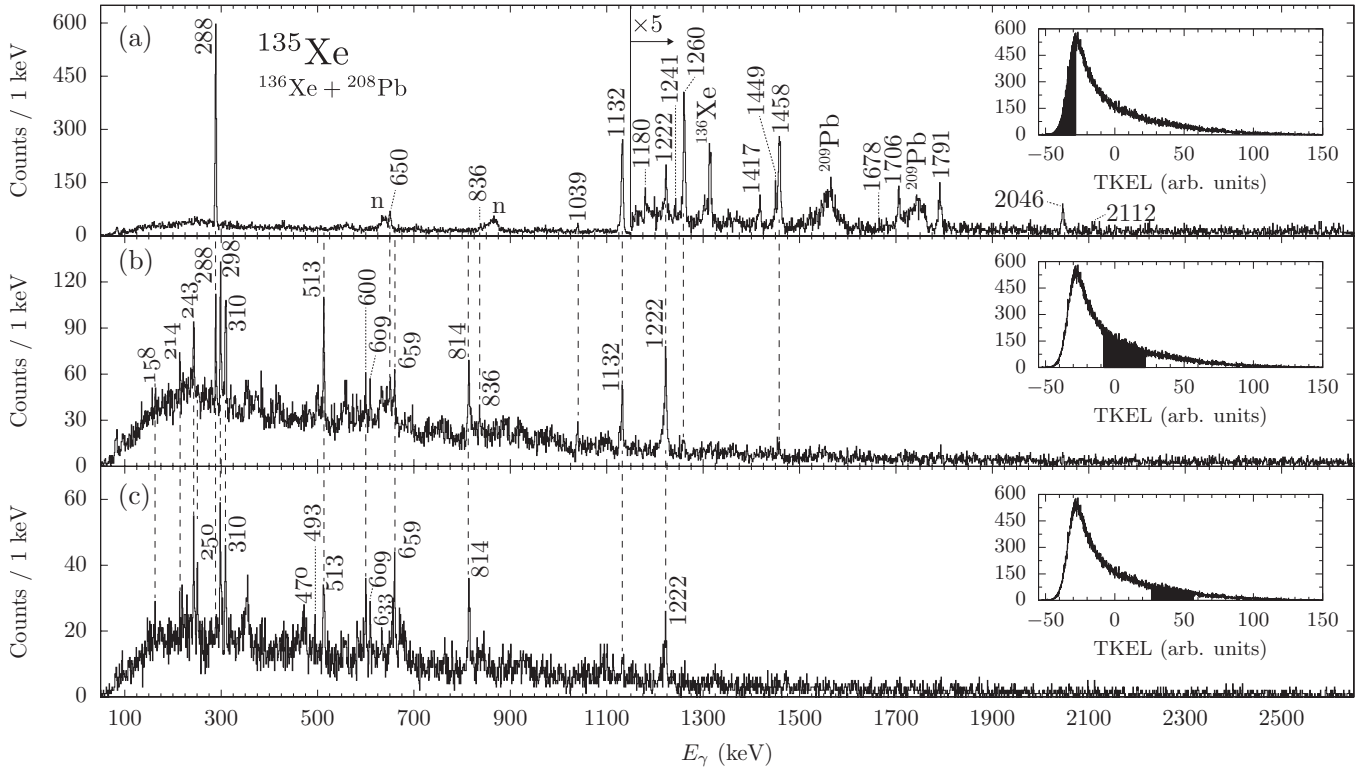


FIG. 3. Doppler-corrected ^{135}Xe γ -ray spectra from the $^{136}\text{Xe} + ^{208}\text{Pb}$ experiment: (a) Gate on low TKEL, (b) gate on intermediate TKEL, and (c) gate on large TKEL corresponding to higher excitation energies after the deep-inelastic MNT reaction. The applied gates on the TKEL distributions are shown in the three insets, respectively. The main peaks of the TKEL distributions are shifted to negative values due to large energy losses in the thick Pb targets. A gate on the prompt time peak between AGATA and PRISMA is applied to all spectra.

delayed-prompt $\gamma\gamma$ matrix, and (iv) a delayed- γ -time matrix for extracting isomeric decay half-lives. The time window for the delayed γ rays was set from 45 to 780 ns. The RADWARE analysis package [60] was used to project and background-subtract the gated spectra.

D. $^{11}\text{B} + ^{130}\text{Te}$

In a fourth experiment, ^{137}Ba was populated via the fusion-evaporation reaction $^{130}\text{Te}(^{11}\text{B}, p3n)^{137}\text{Ba}$, employing a 54 MeV ^{11}B beam delivered by the FN Tandem accelerator of the Institute of Nuclear Physics, University of Cologne. The 99.3% enriched ^{130}Te target with a thickness of 1.8 mg/cm^3 was evaporated onto a 120 mg/cm^3 thick Bi backing plus a 132 mg/cm^3 thick Cu layer for heat dissipation. All residual reaction products are stopped inside the Bi backing. The reaction codes PACE4 [61] and CASCADE [62] predict a relative cross section of approx. 0.8% for the population of the p3n channel at this beam energy. γ rays from excited states were measured employing the HORUS array [50] comprising 14 HPGe detectors, six of them equipped with BGO Compton-suppression shields. The detectors are positioned on the eight corners and six faces of a cube geometry. Evaporated charged particles were detected with a double-sided silicon strip detector mounted at backward direction covering an angular range from 118° to 163° . The count rate of the individual HPGe crystals was maintained around 20 kHz during the experiment. $\gamma\gamma$ coincidences were processed and recorded

utilizing the synchronized 80 MHz XIA Digital Gamma Finder (DGF) data-acquisition system. The data were sorted into various two- and three-dimensional matrices with a time gate of 250 ns using the SOCO-V2 code [63]. In total, 1.5×10^{10} $\gamma\gamma$ and 8.0×10^9 $\gamma\gamma\gamma$ coincidence events were collected. The analysis was performed with the program TV [64].

III. RESULTS

A. ^{135}Xe

The level scheme of ^{135}Xe deduced in the present work is presented in Fig. 2. Ejectile Doppler-corrected singles γ -ray spectra of ^{135}Xe produced in the $^{136}\text{Xe} + ^{208}\text{Pb}$ experiment are shown in Fig. 3 with gates on (a) low, (b) intermediate, and (c) large total kinetic energy losses (TKEL). The applied gates on the TKEL distributions are shown in the three insets and are marked in black. Gates on the TKEL distributions restrict the total excitation energy of the reaction system. In particular, events with small TKEL values are related to reaction products with a lower excitation energy. Thus, by correlating the TKEL distributions with coincident γ rays of AGATA, γ -ray transitions between states with different excitation energies and angular momenta can be suppressed or enhanced [46,65]. ^{135}Xe is produced by a one-neutron stripping reaction; therefore, a multitude of low-lying excited states with spins $J < 11/2\hbar$ are populated with a gate on low TKEL, cf. Figs. 3(a) and 2. In contrast, γ -ray spectra with gates on larger TKEL show prominent γ rays with energies of

TABLE I. Energies, assignments and relative in-beam intensities for transitions observed in ^{135}Xe above the $11/2^-$ isomer. Fitted energies and intensities normalized to the 1222-keV transition are taken from the $^{136}\text{Xe} + ^{208}\text{Pb}$ AGATA experiment.

E_γ (keV)	E_i (keV)	E_f (keV)	I_i^π	I_f^π	I_γ
158					weak
214	2571	2356			5(2)
243	3414	3171			12(2)
250	3664	3414			6(2)
298	2356	2058		(19/2 ⁻)	26(2)
310	2058	1749	(19/2 ⁻)	(15/2 ⁻)	22(2)
470					weak
493	3664	3171			weak
513	2571	2058		(19/2 ⁻)	24(2)
600	3171	2571			12(3)
609					9(2)
633					weak
659	4073	3414			3(1)
814	3171	2356			28(3)
1222	1749	527	(15/2 ⁻)	11/2 ⁻	$\equiv 100$

298, 310, 513, 600, 814, and 1222 keV that were reported by Fotiadis *et al.* [18] to be transitions depopulating medium-spin states above the $11/2^-$ isomer. New γ rays identified in the present work with energies of 158, 214, 243, 250, 470, 493, 609, 633, and 659 keV are labeled in italic characters in Fig. 3 and summarized in Table I. Intensities are taken from the $^{136}\text{Xe} + ^{208}\text{Pb}$ experiment. Various GAMMASPHERE prompt $\gamma\gamma$ -coincidence spectra are shown in Figs. 4(a) to 4(g). Coincidences are marked with arrows. Some spectra are over-subtracted due to considerable nonuniform background contributions by falsely Doppler-corrected target excitations.

The placement of the 298-, 513-, 600-, and 814-keV transitions by Fotiadis *et al.* is verified; the 298–814- and 513–600-keV cascades are mutually coincident. Their placement above the 2058-keV state is also consistent with the TKEL-gated AGATA spectra: The 1222-keV line is already visible for low TKEL in Fig. 3(a), while the 310-keV and the four aforementioned transitions first appear for intermediate TKEL values. The 214-keV γ ray fits the energy difference of the 2571- and 2356-keV state and emerges in the intermediate-TKEL gated spectrum in Fig. 3(b). Furthermore, it is mutually coincident with the 298-keV transition as shown in Figs. 4(a) and 4(g). Consequently, the transition is placed between the two states. The 243-keV γ -ray transition first appears in Fig. 3(b) with a gate on intermediate TKEL; the 250- and 493-keV γ -ray transitions are only visible in panel (c) with gates on large TKEL. Moreover, the 243-keV γ ray is coincident with all major transitions between the 2058- and 3171-keV levels and placed on top of the 3171-keV level. In accordance with the intensity balance, the 250-keV γ ray, which is coincident with the 243-keV γ ray, is placed directly on top. The 493-keV γ ray corresponds to the sum energy of the two aforementioned transitions and is not coincident with either the 243- or the 250-keV transitions. Additionally, Fig. 4(f) shows that the 659-keV transition is coincident with the lines at 243, 298, and 814 keV. The transition is placed

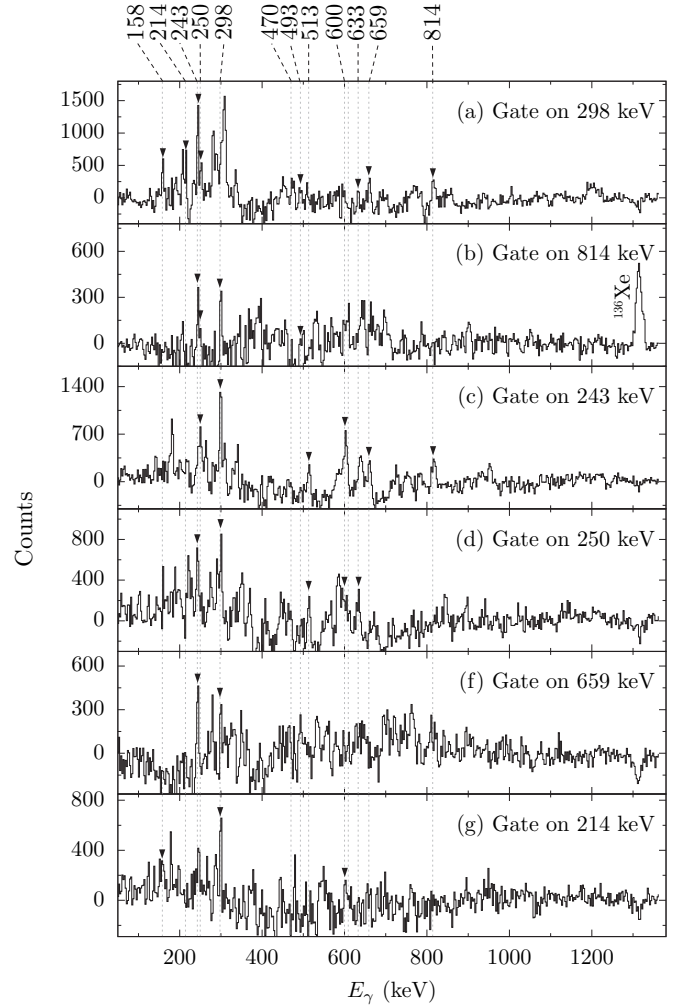


FIG. 4. GAMMASPHERE prompt $\gamma\gamma$ -coincidence spectra with gates on (a) 298, (b) 814, (c) 243, (d) 250, (e) 659, and (f) 214 keV. Coincidences are labeled by arrow heads. Vertical lines corresponding to peak energies observed in ^{135}Xe are drawn to guide the eye.

parallel to the 250-keV transition. No conclusive coincidences and placements are found for the 158-, 470-, 609-, and 633-keV γ rays.

The systematics along the $N = 81$ isotones ranging from ^{133}Te to ^{139}Ce suggests the $J^\pi = (19/2^-)$ state at 2058 keV to be of isomeric character (cf. Fig. 1 in Sec. I). Figures 5(a) and 5(b) show the GAMMASPHERE delayed out-of-beam γ -ray spectra gated by 310 and 1222 keV. Both delayed transitions are mutually coincident with low peak intensities. However, both 310- and 1222-keV transitions depopulating the 2058 keV level are also clearly observed in the prompt AGATA γ -ray spectra. Thus, the lifetime of the 2058-keV state has to be of the order of the width of the prompt peak in the time-difference spectrum between PRISMA and AGATA, i.e. $\Delta t_{\text{PRISMA-AGATA}} \approx 16$ ns. The precise lifetime is determined using the GAMMASPHERE γ -time matrix. The 1222-keV peak is contaminated by the delayed 1220.1-keV $11/2^- \rightarrow 7/2_{\text{g.s.}}^-$ transition which is part of the depopulating γ -ray cascade of the $19/2^-$ isomer with $T_{1/2} = 10.1(9)$ ns in ^{137}Xe [23]. Nonetheless, the peak at 310 keV has an expected

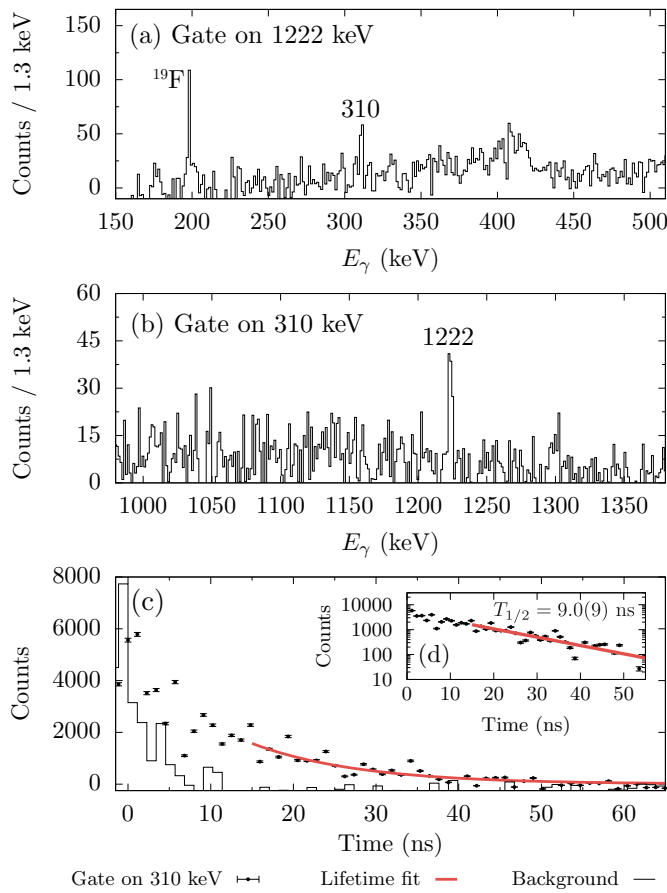


FIG. 5. (a) GAMMASPHERE delayed out-of-beam γ -ray spectrum gated by the delayed 1222-keV transition in ^{135}Xe . (b) Same spectrum as in (a), gated on the 310-keV transition. (c) Linear GAMMASPHERE time spectrum gated by the 310-keV transition (black data points) with an exponential decay-curve fit (red solid line). A background prompt time spectrum is plotted with solid steps. (d) Same as (c), but with a logarithmic scale. The fitted half-life is $T_{1/2} = 9.0(9)$ ns.

FWHM of 1.5 keV and shows no sign of contamination. The corresponding background-subtracted time projection (black points) and the fitted decay curve (solid line) are shown in Fig. 5(c). A time spectrum of a nearby background region around 307 keV is plotted with solid steps. Any residual background of the prompt peak in the time spectrum is negligible for the decay-curve fit. The fit function of the time spectrum $N(t)$ is chosen as $N(t) = a \exp[t \ln(2)/T_{1/2}] + b$. The background parameter b is fitted between 200 and 780 ns and held constant in the decay-curve fit. The fitted half-life is 9.0(9) ns for the 2058-keV state.

B. ^{137}Ba

The level scheme of ^{137}Ba deduced in this work is presented in Fig. 6. Corresponding γ -ray transitions are summarized in Table II. The intermediate-spin region below the long-lived $(19/2^-)$ isomer is accessible by utilizing delayed-delayed as well as delayed-prompt coincidences from the GAMMASPHERE+CHICO dataset. Figure 7(a) presents the

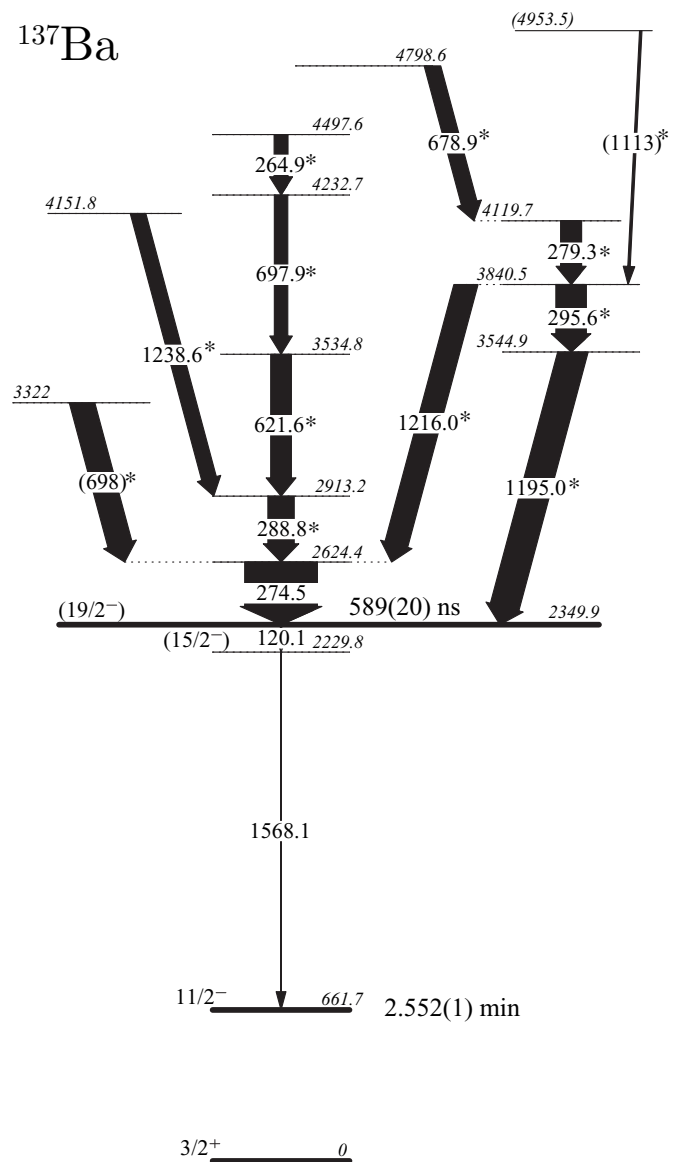


FIG. 6. Level scheme assigned to ^{137}Ba in the present work. Transition and excitation energies are given in keV. The decay of the $11/2^-$ isomer is not observed due to its long half-life. γ -ray intensities of transitions above the 2349.9-keV isomer are deduced from the $^{11}\text{B} + ^{130}\text{Te}$ experiment and normalized to the 274.5-keV transition. Isomeric states are marked with thick lines and labeled with the corresponding half-lives. Spins and parities of the states below 2.35 MeV follow the systematics of the $N = 81$ isotonic chain. New γ -ray transitions are marked with an asterisk. See text for details.

delayed γ -ray spectrum with a gate on the delayed 120-keV transition. The spectrum shows the expected prominent peak at 1568 keV. Some contaminant peaks are caused by the nearby delayed 121-keV $(10^+) \rightarrow (8^+)$ transition in ^{134}Ba [66]. The gate on the 1568-keV γ -ray transition, which directly feeds the $11/2^-$ isomer, shows a distinct peak at 120 keV in Fig. 7(b). Intense peaks at 110 and 197 keV in the spectra originate from the γ -ray decay of long-lived excited states which were populated in $^{19}\text{F}(n, n'\gamma)$ reactions of neutrons evaporated after MNT with fluorine present in Teflon[®] tapes

TABLE II. Energies, assignments and relative in-beam intensities for transitions observed in ^{137}Ba above the $11/2^-$ isomer. Fitted energies and intensities normalized to the 274.5-keV transition are taken from the $^{11}\text{B} + ^{130}\text{Te}$ HORUS experiment. The uncertainties in the transition energies are ± 0.5 keV. Possible spin/parity assignments are discussed in Sec. IV.

E_γ (keV)	E_i (keV)	E_f (keV)	I_i^π	I_f^π	I_γ
120.1	2349.9	2229.8	(19/2 ⁻)	(15/2 ⁻)	
245		≥ 3840.5			10(3)
264.9	4497.6	4232.7			19(2)
274.5	2624.4	2349.9	(21/2 ⁻)	(19/2 ⁻)	$\equiv 100$
279.6	4119.7	3840.5			29(3)
288.8	2913.2	2624.4			38(7)
295.6	3840.5	3544.9			43(7)
621.6	3534.8	2913.2			30(3)
678.9	4798.6	4119.7			23(4)
697.9	4232.7	3534.8			20(5)
780		≥ 3840.5			10(4)
1113	(4953.5)	(3840.5)			4(2)
1195.0	3544.9	2349.9		(19/2 ⁻)	43(8)
1216.0	3840.5	2624.4			34(3)
1238.6	4151.8	2913.2			22(6)
1568.2	2229.8	661.7	(15/2 ⁻)	11/2 ⁻	

within the HPGe detector configuration. As no significant contamination of other delayed γ rays is present in the 1568-keV gated spectrum, the γ -time matrix is exploited for this transition. The inset in Fig. 7(b), marked as 7(c), shows the corresponding decay curve obtained by a gate on the delayed 1568-keV transition. Fits are performed for six different time windows between 100 ns and 700 ns. The half-life of the 2349.9-keV excited state is determined to be 589(20) ns using the weighted arithmetic mean of the individual fits. It is in good agreement with the previously measured value of 590(10) ns [26]. No evidence is found for further few-ns lifetimes above the 2349.9-keV state.

A gate on the GAMMASPHERE delayed 1568-keV transition is applied to generate the prompt γ -ray spectrum shown in Fig. 7(d) that contains the transitions feeding the 2349.9-keV isomer. A series of densely located peaks stands out around the dominating 275-keV peak which was already reported by Kerek *et al.* [26]. Fifteen of the 23 transition candidates visible in the delayed-prompt γ -ray spectrum are also present in the ejectile Doppler-corrected singles γ -ray spectrum of the $^{136}\text{Xe} + ^{238}\text{U}$ AGATA experiment in Fig. 8(a). The improved energy resolution of the AGATA array allows a clear separation of the closely lying lines of the GAMMASPHERE data set. The spectrum is corrected for remaining contaminations of the nearby isobar ^{137}Cs [8] by subtracting the corresponding normalized mass-gated γ -ray spectrum. A smoothed background spectrum including Compton steps is modeled and subsequently subtracted. The corresponding PRISMA mass spectrum along the Ba isotopes is depicted in the inset (b). Random background is significantly suppressed by gating on the prompt time-difference peak between AGATA and PRISMA. In total, the γ -ray spectrum features 24 peaks; 23 of them were previously unknown. The excitation pattern of ^{137}Ba is differ-

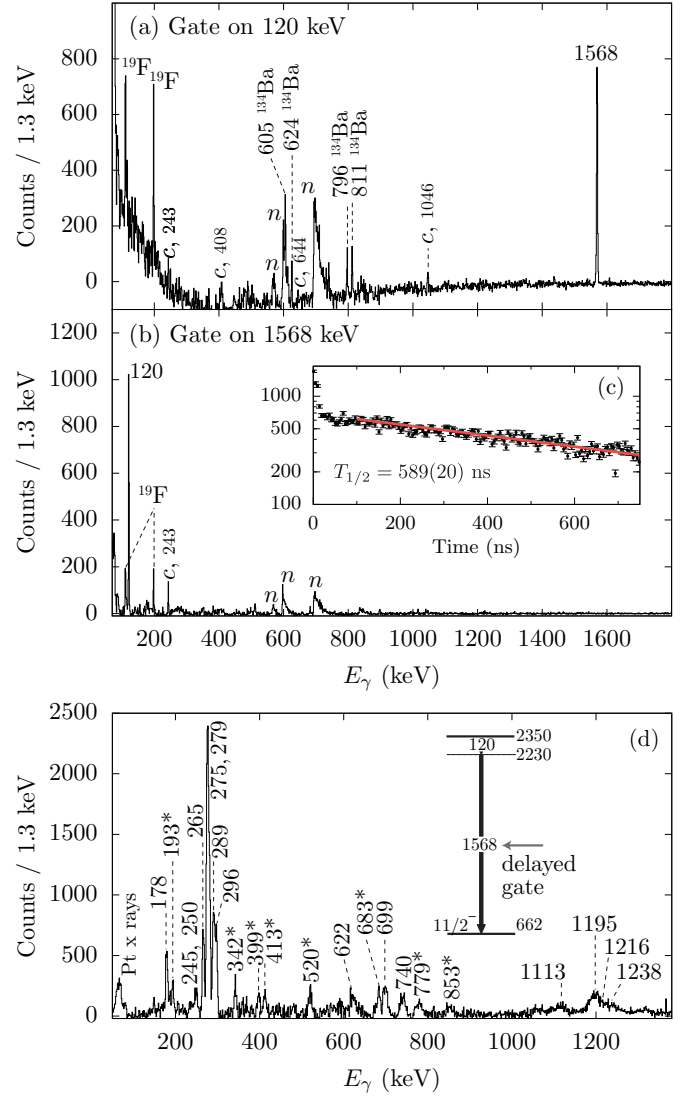


FIG. 7. (a) GAMMASPHERE delayed out-of-beam γ -ray spectrum gated by the delayed 120-keV transition in ^{137}Ba . Contaminants from ^{134}Ba are labeled in the spectrum. Contaminants are marked with c; Ge($n, n'\gamma$) edges with n. (b) Same spectrum as in (a), gated on the 1568-keV transition; no major contaminants are visible. (c) Time spectrum gated by the 1568-keV transition (data points) from which the decay curve (solid line) is obtained with a half-life of $T_{1/2} = 589(20)$ ns. (d) GAMMASPHERE delayed-prompt $\gamma\gamma$ -coincidence spectrum with a gate on the delayed 1568-keV transition (partial level scheme shown in the inset). The spectrum contains prompt transitions feeding the 2349.9-keV isomer.

ent compared to that of ^{135}Xe as more nucleons are transferred. None of the known low-spin positive-parity excited states [23] are observed. Therefore, all new levels and their transitions have to be placed above the 2349.9-keV isomer.

Both $\gamma\gamma$ -double and $\gamma\gamma\gamma$ -triple coincidences are exploited in the analysis of the Cologne fusion-evaporation experiment. Various HORUS prompt $\gamma\gamma$ -coincidence spectra are shown in Figs. 9(a) to 9(e). Coincidences are marked in the spectra. We note that no mass identification was performed in the LBNL and Cologne experiments. Thus, only transitions

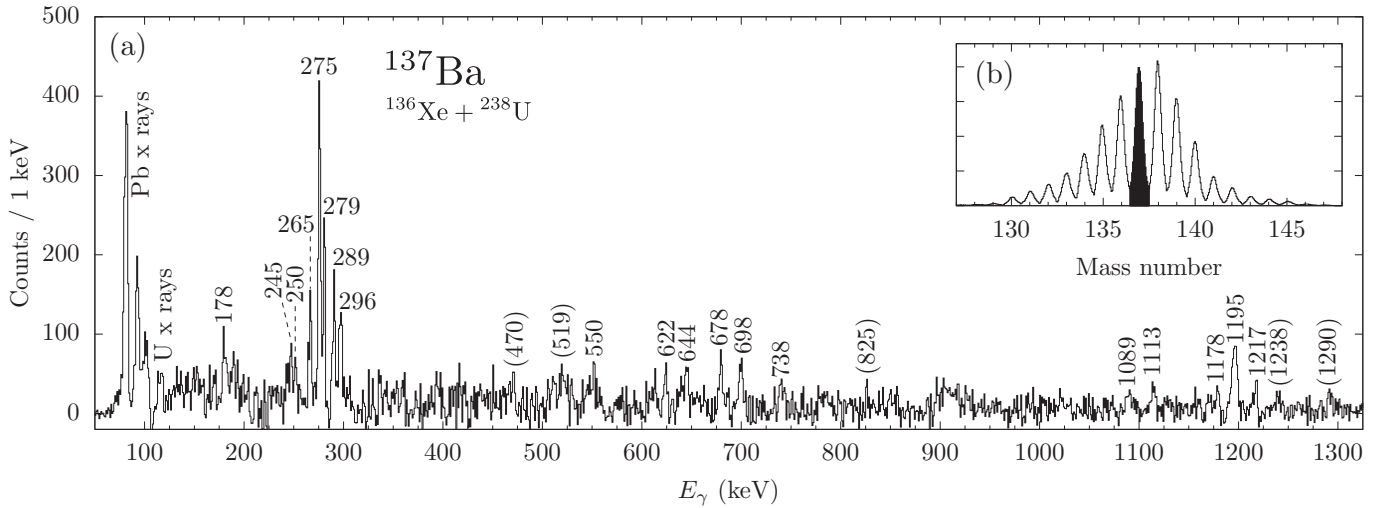


FIG. 8. (a) ^{137}Ba ejectile Doppler-corrected γ -ray spectrum, corrected for contamination of the isobar ^{137}Cs by subtracting the corresponding normalized mass-gated γ -ray spectra. Random background is subtracted with a gate on the prompt peak in the spectrum of time differences between AGATA and PRISMA. Only the 275-keV γ ray was previously known. (b) Mass spectrum of the Ba isotopes obtained with PRISMA. The applied mass gate on ^{137}Ba is marked in black.

identified in the AGATA singles spectrum (see Fig. 8) and the GAMMASPHERE delayed-prompt coincidence spectrum are considered in order to construct the level scheme above the 2349.9 keV isomer. γ -ray energies and intensities, normalized to the intensity of the 274.5-keV γ -ray transition, are listed in Table II.

The 274.5-keV transition is observed to be the most intense one and was already known to directly feed the 2349.9-keV isomer [26]. γ rays with energies of 288.8, 621.6, 698, and 265.9 keV are mutually coincident with the 274.5-keV transition and constitute a cascade feeding the 2624.4-keV state. A 1238.6-keV γ ray is observed to be coincident with

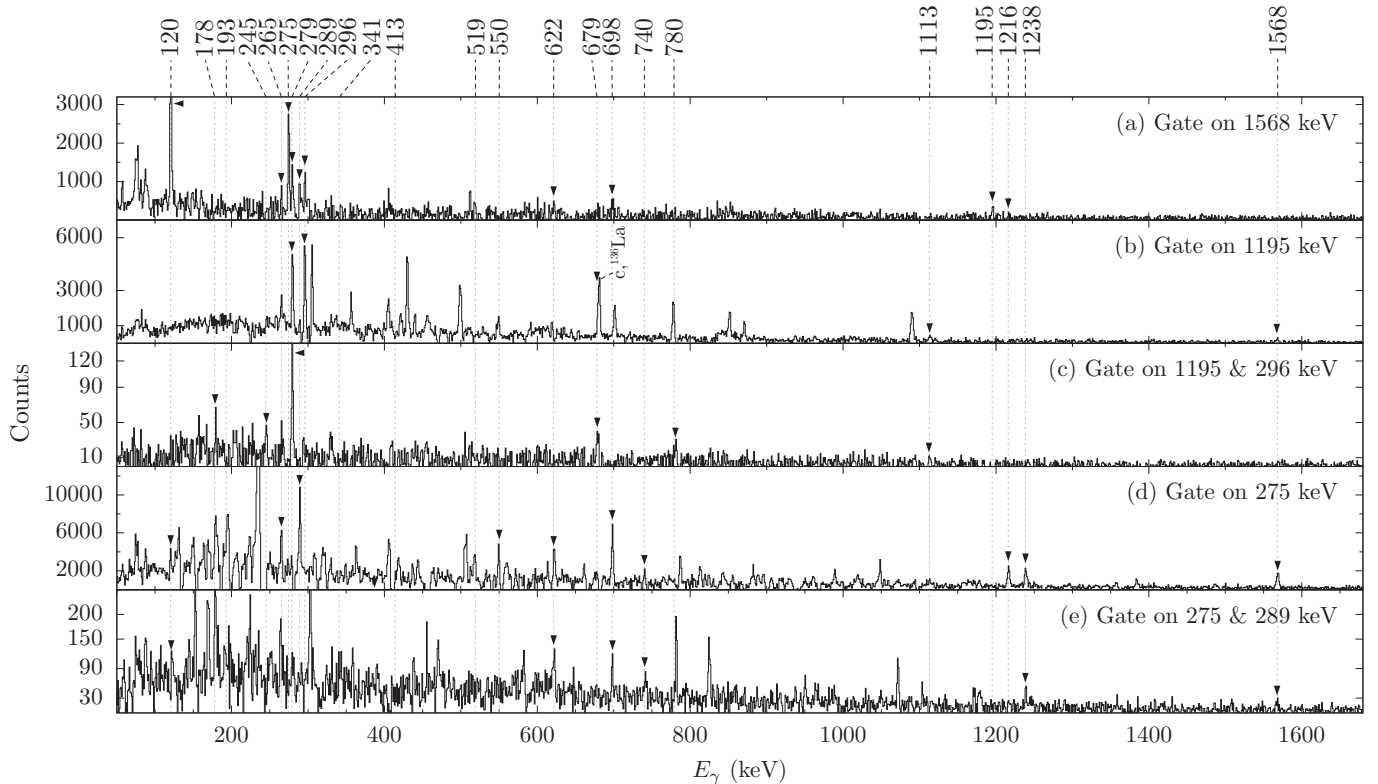


FIG. 9. Prompt HORUS $\gamma\gamma$ double- and $\gamma\gamma\gamma$ triple-coincidence spectra with gates on (a) 1568, (b) 1195, (c) 1195 & 296, (d) 275, (e) 275 & 289 keV. Coincidences are labeled by filled arrow heads. Thin grey lines corresponding to peak energies observed in Figs. 8 and 7(d) are drawn to guide the eye.

the 274.5- and 288.9-keV γ rays, but not with the other transitions of the aforementioned cascade. Hence, the transition has to feed a 2913.2-keV state, decaying by the 288.9-keV transition. The intensity of the 698-keV γ ray in the $\gamma\gamma$ -coincidence spectrum gated on 274.5 keV exceeds the one of the 288.9-keV line. However, the intensity balance in the $\gamma\gamma\gamma$ projection gated on 274.5 and 288.9 keV suggests the 697.9-keV transition to be placed above the 2913.2-keV state. Hence, the line at 698 keV is in fact a doublet, as presented in Fig. 6. The ordering of the 697.9- and 264.9-keV transitions is tentative since the intensities are equal within their uncertainties.

Coincidences with the 1568.1-keV transition [see Fig. 9(a)] as well as the intensity balance require the newly-observed 1195.0-keV transition to be placed parallel to the 274.5-keV transition, directly feeding the isomer. Since the 295.6-, 279.3- and 678.9-keV lines are in mutual coincidence with the 1195.0-keV γ ray [cf. Figs. 9(b) and 9(c)], all three transitions are placed on top of the newly established 3544.9-keV state according to their intensity balance. Peaks at 245 and 780 keV, also observed in the $^{136}\text{Xe} + ^{198}\text{Pt}$ experiment in Fig. 7(d), appear in the $\gamma\gamma\gamma$ spectrum double-gated on 1195 and 296 keV, but cannot be placed unequivocally in the level scheme. A 1216.0-keV γ ray connects the 3840.5- and 2624.4-keV states. This placement is also supported by $\gamma\gamma$ - and $\gamma\gamma\gamma$ coincidences as shown in Figs. 9(d) and 9(e). The 1113-keV transition is tentatively placed above the 3840.5-keV state. The obtained maximum excitation energy is consistent with other populated reaction channels in the present experiments [65]. Two 555.6- and 620.2-keV γ rays that were tentatively assigned by Kerek *et al.* [26] to feed the 2624-keV state are not observed in this work. No conclusive placement is obtained for the other low-intensity transitions.

IV. SHELL-MODEL CALCULATIONS

The extended level scheme and the features of long-lived isomers are compared to results of two different large-scale shell-model calculations for ^{135}Xe and ^{137}Ba . The first calculations were carried out without any truncations for positive- and negative-parity states in the jj55pn model space with the jj55pna Hamiltonian [1] (referred to as the SN100PN interaction) using the code NUSHELLX@MSU [67]. The SN100PN interaction is based on a renormalized G matrix derived from the CD-Bonn nucleon-nucleon interaction [68]; single-particle energies were chosen to reproduce excited states in ^{133}Sb and ^{131}Sn . The model space comprises the full $gdsh$ valence space outside the ^{100}Sn core between the magic numbers 50 and 82, including the $0g_{7/2}$, $1d_{5/2}$, $1d_{3/2}$, $2s_{1/2}$, and $0h_{11/2}$ orbitals for both protons and neutrons. The corresponding single-particle energies for the neutrons are -10.609 , -10.289 , -8.717 , -8.694 , and -8.815 MeV, respectively. Those for the protons are 0.807 , 1.562 , 3.316 , 3.224 , and 3.605 MeV.

An independent extensive theoretical study of nuclei around mass 130 was published by Teruya *et al.* [3]. The results include excited states and electromagnetic transition probabilities for Xe and Ba isotopes within the shell model in the $gdsh$ model space including the $0g_{7/2}$, $1d_{5/2}$, $1d_{3/2}$, $2s_{1/2}$,

and $0h_{11/2}$ orbitals for both protons and neutrons. The interaction [in the following referred to as Pairing+Quadrupole-Quadrupole+Multipole for the mass region 130 (PQM130)] is composed of spherical single-particle energies and phenomenological two-body effective interactions consisting of monopole-pairing, quadrupole-pairing, and quadrupole-quadrupole terms. Further newly introduced higher-order pairing interactions are also taken into account. Single-particle energies (SPEs) were adopted from the experimental excited states of ^{133}Sb (proton SPEs) and ^{131}Sn (neutron SPEs) [3].

The shell-model calculations provide insight into the structure of the isomeric states and the levels built on top. Results of both calculations (middle and right panels) are compared to the experimental levels (left panel) of ^{135}Xe in Fig. 10(a) and to the ones of ^{137}Ba in Fig. 10(b), respectively. The states are separated into columns for the negative- and the positive-parity states. The lowest neutron-hole states with $J^\pi = 3/2^+$, $1/2^+$, and $11/2^-$ are well reproduced by both shell-model calculations for ^{135}Xe as well as for ^{137}Ba . In addition, the excitation energies of the first excited $7/2^+$ and $5/2^+$ states are fairly reproduced by both the PQM130 and the SN100PN interactions; however, the ordering of the states is reversed in both nuclei.

The $(15/2^-)$ and the $(19/2^-)$ states in ^{135}Xe are well reproduced by the SN100PN interaction with deviations to lower energies of only 47 and 86 keV, respectively. The PQM130 interaction predicts both states at slightly higher energies with deviations of 138 and 173 keV. Larger discrepancies between the two calculations emerge in the high-spin regime; e.g., the prediction for the first $25/2^-$ state differs by 0.5 MeV. The 2356-keV state is interpreted as the $21/2^-$ state, as for lower spin values a dominant decay branch to the $15/2^-$ state is expected, which is not observed in this study. Accordingly, the state at 2571 keV has the possible spins $J^\pi = (21/2^-, 23/2^-)$. Positive-parity states with $J > 15/2$ are predicted by both calculations to appear at excitation energies larger than 2.8 MeV. States with spin $25/2^-$ are expected to be located at excitation energies above 3.2 MeV. In comparison with the experimental energy spectrum, neither interaction yields a conclusive assignment of states beyond 2.5 MeV.

The $11/2^-$ and the $(15/2^-)$ states in ^{137}Ba are well reproduced by the PQM130 interaction. In contrast, the SN100PN interaction underestimates the $11/2^-$ level energy by 184 keV. The ordering of the first excited $17/2^-$ and $19/2^-$ levels is predicted differently by the two calculations. The experimental $(19/2^-)$ state is overpredicted by the PQM130 interaction, and underpredicted by the SN100PN interaction, both with an offset of 245 keV. However, the relative positions of the $(15/2^-)$ and $(19/2^-)$ states is better reproduced by the SN100PN interaction. Going to higher spins, the energy differences in the two calculations between states of same spin and parity amount for up to 1 MeV. The 2624.4-keV excited state can most likely be interpreted as the first $21/2^-$ state. Positive-parity states of similar spin are predicted by both calculations to appear only at higher energies; states with spin $J^\pi < 15/2^+$ would also decay into the $15/2^-$ state or the $11/2^-$ isomer. Moreover, the 2913.2-keV state

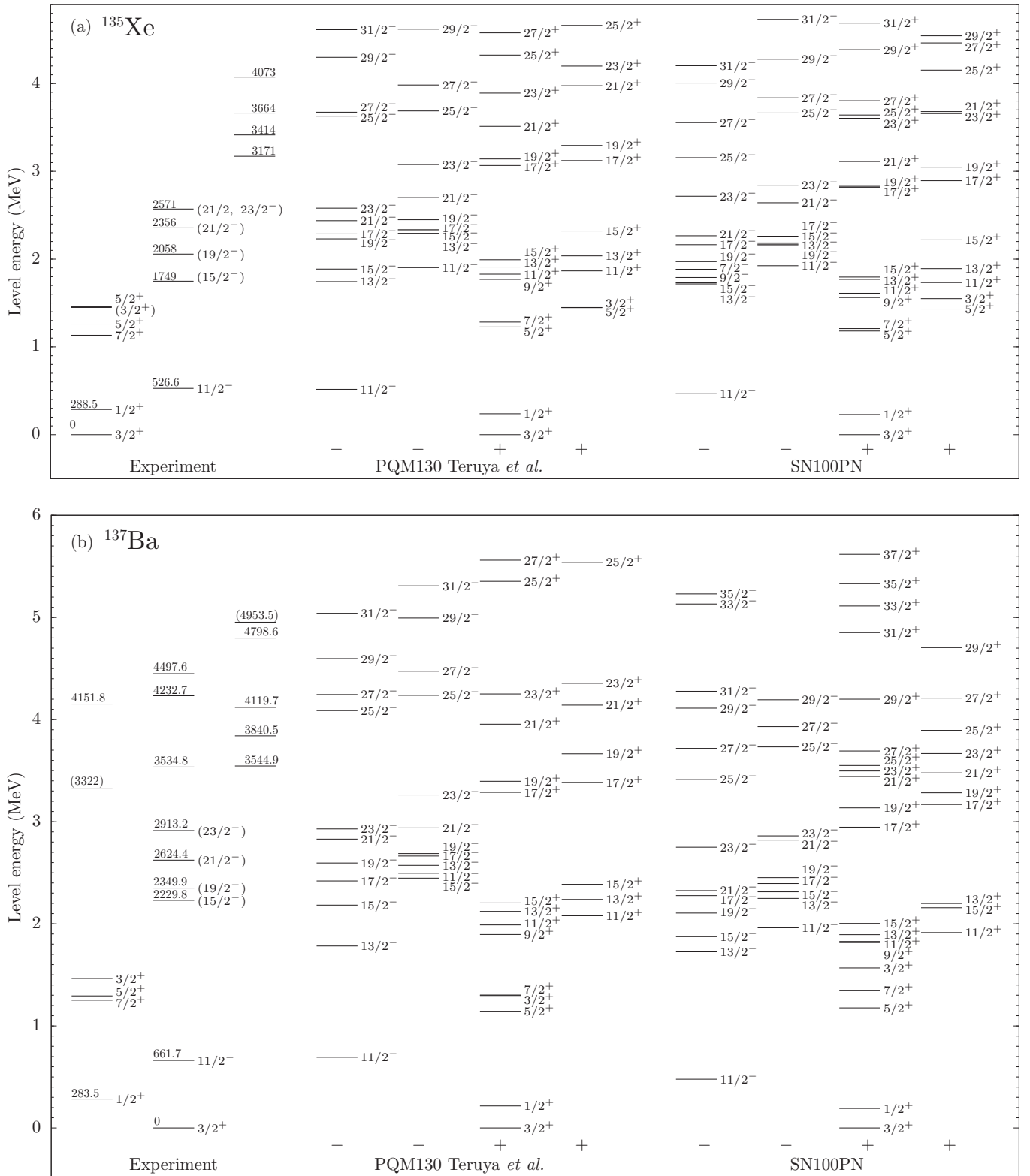


FIG. 10. Comparison of experimental energy spectra with the results of shell-model calculations for (a) ^{135}Xe and (b) ^{137}Ba . Experimental energy spectra are shown in the left panels. The arrangement of experimental levels for ^{137}Ba mirrors the layout of the level scheme shown in Fig. 6. The middle panels show the results for both the first and the second excited states obtained with the PQM130 interaction [3]. The right panels show the results of the shell-model calculations within the SN100PN interaction. Note that the states are separated into columns for the negative- and the positive-parity states. The first columns contain yrast states; second columns with yrare states are added for clarity.

TABLE III. Summary of the experimental and theoretical results for $B(E2; 19/2^- \rightarrow 15/2^-)$ values of ^{133}Te , ^{135}Xe , and ^{137}Ba . Experimental γ -ray transition energies are taken from Refs. [15,23,37]. The experimental results are compared to shell-model calculations employing (i) the PQM130 interaction [3] and (ii) the SN100PN interaction by Brown *et al.* [1]. In the SN100PN calculations effective neutron and proton charges are $e_v = 0.81e$ and $e_\pi = 1.52e$. Experimental $B(E2)$ values are corrected for internal conversion [69]. See text for details.

A	E_i (keV)	Experiment		$J_i^\pi \rightarrow J_f^\pi$	Theory			
					PQM130		SN100PN	
		This work / <i>Previous work</i>			E_i (keV)	$B(E2)$ (W.u.)	E_i (keV)	$B(E2)$ (W.u.)
		$T_{1/2}$ (ns)	$B(E2)$ (W.u.)					
^{133}Te	1610.4	100(5)	2.58(29)	$19/2_1^- \rightarrow 15/2_1^-$	1798	2.26	1606	2.58
				$19/2_2^- \rightarrow 15/2_1^-$			2171	0.02
^{135}Xe	2058	9.0(9)	0.52(6)	$19/2_1^- \rightarrow 15/2_1^-$	2231	0.49	1972	0.02
				$19/2_2^- \rightarrow 15/2_1^-$			2449	2.29
^{137}Ba	2349.9	589(20)	0.46(3)	$19/2_1^- \rightarrow 15/2_1^-$	2595	0.31	2105	0.01
				$19/2_2^- \rightarrow 15/2_1^-$			2688	0.41

is most probably of spin $23/2^-$. The $25/2^-$ state is only predicted above 3.5 MeV. Lower-spin states would preferably decay into states of spin $J < 19/2$. Consequently, the states at 3322, 3534.8, and 4232.7 keV are interpreted to have a spin of $J > 21/2$. Otherwise, they would directly decay to the $19/2^-$ state. The 3544.9-keV state is proposed to be the bandhead of a positive-parity band, which fits the systematics of the calculated level scheme. In the same way, the state at 4151.8 keV may be interpreted as either the $25/2^-$ or the $27/2^-$ state. However, due to the large density of predicted levels above 3.5 MeV, spins and parities cannot be assigned unambiguously solely on the basis of shell-model calculations.

Reduced transition probabilities [$B(E2)$ values] are calculated for the $(19/2^-) \rightarrow (15/2^-)$ transitions in ^{133}Te , ^{135}Xe , and ^{137}Ba . The decays of both the first and the second excited states are considered. In the SN100PN calculations the effective neutron and proton charges are defined as $e_v = \delta e_v$ and $e_\pi = 1e + \delta e_\pi$ with polarization charges $\delta e_v = 0.81e$ and $\delta e_\pi = 0.52e$. The effective neutron polarization charge is tuned to reproduce the reduced transition strength of the first excited 2^+ state in the $Z = 50$ isotope ^{128}Sn , $B(E2; 2^+ \rightarrow 0^+) = 4.2(3)$ W.u. [70]. The obtained value of $\delta e_v = 0.81e$ is in very good agreement with the effective charges used in a previous study of the nearby nucleus ^{136}Ba ($\delta e_{\pi, v} = 0.82e$) [59]. Keeping δe_v fixed, δe_π is modified to reproduce the $B(E2; 19/2^- \rightarrow 15/2^-)$ value in ^{133}Te . In the PQM130 interaction, effective charges are chosen as $e_v = -0.60e - 0.10N_v e$ for neutrons and $e_\pi = +1.80e - 0.05N_\pi e$ for protons. N_π and N_v are the proton-particle and neutron-hole numbers with respect to ^{132}Sn . Note that the neutron effective charge is chosen to be negative, as the calculations are performed for valence-neutron holes. The results are summarized in Table III. The $B(E2)$ value corresponding to the isomeric $(19/2^-) \rightarrow (15/2^-)$ transition in ^{133}Te is well reproduced within the experimental error by the PQM130 interaction and by the SN100PN interaction with modified effective charges. However, the excitation energy of the isomeric state is overpredicted by the PQM130 interaction. In ^{135}Xe the transition probability of the 310-keV transition deexciting the 9.0(9)-ns isomer at 2058 keV yields $B(E2) =$

0.52(6) W.u. assuming a pure $E2$ multipolarity. The transition probability for the 120-keV transition deexciting the 589(20)-ns isomer at 2349.9 keV in ^{137}Ba is 0.46(3) W.u. Particularly, the $B(E2)$ value of ^{135}Xe is well reproduced by the PQM130 interaction. The calculation locates the second $19/2^-$ states slightly higher (0.2 MeV for ^{135}Xe and 0.09 MeV for ^{137}Ba) than the first $19/2^-$ states. Therefore, in ^{137}Ba the calculated states might be reversed, i.e., the second calculated $19/2^-$ state might correspond to the first experimental $19/2^-$ state. In fact, the theoretical $B(E2)$ value of the second excited $19/2^-$ state obtained by the PQM130 interaction generally agrees with the experimental value of ^{137}Ba . The SN100PN interaction does not reproduce the experimental $B(E2; 19/2^- \rightarrow 15/2^-)$ values for ^{135}Xe and ^{137}Ba . The Weisskopf hindrance factors of the $(19/2^-)$ isomers are $F_W = T_{1/2}^{\text{exp}}/T_{1/2}^{\text{W}} = 1.8$ for ^{135}Xe and 1.1 for ^{137}Ba , respectively.

The decomposition of the total angular momentum of the $15/2_1^-$, $19/2_1^-$, and $19/2_2^-$ states in ^{133}Te , ^{135}Xe , and ^{137}Ba into their neutron (I_v) and proton (I_π) spin components in the SN100PN calculation is presented in Fig. 11 while Table IV shows the average proton occupation numbers of each orbital of the $gdsh$ model space for the $15/2_1^-$, $19/2_1^-$, and $19/2_2^-$ states in the PQM130 and SN100PN calculations. The decay of the $19/2^-$ isomer to the $15/2^-$ state in ^{133}Te is comparable to the isomeric $\pi g_{7/2}^2 \rightarrow \pi g_{7/2}^2 6^+ \rightarrow 4^+$ transition in the neighboring $N = 82$ nucleus ^{134}Te , and the $B(E2; 19/2^- \rightarrow 15/2^-)$ in ^{133}Te is found to be only slightly larger than the $B(E2; 6^+ \rightarrow 4^+)$ in ^{134}Te [71]. The SN100PN interaction computes the first excited $19/2^-$ and $15/2^-$ states to have $\nu h_{11/2}^{-1} \otimes \pi g_{7/2}^2$ configurations with fractions of 88% and 92%, respectively. The $15/2_1^-$ state is predicted to have a 75% fully stretched $[\nu 11/2^- \otimes \pi 2^+]$ and a 21% $[\nu 11/2^- \otimes \pi 4^+]$ configuration, whereas the $19/2_1^-$ state is predominantly $\nu 11/2^-$ coupled to $\pi 4^+$ (41%) and $\pi 6^+$ (58%) configurations. The similar $g_{7/2}$ occupation numbers of the $19/2^-$ and $15/2^-$ states in both interactions (see Table IV) emphasize the $\pi g_{7/2}^2 \rightarrow \pi g_{7/2}^2$ character of the $19/2_1^- \rightarrow 15/2_1^-$ transition which $B(E2)$ is well reproduced by both calculations (see Table III). For the $19/2_2^-$ state, the occupancy of the $d_{5/2}$ orbital is predicted to be much larger by the SN100PN calculation.

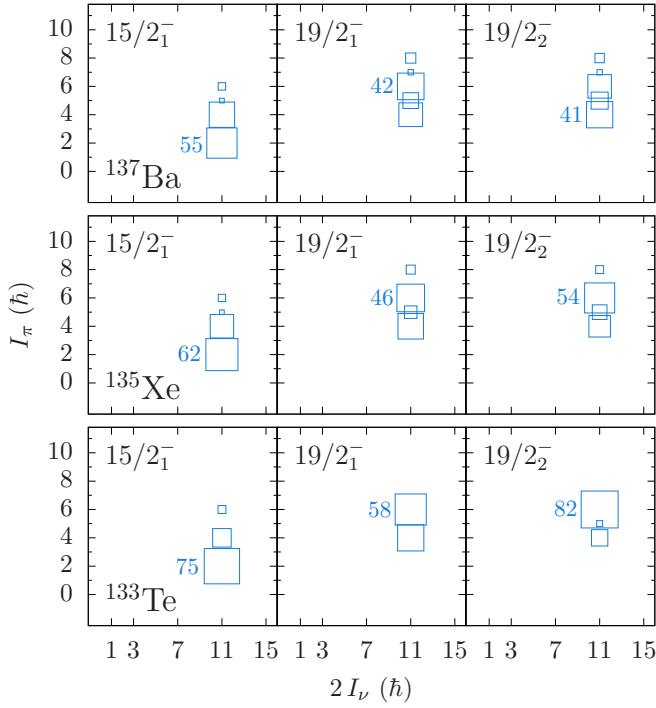


FIG. 11. Decomposition of the total angular momentum of the $15/2_1^-$, $19/2_1^-$, and $19/2_2^-$ states in ^{133}Te , ^{135}Xe , and ^{137}Ba into their neutron (I_n) and proton (I_π) spin components in the SN100PN calculation. The area of the boxes corresponds to the percentage of the particular $I_n \otimes I_\pi$ configuration. Percentages above 1% are shown; percentages of the largest component are also given in numbers for scale.

TABLE IV. Average proton occupation numbers in each single-particle orbit of the $gdsh$ model space for the $15/2_1^-$, $19/2_1^-$, and $19/2_2^-$ states in ^{133}Te , ^{135}Xe , and ^{137}Ba , calculated using the SN100PN and the PQM130 interactions.

Isotope	J^π	$g_{7/2}$	$d_{5/2}$	$d_{3/2}$	$s_{1/2}$	$h_{11/2}$
PQM130						
^{133}Te	$15/2_1^-$	1.96	0.01	0.02	0.00	0.00
	$19/2_1^-$	1.97	0.02	0.01	0.00	0.00
	$19/2_2^-$	1.96	0.02	0.02	0.00	0.00
^{135}Xe	$15/2_1^-$	3.28	0.51	0.12	0.03	0.06
	$19/2_1^-$	3.45	0.39	0.08	0.02	0.06
	$19/2_2^-$	3.28	0.55	0.08	0.03	0.06
^{137}Ba	$15/2_1^-$	4.06	1.46	0.23	0.12	0.13
	$19/2_1^-$	4.36	1.30	0.15	0.06	0.13
	$19/2_2^-$	4.37	1.28	0.15	0.07	0.13
SN100PN						
^{133}Te	$15/2_1^-$	1.90	0.06	0.02	0.01	0.01
	$19/2_1^-$	1.88	0.11	0.01	0.00	0.00
	$19/2_2^-$	1.09	0.89	0.01	0.01	0.00
^{135}Xe	$15/2_1^-$	3.00	0.69	0.12	0.05	0.14
	$19/2_1^-$	3.05	0.71	0.09	0.03	0.12
	$19/2_2^-$	2.97	0.84	0.07	0.03	0.09
^{137}Ba	$15/2_1^-$	3.48	1.81	0.25	0.13	0.34
	$19/2_1^-$	3.75	1.70	0.18	0.08	0.28
	$19/2_2^-$	3.74	1.67	0.19	0.10	0.30

Likewise, the observed high-spin level structures in ^{135}Xe and ^{137}Ba are interpreted as the coupling of the $h_{11/2}$ neutron hole to proton configurations. However, the theoretical wave functions of the high-spin states are much more complex and fragmented than in ^{133}Te . While the character of the $19/2^- \rightarrow 15/2^-$ transition is clear for ^{133}Te , it is not trivial for ^{135}Xe and ^{137}Ba . In ^{135}Xe , the first two $19/2^-$ states are predicted by the PQM130 interaction to consist mainly (64%) of the $(\nu h_{11/2}^{-1} \otimes \pi g_{7/2}^4)$ configuration, approximately 23% of the $(\nu h_{11/2}^{-1} \otimes \pi g_{7/2}^3 d_{5/2}^1)$ configuration, and about 9% of the $(\nu h_{11/2}^{-1} \otimes \pi g_{7/2}^2 d_{5/2}^2)$ configuration. The SN100PN interaction computes the $19/2_1^-$ state as a mixture of 42% $(\nu h_{11/2}^{-1} \otimes \pi g_{7/2}^4)$ and 26% $(\nu h_{11/2}^{-1} \otimes \pi g_{7/2}^3 d_{5/2}^1)$ configurations. The $19/2_2^-$ state is predicted to have a dominant 51% $\nu h_{11/2}^{-1} \otimes \pi g_{7/2}^3 d_{5/2}^1$ and a 26% $\nu h_{11/2}^{-1} \otimes \pi g_{7/2}^4$ configuration. Couplings of the $\nu h_{11/2}^{-1}$ hole to proton configurations with spins of 4^+ (28%), 5^+ (13%), and 6^+ (54%) contribute to the configuration of the $19/2_2^-$ state. The calculated $B(E2; 19/2_2^- \rightarrow 15/2_1^-)$ value reproduces the experimental transition strength better than the decay of the corresponding $19/2_1^-$ state, although overestimating it. The SN100PN interaction predicts in ^{135}Xe a higher degree of $d_{5/2}$ occupancy than in ^{133}Te (see Table IV). A similar situation is found in ^{137}Ba , suggesting a reduced spacing between the $\pi g_{7/2}$ and $\pi d_{5/2}$ orbitals. Both the SN100PN and PQM130 interactions predict the $19/2_{1,2}^-$ states in ^{137}Ba to mainly consist of the $[\nu h_{11/2}^{-1} \otimes \pi (g_{7/2} d_{5/2})^6]$ configuration. The configurations are predicted to be highly fragmented. Like in ^{135}Xe , the occupation numbers are almost the same between the two $19/2^-$ states, but internal couplings are different. The $g_{7/2}^6$ configuration is nearly missing in the SN100PN calculation, which is further evidence for easy redistribution of protons from $g_{7/2}$ to $d_{5/2}$ orbitals, i.e., these orbitals are close together. Continuing the analogy to the isomeric $6^+ \rightarrow 4^+$ decays along the $N = 82$ isotones, the SN100PN interaction yields the transition probability of the $19/2_1^- \rightarrow 15/2_1^-$ decay to be 0.02 W.u. in ^{135}Xe and 0.01 W.u. in ^{137}Ba , missing the experimental transition strengths (see Table III) by an order of magnitude; but they are very similar to the measured values of $B(E2; 6^+ \rightarrow 4^+) = 0.013(1)$ W.u. in ^{136}Xe [72] and 0.055(7) W.u. in ^{138}Ba [73]. Therefore, we assume that the calculated proton configurations follow the nuclear structure of the closed $N = 82$ shell nuclei, validating the proton-proton part of the SN100PN interaction. Thus, most probably, the proton-neutron part falls short in reproducing the decay features of the isomeric states in ^{135}Xe and ^{137}Ba . Similar conclusions were discussed in Ref. [74]. There, the p - n monopole part of the SN100PN interaction was replaced by new shell-model developments. The new interaction combines the well-established proton-proton part of the SN100PN interaction with the semiempirical SNBG3 neutron-neutron interaction by Honma *et al.* [75] and the novel universal V_{MU} interaction [76] for the proton-neutron part. The SNBG3 interaction is obtained by combining the next-to-next-to-next-to-leading order ($N^3\text{LO}$) interaction with a χ^2 fit of levels including 3^- states in $50 < N < 82$ Sn isotopes. The interaction successfully described the shell evolution along Sb isotopes

[74] and may provide insight into Xe and Ba isotopes in the future.

V. CONCLUSIONS

In summary, four experiments employing the $^{136}\text{Xe} + ^{198}\text{Pt}$, $^{136}\text{Xe} + ^{208}\text{Pb}$, and $^{136}\text{Xe} + ^{238}\text{U}$ multinucleon-transfer reactions as well as the $^{11}\text{B} + ^{130}\text{Te}$ fusion-evaporation reaction were used to measure lifetimes of high-spin isomers and to establish high-spin states in ^{135}Xe and ^{137}Ba . Several new levels and γ -ray transitions are assigned to ^{135}Xe . The level scheme of ^{137}Ba is extended up to an excitation energy of 5.0 MeV. The half-life of the 2058-keV ($19/2^-$) state in ^{135}Xe is measured to be 9.0(9) ns, corresponding to a transition probability of $B(E2, 19/2^- \rightarrow 15/2^-) = 0.52(6)$ W.u. The identification of this isomeric state completes the systematics for the $N = 81$ isotones. Large-scale shell-model calculations employing the novel PQM130 interaction perform well in predicting electromagnetic transition probabilities of high-spin isomers in the $N = 81$ isotones that cannot be reproduced by the SN100PN interaction. Some ambiguities remain for the interpretation of high-spin states in both interactions. In the future, a novel microscopic effective interaction by Utsuno, Otsuka, Shimizu *et al.* [74] may provide a more unified description of the $50 \leq Z, N \leq 82$ shells.

Although ^{137}Ba and ^{135}Xe are stable or located between two stable isotopes, respectively, there is a lack of beam and target combinations to populate high spins via nuclear reactions. Refined detection capabilities are needed to address these indeed

hard-to-reach nuclei via MNT or fission reactions. In future, detailed angular correlation and polarization measurements are desirable to determine proper spin, parity, and multipolarity assignments. In perspective, the extended AGATA spectrometer coupled to the Variable Mode Spectrometer at the Grand Accélérateur National d'Ions Lourds will allow for a more detailed spectroscopy of the $N = 81$ nuclei.

ACKNOWLEDGMENTS

We thank the IKP FN Tandem accelerator team for the professional support during the experiment. The research leading to these results has received funding from the German BMBF under Contract No. 05P12PKFNE TP4, from the European Union Seventh Framework Programme FP7/2007-2013 under Grant Agreement No. 262010-ENSAR, from the Spanish Ministerio de Ciencia e Innovación under Contract No. FPA2011-29854-C04, from the Spanish Ministerio de Economía y Competitividad under Contract No. FPA2014-57196-C5, from the UK Science and Technology Facilities Council (STFC), and from the US National Science Foundation (NSF). E.T. and N.Y. were supported by a Grant-in-Aid for Japan Society for the Promotion of Science (JSPS) Fellows (Grant No. 26.10429). A.V. and L.K. thank the Bonn-Cologne Graduate School of Physics and Astronomy (BCGS) for financial support. One of the authors (A. Gadea) has been supported by the Generalitat Valenciana, Spain, under the grant PROMETEOII/2014/019, and by the EU under the Fonds Européen de Développement Économique et Régional program.

-
- [1] B. A. Brown, N. J. Stone, J. R. Stone, I. S. Towner, and M. Hjorth-Jensen, Magnetic moments of the 2_1^+ states around ^{132}Sn , *Phys. Rev. C* **71**, 044317 (2005).
 - [2] K. Higashiyama and N. Yoshinaga, Pair-truncated shell-model analysis of nuclei around mass 130, *Phys. Rev. C* **83**, 034321 (2011).
 - [3] E. Teruya, N. Yoshinaga, K. Higashiyama, and A. Odahara, Shell-model calculations of nuclei around mass 130, *Phys. Rev. C* **92**, 034320 (2015).
 - [4] L. Coraggio, A. Covello, A. Gargano, N. Itaco, and T. T. S. Kuo, Shell-model study of the $N = 82$ isotonic chain with a realistic effective Hamiltonian, *Phys. Rev. C* **80**, 044320 (2009).
 - [5] E. Caurier, F. Nowacki, A. Poves, and K. Sieja, Collectivity in the light xenon isotopes: A shell model study, *Phys. Rev. C* **82**, 064304 (2010).
 - [6] A. Astier, M.-G. Porquet, Ch. Theisen, D. Verney, I. Deloncle, M. Houry, R. Lucas, F. Azaiez, G. Barreau, D. Curien, O. Dorvaux, G. Duchêne, B. J. P. Gall, N. Redon, M. Rousseau, and O. Stézowski, High-spin states with seniority $\nu = 4, 5$, and 6 in $^{119-126}\text{Sn}$, *Phys. Rev. C* **85**, 054316 (2012).
 - [7] Ł. W. Iskra, R. Broda, R. V. F. Janssens, C. J. Chiara, M. P. Carpenter, B. Fornal, N. Hoteling, F. G. Kondev, W. Królas, T. Lauritsen, T. Pawlat, D. Seweryniak, I. Stefanescu, W. B. Walters, J. Wrzesiński, and S. Zhu, Shell-model states with seniority $\nu = 3, 5$, and 7 in odd- A neutron-rich Sn isotopes, *Phys. Rev. C* **93**, 014303 (2016).
 - [8] A. Astier, M.-G. Porquet, Ts. Venkova, D. Verney, Ch. Theisen, G. Duchêne, F. Azaiez, G. Barreau, D. Curien, I. Deloncle, O. Dorvaux, B. J. P. Gall, M. Houry, R. Lucas, N. Redon, M. Rousseau, and O. Stézowski, High-spin structures of five $N = 82$ isotopes: ^{136}Xe , ^{137}Cs , ^{138}Ba , ^{139}La , and ^{140}Ce , *Phys. Rev. C* **85**, 064316 (2012).
 - [9] P. C. Srivastava, M. J. Ermatov, and Irving O. Morales, High-spin structures of ^{136}Xe , ^{137}Cs , ^{138}Ba , ^{139}La , and ^{140}Ce : a shell model description, *J. Phys. G* **40**, 035106 (2013).
 - [10] A. Astier, M. G. Porquet, Ts. Venkova, Ch. Theisen, G. Duchêne, F. Azaiez, G. Barreau, D. Curien, I. Deloncle, O. Dorvaux, B. J. P. Gall, M. Houry, R. Lucas, N. Redon, M. Rousseau, and O. Stézowski, High-spin structures of $^{124-131}\text{Te}$: Competition of proton- and neutron-pair breakings, *Eur. Phys. J. A* **50**, 1 (2014).
 - [11] V. Kumar, P. C. Srivastava, M. J. Ermatov, and I. O. Morales, Analysis of proton and neutron pair breakings: High-spin structures of $^{124-127}\text{Te}$ isotopes, *Nucl. Phys. A* **942**, 1 (2015).
 - [12] S. Biswas, R. Palit, A. Navin, M. Rejmund, A. Bisoi, M. S. Sarkar, S. Sarkar, S. Bhattacharyya, D. C. Biswas, M. Caamaño, M. P. Carpenter, D. Choudhury, E. Clément, L. S. Danu, O. Delaune, F. Farget, G. de France, S. S. Hota, B. Jacquot, A. Lemasson, S. Mukhopadhyay, V. Nanal, R. G. Pillay, S. Saha, J. Sethi, Purnima Singh, P. C. Srivastava, and S. K. Tandel, Structure of $^{132}\text{Te}_{80}$: The two-particle and two-hole spectrum of $^{132}_{50}\text{Sn}_{82}$, *Phys. Rev. C* **93**, 034324 (2016).

- [13] W. B. Walters, S. M. Lane, N. L. Smith, R. J. Nagle, and R. A. Meyer, Shell model description of $N = 81$ five-exciton ^{135}Xe and the decay of ^{135}I , *Phys. Rev. C* **26**, 2273 (1982).
- [14] J. A. C. Gonçalves and R. N. Saxena, Directional correlations of γ transitions in ^{135}Xe following the decay of ^{135}I , *Phys. Rev. C* **43**, 2586 (1991).
- [15] B. Singh, A. A. Rodionov, and Y. L. Khazov, Nuclear data sheets for $A = 135$, *Nucl. Data Sheets* **109**, 517 (2008).
- [16] H. Götte, Eine bei der Uranspaltung auftretende Kernisomerie bei Xenon, *Naturwissenschaften* **28**, 449 (1940).
- [17] C.-S. Wu and E. Segrè, Radioactive Xenons, *Phys. Rev.* **67**, 142 (1945).
- [18] N. Fotiades, R. O. Nelson, M. Devlin, J. A. Cizewski, J. A. Becker, W. Younes, R. Krücken, R. M. Clark, P. Fallon, I. Y. Lee, A. O. Macchiavelli, T. Ethvignot, and T. Granier, High-spin states in ^{135}Xe , *Phys. Rev. C* **75**, 054322 (2007).
- [19] B. K. Wagner, P. E. Garrett, M. Yeh, and S. W. Yates, On the first excited state of ^{137}Ba , *J. Radioanal. Nucl. Chem.* **219**, 217 (1997).
- [20] I. Bikit, I. Aničin, J. Slivka, M. Krmar, J. Puzović, and Lj. Čonkić, Population of the 283 keV level of ^{137}Ba by the β decay of ^{137}Cs , *Phys. Rev. C* **54**, 3270 (1996).
- [21] V. A. Bondarenko, I. L. Kuvaga, P. T. Prokofjev, A. M. Sukhovoij, V. A. Khitrov, Yu. P. Popov, S. Brant, and V. Paar, Levels of ^{137}Ba studied with neutron-induced reactions, *Nucl. Phys. A* **582**, 1 (1995).
- [22] E. Dragulescu, M. Ivascu, R. Miha, D. Popescu, G. Semenescu, A. Velenik, and V. Paar, Coulomb excitation of levels in ^{135}Ba and ^{137}Ba , *J. Phys. G* **10**, 1099 (1984).
- [23] E. Browne and J. K. Tuli, Nuclear data sheets for $A = 137$, *Nucl. Data Sheets* **108**, 2173 (2007).
- [24] K. Moran, E. A. McCutchan, C. J. Lister, S. Zhu, M. P. Carpenter, P. Chowdhury, J. P. Greene, T. Lauritsen, E. Merchan, and R. Shearman, $E5$ decay from the $J^\pi = 11/2^-$ isomer in ^{137}Ba , *Phys. Rev. C* **90**, 041303 (2014).
- [25] C. Walz, H. Scheit, N. Pietralla, T. Aumann, R. Lefol, and V. Yu Ponomarev, Observation of the competitive double-gamma nuclear decay, *Nature (London)* **526**, 406 (2015).
- [26] A. Kerek and J. Kownacki, The level structure of the $N = 81$ and 82 nucleides $^{137,138}\text{Ba}$ as investigated in $^{136}\text{Xe}(\alpha, xn)$ reactions, *Nucl. Phys. A* **206**, 245 (1973).
- [27] Evaluated Nuclear Structure Data File (ENSDF), online resource: <http://www.nndc.bnl.gov/ensdf/>
- [28] P. Bhattacharyya, P. J. Daly, C. T. Zhang, Z. W. Grabowski, S. K. Saha, R. Broda, B. Fornal, I. Ahmad, D. Seweryniak, I. Wiedenhöver, M. P. Carpenter, R. V. F. Janssens, T. L. Khoo, T. Lauritsen, C. J. Lister, P. Reiter, and J. Blomqvist, Magic Nucleus ^{132}Sn and Its One-Neutron-Hole Neighbor ^{131}Sn , *Phys. Rev. Lett.* **87**, 062502 (2001).
- [29] B. Fogelberg, H. Gausemel, K. A. Mezilev, P. Hoff, H. Mach, M. Sanchez-Vega, A. Lindroth, E. Ramström, J. Genevey, J. A. Pinston, and M. Rejmund, Decays of ^{131}In , ^{131}Sn , and the position of the $h_{11/2}$ neutron hole state, *Phys. Rev. C* **70**, 034312 (2004).
- [30] J. K. Hwang, A. V. Ramayya, J. H. Hamilton, C. J. Beyer, J. O. Rasmussen, Y. X. Luo, S. C. Wu, T. N. Ginter, C. M. Folden, P. Fallon, P. M. Zielinski, K. E. Gregorich, A. O. Macchiavelli, M. Stoyer, S. J. Asztalos, A. Covello, and A. Gargano, Particle-hole excited states in ^{133}Te , *Phys. Rev. C* **65**, 034319 (2002).
- [31] S. Kaim, C. M. Petrache, A. Gargano, N. Itaco, T. Zerrouki, R. Leguillon, A. Astier, I. Deloncle, T. Konstantinopoulos, J. M. Régis, D. Wilmsen, B. Melon, A. Nannini, C. Ducoin, D. Guinet, and T. Bhattacharjee, High-spin spectroscopy of ^{139}Ce , *Phys. Rev. C* **91**, 024318 (2015).
- [32] T. Zerrouki, C. M. Petrache, R. Leguillon, K. Hauschild, A. Korichi, A. Lopez-Martens, S. Frauendorf, I. Ragnarsson, H. Hübel, A. Neußer-Neffgen, A. Al-Khatib, P. Bringel, A. Bürger, N. Nenoff, G. Schönwaßer, A. K. Singh, D. Curien, G. B. Hagemann, B. Herskind, G. Sletten, P. Fallon, A. Görgen, and P. Bednarczyk, Shape evolution and magnetic rotation in ^{141}Nd , *Eur. Phys. J. A* **51**, 1 (2015).
- [33] J. Ludziejewski, J. Bialkowski, Z. Haratym, L.-E. de Geer, A. Kerek, and J. Kozyczkowski, The life-time measurements of some high-spin states in the $^{138,139}\text{Ce}$ and $^{141,142}\text{Nd}$ nuclei, *Phys. Scr.* **14**, 133 (1976).
- [34] A. Pakkanen, J. Muhonen, M. Piiparinen, and J. Blomqvist, Medium-spin levels and the character of the 20.4 ns $13/2^+$ isomer in ^{145}Gd , *Nucl. Phys. A* **373**, 237 (1982).
- [35] K. Heyde and P. J. Brussaard, Neutron hole states in the $N = 81$ nuclei, *Z. Phys. A* **259**, 15 (1972).
- [36] K. Kotajima and H. Morinaga, Isomers in $N = 81$ Nuclei, *Nucl. Phys.* **16**, 231 (1960).
- [37] Yu. Khazov, A. Rodionov, and F. G. Kondev, Nuclear data sheets for $A = 133$, *Nucl. Data Sheets* **112**, 855 (2011).
- [38] S. Chanda, T. Bhattacharjee, S. Bhattacharyya, A. Mukherjee, S. Kumar Basu, I. Ragnarsson, R. K. Bhowmik, S. Muralithar, R. P. Singh, S. S. Ghugre, and U. D. Pramanik, Seven-quasiparticle bands in ^{139}Ce , *Phys. Rev. C* **79**, 054332 (2009).
- [39] T. W. Burrows, Nuclear data sheets for $A = 139$, *Nucl. Data Sheets* **92**, 623 (2001).
- [40] D. A. Volkov, B. A. Gorbachev, A. I. Levon, O. F. Nemets, and V. A. Stepanenko, Measurement of the nuclear g factor of the $19/2^-$ isomer in ^{139}Ce , *Yad. Fiz.* **40**, 289 (1984) [*Sov. J. Nucl. Phys.* **40**, 183 (1984)].
- [41] S. Bhowal, C. Lahiri, R. Raut, P. Singh, M. Kumar Raju, A. Goswami, A. K. Singh, S. Bhattacharya, T. Bhattacharjee, G. Mukherjee, S. Bhattacharyya, S. Muralithar, R. K. Bhowmik, N. Madhavan, R. P. Singh, and G. Gangopadhyay, Energy levels in ^{141}Nd from fusion evaporation study, *J. Phys. G* **38**, 035105 (2011).
- [42] J. Kownacki, J. Ludziejewski, Z. Sujkowski, H. Arnold, and H. Ryde, High-spin states and evidence for hole-core coupling in the $^{143}\text{Sm}_{81}$ and $^{145}\text{Gd}_{81}$ nuclei, *Nucl. Phys. A* **236**, 125 (1974).
- [43] R. Raut, S. Ganguly, R. Kshetri, P. Banerjee, S. Bhattacharya, B. Dasmahapatra, A. Mukherjee, G. Mukherjee, M. Saha Sarkar, A. Goswami, G. Gangopadhyay, S. Mukhopadhyay, Krishichayan, A. Chakraborty, S. S. Ghugre, T. Bhattacharjee, and S. K. Basu, High spin states in ^{143}Sm , *Phys. Rev. C* **73**, 044305 (2006).
- [44] S. Akkoyun *et al.*, AGATA—Advanced GAMMA Tracking Array, *Nucl. Instrum. Methods Phys. Res., Sect. A* **668**, 26 (2012).
- [45] A. M. Stefanini, L. Corradi, G. Maron, A. Pisent, M. Trotta, A. M. Vinodkumar, S. Beghini, G. Montagnoli, F. Scarlassara, G. F. Segato, A. De Rosa, G. Inglima, D. Pierrousakou, M. Romoli, M. Sandoli, G. Pollarolo, and A. Latina, The heavy-ion magnetic spectrometer PRISMA, *Nucl. Phys. A* **701**, 217 (2002).
- [46] S. Szilner, C. A. Ur, L. Corradi, N. Marginean, G. Pollarolo, A. M. Stefanini, S. Beghini, B. R. Behera, E. Fioretto, A. Gadea, B. Guiot, A. Latina, P. Mason, G. Montagnoli, F. Scarlassara, M. Trotta, G. de Angelis, F. Della Vedova, E. Farnea, F. Haas, S. Lenzi, S. Lunardi, R. Marginean, R. Menegazzo, D. R. Napoli, M. Nespolo, I. V. Pokrovsky, F. Recchia, M. Romoli, M.-D.

- Salsac, N. Soić, and J. J. Valiente-Dobón, Multinucleon transfer reactions in closed-shell nuclei, *Phys. Rev. C* **76**, 024604 (2007).
- [47] L. Corradi, S. Szilner, G. Pollarolo, D. Montanari, E. Fioretto, A. M. Stefanini, J. J. Valiente-Dobón, E. Farnea, C. Michelagnoli, G. Montagnoli, F. Scarlassara, C. A. Ur, T. Mijatović, D. Jelavić Malenica, N. Soić, and F. Haas, Multinucleon transfer reactions: Present status and perspectives, *Nucl. Instrum. Methods Phys. Res., Sect. B* **317**, Part B, 743 (2013).
- [48] I-Yang Lee, The GAMMASPHERE, *Nucl. Phys. A* **520**, c641 (1990).
- [49] M. W. Simon, D. Cline, C. Y. Wu, R. W. Gray, R. Teng, and C. Long, CHICO, a heavy ion detector for Gammasphere, *Nucl. Instrum. Methods Phys. Res., Sect. A* **452**, 205 (2000).
- [50] L. Netterdon, V. Derya, J. Endres, C. Fransen, A. Hennig, J. Mayer, C. Müller-Gatermann, A. Sauerwein, P. Scholz, M. Spieker, and A. Zilges, The γ -ray spectrometer HORUS and its applications for nuclear astrophysics, *Nucl. Instrum. Methods Phys. Res., Sect. A* **754**, 94 (2014).
- [51] A. Gadea, E. Farnea, J. J. Valiente-Dobón, B. Million, D. Mengoni, D. Bazzacco, F. Recchia, A. Dewald, Th. Pissulla, W. Rother, G. de Angelis *et al.*, Conceptual design and infrastructure for the installation of the first AGATA sub-array at LNL, *Nucl. Instrum. Methods Phys. Res., Sect. A* **654**, 88 (2011).
- [52] A. Wiens, H. Hess, B. Birkenbach, B. Bruyneel, J. Eberth, D. Lersch, G. Pascovici, P. Reiter, and H.-G. Thomas, The AGATA triple cluster detector, *Nucl. Instrum. Methods Phys. Res., Sect. A* **618**, 223 (2010).
- [53] B. Bruyneel, B. Birkenbach, and P. Reiter, Pulse shape analysis and position determination in segmented HPGe detectors: The AGATA detector library, *Eur. Phys. J. A* **52**, 70 (2016).
- [54] A. Lopez-Martens, K. Hauschild, A. Korichi, J. Roccas, and J.-P. Thibaud, γ -ray tracking algorithms: A comparison, *Nucl. Instrum. Methods Phys. Res., Sect. A* **533**, 454 (2004).
- [55] A. Vogt, B. Birkenbach, P. Reiter, L. Corradi, T. Mijatović, D. Montanari, S. Szilner, D. Bazzacco, M. Bowry, A. Bracco, B. Bruyneel, F. C. L. Crespi, G. de Angelis, P. Désesquelles, J. Eberth, E. Farnea, E. Fioretto, A. Gadea, K. Geibel, A. Gengelbach, A. Giaz, A. Görgen, A. Gottardo, J. Grebosz, H. Hess, P. R. John, J. Jolie, D. S. Judson, A. Jungclaus, W. Korten, S. Leoni, S. Lunardi, R. Menegazzo, D. Mengoni, C. Michelagnoli, G. Montagnoli, D. Napoli, L. Pellegri, G. Pollarolo, A. Pullia, B. Quintana, F. Radeck, F. Recchia, D. Rosso, E. Şahin, M. D. Salsac, F. Scarlassara, P.-A. Söderström, A. M. Stefanini, T. Steinbach, O. Stezowski, B. Szpak, Ch. Theisen, C. Ur, J. J. Valiente-Dobón, V. Vandone, and A. Wiens, Light and heavy transfer products in $^{136}\text{Xe} + ^{238}\text{U}$ multinucleon transfer reactions, *Phys. Rev. C* **92**, 024619 (2015).
- [56] A. B. Brown, C. W. Snyder, W. A. Fowler, and C. C. Lauritsen, Excited States of the Mirror Nuclei, ^7Li and ^7Be , *Phys. Rev.* **82**, 159 (1951).
- [57] R. S. Kempley *et al.*, Cross Coincidences in the $^{136}\text{Xe} + ^{208}\text{Pb}$ deep-inelastic reaction, *Acta. Phys. Pol. B* **42**, 717 (2011).
- [58] M. Siciliano *et al.*, Neutron-rich nuclei in the vicinity of ^{208}Pb , LNL Annual Report 2014 **241**, 63 (2015).
- [59] J. J. Valiente-Dobón, P. H. Regan, C. Wheldon, C. Y. Wu, N. Yoshinaga, K. Higashiyama, J. F. Smith, D. Cline, R. S. Chakrawarthy, R. Chapman, M. Cromaz, P. Fallon, S. J. Freeman, A. Görgen, W. Gelletly, A. Hayes, H. Hua, S. D. Langdown, I. Y. Lee, X. Liang, A. O. Macchiavelli, C. J. Pearson, Zs. Podolyák, G. Sletten, R. Teng, D. Ward, D. D. Warner, and A. D. Yamamoto, ^{136}Ba studied via deep-inelastic collisions: Identification of the $(\nu h_{11/2})_{10+}^{-2}$ isomer, *Phys. Rev. C* **69**, 024316 (2004).
- [60] D. C. Radford, ESCL8R and LEVIT8R: Software for interactive graphical analysis of HPGe coincidence data sets, *Nucl. Instrum. Methods Phys. Res., Sect. A* **361**, 297 (1995).
- [61] O. B. Tarasov and D. Bazin, Development of the program LISE: Application to fusion-evaporation, in *14th International Conference on Electromagnetic Isotope Separators and Techniques Related to their Applications* [Nucl. Instrum. Methods Phys. Res., Sect. B **204**, 174 (2003)].
- [62] F. Pühlhofer, On the interpretation of evaporation residue mass distributions in heavy-ion induced fusion reactions, *Nucl. Phys. A* **280**, 267 (1977).
- [63] N. Saed-Samii, Diplomarbeit, Universität zu Köln, 2013 (unpublished).
- [64] J. Theuerkauf, Ph.D. thesis, Universität zu Köln, 1994.
- [65] A. Vogt, B. Birkenbach, P. Reiter, A. Blazhev, M. Siciliano, J. J. Valiente-Dobón, C. Wheldon, D. Bazzacco, M. Bowry, A. Bracco, B. Bruyneel, R. S. Chakrawarthy, R. Chapman, D. Cline, L. Corradi, F. C. L. Crespi, M. Cromaz, G. de Angelis, J. Eberth, P. Fallon, E. Farnea, E. Fioretto, S. J. Freeman, A. Gadea, K. Geibel, W. Gelletly, A. Gengelbach, A. Giaz, A. Görgen, A. Gottardo, A. B. Hayes, H. Hess, H. Hua, P. R. John, J. Jolie, A. Jungclaus, W. Korten, I. Y. Lee, S. Leoni, X. Liang, S. Lunardi, A. O. Macchiavelli, R. Menegazzo, D. Mengoni, C. Michelagnoli, T. Mijatović, G. Montagnoli, D. Montanari, D. Napoli, C. J. Pearson, L. Pellegri, Zs. Podolyák, G. Pollarolo, A. Pullia, F. Radeck, F. Recchia, P. H. Regan, E. Şahin, F. Scarlassara, G. Sletten, J. F. Smith, P.-A. Söderström, A. M. Stefanini, T. Steinbach, O. Stezowski, S. Szilner, B. Szpak, R. Teng, C. Ur, V. Vandone, D. Ward, D. D. Warner, A. Wiens, and C. Y. Wu, High-spin structure of ^{134}Xe , *Phys. Rev. C* **93**, 054325 (2016).
- [66] A. A. Sonzogni, Nuclear data sheets for $A = 136$, *Nucl. Data Sheets* **95**, 837 (2002).
- [67] B. A. Brown and W. D. M. Rae, The shell-model code NuShellX@MSU, *Nucl. Data Sheets* **120**, 115 (2014).
- [68] R. Machleidt, F. Sammarruca, and Y. Song, Nonlocal nature of the nuclear force and its impact on nuclear structure, *Phys. Rev. C* **53**, R1483 (1996).
- [69] T. Kibédi, T. W. Burrows, M. B. Trzhaskovskaya, P. M. Davidson, and C. W. Nestor, Jr., Evaluation of theoretical conversion coefficients using BrIcc, *Nucl. Instrum. Methods Phys. Res., Sect. A* **589**, 202 (2008).
- [70] J. M. Allmond, D. C. Radford, C. Baktash, J. C. Batchelder, A. Galindo-Uribarri, C. J. Gross, P. A. Hausladen, K. Lagergren, Y. Larochelle, E. Padilla-Rodal, and C.-H. Yu, Coulomb excitation of $^{124,126,128}\text{Sn}$, *Phys. Rev. C* **84**, 061303 (2011).
- [71] P. Bhattacharyya, P. J. Daly, C. T. Zhang, Z. W. Grabowski, S. K. Saha, B. Fornal, R. Broda, W. Urban, I. Ahmad, D. Seweryniak, I. Wiedenhöver, M. P. Carpenter, R. V. F. Janssens, T. L. Khoo, T. Lauritsen, C. J. Lister, P. Reiter, and J. Blomqvist, Yrast excitations in $N = 81$ nuclei ^{132}Sb and ^{133}Te from ^{248}Cm fission, *Phys. Rev. C* **64**, 054312 (2001).

- [72] A. A. Sonzogni, Nuclear data sheets for $A = 134$, Nucl. Data Sheets **103**, 1 (2004).
- [73] A. A. Sonzogni, Nuclear data sheets for $A = 138$, Nucl. Data Sheets **98**, 515 (2003).
- [74] Y. Utsuno, T. Otsuka, N. Shimizu, M. Honma, T. Mizusaki, Y. Tsunoda, and T. Abe, Recent shell-model results for exotic nuclei, EPJ Web Conf. **66**, 02106 (2014).
- [75] M. Honma, T. Otsuka, T. Mizusaki, and M. Hjorth-Jensen, Shell-model fits for Sn isotopes, RIKEN Accel. Prog. Rep. **45**, 35 (2012).
- [76] T. Otsuka, T. Suzuki, M. Honma, Y. Utsuno, N. Tsunoda, K. Tsukiyama, and M. Hjorth-Jensen, Novel Features of Nuclear Forces and Shell Evolution in Exotic Nuclei, Phys. Rev. Lett. **104**, 012501 (2010).

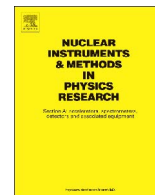
Publication V:

**Characterization and calibration
of radiation-damaged double-sided
silicon strip detectors**



Contents lists available at ScienceDirect

Nuclear Instruments and Methods in Physics Research A

journal homepage: www.elsevier.com/locate/nima

Characterization and calibration of radiation-damaged double-sided silicon strip detectors



L. Kaya^a, A. Vogt^{a,*}, P. Reiter^a, B. Birkenbach^a, R. Hirsch^a, K. Arnsward^a, H. Hess^a, M. Seidlitz^a, T. Steinbach^a, N. Warr^a, K. Wolf^a, C. Stahl^b, N. Pietralla^b, T. Limböck^c, K. Meerholz^c, R. Lutter^d

^a Institut für Kernphysik, Universität zu Köln, D-50937 Köln, Germany

^b Institut für Kernphysik, Technische Universität Darmstadt, D-64291 Darmstadt, Germany

^c Physikalische Chemie, Universität zu Köln, D-50939 Köln, Germany

^d Maier-Leibnitz-Laboratorium, Ludwig-Maximilians-Universität München, D-85748 Garching, Germany

ARTICLE INFO

Keywords:

Double-sided silicon strip detector (DSSD),
DSSSD

Radiation damage

Charge loss

Calibration method

ABSTRACT

Double-sided silicon strip detectors (DSSSD) are commonly used for event-by-event identification of charged particles as well as the reconstruction of particle trajectories in nuclear physics experiments with stable and radioactive beams. Intersecting areas of both p- and n-doped front- and back-side segments form individual virtual pixel segments allowing for a high detector granularity. DSSSDs are employed in demanding experimental environments and have to withstand high count rates of impinging nuclei. The illumination of the detector is often not homogeneous. Consequently, radiation damage of the detector is distributed non-uniformly. Position-dependent incomplete charge collection due to radiation damage limits the performance and lifetime of the detectors, the response of different channels may vary drastically. Position-resolved charge-collection losses between front- and back-side segments are investigated in an in-beam experiment and by performing radioactive source measurements. A novel position-resolved calibration method based on mutual consistency of p-side and n-side charges yields a significant enhancement of the energy resolution and the performance of radiation-damaged parts of the detector.

1. Introduction

Segmented silicon-strip detectors are indispensable detectors for charged particles in nuclear physics experiments to obtain precise information on the position (x, y), energy E , and energy loss ΔE of impinging particles. Typically, particles and energies may vary from electrons or protons with a few hundreds of keV up to heavy ions with energies of some hundreds of MeV/u [1]. When employed as ancillary detectors in in-beam γ -ray spectroscopy experiments for event-by-event particle identification as well as reconstruction of particle trajectories, both energy and precise position information are crucial for an accurate Doppler correction of emitted γ rays [2–5]. In particular, segmented silicon detectors are used to investigate super-heavy elements [6] and exotic radioactive nuclei by detecting the heavy ions that are implanted into the detector and measuring the subsequent light charged decay products like electrons/positrons from β decay [7], protons [8] or α particles [9].

Double-sided segmented silicon strip detectors (DSSSD) are manufactured from large silicon wafers and are segmented with doped p-

side and n-side contacts on their front and back side, respectively. Intersecting areas of both N_p p- and N_n n-side segments form $N_n \times N_p$ individual *pixel* segments allowing for a high two-dimensional detector granularity. This is required to obtain an optimum position resolution, to measure high multiplicities, and to reject signal pile-up. DSSSDs are often employed in demanding experimental environments and have to withstand high count rates of impinging nuclei.

Livingston et al. reported on heavy ion radiation damage induced by α particles and fission fragments of a ^{252}Cf source in a 100 μm thick DSSSD in 1995 [10]. The amount of collected charge was observed to increasingly decline, resulting in a gradual downward shift of the measured particle energies and a reduced energy resolution for an integrated incident particle flux of up to $\approx 4 \times 10^6$ particles/ mm^2 . In addition, higher accumulated radiation doses caused a fatal resistance breakdown of the SiO_2 inter-strip isolation on the detector side facing the impinging ions, effectively destroying the segmentation of the detector. Barlini et al. [11] reported on the impact of radiation damage on the pulse-shape analysis performance of silicon detectors irradiated by heavy ions with $A \sim 120 - 130$. A linear decrease of the total

* Corresponding author.

E-mail address: andreas.vogt@ikp.uni-koeln.de (A. Vogt).

collected charge was observed as a function of the increasing fluence.

These effects limit the lifetime of the detector in an experiment and, in an early stage, the quality and the resolution of the recorded energy spectra. The illumination of the detector is often not homogeneous due to the angular dependence of scattering cross sections, beam defocusing, local target inhomogeneities or diverging target thicknesses. Consequently, radiation damage of the detector may also be distributed non-homogeneously. Position-dependent effects of radiation damage in DSSSDs were first described by Iwata et al. [12]. The group measured signal amplitudes as a function of the bias voltage and hit position on irradiated detectors by using a laser test stand. Position-dependent signal amplitudes and charge losses were observed both below and above the full depletion voltage.

A careful energy calibration of the detector system is crucial for e.g. spectroscopic applications in which a precise energy has to be measured. Modern self-consistent or *intrinsic* calibration approaches [13–15] employ the information from the strips on one side of the detector as references to calibrate the strips on the other side and vice versa. However, these calibration methods require that the response and the resolution of the segments are independent of the position of the impinging particle on the detector. Detector parts that are subject to heavier radiation damage yield an incomplete charge collection on the front- and back-side electrodes which needs to be corrected in calibration procedures that are highly position dependent.

This paper discusses the impacts of radiation damage and degradation effects on the detector response of double-sided silicon strip detectors and is organized as follows: The experimental setup and the data acquisition are comprised in Section 2. Data from an in-beam experiment employing a DSSSD, presented in Section 3, show an advancing degradation with increasing irradiation. A refined analysis of another irradiated detector is featured in Section 4. The response of both p and n-side faces is investigated. A position-resolved calibration method is presented in Section 6. It is based on the fact that each event is registered simultaneously on the p- and n-side segments. This enables an optimum performance of the degraded detector. The paper closes with a summary and conclusions.

2. Experimental setup and detectors

The two circular DSSSDs described in this article are $\sim 310(10)$ μm thick. They have a geometrical outer diameter of 100 mm and an inner hole of 28 mm diameter. Inner and outer diameter of the active area are 32 and 85 mm, respectively. The silicon wafers were manufactured by RADCON Ltd. (Zelenograd, Russia). The silicon disks were mounted and bonded onto printed circuit boards at the University of Lund, Sweden. The active area is divided into 64 radial segments (sectors) on the p-type junction side and into 32 annular segments (rings) on the ohmic n-side. Therefore, the detectors have a granularity of 2048 virtual pixels by combining the intersecting areas on the front and back side. The pixels cover areas from (innermost) 5.3 to (outermost) 13.7 mm². Photographs of both front and back side are presented in Fig. 1. Full depletion in reversed bias is reached at a voltage of 50 V. The SiO₂ surface passivation layer is reported to be 0.48 μm thick on the junction side and 1.9(2) μm on the ohmic side. Adjacent sectors and rings are isolated against each other by an inter-sector or inter-ring area of quoted 110 μm width.

Surface features of a DSSSD of the same type as described above were investigated employing atomic-force microscopy (AFM). The AFM measurements were obtained on an Asylum Research MFP-3D Infinity (Santa Barbara, CA, USA), using the non-contact AC mode under ambient conditions. The used cantilevers were AC200TS-R3 (Olympus, Tokyo, Japan) with a nominal resonance frequency of 115 kHz and a spring constant of 9 N/m. Fig. 1(c) shows an area of 90 \times 90 μm^2 from an AFM measurement of the sector side. The image is made at the edge between a sector and an inter-sector area as visible as black lines in Fig. 1(a). The roughness [16] in the measured section is

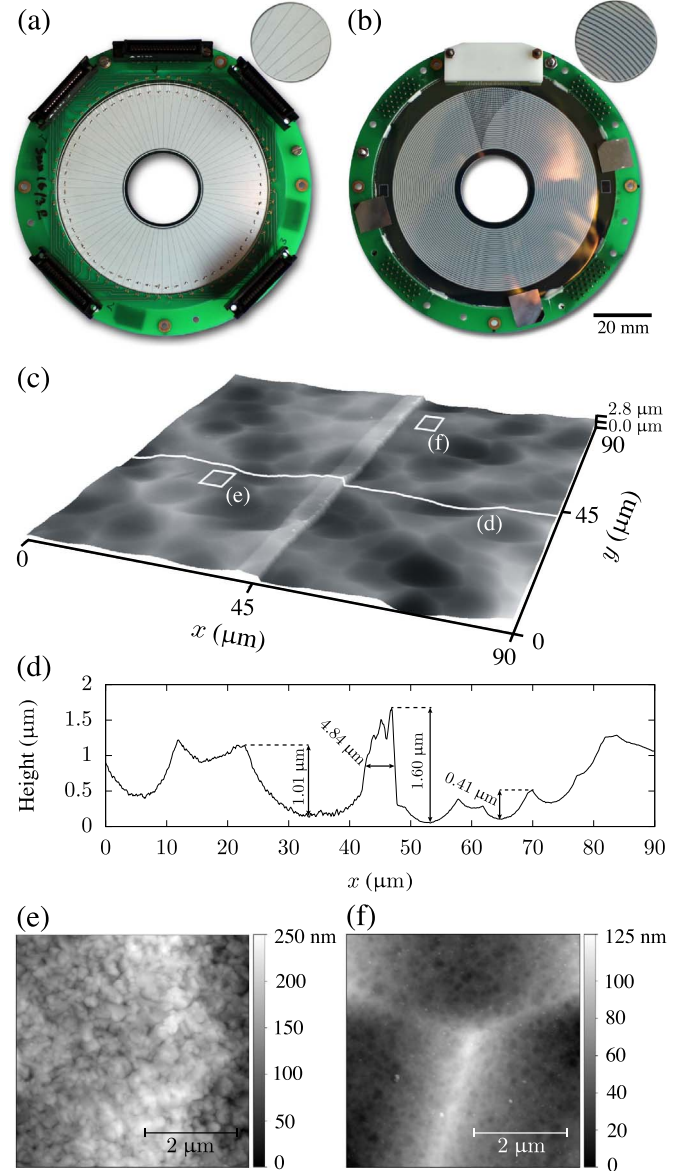


Fig. 1. (a) Photograph of the front side of the DSSSD segmented into sectors, (b) back side of the detector with ring segments. Closeups of the ring and sector segmentation are shown in the insets. (c) 90 \times 90 μm^2 AFM image of the DSSSD surface of the sector side at the edge between a sector and an inter-sector area. (d) One-dimensional projection along the white line marked in (c). (e) and (f): Closeup AFM measurements of the insets marked in (c).

$R_a = 0.322$ μm . A one-dimensional projection along the white line in Fig. 1(c) is shown in panel (d). The coating at the ≈ 5 μm wide sector boundary between the sector and the inter-sector area has a height of $\Delta z = 1.6$ μm . The DSSSD's SiO₂ passivation layer surface features irregular piles and valleys with relative heights of up to 1 μm . More detailed images of the depicted insets in Fig. 1(c) are presented in Figs. 1(e) and (f). Here, different substructures exhibit grainy textures with height differences in the order of $\Delta z = 100$ to 200 nm.

A first DSSSD was investigated in a dedicated experimental setup at the University of Cologne. The detector was previously used in an in-beam experiment to detect light particles from (d,p) reactions in inverse kinematics using a ⁴⁸Ti beam at an energy of 100 MeV, impinging on a deuterated titanium target [4,17]. The detector was mounted under forward direction with respect to the target position. The detector was then stored in darkness at room temperature for five years. In the present setup the DSSSD was operated under a vacuum of 2.0×10^{-2} mbar at room temperature with an operating voltage of 60 V.

The leakage currents of 1.6 μA did not change with larger voltages. The DSSSD was irradiated with a 3 kBq mixed triple- α source containing ^{239}Pu , ^{241}Am , and ^{244}Cm with α energies of 5157, 5486, and 5805 keV, respectively. The radioactive source was aligned to the center of the DSSSD and mounted within a distance of ≈ 3 cm, facing the ring side. The signals of the DSSSD are amplified by custom-made, charge-sensitive preamplifiers. Thereafter, the differential preamplifier signals are transmitted via shielded cables to MesytecTM STM-16 shaping/timing filter amplifiers and are then digitized by three CaenTM V 785 analog-to-digital converters. Time signals relative to time stamps produced by the data-acquisition system are recorded by a CaenTM V 775 time-to-digital converter. Data readout, event building and data transport is managed by a front-end VME PowerPC (PPC) with a 200 MHz CES RIO2-8064 WL processor running the head- and diskless operating system LynxOS together with the GSI Multi-Branch System (MBS) software [18]. The PPC sends blocks of formatted events to a linux host computer via ethernet running the data-acquisition software MAR₂BQU [19]. A Triva 5 trigger module [20] synchronizes the readout. This setup enables the readout of all 96 DSSSD channels independently and simultaneously.

A second DSSSD detector was employed in combination with the Advanced Gamma-Ray Tracking Array (AGATA) in its demonstrator configuration [21,22] in an in-beam γ -ray spectroscopy experiment [5,23] performed in inverse kinematics to populate excited states in ^{140}Ba at the Laboratori Nazionali di Legnaro (LNL). A beam of ^{136}Xe was accelerated by the PIAVE-ALPI accelerator complex with an intensity of 0.5–1 pA onto a 0.915(11) mg/cm² thick self-supporting target made of ^{12}C . Runs were performed at two different beam energies of 500 and 546 MeV, respectively. The data acquisition required at least one particle and one γ -ray in coincidence. Hence, the detection of elastically (Rutherford-) scattered beam ions did not trigger the data-acquisition system. The detector was mounted under forward angles covering a polar-angular range from 25.6° to 51.8° at a distance of 33.4 mm from the target. The radial sector segments faced the beam. The DSSSD detected recoiling ^{12}C ions, target-like few-nucleon transfer products, and α particles from the breakup of ^8Be produced in the α -transfer reaction $^{12}\text{C}(^{136}\text{Xe}, ^{140}\text{Ba})^8\text{Be}$. All heavy ions were completely stopped in the DSSSD. The accumulated radiation dosage during the experiment is estimated to be approx. 3×10^6 ^{12}C ions/mm², which is comparable to the dosage described by Livingston et al. [10] to cause deteriorated energy spectra. Two adjacent sectors were interconnected to reduce the 64 back-side sectors to only 32 channels. In the following, the outermost ring is labeled as 0 and, subsequently, the innermost one as ring 31. The sectors are labeled counterclockwise from 0 to 63 (Cologne DSSSD) or 0–31 (AGATA +DSSSD setup), respectively.

3. Degradation in in-beam experiments

During the AGATA+DSSSD experiment, a drastic change of the detected energy spectrum is observed with increasing irradiation. The pulse-height spectrum of DSSSD ring 5 as a function of the event number is presented in Fig. 2 for the 546-MeV run with a thin carbon target. The label (i) denotes events of impinging ^{12}C nuclei after Coulomb excitation of the ^{136}Xe beam. ^{11}B and ^{10}Be recoils after proton pick-up reactions are labeled as (ii). The pattern labeled as (iii), originates from fusion-evaporation reactions with α particles in the exit channel. The corresponding detector signal even drops below the detector threshold and gradually disappears after half of the run time. Hence, these events of interest could not be recorded by the data-acquisition system any more. Moreover, the shape of the measured pulse-height distribution changes with increasing irradiation; the separability between the distributions (i) and (ii) becomes less pronounced and vanishes at the end of the experiment (marked as B). The decrease in pulse height over the experiment is attributed to the advancing degradation of the detector and a reduced charge collection

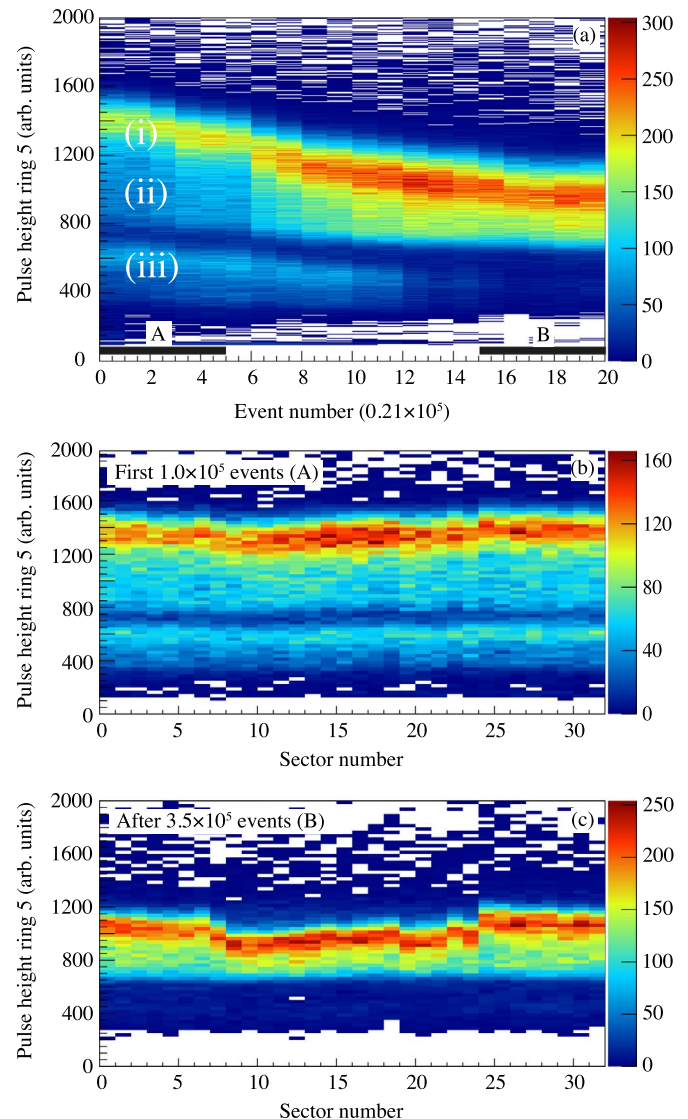


Fig. 2. (a) Spectrum of measured pulse heights in ring 5 as a function of the event number in the 546 MeV run with a thin carbon target. The first 25% events of the run are labeled as region A, the last 25% of the data are labeled as region B. (b) Front-back coincidence matrix of ring 5 for region A. (c) A similar matrix for region B. Pairs of adjacent strips are short-circuited and joined together. The resulting 32 sectors are labeled counterclockwise.

as discussed before.

As the generated electron and hole charges have to be registered on both p-side and n-side for each event, mutual consistency of p-side and n-side charges is anticipated. To cope with the observed pulse-height shifts and the peak-shape distortions, the 64-fold electric segmentation of the DSSSD into 32 rings and 32 combined sectors is discarded. Instead, a software-based segmentation into 1024 virtual pixels, characterized by the intersection between one sector and one ring, is employed to study the response of the detector.

Fig. 2(b) shows an example of a two-dimensional matrix of the pulse-height measured by the fifth front-side ring plotted against the back-side sector number in which a coincident signal above 300 arb. units was detected. Only the first 25% of the recorded dataset (1.0×10^5 particles impinging into the ring, marked as region A in Fig. 2(a)) were taken into account. In this representation the pulse-height spectrum of ring 5 is split with respect to the simultaneously hit sector and comprises all 32 single pixel spectra along the ring. The shapes of the pulse-height distributions are expected to be the same in all pixels along the ring for a non-degraded detector. Small deviations are

observed already at the beginning of the experiment, partially, due to the breaking of the symmetry of the setup as a consequence of a small displacement of the detector with respect to the beam axis. Fig. 2(c) shows a similar plot for the last 25% of the events (after 3.2×10^5 impinging particles, marked as region B in Fig. 2(a)) of the run. Obviously, the detected pulse heights decrease substantially by approx. 30% after a considerable irradiation of the detector. Furthermore, a strong dependence of the detected pulse heights on the location of the impinging particles within the ring area is observed. A much larger decrease in pulse-height is observed for the pixels formed by the sectors from no. 8 to no. 24. These differences in the deduced particle energies result in a broadening of the peak when summing over all sectors, and, therefore, a worse energy resolution.

The non-uniform decrease in measured pulse height is quantified by introducing a *damage parameter* κ_j which is defined as follows:

$$\kappa_j = \frac{A_j}{A_0} \sum_{i=0}^{31} \left| 1 - \frac{E_i^j}{\bar{E}_j} \right| \quad (1)$$

In this definition, \bar{E}_j is the mean pulse height of all peak positions in the pixel pulse-height spectra for ring j ; E_i^j is the peak position in the spectrum of the i -th pixel for ring j . The damage parameter is normalized to the area by weighting the area A_j of ring j to the one of the outermost ring, A_0 . In the case of an ideal detector, $\bar{E}_j = E_i^j$ is expected for a given ring number j and all involved pixels $i \in [0: 31]$; consequently, the damage parameter κ_j would be zero. κ_j is plotted against several accumulated event numbers for the rings 1, 2, 5, 14, 21, 28, and 30 in Fig. 3. In the example given in Fig. 2, $\kappa_{\text{ring } 5}$ increases from 0.40 up to 1.70 at the end of the experiment.

The first κ_j values are calculated after an overall accumulated dose of 1.0×10^5 particles in the experiment. The damage parameters of all rings already have a small non-zero value at the beginning of the measurement due to a slight displacement of the detector within the scattering chamber. The particle load of the DSSSD is dominated by Rutherford-scattered beam particles. The Rutherford cross section's maximum is at 0° and rapidly decreases with increasing angles θ in the center-of-mass system. In inverse kinematics, $\theta_{\text{cm}} = 0^\circ$ for recoils corresponds to $\theta_{\text{lab}} = 90^\circ$ in the laboratory system; here the scattering cross section for ^{12}C target particles reaches its maximum and decreases to smaller scattering angles. ^{136}Xe beam particles are maximally scattered by 5° and do not impinge the DSSSD. Consequently, more severe radiation damage is expected at the outer rings with the $^{12}\text{C}(^{136}\text{Xe}, x)$ reaction. Indeed, a large increase of κ_j is observed along outer rings which were exposed to larger accumulated radiation doses. On the contrary, the damage parameters of the inner

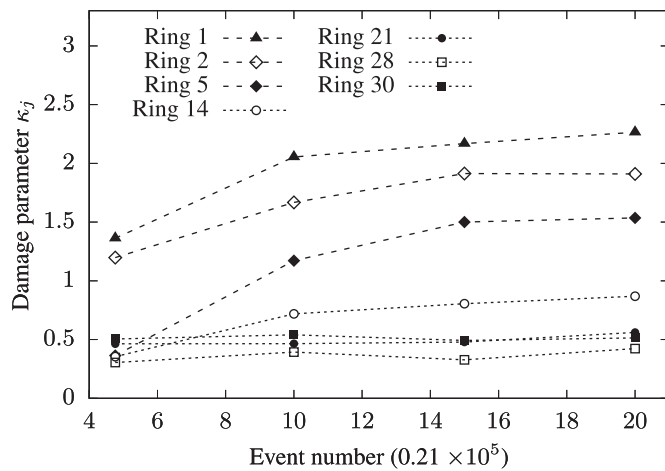


Fig. 3. Damage parameters κ_j of several DSSSD rings which were exposed to varying accumulated doses in the AGATA experiment. The outermost ring is labeled as 0 was exposed to the highest dose, the innermost ring is labeled as 31 and was exposed to the lowest dose. See text for details.

rings stay constant during the beam time as the scattering cross section is much lower for those small angles. It is worthwhile to mention that the extent of radiation damage, quantified by the damage parameter, does not increase linearly with the number of impinging particles.

4. Detector response and energy correlations

Precise knowledge of the detector response and correlations between the detector segments is crucial in order to investigate the behavior of a DSSSD after degradation. In-depth studies of charge-sharing effects along inter-ring and inter-sector gaps between adjacent segments were subject to recent publications. Yorkston et al. [24] first reported on anomalous charge-sharing effects for α particles penetrating the inter-strip gaps in silicon strip detectors in 1987. Signals of opposite polarity were induced on adjacent strips and explained by a model that incorporates surface charges trapped on the Si-SiO₂ interface between the adjacent strips. The effect was also described for impinging α particles [25], proton and Li beams [26], γ rays [27], infrared laser light [28,29], as well as low-energy x rays [30]. Positive charges within the SiO₂ surface layers induce an electron-accumulation layer at the interface between the SiO₂ and n-type silicon. Ionizing radiation may further increase the density of positive oxide charges and, therefore, produces hole traps at the Si-SiO₂ interface, resulting in charge collection losses [30].

Recently, Torresi et al. [31] characterized the impact of ^7Li and ^{16}O beams at various energies from 6 to 50 MeV and different applied bias voltages on inter-strip gaps. Signals of positive and negative polarities were recorded at the same time. The study showed that when particles are injected from the ohmic side, opposite-polarity signals for inter-strip events are observed in the front strips and disappear in the back strips. In 2014, Grassi et al. [32] performed a systematic study of signal amplitudes from adjacent strips and energy correlations at the inter-strip gaps. Two DSSSDs of different thicknesses at various detector bias voltages were scanned along front and back inter-strip regions using proton micro-beams. Again, the group detected inverted-polarity signals at the front-face. Inverted polarity signals in the back were only observed for protons punching through a thinner detector. The experimental observations were compared with the results of simulations based on the Shockley-Ramo-Gunn framework. A qualitative reproduction of all the observed charge-sharing effects was obtained by assuming a buildup of positive charge at the oxide interface in the front inter-strip region.

Compatible results were obtained in this study; Fig. 4(a) shows a correlation matrix of the pulse heights detected in sector 9 plotted against the pulse heights of sector 8 of the DSSSD in the Cologne setup. The pedestal, labeled as region A, was not calibrated to zero in order to investigate charge-sharing effects in detail. The additional event clusters in the pedestal region originate from crosstalk with full-energy depositions in next-neighboring sectors. Events within region B correspond to full-energy events in sector 8 or sector 9, respectively. Events located along the diagonal line C joining the two regions B correspond to a charge sharing between two adjacent sectors when a particle impinges the inter-sector gap. Both the ratio of the inter-gap area and the geometric active area as well as the ratio of inter-gap events and full-energy events amount to $\sim 1.2\%$. The lines between A and B are not perpendicular but close in a scissors-like manner due to electronic crosstalk within the preamplifiers. Events between A and B correspond to charge sharing between sectors 8 and 7, or 9 and 10, respectively.

A typical pulse-height correlation of adjacent rings is shown in Fig. 4(b). The measured pulse-height of ring 5 is correlated to the one of ring 6. Whereas a more pronounced region A and the full-energy deposition in region B resemble the behavior of the sector-sector correlation shown in Fig. 4(a), the events on the charge-sharing diagonal are not present. A more complicated structure, marked as region C, emerges in the matrix. These structures are interpreted as signals of

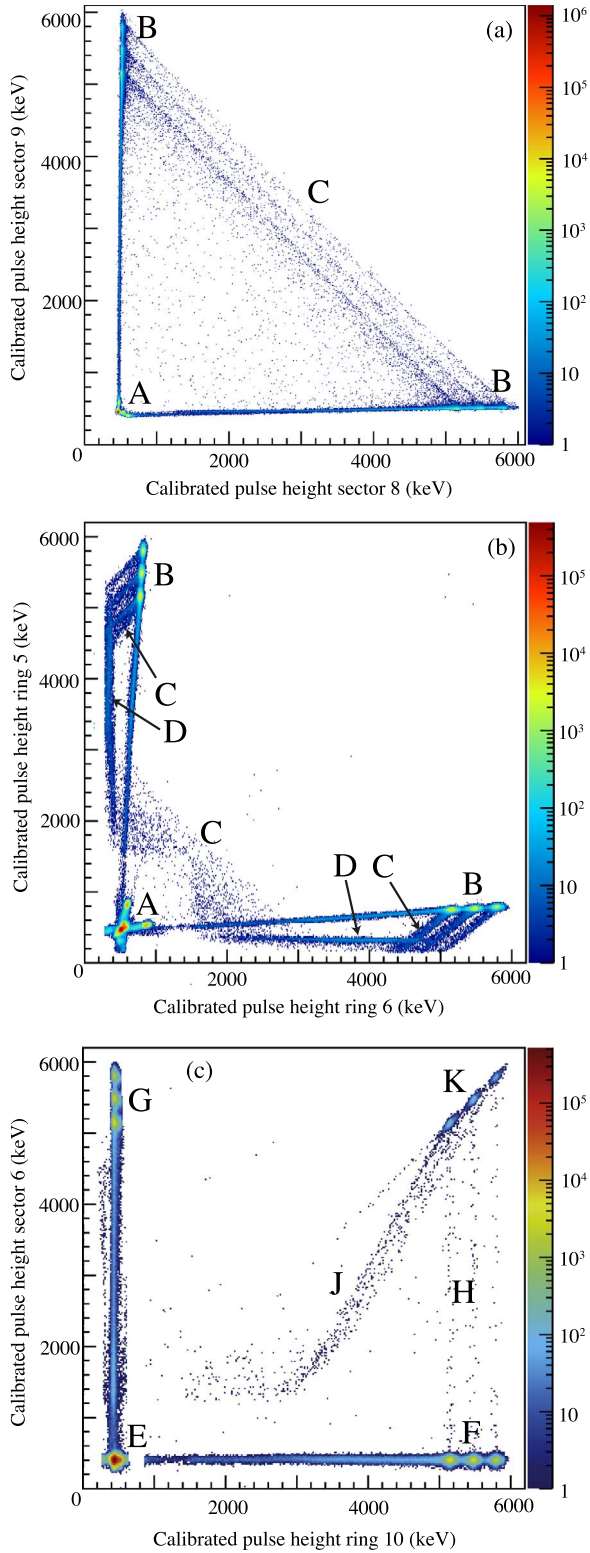


Fig. 4. Pulse-height correlation matrices of (a) two neighboring back sectors and (b) two neighboring front rings. (c) Pulse-height correlation between front-side ring 10 and back-side sector 6. See text for details.

reversed polarity, comparable to the ones observed in Refs. [24,27,31,32]. We note that the employed analog-to-digital converters are only able to read out one signal polarity. Signals with opposite polarity are only visible in the correlation matrix since the electronic crosstalk creates measurable signals above the baseline in adjacent rings, even though no particle is

impinging that segment. The electronic crosstalk between adjacent rings is more pronounced than between neighboring sector, possibly due to a stronger capacitive coupling. Crosstalk with other neighboring rings causes the structures labeled as D.

A correlation matrix between sector 6 and ring 10 is depicted in Fig. 4(c). The pedestal is labeled as region E, region K comprises particles depositing their full energy in the pixel defined by ring 10 and sector 6. The region labeled as F comprises particles which impinge into ring 10 and a corresponding front sector different than sector 6. Similarly, region G contains all events in which the particles enter sector 6 and not ring 10. Events for which the particles impinge through the inter-sector area of sector 6 and deposit their full energy in ring 10 are highlighted in region H. The charge collection of inter-ring events is, as aforementioned, influenced by an effective surface charge, yielding a reduced pulse-height measured at the (back) sector side of the detector. Therefore, sector 6 never registered the full energy in region J. Front-back coincidence matrices as shown in Fig. 2(b) and (c) are independent from the behavior of the electronics since only the pulse-height of one ring or sector is plotted with a gate on the energy detected by the segment behind. All of these events are comprised in region K of the front-back correlation matrices in Fig. 4(c).

The radiation damage of the Cologne DSSSD is visualized in Fig. 5. The color code displays the absolute energy difference between the 5.486 MeV ^{241}Am α -particle and the measured energy for each pixel after fitting the peaks in the front-back correlation matrices (cf. region K in Fig. 4(c)). Black-colored pixels do not show sufficient peak resolution. The innermost parts of the detector are subject to more severe radiation damage compared to the outer parts of the detector in the Cologne experiment, resulting in reduced measured energies due to incomplete charge collection on one of the ring or sector electrodes. Summarizing, radiation damage has no significant effects on the general behavior of the DSSSD, as previously described by Torresi et al. [31] and by Grassi et al. [32].

5. Position-resolved degradation effects

The dependence of the detected pulse heights with respect to the location of the impinging particle is investigated in detail with the Cologne DSSSD setup. In a first approach, all ring and sector channels are calibrated by fitting linear functions to the ring and sector pulse-height spectra. Thus, the 2×96 absolute calibration coefficients (gain and offset) map the measured amplitudes to units of energy. Fig. 6(a)

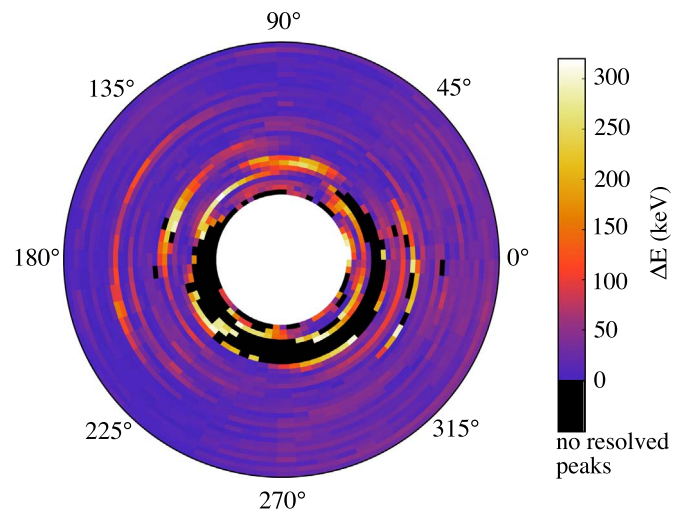


Fig. 5. Visualization of all 2048 virtual pixels formed by 32 ring and 64 sector segments of the Cologne DSSSD. The color code displays the absolute value of the deviation of the measured peak position with respect to the expected one at 5.486 MeV. This deviation is a measure for the effects of the radiation damage on the charge collection within the pixels.

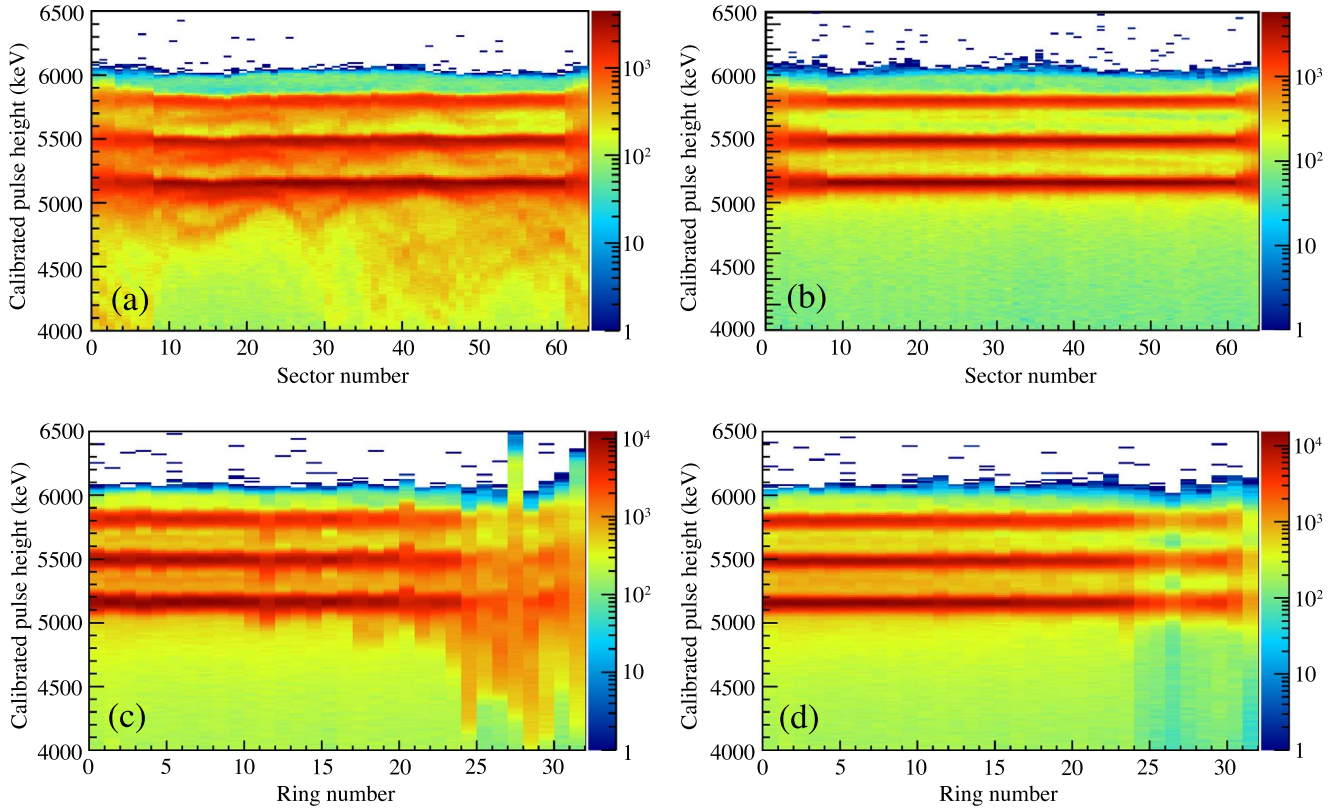


Fig. 6. (a) Calibrated pulse-height spectra of all 64 sectors of the Cologne DSSSD employing a linear calibration for each sector. Alongside the expected three peaks of the mixed triple- α source with α energies of 5157, 5486, and 5805 keV, additional repetitive patterns and tails are observed. (b) Same diagram as (a), with the new position-resolved calibration method based on front-back correlation; see text for details. (c) Similar diagram as presented in (a) for all 32 rings. The outermost ring is labeled as 0 and, consequently the innermost as 31. Note the broadening and blurring of the spectra in the seven innermost rings. (d) All ring spectra calibrated by the new position-resolved method.

and (c) show all calibrated sector and ring pulse-height spectra arranged in a matrix. For an ideal detector, three peaks above the background are expected for all ring and sector spectra. Instead, additional features are observed: The sector spectra in 6(a) exhibit low-energy tails and double-peak structures with a repetitive pattern along the sector number. Blurred and unresolved spectra are observed in the seven innermost rings (see Fig. 6(c)) where the most severe radiation damage is expected. In contrast to the detector used in the AGATA+DSSSD setup (Fig. 2), the Cologne DSSSD had been used, among others, in a $d(^{48}\text{Ti}, ^{49}\text{Ti})p$ experiment with a deuterated titanium target of $220 \mu\text{g}/\text{cm}^2$ thickness. The ring side of the DSSSD faced the beam. Despite the use of a thin Al absorber foil in front of the DSSSD, scattering Ti ions as well as ^{16}O target contaminants could still reach the detector. In the case of $^{48}\text{Ti}+^{16}\text{O}$ and symmetric $^{48}\text{Ti}+\text{Ti}$ scattering, the Rutherford cross section is maximum for small scattering angles in the laboratory frame. The impinging ions deposited their full energy within the first $30 \mu\text{m}$ of the detector. Inhomogeneous radiation damage is expected due to a 4.5° misalignment of the detector with respect to the plane perpendicular to the beam axis. Further details on the experiment and the rates are given in Ref. [4,17].

Fig. 7(a) shows a two-dimensional matrix of the pulse height measured by sector 17 plotted against the ring number in which a signal above 3 MeV was simultaneously detected [similar to the matrices in Figs. 2(b) and (c)]. Therefore, each bin on the abscissa contains the pulse-height spectrum of a single pixel formed by sector 17 with the corresponding ring behind. The projection onto the pulse-height axis yields the complete one-dimensional pulse-height spectrum of sector 17 and corresponds to the pulse-height spectrum in the bin for sector number 17 in Fig. 6(a). It exposes double-peak structures and tails. Fluctuations and a decrease in pulse-height are observed along the rings that were hit simultaneously with the sector – uncorrelated to the interconnected channels of the four sector pre-

amplifiers. The observed incomplete charge collection, especially in the innermost rings, is due to radiation damage as described by Livingston et al. [10]. A similar two-dimensional matrix shown in Fig. 7(c) shows the same decomposition of ring 20 into its 64 pixels (defined by the sectors). Again, the projection of the complete pulse-height spectrum is depicted on the right hand side and shows a wiggly pattern instead of the expected three straight lines. The projection corresponds to the spectrum in the bin corresponding to ring 20 in Fig. 6(b) and exhibits broad, overlapping peaks with a non-Gaussian shape. Subsequently, it is apparent that a precise energy calibration of the DSSSD is not feasible by means of a basic calibration set employing two parameters (offset and gain) for each ring and sector.

As there are no unexpected structures in the front-back correlation matrices for a single detector pixel as shown in Fig. 4(c), the origin of the distortions and the pulse-height shifts have to be attributed to the condition of the silicon wafer. Comprehensive measurements employing a signal generator (pulser) were performed to exclude any contributions of the preamplifiers and the subsequent electronics. In order to generate a correlation matrix as shown in Fig. 7(c), the pulser signal was injected into the read-out channel of a sector. Simultaneously, the pulser signal was also used to generate a signal in one of the ring-side read-out channels. This procedure was subsequently repeated for each of the 32 ring channels. The variation in the amplitude of the pulser signal is in the range of 0.2%, compared to observed shifts in pulse height of the order of several percent along the sectors. Thus, pulse-height shifts caused by the electronics are negligible.

6. Position-resolved calibration method

In order to correct for the distortions and pulse-height shifts, the software-based segmentation into virtual pixels is exploited. The

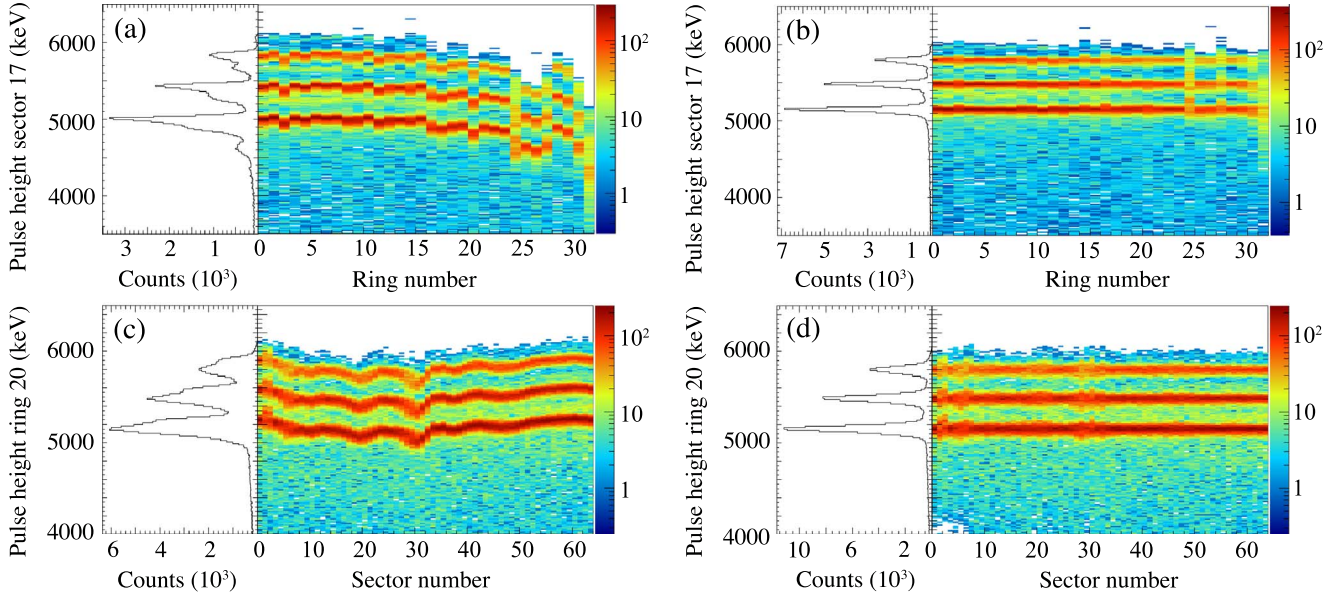


Fig. 7. (a) Right: Front-back pulse-height coincidence matrix of sector 17 of the Cologne DSSSD with the calibration as applied in Fig. 6(a). The outermost ring is labeled as 0, the innermost ring as 31. Left: Projection of the front-back pulse-height coincidence matrix on the y-axis, note the distorted spectrum with severe tails. (b) The same matrix as in (a), employing the new position-resolved calibration method. Note the improved energy resolution in the projection. (c) Front-back pulse-height coincidence matrix of ring 20. The 64 sectors are labeled counterclockwise. The projection of the pulse-height spectrum of the whole ring exhibits a poor energy resolution, due to the wiggly pattern in the coincidence matrix. Applying the new position-resolved calibration method (d), the resolution is improved dramatically.

granular segmentation of the DSSSD enables a position-resolved calibration which is employed by fitting all 2048 pixel ring-sector coincidence spectra like the examples in Figs. 7(a) and (c). In a brute-force approach a function comprising three Gaussian distributions, each with two exponential tails, is automatically fitted to the ring-sector coincidence spectra. Following the fit procedure, the spectra of all 2048 pixels are properly calibrated to the three α energies of the mixed- α source and reassembled to the corresponding 64 sector and 32 ring spectra.

As an example, the resulting spectra of ring 27 and sector 17 in their matrix representation are shown in Figs. 7(b) and (d) after the position-resolved calibration. All pixel pulse-height spectra are now well-calibrated in both the sector and ring matrices, exhibiting three Gaussian-like peaks at the energies of the mixed α source. The resulting one-dimensional projections are shown in the left panels of Figs. 7(b) and (d). The energy resolution for each entire ring and each entire sector is only limited by the resolution of the individual pixels, and, thus, is the optimum achievable with the detector. If the observed height variance presented in Figs. 1(c) and (d) also corresponds to a variation of the dead-layer thickness, and, thus, a variation in energy loss of the impinging particles, the energy resolution of the single pixels might *a priori* be limited – besides by microscopic defects or by the influence of the detector temperature. The results of the position-resolved calibration method are summarized in Fig. 6. Subfigs. (b) and (d) show all ring and sector pulse-height spectra summed over all simultaneously hit sector and rings, respectively, comprised in a two-dimensional matrix. The additional tails and repetitive patterns, that were visible after the conventional calibration in Fig. 6(a), vanish. Remaining tails originate from the local radiation damage effects in the individual pixels or changes in radiation damage level on scales smaller than the detector segmentation. Such cases cannot be treated by the position-resolved calibration method. The pulse-height spectra of the innermost rings, initially heavily distorted as shown in Fig. 6(c), show three distinct and resolved peaks for all rings after employing the new calibration procedure. Note that few of the pixels do not have a sufficient energy resolution to be fitted with three Gaussians due to severe radiation damage. Consequently, these pixels are excluded in the further analysis (cf. black colored pixels in Fig. 5), reducing the

statistics for the innermost rings in Fig. 6(d). However, the poor energy resolution of such pixels renders them useless for typical applications of DSSSD detectors such as particle identification. The corresponding events would mainly contribute to background and, thus, degrade the overall quality of the data. Regarding the example of ring 27, a total of 28 out of 64 pixels do not show resolvable peak structures. The corresponding ring pulse-height spectrum is shown in the inset of Fig. 8. However, by restricting the analysis to the remaining 36 pixels for that ring, approx. 60% of the ring's active area can be calibrated by the new method and provides good energy resolution. The whole ring would have been discarded by employing a standard calibration procedure. The number of excluded pixels per ring is given in the top panel of Fig. 8, in total, 89.7% of the active area is recovered by employing the position-resolved calibration method.

The energy resolution and valley-to-peak ratio of the Cologne DSSSD prior and after the enhanced position-resolved calibration are presented in Fig. 8. The damage parameters κ , introduced in Section 3 are shown in the bottom panel of Fig. 8. An improvement of approx. one order of magnitude is observed for most of the rings. The parameter κ is close to 0 in the outer rings and is significantly reduced along the severely radiation-damaged inner rings. The mid panel of Fig. 8 compares the FWHM and the valley-to-peak ratio at 5.5 MeV prior and after the calibration. The resolution for the severely-damaged inner rings is improved drastically by up to a factor of 3.5. The valley-to-peak ratio is defined as the inverse ratio of the peak height at 5486 keV and the valley between that peak and the one at 5157 keV (marked by arrows in the inset of Fig. 8). It decreases significantly along the innermost rings. Altogether, the quality of the peaks is considerably increased.

7. Conclusions and outlook

The response and pulse-height correlations of two radiation-damaged DSSSDs were subject of this study. A first DSSSD was investigated in a dedicated experimental setup at the University of Cologne, another one was employed in an in-beam experiment in combination with the Advanced Gamma-Ray Tracking Array (AGATA). The DSSSDs are divided into 64 radial sectors and into 32 rings,

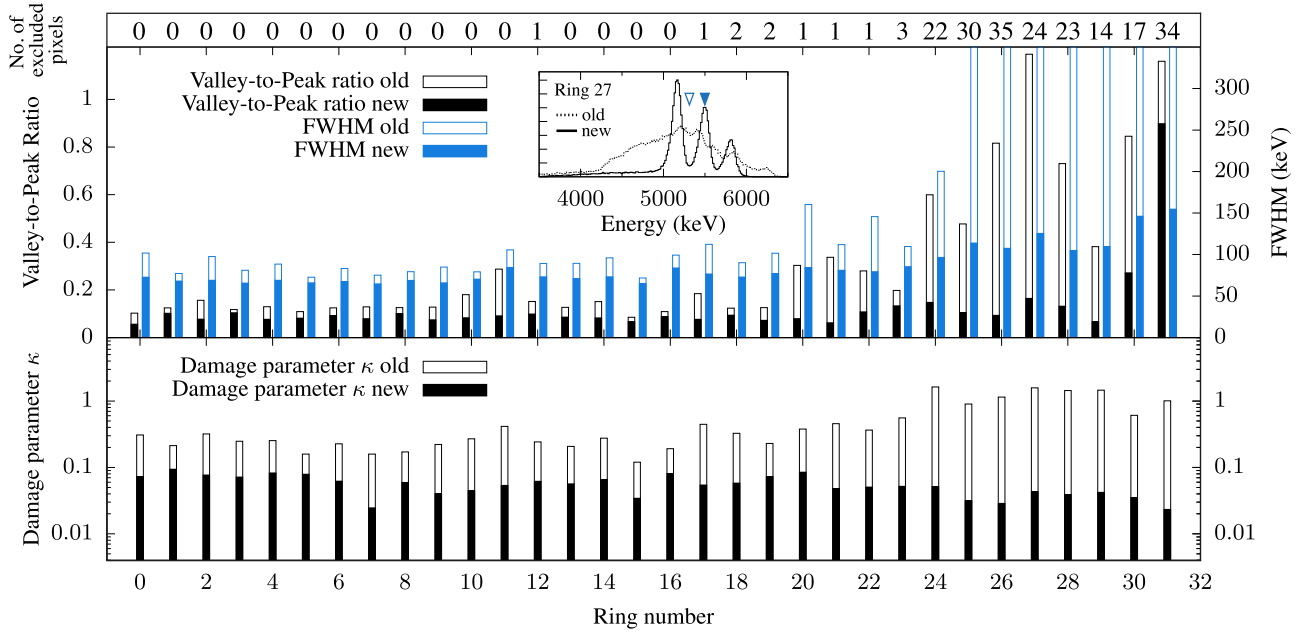


Fig. 8. (Top panel) Valley-to peak ratio (black) and FWHM (blue) prior (open bars) and after (filled bars) calibration with the novel calibration method. Note the clear decrease of the damage parameter and the valley-to-peak ratio after applying the position-resolved calibration method. The outermost ring is labeled as 0 and the innermost one as 31. The number of excluded pixels (see text for details) is given at the on top of the panel. (Inset) Pulse-height spectrum of ring 27 prior (dotted line) and after (solid line) the position-resolved calibration. Filled and open arrows mark the position of the two bins employed in the definition of the valley-to-peak ratio. (Bottom panel) Damage parameters κ (see Section 3 for details) of the Cologne DSSSD prior (unfilled bars) and after (filled bars) calibration with the position-resolved calibration method.

yielding a granularity of 2048 individual virtual pixels. After a considerable irradiation of the detector, the detected pulse heights decrease substantially. Different parts of the detector were exposed non-homogeneously to varying accumulated doses. A strong dependence of the detected energies on the location of the impinging particles within the ring or sector area is observed. Position-dependent incomplete charge collection due to radiation damage leads to different responses along single detector rings and sectors. This position-resolved radiation damage is quantified by introducing a damage parameter κ_j . A software-based segmentation into virtual pixels and corresponding front-back energy correlations were exploited to obtain a position-resolved calibration of DSSSDs. This calibration method allows for a significant enhancement of the energy resolution of radiation-damaged detectors. Single locally damaged pixels are excluded without losing the information of complete p- or n-side sectors. As DSSSDs are often employed in demanding experimental environments with high count rates of impinging nuclei for several days of beam time, the new calibration method is eminently suitable to cope and correct for advancing degradation and position-resolved radiation damage. Nevertheless, also non-instrumental modification of the pulse height is subject of the calibration procedure and is corrected for. In the future, an extension to correct for dead-layer effects can be straightforwardly implemented in the analysis. The introduced damage parameter κ may be applied in acceptance tests of segmented silicon detectors to judge the quality and homogeneity of the SiO₂ dead layers of factory-fresh DSSSDs. In a future study, one may further investigate to which extent annealing and a variation of the bias voltage might partially recover the standard calibration of each ring and strip and improve the spectroscopy performance. Ion-surface interactions of charged ions with grown mono-crystalline silicon and silicon-dioxide layers are subject to an active field of research. The formation of deep crater structures with widths of some few nanometers after heavy-ion impacts was observed in a variety of experiments [33–35]. Moreover, heavy-ion irradiation was found to induce phase separation at Si/SiO₂ interfaces [36]. In the future, surface features of silicon detectors before and after radiation damage are accessible to atomic-force microscopy or equivalent imaging techniques.

Acknowledgements

The research leading to these results has received funding from the German BMBF Grants No. 05P15PKFNA, No. 05P15PKFN1, No. 05P09RDFN4, No. 05P12RDFN8, and HIC for FAIR. A.V. and L.K. acknowledge support from the Bonn-Cologne Graduate School of Physics and Astronomy (BCGS). We thank the mechanics and electronics workshops of the IKP Cologne for their close cooperation and support.

References

- [1] P. Golubev, et al., The Lund-York-Cologne Calorimeter (LYCCA) concept, design and prototype developments for a FAIR-NUSTAR detector system to discriminate relativistic heavy-ion reaction products, Nucl. Instr. Meth. Phys. Res. A 723 (2013) 55–66. <http://dx.doi.org/10.1016/j.nima.2013.04.058>.
- [2] A. Ostrowski, et al., CD: a double sided silicon strip detector for radioactive nuclear beam experiments, Nucl. Instr. Meth. Phys. Res. A 480 (2–3) (2002) 448–455. [http://dx.doi.org/10.1016/S0168-9002\(01\)00954-8](http://dx.doi.org/10.1016/S0168-9002(01)00954-8).
- [3] N. Warr, et al., The Miniball spectrometer, EPJ A 49 (3) (2013) 1–32. <http://dx.doi.org/10.1140/epja/i2013-13040-9>.
- [4] F. Recchia, et al., Position resolution of the prototype AGATA triple-cluster detector from an in-beam experiment, Nucl. Instr. Meth. Phys. Res. A 604 (3) (2009) 555–562. <http://dx.doi.org/10.1016/j.nima.2009.02.042>.
- [5] C. Stahl, et al., Population of the 2_{ms}^+ mixed-symmetry state of ^{140}Ba with the α -transfer reaction, Phys. Rev. C. 92 (2015) 044324. <http://dx.doi.org/10.1103/PhysRevC.92.044324>.
- [6] R.-D. Herzberg, P. Greenlees, In-beam and decay spectroscopy of transfermium nuclei, Prog. Part. Nucl. Phys. 61 (2) (2008) 674–720. <http://dx.doi.org/10.1016/j.ppnp.2008.05.003>.
- [7] J. Taprogge, et al., $1p_{3/2}$ proton-hole state in ^{132}Sn and the shell structure along $N = 82$, Phys. Rev. Lett. 112 (2014) 132501. <http://dx.doi.org/10.1103/PhysRevLett.112.132501>.
- [8] K. Geibel, Search for Proton Emission in ^{54}Ni and Multi-Nucleon Transfer Reactions in the Actinide Region, (Ph.D. thesis), Universität zu Köln, 2012.
- [9] P. Reiter, et al., Ground-state band and deformation of the $Z = 102$ isotope ^{254}No , Phys. Rev. Lett. 82 (1999) 509–512. <http://dx.doi.org/10.1103/PhysRevLett.82.509>.
- [10] K. Livingston, P. Woods, T. Davinson, A. Shotton, Heavy ion radiation damage in double-sided silicon strip detectors, Nucl. Instr. Meth. Phys. Res. A 370 (23) (1996) 445–451. [http://dx.doi.org/10.1016/0168-9002\(95\)00808-X](http://dx.doi.org/10.1016/0168-9002(95)00808-X).
- [11] S. Barlini, et al., Effects of irradiation of energetic heavy ions on digital pulse shape analysis with silicon detectors, Nucl. Instr. Meth. Phys. Res. A 707 (2013) 89–98. <http://dx.doi.org/10.1016/j.nima.2012.12.104>.
- [12] Y. Iwata, et al., A radiation damage test for double-sided silicon strip detectors,

- Nucl. Instr. Meth. Phys. Res. A 489 (1–3) (2002) 114–120. [http://dx.doi.org/10.1016/S0168-9002\(02\)00892-6](http://dx.doi.org/10.1016/S0168-9002(02)00892-6).
- [13] M. Reese, J. Gerl, P. Golubev, N. Pietralla, Automatic intrinsic calibration of double-sided silicon strip detectors, Nucl. Instr. Meth. Phys. Res. A 779 (2015) 63–68. <http://dx.doi.org/10.1016/j.nima.2015.01.032>.
- [14] R. Qiao, Y. Ye, J. Wang, Z. Li, H. You, Z. Yang, B. Yang, A. New, Uniform calibration method for double-sided silicon strip detectors, IEEE Trans. Nucl. Sci. 61 (1) (2014) 596–601. <http://dx.doi.org/10.1109/TNS.2013.2295519>.
- [15] M. Uroić, et al., Improvements in data analysis obtained by large-area silicon ΔE - E detector telescopes, Eur. Phys. J. A 51 (8) (2015) 93. <http://dx.doi.org/10.1140/epja/i2015-15093-0>.
- [16] Asylum Research, Measuring Surface Roughness with Atomic Force Microscopy 2013. <https://www.asylumresearch.com/Applications/SurfaceRoughness/SurfaceRoughness.pdf>.
- [17] F. Recchia, In-beam test and imaging capabilities of the AGATA prototype detector, (Ph.D. thesis), Università degli Studi di Padova, 2008.
- [18] H.G. Essel, N. Kurz, The general purpose data acquisition system MBS, IEEE Trans. Nucl. Sci. 47 (2) (2000) 337–339. <http://dx.doi.org/10.1109/23.846176>.
- [19] R. Lutter, et al., MARaBOU - a MBS and ROOT based online/offline utility, IEEE Trans. Nucl. Sci. 47 (2) (2000) 280–283. <http://dx.doi.org/10.1109/23.846164>.
- [20] J. Hoffmann, N. Kurz, M. Richter, TRIVA5 VME Trigger Module Handbook, Gesellschaft für Schwerionenforschung mbH Darmstadt, 2009. https://www.gsi.de/fileadmin/EE/Module/TRIVA/triva5_5.pdf.
- [21] S. Akkoyun, et al., AGATA - Advanced GAMMA Tracking Array, Nucl. Instr. Meth. Phys. Res. A 668 (2012) 26. <http://dx.doi.org/10.1016/j.nima.2011.11.081>.
- [22] A. Gadea, et al., Conceptual design and infrastructure for the installation of the first AGATA sub-array at LNL, Nucl. Instr. Meth. Phys. Res. A 654 (1) (2011) 88–96. <http://dx.doi.org/10.1016/j.nima.2011.06.004>.
- [23] C. Stahl, New methods for the γ -ray spectroscopy with position-sensitive detector systems, (Ph.D. thesis), TU Darmstadt, 2015. <http://tuprints.ulb.tu-darmstadt.de/id/eprint/4955>.
- [24] J. Yorkston, A. Shotter, D. Syme, G. Huxtable, Interstrip surface effects in oxide passivated ion-implanted silicon strip detectors, Nucl. Instr. Meth. Phys. Res. A 262 (2) (1987) 353–358. [http://dx.doi.org/10.1016/0168-9002\(87\)90873-4](http://dx.doi.org/10.1016/0168-9002(87)90873-4).
- [25] Y. Blumenfeld, et al., MUST: A silicon strip detector array for radioactive beam experiments, Nucl. Instrum. Methods Phys. Res. Sect. A. 421 (3) (1999) 471–491. [http://dx.doi.org/10.1016/S0168-9002\(98\)01178-4](http://dx.doi.org/10.1016/S0168-9002(98)01178-4).
- [26] A. Castoldi, et al., Experimental investigation of the impact of inter-strip incidence on the signal shape in Double Sided Silicon Strip Detectors for particle identification, in: 2013 IEEE Nuclear Science Symposium and Medical Imaging Conference (2013 NSS/MIC), 2013, pp. 1–7. <http://dx.doi.org/10.1109/NSSMIC.2013.6829489>.
- [27] S. Takeda, et al., Development of double-sided silicon strip detectors (DSSD) for a Compton telescope, Nucl. Instr. Meth. Phys. Res. A 579 (2) (2007) 859–865. <http://dx.doi.org/10.1016/j.nima.2007.05.305> (Proceedings of the 6th Hiroshima Symposium on the Development and Application of Semiconductor Detectors).
- [28] V. Eremin, et al., The charge collection in single side silicon microstrip detectors, Nucl. Instr. Meth. Phys. Res. A 500 (1–3) (2003) 121–132. [http://dx.doi.org/10.1016/S0168-9002\(03\)00330-9](http://dx.doi.org/10.1016/S0168-9002(03)00330-9).
- [29] A. Castoldi, et al., Laser mapping of the inter-strip response in double sided silicon strip detectors for particle identification, J. Instrum. 10 (01) (2015) C01017. <http://stacks.iop.org/1748-0221/10/i=01/a=C01017>.
- [30] T. Poehlsen, et al., Charge losses in segmented silicon sensors at the Si – SiO₂ interface, Nucl. Instr. Meth. Phys. Res. A 700 (2013) 22–39. <http://dx.doi.org/10.1016/j.nima.2012.10.063>.
- [31] D. Torresi, et al., Influence of the interstrip gap on the response and the efficiency of Double Sided Silicon Strip Detectors, Nucl. Instr. Meth. Phys. Res. A 713 (2013) 11–18. <http://dx.doi.org/10.1016/j.nima.2013.02.027>.
- [32] L. Grassi, et al., Study of the inter-strip gap effects on the response of Double Sided Silicon Strip Detectors using proton micro-beams, Nucl. Instr. Meth. Phys. Res. A 767 (2014) 99–111. <http://dx.doi.org/10.1016/j.nima.2014.08.009>.
- [33] F. Aumayr, S. Facsko, A. El-Said, C. Trautmann, M. Schleberger, Single ion induced surface nanostructures a comparison between slow highly charged and swift heavy ions, J. Phys. Condens. Matter 23 (39) (2011) 393001. <http://dx.doi.org/10.1088/0953-8984/23/39/393001>.
- [34] M. Tona, H. Watanabe, S. Takahashi, N. Nakamura, N. Yoshiyasu, M. Sakurai, T. Terui, S. Mashiko, C. Yamada, S. Ohtani, Nano-crater formation on a Si(1 1 1)-(7×7) surface by slow highly charged ion-impact, Surf. Sci. 601 (3) (2007) 723–727. <http://dx.doi.org/10.1016/j.susc.2006.11.002>.
- [35] E.M. Bringa, R.E. Johnson, Coulomb explosion and thermal spikes, Phys. Rev. Lett. 88 (2002) 165501. <http://dx.doi.org/10.1103/PhysRevLett.88.165501>.
- [36] W. Arnoldbik, D. Knoesen, N. Tomozeiu, F. Habraken, Nano-scale effects of swift heavy ion irradiation in sio_x layers and multilayers, Nucl. Instr. Meth. Phys. Res. B 258 (1) (2007) 199–204. <http://dx.doi.org/10.1016/j.nimb.2006.12.103> (Proceedings of the 16th International Workshop on Inelastic Ion-Surface Collisions).

Publication VI:
High-spin structures
in ^{132}Xe and ^{133}Xe
and evidence for isomers
along the $N = 79$ isotones

High-spin structures in ^{132}Xe and ^{133}Xe and evidence for isomers along the $N = 79$ isotones

A. Vogt,^{1,*} M. Siciliano,^{2,3} B. Birkenbach,¹ P. Reiter,¹ K. Hadyńska-Kłęk,³ C. Wheldon,⁴ J. J. Valiente-Dobón,³ E. Teruya,⁵ N. Yoshinaga,⁵ K. Arnsward,¹ D. Bazzacco,⁶ A. Blazhev,¹ A. Bracco,⁷ B. Bruyneel,⁸ R. S. Chakrawarthy,⁹ R. Chapman,¹⁰ D. Cline,¹¹ L. Corradi,³ F. C. L. Crespi,⁷ M. Cromaz,¹² G. de Angelis,³ J. Eberth,¹ P. Fallon,¹² E. Farnea,^{6,†} E. Fioretto,³ C. Fransen,¹ S. J. Freeman,⁹ B. Fu,¹ A. Gadea,¹³ W. Gelletly,¹⁴ A. Giaz,⁷ A. Görgen,^{15,16,12} A. Gottardo,³ A. B. Hayes,¹¹ H. Hess,¹ R. Hetzenegger,¹ R. Hirsch,¹ H. Hua,¹¹ P. R. John,^{2,6} J. Jolie,¹ A. Jungclaus,¹⁷ V. Karayonchev,¹ L. Kaya,¹ W. Korten,¹⁶ I. Y. Lee,¹² S. Leoni,⁷ X. Liang,¹⁰ S. Lunardi,^{2,6} A. O. Macchiavelli,¹² R. Menegazzo,⁶ D. Mengoni,^{18,2,6} C. Michelagnoli,¹⁹ T. Mijatović,²⁰ G. Montagnoli,^{2,6} D. Montanari,²¹ C. Müller-Gatermann,¹ D. Napoli,³ C. J. Pearson,²² Zs. Podolyák,¹⁴ G. Pollaro,²³ A. Pullia,⁷ M. Queiser,¹ F. Recchia,^{2,6} P. H. Regan,^{14,24} J.-M. Régis,¹ N. Saed-Samii,¹ E. Şahin,¹⁵ F. Scarlassara,^{2,6} M. Seidlitz,¹ B. Siebeck,¹ G. Sletten,²⁵ J. F. Smith,¹⁰ P.-A. Söderström,²⁶ A. M. Stefanini,³ O. Stezowski,²⁷ S. Szilner,²⁰ B. Szpak,²⁸ R. Teng,¹¹ C. Ur,⁶ D. D. Warner,^{29,†} K. Wolf,¹ C. Y. Wu,³⁰ and K. O. Zell¹

¹*Institut für Kernphysik, Universität zu Köln, D-50937 Köln, Germany*

²*Dipartimento di Fisica e Astronomia, Università di Padova, I-35131 Padova, Italy*

³*Istituto Nazionale di Fisica Nucleare, Laboratori Nazionali di Legnaro, I-35020 Legnaro, Italy*

⁴*School of Physics and Astronomy, University of Birmingham, Birmingham B15 2TT, United Kingdom*

⁵*Department of Physics, Saitama University, Saitama City 338-8570, Japan*

⁶*Istituto Nazionale di Fisica Nucleare, Sezione di Padova, I-35131 Padova, Italy*

⁷*Dipartimento di Fisica, Università di Milano and INFN Sezione di Milano, I-20133 Milano, Italy*

⁸*CEA Saclay, Service de Physique Nucleaire, F-91191 Gif-sur-Yvette, France*

⁹*Department of Physics and Astronomy, Schuster Laboratory, University of Manchester, Manchester M13 9PL, United Kingdom*

¹⁰*SUPA, School of Engineering and Computing, University of the West of Scotland, Paisley PA1 2BE, United Kingdom*

¹¹*Department of Physics, University of Rochester, Rochester, New York 14627, USA*

¹²*Lawrence Berkeley National Laboratory, Berkeley, California 94720, USA*

¹³*Instituto de Física Corpuscular, CSIC - Universidad de Valencia, E-46071 Valencia, Spain*

¹⁴*Department of Physics, University of Surrey, Guildford, Surrey GU2 7XH, United Kingdom*

¹⁵*Department of Physics, University of Oslo, P.O. Box 1048 Blindern, N-0316 Oslo, Norway*

¹⁶*Institut de Recherche sur les lois Fondamentales de l'Univers - IRFU, CEA/DSM, Centre CEA de Saclay, F-91191 Gif-sur-Yvette Cedex, France*

¹⁷*Instituto de Estructura de la Materia, CSIC Madrid, E-28006 Madrid, Spain*

¹⁸*Nuclear Physics Research Group, University of the West of Scotland, High Street, Paisley PA1 2BE, Scotland, United Kingdom*

¹⁹*Institut Laue-Langevin (ILL), 38042 Grenoble Cedex 9, France*

²⁰*Ruder Bošković Institute, HR-10 002 Zagreb, Croatia*

²¹*USIAS - Université de Strasbourg, IPHC-CNRS, F-67037 Strasbourg Cedex 2, France*

²²*TRIUMF, 4004 Wesbrook Mall, Vancouver, British Columbia, V6T 2A3 Canada*

²³*Dipartimento di Fisica Teorica dell'Università di Torino and INFN, I-10125 Torino, Italy*

²⁴*Radioactivity Group, National Physical Laboratory, Teddington, Middlesex TW11 0LW, United Kingdom*

²⁵*The Niels Bohr Institute, University of Copenhagen, Blegdamsvej 17, 2100 Copenhagen, Denmark*

²⁶*RIKEN Nishina Center, Wako, 351-0198 Saitama, Japan*

²⁷*Université de Lyon, Université Lyon-1, CNRS/IN2P3, UMR5822, IPNL, F-69622 Villeurbanne Cedex, France*

²⁸*Henryk Niewodniczański Institute of Nuclear Physics PAN, PL-31342 Kraków, Poland*

²⁹*CCLRC Daresbury Laboratory, Warrington WA4 4AD, United Kingdom*

³⁰*Lawrence Livermore National Laboratory, Livermore, California 94551, USA*

(Received 9 June 2017; published 24 August 2017)

The transitional nuclei ^{132}Xe and ^{133}Xe are investigated after multinucleon-transfer (MNT) and fusion-evaporation reactions. Both nuclei are populated (i) in $^{136}\text{Xe} + ^{208}\text{Pb}$ MNT reactions employing the high-resolution Advanced Gamma Tracking Array (AGATA) coupled to the magnetic spectrometer PRISMA, (ii) in the $^{136}\text{Xe} + ^{198}\text{Pt}$ MNT reaction employing the GAMMASPHERE spectrometer in combination with the gas-detector array CHICO, and (iii) as an evaporation residue after a $^{130}\text{Te}(\alpha, xn)^{134-xn}\text{Xe}$ fusion-evaporation reaction employing the HORUS γ -ray array at the University of Cologne. The high-spin level schemes are considerably extended above the $J^\pi = (7^-)$ and (10^+) isomers in ^{132}Xe and above the $11/2^-$ isomer in ^{133}Xe . The results are compared to the high-spin systematics of the $Z = 54$ as well as the $N = 78$ and $N = 79$ chains. Furthermore, evidence is found for a long-lived ($T_{1/2} \gg 1 \mu\text{s}$) isomer in ^{133}Xe which closes a gap along the $N = 79$

*Corresponding author: andreas.vogt@ikp.uni-koeln.de

†Deceased.

isotones. Shell-model calculations employing the SN100PN and PQM130 effective interactions reproduce the experimental findings and provide guidance to the interpretation of the observed high-spin features.

DOI: 10.1103/PhysRevC.96.024321

I. INTRODUCTION

The $50 \leq N, Z \leq 82$ region of the Segrè chart, spanning the nuclei “northwest” of doubly-magic ^{132}Sn , is an intriguing study ground to test the suitability and predictive power of nuclear models at both low and high spins. Low-spin excited states in the nearly spherical nuclei near proton- and neutron-shell closures are well described as anharmonic vibrations [1] with a gradual change to rotational structures further away from the closed shells. Further on, quasiparticle excitations play a key role and are responsible for the presence of yrast-trap isomers. These long-lived states interrupt and fragment the decay flux in spectroscopic investigations. High- j couplings involving the unique-parity $h_{11/2}$ neutron-hole orbital give rise to a wealth of high-spin states with multi-quasiparticle character. In particular, detailed knowledge of isomers is crucial to ascertain the active quasiparticle configurations in the specific nucleus.

^{132}Xe and ^{133}Xe are located in the proton midshell between the $Z = 50$ shell and the $Z = 64$ subshell closures. Three and four neutrons away from the $N = 82$ shell closure, the respective Xe isotopes have come within reach of advanced untruncated shell-model calculations. Several recently developed effective shell-model interactions [2–7] take aim toward a unified description of the $50 \leq N, Z \leq 82$ region.

The available data on low-spin states in both ^{132}Xe and ^{133}Xe originate from earlier work employing β decay, Coulomb excitation [8–10], and neutron scattering [11]. Intermediate-spin states were investigated via $^{130}\text{Te}(\alpha, 2n\gamma)$ [12] and $^{130}\text{Te}(\alpha, n\gamma)$ [13] reactions, respectively. The lack of suitable stable beam-target combinations obstructs the population of high-spin states via fusion-evaporation processes involving higher-mass reaction partners. Multinucleon-transfer (MNT) reactions offer an efficient gateway to moderately neutron-rich nuclei that cannot be reached by means of fusion-evaporation reactions. These heavy-ion collisions proved to be capable of populating both high spins and excitation energies. The identification of the often elusive multinucleon-transfer channels takes advantage of the high analyzing power of modern detector arrays and mass spectrometers [14,15].

Isomeric $J^\pi = 10^+$ states were reported in all even-mass $N = 78$ isotones from ^{128}Sn up to ^{142}Gd . The states are interpreted as fully aligned $\nu h_{11/2}^{-2}$ two-neutron hole configurations. A decreasing trend in lifetimes is observed with increasing proton number Z [12,16–22]. Compared to the other $N = 78$ isotones, the yrast 10_1^+ state in ^{132}Xe has an exceptionally long half-life of $T_{1/2} = 8.39(11)$ ms [23] and decays predominantly via an 538-keV $E3$ γ ray to the (7_1^-) state, whereas the location of the 8_1^+ state in the level scheme is still unknown [8]. In fact, the long half-life suggests that the 10_1^+ state might be located very close to the 8_1^+ state. The (7_1^-) state in ^{132}Xe is also an isomer with a half-life of $T_{1/2} = 87(3)$ ns and a $\nu(h_{11/2}^{-1} d_{3/2}^{-1})$ configuration [12,24].

For the odd-mass $50 \leq N, Z \leq 82$ nuclei, a long-lived $11/2^-$ isomer above the $3/2^+$ ground state is a typical feature which is also present in ^{133}Xe at 233.221(15) keV with a half-life of 2.198(13) days [9]. Lönnroth *et al.* [13] assigned three γ rays with energies of 247.4, 947.8, and 695.2 keV to form a $(23/2^-) \rightarrow 19/2_1^- \rightarrow 15/2_1^- \rightarrow 11/2_1^-$ cascade on top of the $11/2^-$ isomer. Firm spin-parity assignments in the intermediate-spin regime were made up to $J^\pi = 19/2^-$. Along the $N = 79$ chain [partial level schemes presented in Figs. 1(a) to 1(f)], $J^\pi = (23/2^+)$ isomers were reported in ^{129}Sn [$T_{1/2} = 2.22(14)$ μs at 1762 keV] [25,26], ^{131}Te [93(12) ms at 1941 keV] [27], and ^{139}Nd [277(2) ns at 2617 keV] [28]. These states are explained as $\nu(h_{11/2}^{-2} d_{3/2}^{-1})$ configurations [26,29,30]. Further $J^\pi = 19/2^+$ isomers below and $J^\pi = 27/2^-$ isomers above the $23/2^+$ state were observed with half-lives in the ns to μs regime in ^{129}Sn [31,32].

First spectroscopic data on the $(23/2^+)$ isomer in ^{131}Te were obtained in a $^{64}\text{Ni} + ^{130}\text{Te}$ multinucleon-transfer experiment at the GASP γ -ray spectrometer [33]. A 361-564-833-keV triple coincidence was assigned to a $(21/2^-) \rightarrow (19/2^-) \rightarrow (15/2^-) \rightarrow 11/2^-$ band based on isotopic systematics. A delayed component ($T_{1/2} \gg 1$ μs) in the off-beam spectra led to the assumption that a $23/2^+$ isomer was located above the $(21/2^-)$ state. Fogelberg *et al.* determined a very long half-life of 93(12) ms employing thermal fission of U isotopes at the OSIRIS mass separator [34] and assigned an $E3$ character to the 361-keV transition. Furthermore, a conversion-electron measurement corroborated that only the 361-keV transition is the delayed transition depopulating the $(23/2^+)$ state. Finally, the $15/2_1^-$ and $19/2_1^-$ levels were confirmed and a prompt negative-parity cascade was added to the level scheme by Astier *et al.* [29]. The half-life of the $(23/2^+)$ state was constrained to be longer than 10 μs and the decay to the $19/2_1^-$ state was reaffirmed to be of $M2$ character. Based on the OSIRIS result, a reduced transition strength of $B(M2; 23/2_1^+ \rightarrow 19/2_1^-) = 2 \times 10^{-6}$ W.u. was deduced [29].

The elusive $23/2^+$ isomer in ^{139}Nd was first reported by Müller-Veggian *et al.* who observed a long-living delayed component in off-beam $\gamma\gamma$ -coincidence spectra and reported a first lower half-life limit [35]. Later, the isomer's location was constrained to be above the $19/2_1^+$ state and a first precise half-life of $T_{1/2} = 272(4)$ ns could be obtained [36]. Recently, in 2013, Vancraeynest *et al.* [30] confirmed these results employing the sophisticated Jyväskylä recoil-decay tagging setup. The group finally achieved an unambiguous placement of the isomer in the level scheme as it is populated by the decay of three higher-lying $(25/2^-)$ states. In ^{137}Ce , a $J = (31/2)$ state was observed to be isomeric with a half-life of 5 ns [37]. Up to now, no high-lying isomeric states have been reported for ^{133}Xe and ^{135}Ba . Any experimental information on high-spin states is missing for ^{132}Xe beyond 2.8 MeV and for ^{133}Xe beyond 2.1 MeV. The scarce experimental data together with

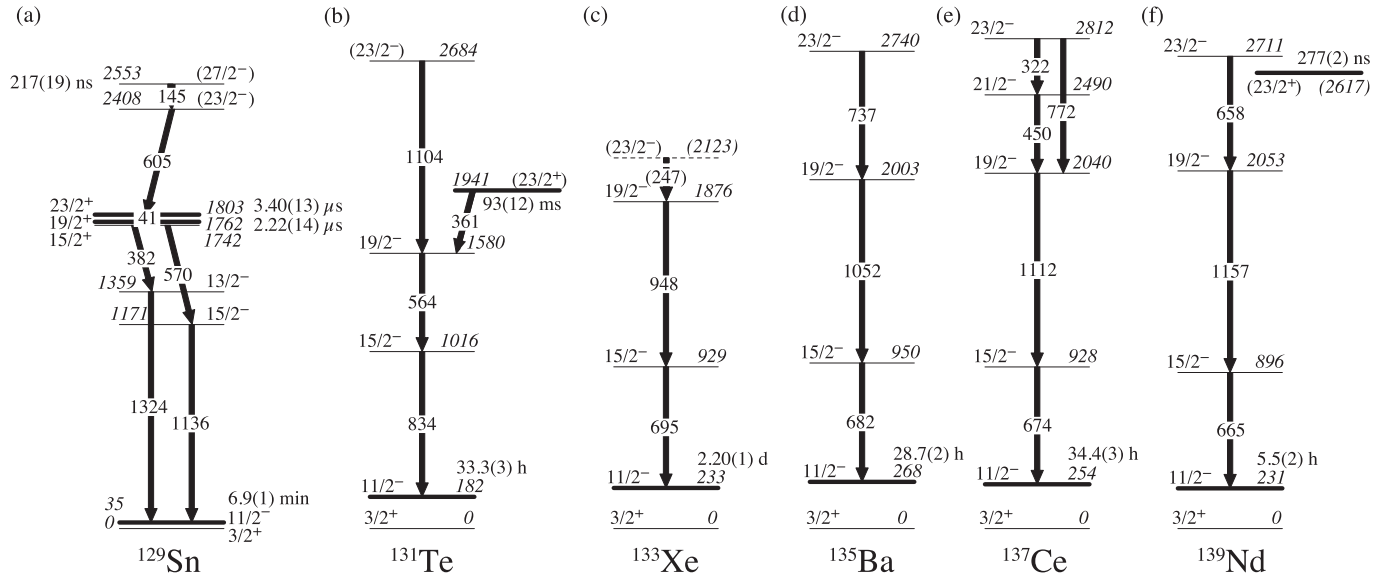


FIG. 1. Comparison of high-spin states and isomer half-lives along the $N = 79$ isotones ranging from ^{129}Sn to ^{139}Nd ; data are taken from Refs. [13,25,28–30,32,38–40]. Tentative assignments are written in parentheses. See text for details.

recent theoretical advances motivate a refined investigation of high-spin features in both nuclei.

In this article, we report and discuss new results for the high-spin regimes of ^{132}Xe and ^{133}Xe . Excited states of ^{132}Xe and ^{133}Xe were populated in three different experiments: The combination of the high-resolution position-sensitive Advanced Gamma Tracking Array (AGATA) [41] and the PRISMA magnetic mass spectrometer [42–44] was employed to study the nuclei after $^{136}\text{Xe} + ^{208}\text{Pb}$ multinucleon transfer. Moreover, excited states in both nuclei were populated after a $^{136}\text{Xe} + ^{198}\text{Pt}$ MNT reaction employing the GAMMASPHERE+CHICO setup [45,46] at Lawrence Berkeley National Laboratory (LBNL). The $^{130}\text{Te}(\alpha, n)^{133}\text{Xe}$ and $^{130}\text{Te}(\alpha, 2n)^{132}\text{Xe}$ fusion-evaporation reactions were utilized in a third experiment employing the High-efficiency Observatory for γ -Ray Unique Spectroscopy (HORUS) [47] at the Institute of Nuclear Physics, University of Cologne.

During the preparation of this manuscript, we became aware of a parallel study of ^{133}Xe by Reed, Lane *et al.* [48]. The results are consistent with those presented in the current work.

This paper is organized as follows: the experimental setup and data analysis of the three experiments are described in Sec. II, followed by the experimental results in Sec. III. A comparison with modern shell-model calculations is presented in Sec. IV before the paper closes with a summary and conclusions.

II. EXPERIMENTAL PROCEDURE AND DATA ANALYSIS

^{132}Xe and ^{133}Xe were populated in a $^{136}\text{Xe} + ^{208}\text{Pb}$ multinucleon-transfer experiment at the Laboratori Nazionali di Legnaro, Italy. In this experiment, a 6.84 MeV/nucleon ^{136}Xe beam was accelerated by the PIAVE+ALPI accelerator complex onto a 1-mg/cm 2 ^{208}Pb target. The Advanced Gamma Tracking Array (AGATA) [41] in a first demonstrator configuration [49] was placed at a distance of 18.8 cm from

the target position to measure γ rays from excited states. The array consisted of nine large-volume electronically segmented high-purity Ge (HPGe) detectors in three triple cryostats [50]. An isotopic identification of the nuclei of interest was provided by the magnetic spectrometer PRISMA placed at the reaction's grazing angle of $\theta_{\text{lab}} = 42^\circ$. An event registered by the PRISMA focal-plane detector in coincidence with an AGATA event was taken as a trigger for the data acquisition. Pulse-shape analysis of the digitized detector signals was applied to determine the individual interaction points within the HPGe shell [51], enabling the Orsay forward-tracking algorithm [52] to reconstruct the individual emitted γ -ray energies and to determine the first interaction point of the γ ray in the germanium and, thus, the emission angle. Together with the kinematic information from PRISMA, a precise Doppler correction is performed. Furthermore, the fully reconstructed momentum vector of the ejectile nucleus enables a reconstruction of the total kinetic energy loss (TKEL) of the reaction by assuming a binary process and by incorporating the excitation energies of both binary partners. The TKEL is defined as the reaction's Q -value distribution with an opposite sign [43,53].

In a second experiment, the 88-Inch Cyclotron facility at LBNL provided a 6.25-MeV/nucleon ^{136}Xe beam that impinged onto a 92% isotopically enriched self-supporting 420- $\mu\text{g}/\text{cm}^2$ ^{198}Pt target. The GAMMASPHERE array, which in this experiment consisted of 103 Compton-suppressed HPGe detectors, was employed for γ -ray spectroscopy [45]. Both polar and azimuthal angles and the time-of-flight difference Δt_{TOF} between the detection of beam-like and target-like reaction products were measured with the gas-filled parallel plate avalanche chamber ancillary detector CHICO, allowing for an event-by-event Doppler-shift correction for emitted γ rays. The time window for prompt events was set to ± 45 ns around the master trigger, requiring three prompt γ rays and the binary fragments being detected in CHICO; the one

for the delayed γ rays was set from 45 to 780 ns. Further details are given in Ref. [24]. The data of the experiment were sorted into four two-dimensional matrices gated on beam-like fragments: (i) an in-beam Doppler-corrected prompt $\gamma\gamma$ matrix, (ii) an out-of-beam delayed-delayed $\gamma\gamma$ matrix, (iii) a delayed-prompt $\gamma\gamma$ matrix, and (iv) a delayed γ -time matrix. The RADWARE analysis software [54] was used to project and background-subtract the gated spectra.

Furthermore, ^{132}Xe and ^{133}Xe were populated via the fusion-evaporation reaction $^{130}\text{Te}(\alpha, xn)^{134-xn}\text{Xe}$, employing a 19-MeV α beam delivered by the FN Tandem accelerator located at the Institute for Nuclear Physics, University of Cologne. The ^{130}Te target with a thickness of 1.8 mg/cm² was evaporated onto a 120 mg/cm² thick Bi backing plus a 132 mg/cm² thick Cu layer for heat dissipation. All residual reaction products as well as the beam were stopped inside the Bi backing. γ rays from excited states were measured employing the Cologne fast-timing setup, comprising eight HPGe detectors from the HORUS array [47] and eight LaBr₃:Ce scintillators. The count rate of the individual HPGe crystals was maintained around 20 kHz during the experiment. Coincident events were processed and recorded utilizing the synchronized 80-MHz XIA Digital Gamma Finder (DGF) data-acquisition system and stored to disk. The data were analyzed offline using the SOCO-V2 [55,56] and TV [57] codes. Recorded γ rays were sorted into (i) a general symmetrized two-dimensional matrix to study $\gamma\gamma$ coincidence relations, (ii) a three-dimensional cube, and (iii) a total of six group matrices each corresponding to different relative angles θ_1 , θ_2 , and ϕ between all HPGe detector pairs with respect to the beam axis to investigate multipolarities via angular correlations.

Spins and parities of excited states are investigated with the $\gamma\gamma$ angular-correlation code CORLEONE [59,60] employing the DCO (directional correlation from oriented states) formalism based on the phase convention by Krane, Steffen, and Wheeler [61,62]. The angular distribution of two coincident γ rays in a recoiling nucleus, subsequently emitted from the initial state J_1 through an intermediate state J_2 to the final state J_3 , is described by the following equation:

$$W(\theta_1, \theta_2, \phi) = \sum_{\lambda, \lambda_1, \lambda_2} B_{\lambda_1}(J_1) A_{\lambda}^{\lambda_1 \lambda_2}(\gamma_1, \delta_1) A_{\lambda_2}(\gamma_2, \delta_2) \times H_{\lambda \lambda_1 \lambda_2}(\theta_1, \theta_2, \phi), \quad (1)$$

where $B_{\lambda_1}(J_1)$ is a statistical tensor describing the orientation of the initial state with respect to the orientation axis. Correlation coefficients $A_{\lambda}^{\lambda_1 \lambda_2}$ and A_{λ_2} parametrize the spins J_i and multipole-mixing ratios δ_i of the corresponding transitions between the excited states of interest. The angular-correlation function $H_{\lambda \lambda_1 \lambda_2}(\theta_1, \theta_2, \phi)$ depends on the polar angles of emission θ_1 and θ_2 of γ_1 and γ_2 in the polarization plane and on the azimuthal rotation ϕ of the emission (cf. Fig. 2 for further definition). The tensor ranks λ_1 and λ_2 describe the orientation of the states J_1 and J_2 , and λ is defined as the tensor rank of the radiation field. Detailed expressions for the coefficients $A_{\lambda}^{\lambda_1 \lambda_2}$, A_{λ_2} , B_{λ_1} , and $H_{\lambda \lambda_1 \lambda_2}$ are given in Ref. [62]. Different hypotheses of involved spins and multipole-mixing ratios are evaluated in χ^2 fits of experimental transition intensities in the different angular-correlation groups to the correlation function

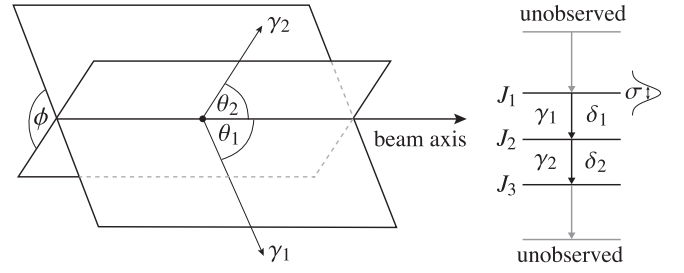


FIG. 2. Correlation of two coincident γ rays between excited states of spin J_i . The transitions are further characterized by their multipole-mixing ratios δ_i (adapted from Ref. [58]).

$W(\theta_1, \theta_2, \phi) \equiv W(J_1, J_2, J_3, \delta_1, \delta_2, \sigma)$. The parameter σ denotes the width of the alignment distribution, i.e., the distribution of the magnetic substates m of J_1 .

A small anisotropy behavior of theoretically isotropic γ -ray transitions required a correction of the measured intensities in the individual angular-correlation groups [63]. This anisotropy of the efficiency-corrected intensities is mainly caused by different dead times in the digital data-acquisition system as count rates differed between the ^{226}Ra efficiency-calibration source run and the actual experiment. A fit to the well-known $4_1^+ \rightarrow 2_1^+ \rightarrow 0_1^+$ cascade in ^{132}Xe , comprising two pure electric quadrupole transitions, was used to renormalize the initial efficiency-corrected intensities of the angular-correlation groups to their theoretical values with the assumption that both transitions are of pure $E2$ character. The anisotropy corrections are in the order of 2% to 11% and were subsequently applied to fits of other cascades.

III. RESULTS

A. ^{132}Xe

A partial level scheme of ^{132}Xe obtained in the present work is displayed in Fig. 3 (followed by the level scheme for ^{133}Xe in Fig. 4). Intensities above the isomers are extracted from the in-beam $^{136}\text{Xe} + ^{208}\text{Pb}$ data and normalized to the intensity of the 650-keV transition. Correlations of the reconstructed TKEL with coincident prompt in-beam γ rays of AGATA allow the total excitation energy of the nucleus of interest to be restricted. Gates on different TKEL regions either suppress or enhance γ -ray transitions between states with different excitation energies and angular momenta. Due to the presence of the two long-lived isomers in the level scheme of ^{132}Xe , TKEL gates allow for a discrimination between γ -ray transitions below and above the isomeric states. AGATA γ -ray spectra of ^{132}Xe identified in PRISMA are presented in Fig. 5 with gates on (a) small TKEL and (b) large TKEL. The applied gates are shown in the corresponding insets. The 668-keV $2_1^+ \rightarrow 0_1^+$, 727-keV $5_1^+ \rightarrow 4_1^+$, and 773-keV $4_1^+ \rightarrow 2_1^+$ transitions dominate the low-TKEL gated γ -ray spectrum, which can be attributed to the low-spin structure below the isomers [8]. In contrast, all transitions between low-spin states are completely suppressed with the gate on large TKEL. Seven new γ -ray transitions with energies of 208, 298, 476, 559, 650, 1133, and 1240 keV are observed in this spectrum. A new 940-keV line is visible in Fig. 5(a).

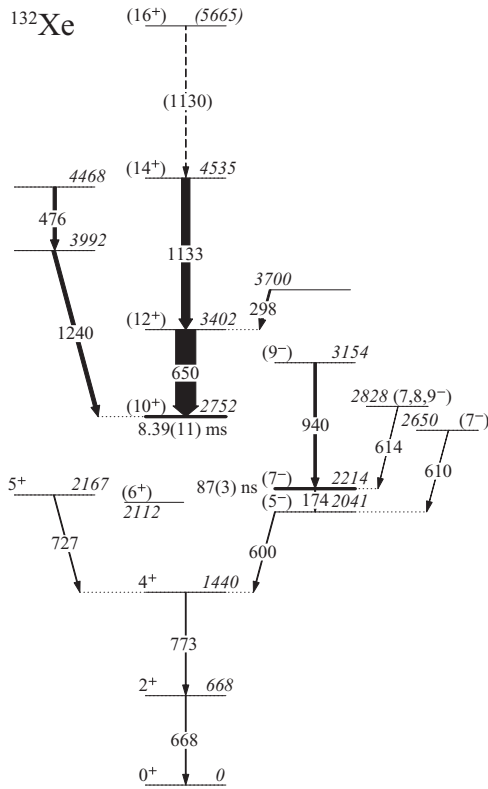
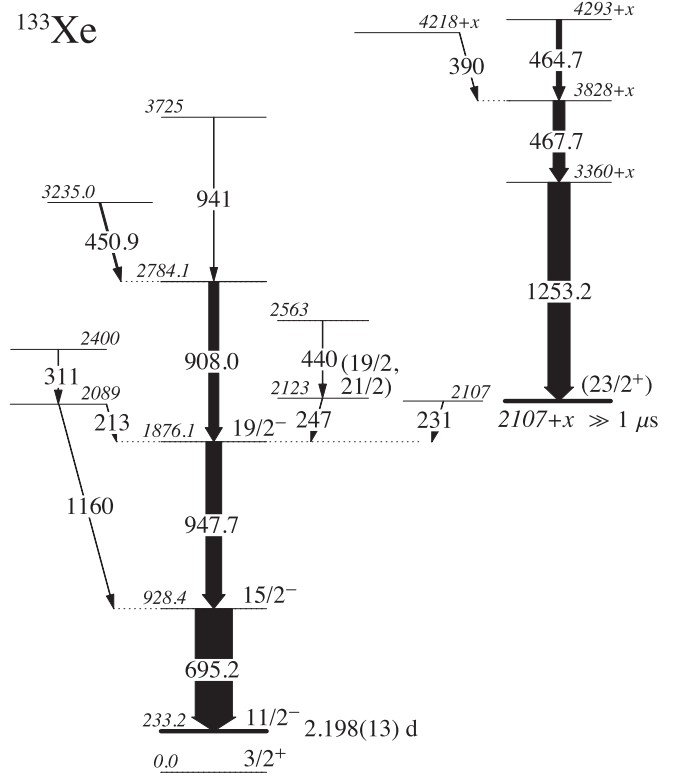


FIG. 3. Partial level scheme of ^{132}Xe with the newly observed γ rays above the 8.39(11)-ms (10_1^+) and 87-ns (7_1^-) isomers. Energies are given in keV. Intensities above the isomers are extracted from the in-beam $^{136}\text{Xe} + ^{208}\text{Pb}$ AGATA data and normalized to the intensity of the 650-keV transition.

$\gamma\gamma$ coincidences are exploited in the $^{136}\text{Xe} + ^{198}\text{Pt}$ dataset. The 650- and 1133-keV, as well as the 1240- and 476-keV transitions are mutually coincident. Corresponding gated spectra are depicted in Figs. 5(e) to 5(h). Correlations of prompt transitions populating isomers with the respective depopulating γ rays were enabled by the $^{136}\text{Xe} + ^{198}\text{Pt}$ experiment. Delayed-prompt $\gamma\gamma$ coincidences with a gate on the delayed 668-keV $2_1^+ \rightarrow 0_1^+$ transition are presented in Fig. 5(h). The 8.39(11)-ms half-life of the (10^+) isomer is too long to observe delayed-prompt coincidences within the experimental time window. Instead, a gate on the delayed transitions provides a spectrum only containing the transitions feeding the 87(3)-ns 7^- isomer. The corresponding half-life of the delayed component of the 668-keV transition used in the gate is validated to be 88(5) ns. Consequently, the 940-keV transition is placed on top of the 2214-keV state. The line at 614 keV is identified as the decay of a ($7,8,9^-$) state, previously observed in a β -decay study of ^{132m}I [64]. Other lines visible in Fig. 5(h) at 348, 373, 402, 451, 783, and 869 keV are not observed in the AGATA spectra. Since the high-lying 650-, 1133-, 476-, and 1240-keV γ -ray transitions are not present in the delayed-prompt coincidence spectrum, these transitions have to feed the (10^+) isomer. The intensity balance suggests the 1133-keV transition to be placed above the 650-keV γ ray feeding the (10^+) isomer. Furthermore, the 1133-keV transition is in coincidence with another close-lying



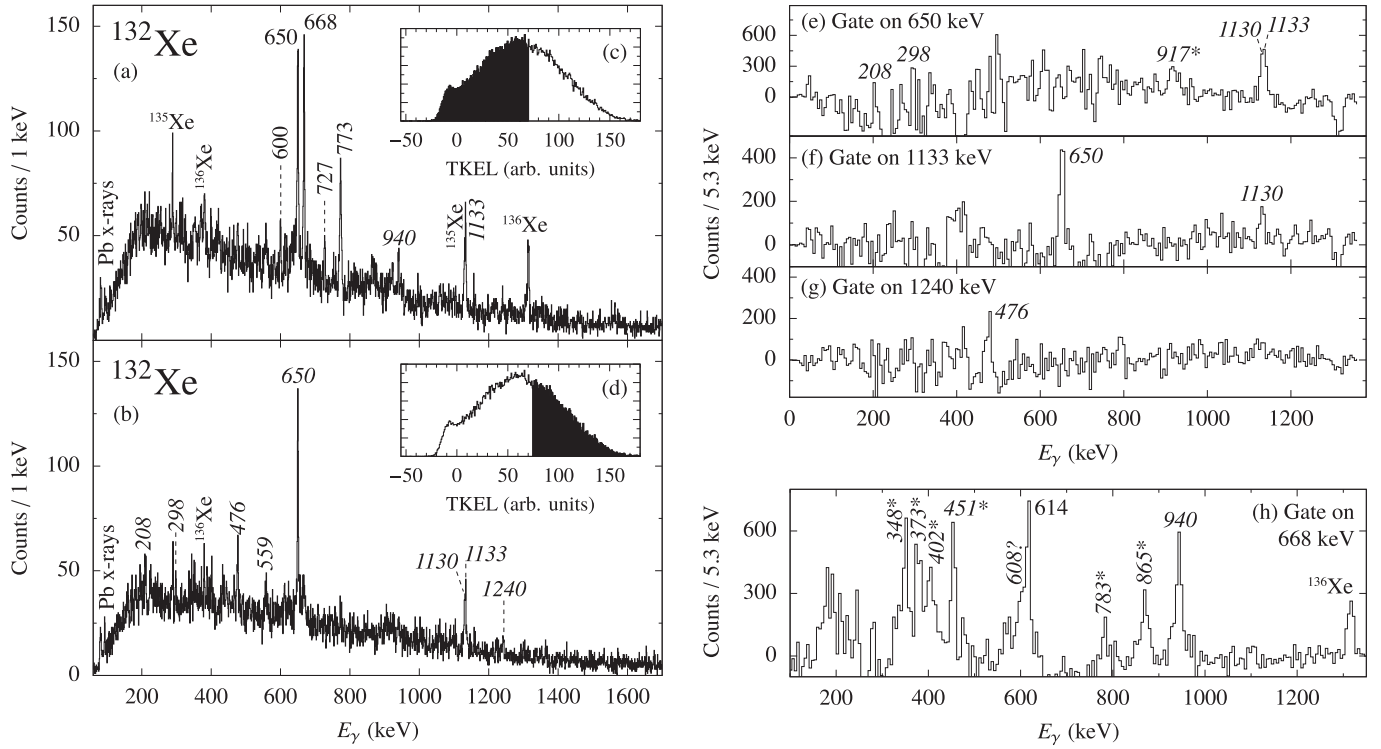


FIG. 5. Left: AGATA γ -ray spectra for ^{132}Xe identified with PRISMA after the $^{136}\text{Xe} + ^{208}\text{Pb}$ MNT reaction. (a) Gate on small TKEL. (b) Gate on large TKEL; the transitions below the long-lived (10^+) and (7^-) isomers are not present any more. The applied gates on the TKEL distributions are presented in the insets (c) and (d). Previously unknown γ rays are labeled with italic characters. Right, (e)–(g): Prompt GAMMASPHERE $\gamma\gamma$ coincidences from the $^{136}\text{Xe} + ^{198}\text{Pt}$ experiment, gated on 650, 1133, and 1240 keV. (h) Delayed-prompt GAMMASPHERE coincidence spectrum with a gate on the delayed 668-keV $2_1^+ \rightarrow 0_1^+$ transition. Asterisks mark transitions not observed in the HORUS and AGATA experiments. See text for details.

coincidences between the 695.2- and 947.7-keV γ rays and the newly observed 450.9- and 908.0-keV transitions [cf. Fig. 6(e)]. The 908.0-keV transition has to be placed on top of the 1876.1-keV state, which is further supported by the HORUS $\gamma\gamma$ coincidences. As presented in Figs. 6(h) and 6(j), both gates on 695 and 948 keV show coincident 908-keV peaks. Vice versa, a gate on 908 keV, although contaminated by the 910.1-keV decay of the 2350.6-keV level in ^{132}Xe [8], shows clear mutual coincidence with the two established γ -ray transitions. Also the 695-, 1160- and 311-keV γ -ray transitions are coincident with each other in $\gamma\gamma$ gates [cf. Figs. 6(h) and 6(k)]. The newly established state at 2089 keV decays via a 213-keV γ -ray to the $19/2_1^-$ state. The 213-keV transition also appears in the prompt GAMMASPHERE data in gates on 695 and 948 keV.

As observed in the prompt GAMMASPHERE $\gamma\gamma$ coincidences in Figs. 6(f) and 6(g), the 1253-keV γ -ray transition is mutually coincident to the ones at 465 and 468 keV. Moreover, these three γ rays appear only for gates on large TKEL in Fig. 6(b). Thus, the transitions have to be located at comparatively large excitation energies. However, there is no connection to any previously observed γ ray: neither to the bands based on the previously known positive-parity states nor to the negative-parity states above the $11/2_1^-$ state. This observation corroborates the presence of a yet unobserved isomer in ^{133}Xe , fed by the 464.7-, 467.7-, and 1253.2-keV

γ rays. A 390-keV transition is coincident to 468 and 1253 keV and placed parallel to the 465-keV transition. Based on intensity relations and $\gamma\gamma$ coincidences, the 451- and 941-keV transitions are placed parallel, feeding the 2784-keV state. The 654- and 1096-keV γ -ray transitions are not visible in the coincidence data. None of the known transitions between low-spin or negative-parity intermediate-spin states appear in the delayed GAMMASPHERE data. Consequently, in accordance with previous studies performed with the GAMMASPHERE dataset [24], the half-life of the new isomer is estimated to be $T_{1/2} \gg 1 \mu\text{s}$.

Strong peaks at 231- and 247-keV are mutually coincident with 695- and 948-keV lines in the HORUS dataset. The 231-keV transition is not to be confused with the isomeric 233.2-keV transition from the $11/2_1^-$ state to the ground state, which is too weak to be observed. No coincidence is found with the 908-keV γ ray. Moreover, triple- γ coincidences and intensity relations support the placement of a 440-keV γ ray on top of the 247-keV transition. Although these transitions are clearly visible in the HORUS coincidence data, neither of them are observed in the AGATA or in the GAMMASPHERE in-beam data. Arrows mark the expected positions in Figs. 6(a) and 6(b). The 247-keV γ ray was first reported by Lönnroth *et al.* [13]. The group measured an $\ell = 2$ multipolarity and assigned a $(23/2^-) \rightarrow 19/2_1^-$ transition. An $M2$ character was excluded since no delayed component was observed in the data. Due to

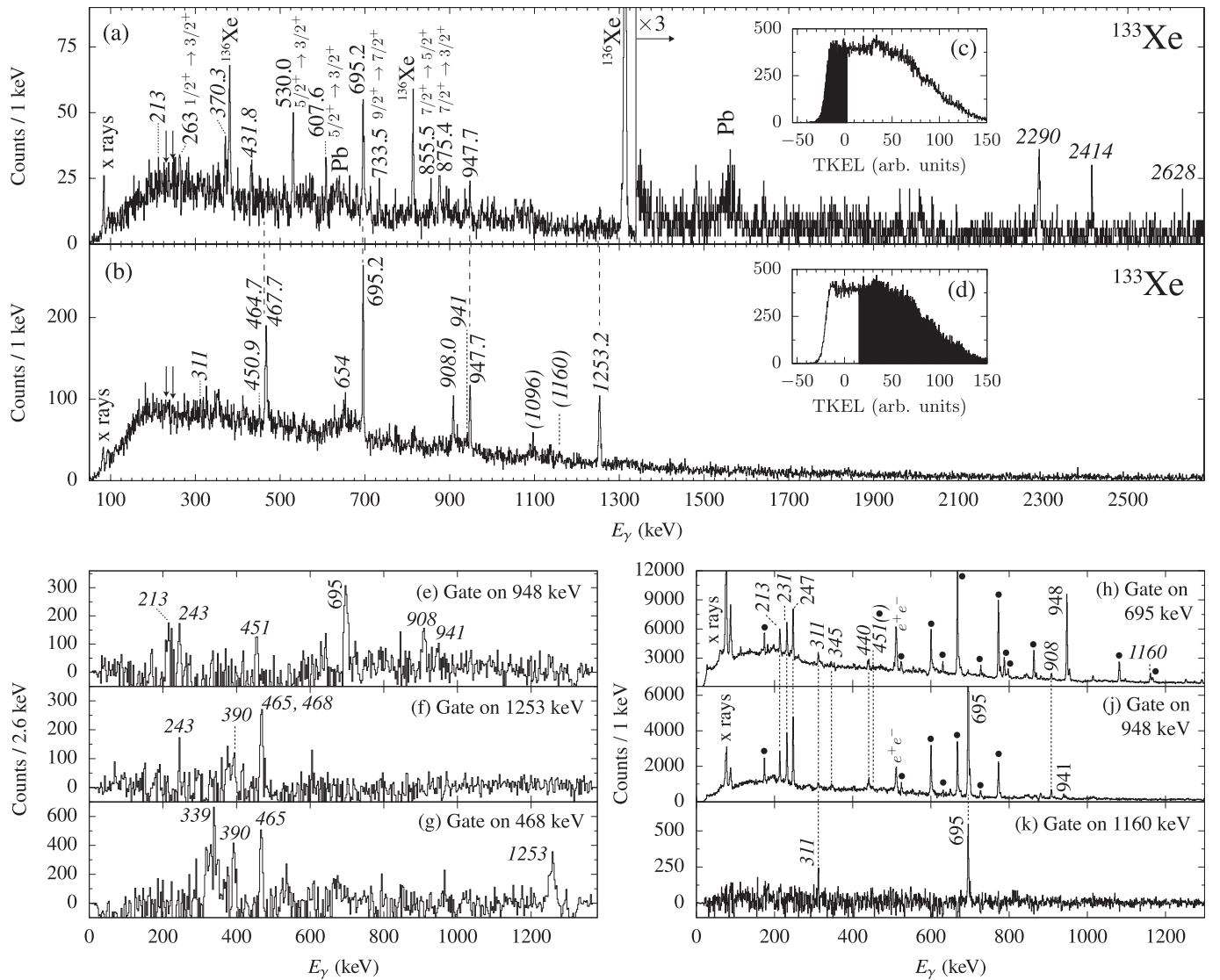


FIG. 6. AGATA γ -ray spectra of ^{133}Xe selected by PRISMA with gates on (a) small TKEL and (b) large TKEL; corresponding TKEL spectra in (c) and (d) with gates marked in black. Previously unknown γ -ray transitions are labeled with italic characters. Arrows label the supposed positions of the 231- and 247-keV γ -ray transitions. (e)–(g) GAMMASPHERE prompt $\gamma\gamma$ coincidences with gates on 948, 1253, and 468 keV. (h), (i), (j), (k) HORUS prompt $\gamma\gamma$ coincidences with gates on 695, 948, and 1160 keV. Contaminations originating from the dominating $2n$ evaporation channel ^{132}Xe are labeled with filled black circles.

the prompt character of the 213- and 908-keV transitions in both AGATA and GAMMASPHERE experiments, both the 2089- and 2784-keV states can be excluded to be isomeric or as a corresponding decay path of an isomeric state.

Spin assignments can be tested in the HORUS experiment with the procedure discussed in Sec. II. Angular-distribution functions $W(\theta_1, \theta_2, \phi)$ of two coincident γ -ray transitions are fitted to experimental γ -ray intensity distributions obtained by gates on depopulating transitions in the $\gamma\gamma$ -coincidence matrices of six angular-correlation groups. Figure 7(a) shows a benchmark angular-correlation fit of the 727-keV $5_1^+ \rightarrow 4_1^+$ decay from the quasi- γ band of ^{132}Xe . Anisotropy corrections to the intensity distributions, applied to all six angular-correlation groups, are validated in this way. The fit of a $5^+ \xrightarrow{\delta} 4^+ \xrightarrow{E2} 2^+$ hypothesis yields a good agreement with

the experimental distribution. Moreover, the obtained $E2/M1$ multipole-mixing ratio of $\delta_{\text{exp.}} = +0.40(5)$ compares well with the evaluated value of $\delta_{\text{lit.}} = +0.41_{-8}^{+7}$ [8]. Similarly, Fig. 7(b) shows angular correlations for the 247-948-keV cascade in ^{133}Xe . Obviously, a pure $E2$ transition does not fit the data. A $19/2 \xrightarrow{\delta} 19/2^- \rightarrow 15/2^-$ hypothesis with $\delta = -0.69(11)$ ($\chi^2 = 0.8$) yields the best agreement with the experimental $W(\theta_1, \theta_2, \phi)$ distribution. Nevertheless, based on the fit quality, neither a $21/2 \xrightarrow{\delta} 19/2^-$ scenario with $\delta = +0.24(3)$ (slightly worse agreement with $\chi^2 = 3.7$) nor a $23/2 \xrightarrow{\delta} 19/2^-$ transition with $\delta = -0.32(6)$ ($\chi^2 = 5.4$) can be entirely excluded. Statistics are not sufficient to perform fits for the 213-, 231-, and 1160-keV γ -ray transitions.

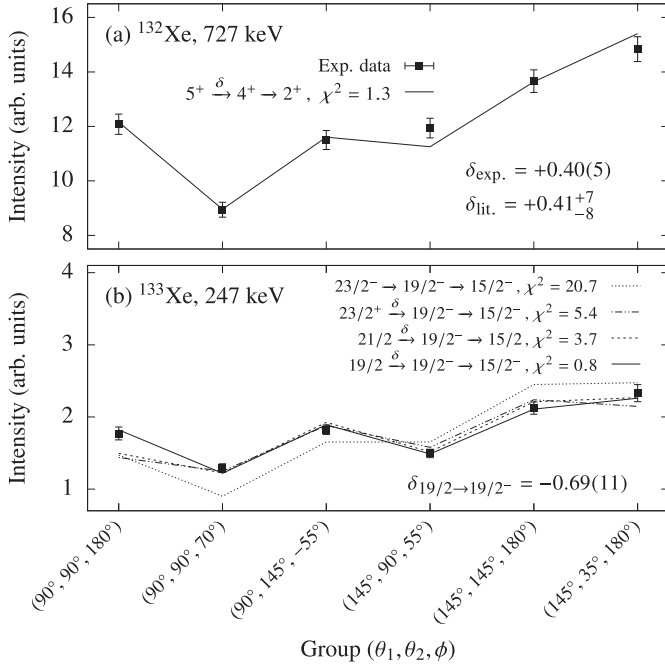


FIG. 7. (a) $\gamma\gamma$ angular correlations for the $5^+ \xrightarrow{\delta} 4^+ \xrightarrow{E2} 2^+$ 727-773-keV cascade in ^{132}Xe . Experimental values (data points) are compared to calculated angular-correlation functions $W(\theta_1, \theta_2, \phi)$ (lines) for six correlation groups $(\theta_1, \theta_2, \phi)$ using the code CORLEONE. The known multipole-mixing ratio of the 727-keV transition in ^{132}Xe is well reproduced by the CORLEONE calculation. (b) Same as (a), but for the 247-948-keV cascade in ^{133}Xe . Several spin hypotheses are plotted. The $19/2^+ \xrightarrow{\delta} 19/2^- \xrightarrow{E2} 15/2^-$ hypothesis (solid line) with $\delta = -0.69(11)$ yields the best agreement.

IV. DISCUSSION

Shell-model calculations for both positive- and negative-parity states were performed in the $50 \leq Z, N \leq 82$ single-particle space generated by the valence nucleons occupying the $0g_{7/2}$, $1d_{5/2}$, $1d_{3/2}$, $2s_{1/2}$, and $0h_{11/2}$ orbitals. Two different interactions were employed: (i) The first calculation was carried out using a phenomenological interaction, called PQM130 (Pairing + Quadrupole-Quadrupole + Multipole for mass region 130), constructed from a pairing-plus-quadrupole interaction that consists of spherical single-particle energies, a monopole-pairing interaction, a quadrupole-pairing interaction, and a quadrupole-quadrupole interaction. It is combined with newly introduced higher multipole-pairing interactions. Valence neutrons and protons are treated as holes and particles relative to the closed shells. Details on the calculation are given in Ref. [4]. (ii) The second calculation was performed in the above mentioned model space (also called jj55pn) outside ^{100}Sn using the jj55pna Hamiltonian [2] (referred to as the SN100PN interaction) employing the computer code NUSHELLX@MSU [65] without any truncations. The SN100PN interaction is constructed from a renormalized G matrix derived from the CD-Bonn nucleon-nucleon interaction [66]; single-particle energies are deduced from the experimentally observed level energies in ^{133}Sb and ^{131}Sn . The interaction has four parts: neutron-neutron, neutron-proton, proton-proton, and Coulomb repulsion between the protons.

A comparison of experimental energy spectra with the results of the shell-model calculations is presented in Fig. 8 for (a) ^{132}Xe and (b) ^{133}Xe . Both calculations reproduce the hitherto known members of the yrast ground-state band of ^{132}Xe quite well. Furthermore, both interactions reproduce the position of the 5_1^+ state. However, the 3_1^+ and 4_2^+ states are interchanged in the SN100PN calculation, while in the PQM130 calculation the 4_2^+ state is calculated to be above the 6_1^+ . The negative-parity 5_1^- , 7_1^- , and 7_2^- states are well reproduced by the SN100PN interaction; on the other hand, 5_1^- and 7_1^- states are permuted in the PQM130 calculation. Another ambiguity remains for the ordering of the 7_2^- and 8_1^- states. The experimental location of the 8_1^+ state is still experimentally unresolved. The SN100PN calculation predicts the state to be degenerate with the 10_1^+ state in excitation energy, whereas the PQM130 interaction computes the first two 8^+ levels below the 10_1^+ state. Earlier pair-truncated shell-model calculations predicted the yrast 8_1^+ about 0.05 MeV above the 10_1^+ state [67]. The next even-even isotope ^{134}Xe exhibits a $10_1^+ \rightarrow 8_1^+$ transition of 28 keV. Likewise, in ^{130}Te the corresponding transition amounts to only 18 keV [17]. Backbending phenomena in the yrast bands were observed systematically in $^{122-130}\text{Xe}$, among others, visible in a reduced energy spacing between the 8_1^+ and 10_1^+ states [68]. It is explained by the band crossing of the quasi-ground-state band with another quasiband with a $\nu(h_{11/2}^2)$ configuration [68]. As mentioned in Sec. I, the long 8.39(11)-ms half-life of the 10_1^+ state and its dominant $E3$ decay to the 7_1^- state even suggest a placement below the 8_1^+ state. Therefore, each assignment above the 10_1^+ state is tentative. Nonetheless, both shell-model calculations support a $14_1^+ \rightarrow 12_1^+ \rightarrow 10_1^+$ assignment to the 1133-650-keV cascade based on the predicted energy differences. Although the 10_1^+ state is underpredicted by 423 keV in the SN100PN calculation, the calculated transition energies of 1024 and 685 keV match well the observed 1133- and 650-keV γ -ray transitions. The 10_2^+ state is predicted to be 29 keV above the 12_1^+ state by the PQM130 interaction, and 203 keV above by the SN100PN calculation. Thus, the observed 476-1240-keV cascade might be interpreted as the $(12_2^+, 13_1^+) \rightarrow 11_1^+ \rightarrow 10_1^+$ decay. However, no conclusive assignment can be made, since, foremost, the exact position of the 8_1^+ state with respect to the 10_1^+ state remains unclear.

Above the 7_1^- isomer, the $(7, 8, 9)^-$ level at 2829 keV may be interpreted as the 8_1^- state. Therefore, the 3155-keV state is most probably of spin 9_1^- . This assignment is also supported by the PQM130 interaction. Figure 9(a) shows the evolution of the positive-parity ground-state band and of 7_1^- and 9_1^- states along the $N = 78$ isotones from $Z = 50$ to $Z = 64$. Accordingly, positive-parity yrast states along the Xe chain are shown in Fig. 9(b). The newly assigned states are marked with thicker lines. The 9_1^- , 12_1^+ , and 14_1^+ candidates in ^{132}Xe fit the systematics. Moreover, the systematics suggest the 5665-keV level to be interpreted as the 16_1^+ state. Nonetheless, transposed 8_1^+ and 10_1^+ states could also fit into the isotone systematics.

The level structure of the even-odd isotope ^{133}Xe is more complex. Both interactions reproduce the low-spin positive-parity states generally well but predict several possibly yrare states in a reversed order with regard to the yrast

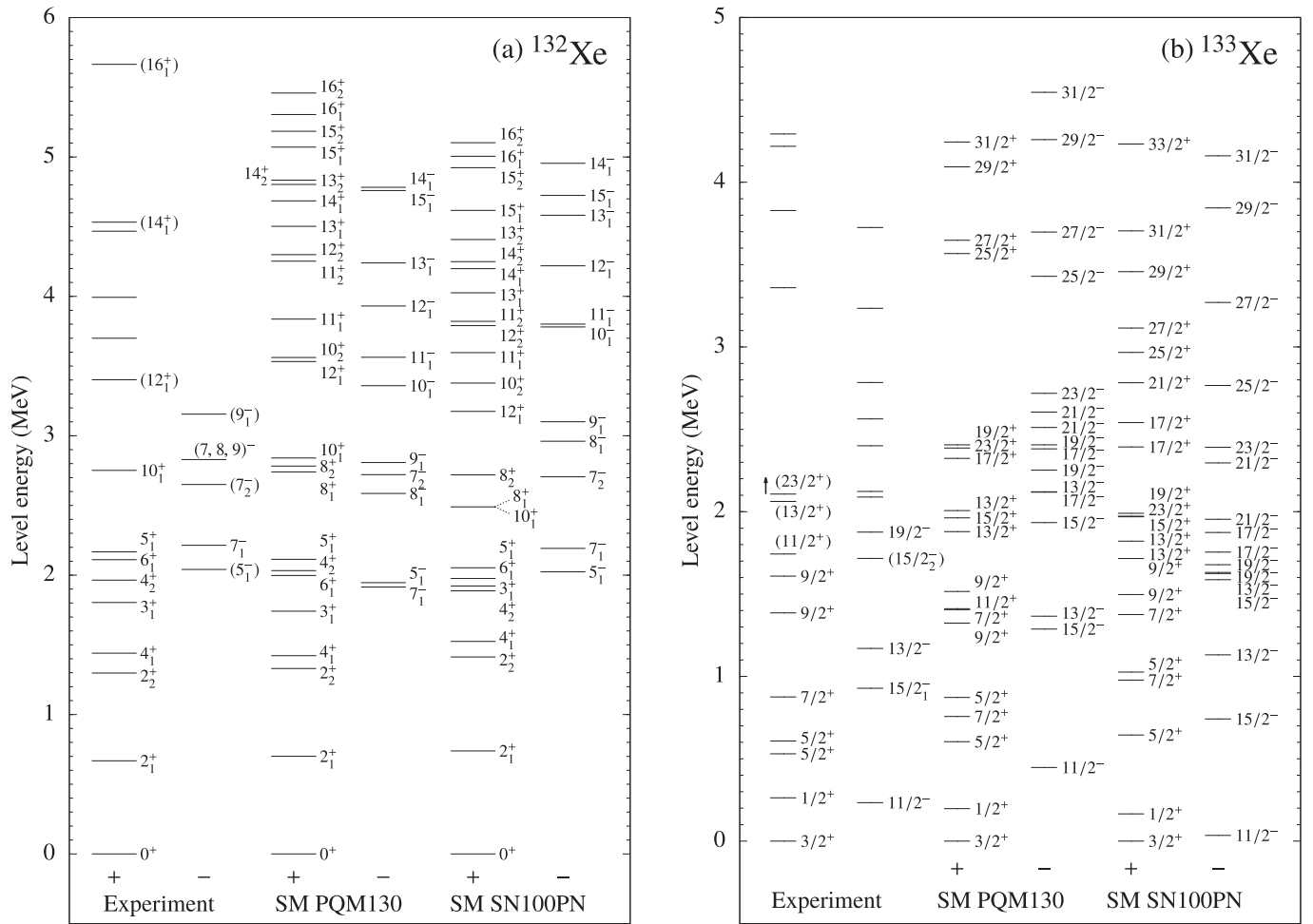


FIG. 8. Comparison of experimental energy spectra with the results of shell-model calculations for (a) ^{132}Xe and (b) ^{133}Xe . Experimental energy spectra are shown in the left panels. The middle panels present the results obtained with the PQM130 interaction [4]. The right panels show the computed levels using the SN100PN interaction. For clarity, the states are separated into columns for the negative- and the positive-parity states.

levels. The PQM130 interaction overpredicts the 233-keV $11/2_1^-$ state by 214 keV while the SN100PN interaction places the $11/2_1^-$ state at an excitation energy of only 35 keV. The SN100PN interaction reproduces the $19/2_1^- \rightarrow 15/2_1^- \rightarrow 11/2_1^-$ cascade very well. Deviations amount to only 12 and 65 keV for the 695- and 948-keV transitions, respectively. The $23/2_1^-$ state is predicted to be located 766 or 466 keV above the $19/2_1^-$ state by the SN100PN and the PQM130 interactions, respectively. Additionally, the $21/2_1^- \rightarrow 19/2_1^-$ transition is computed as $E_\gamma = 329$ keV by the SN100PN or $E_\gamma = 259$ keV by the PQM130 interaction. Therefore, the novel 908-keV γ -ray transition may be assigned to the decay of the $23/2_1^-$ state. The 465-468-1254-keV cascade, unconnected to any other band, implies the existence of an isomer with a half-life of $T_{1/2} \gg 1 \mu\text{s}$ in ^{133}Xe . A prompt character excludes the 908-keV transition as following an isomeric decay. Hence, the newly observed isomer is placed at $2107 + x$ keV. Excluding a nonobserved transition, it could decay either via a 440-247-keV cascade or via the 231-keV transition to the $19/2_1^-$ state. An isomeric $J^\pi = 19/2_1^+$ state with a half-life of 14(3) ns, decaying into the $19/2_1^-$ state, is observed in the neighboring isotope ^{131}Xe [27]. The $(23/2^+)$ state is observed

well above the isomer in this nucleus. Nevertheless, in both ^{133}Xe and the $-2p$ isotope ^{131}Te , the SN100PN as well as the PQM130 interaction predict the two unobserved $19/2_1^+$ and $21/2_1^+$ states to be above the $23/2_1^+$ state. Therefore, a $23/2_1^+$ assignment to the $(2107 + x)$ -keV isomer is most likely. Based on angular correlations, the 247-keV transition needs to be revised to be the decay of either the $19/2_2^-$ or the $21/2_1^-$ state. The $19/2^+ \rightarrow 19/2^-$ or $21/2^+ \rightarrow 19/2^-$ assignments with multipolarity $E1 + (M2)$ cannot be necessarily excluded in the present angular-correlation measurements, but the spin-trap character of the $23/2_1^+$ state, as computed by both shell-model calculations, obstructs this assignment. This makes a 440-247-keV two-step decay via positive-parity states unlikely. Consequently, the 440-keV transition could be explained as the decay of a higher-lying $21/2_{1,2}^-$ state. The decay of the $(23/2^+)$ isomer may proceed via a $21/2_1^-$ state (via either 231 or 440-247 keV). This requires the presence of a yet unobserved low-energy γ -ray transition, which could also be highly converted. In fact, the energy difference between the calculated $21/2_1^-$ and $23/2_1^+$ states amounts to only 125 keV in the PQM130 and 19 keV in the SN100PN interaction. Otherwise, the shell-model calculations would also support the

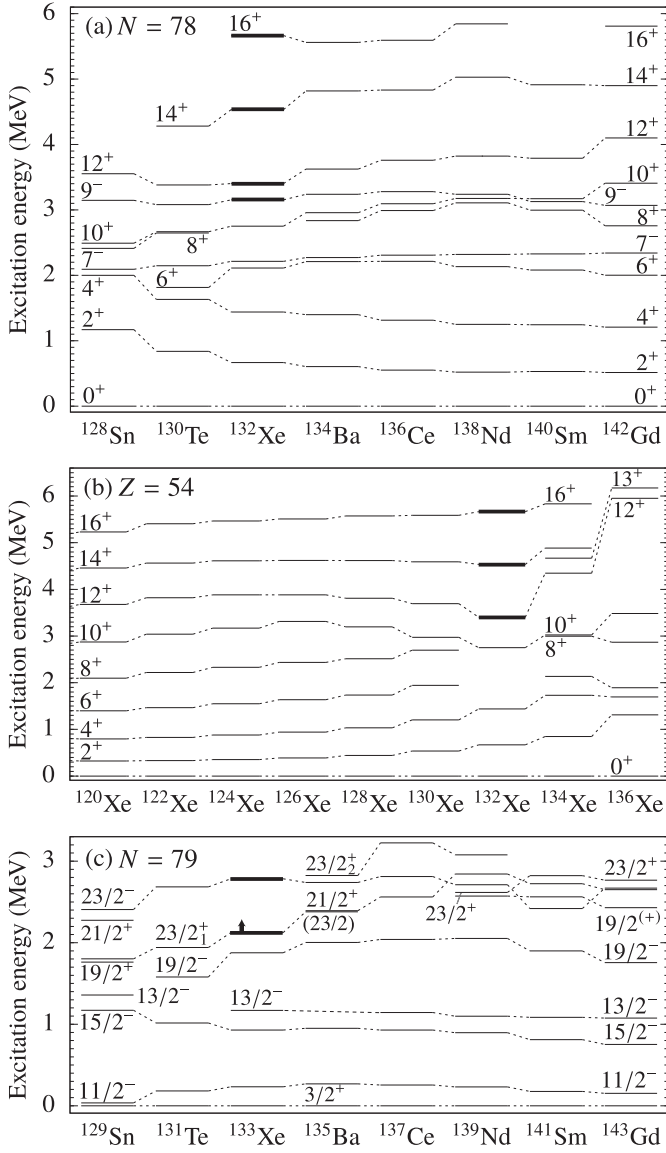


FIG. 9. Evolution of excited states (a) along the $N = 78$ isotones from $Z = 50$ to $Z = 64$, (b) along the Xe isotopes, and (c) along the odd-mass $N = 79$ isotones. Data are from Refs. [40,69–71]. Newly discovered states are marked with thick lines.

231-keV transition to be a long-lived $(23/2^+) \rightarrow 19/2_1^-$ decay with an assumed $M2$ multipolarity. Considering the single-step decay via a 361-keV γ ray in ^{131}Te , isotope systematics suggest the 231-keV transition to follow the $(2107 + x)$ -keV isomer decay. In ^{133}Xe , for $E_\gamma = 231$ keV, the half-lives corresponding to one Weisskopf unit are 1.8 μs for an $M2$ and 32 ms for an $E3$ transition. Without experimental lifetime information, there is yet no decisive distinction between these possibilities. In the case of a 231-keV transition with pure $M2$ character, the reduced transition strength is constrained to $B(M2; 23/2_1^+ \rightarrow 19/2_1^-) < 1.4$ W.u.

The nuclear structures of ^{133}Xe and the $-2p$ isotope ^{131}Te have similar characteristics. Figure 10 shows the decomposition of the total angular momentum $I = I_\pi \otimes I_\nu$ into its proton and neutron components for several selected states in these

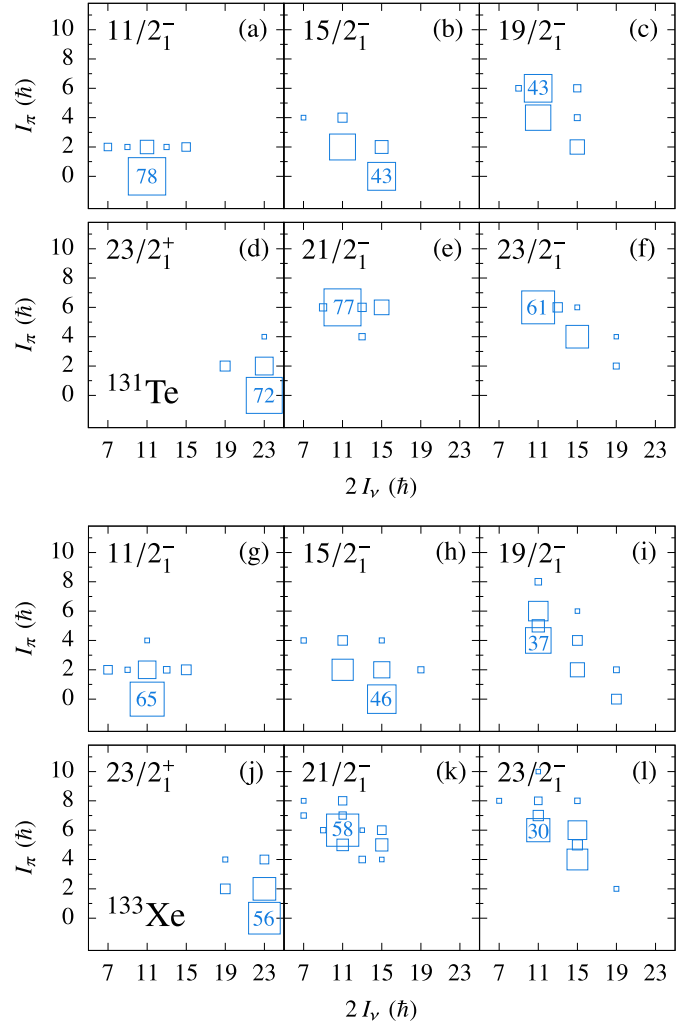


FIG. 10. Decomposition of the total angular momentum $I = I_\pi \otimes I_\nu$ of the SN100PN calculation into its proton and neutron components for several selected negative-parity states as well as the $J^\pi = 23/2^+$ isomer candidate in (a) to (f) ^{131}Te and (g) to (l) ^{133}Xe . Strongest components are labeled with corresponding percentages.

two nuclei using the SN100PN interaction. Although more fragmented in ^{133}Xe , the structures of the negative-parity states above $J^\pi = 11/2_1^-$ resemble the ones in ^{131}Te . The SN100PN interaction predicts the $23/2_1^+$ state in ^{133}Xe to predominantly have 56% stretched $\nu 23/2^+ \otimes \pi 0^+$ and 29% $\nu 23/2^+ \otimes \pi 2^+$ configurations. Neutron $\nu(h_{11/2}^{-2}d_{3/2}^{-1})$ components account for 75% of the configurations. Significant proton configurations coupled to this neutron configuration are 33% of $\pi g_{7/2}^4$, 23% of $\pi(g_{7/2}^3d_{5/2}^1)$, and 8% of $\pi(g_{7/2}^2h_{11/2}^2)$. Also, the occupation numbers of the PQM130 calculation support a dominant $\nu(h_{11/2}^{-2}d_{3/2}^{-1})$ neutron configuration. In the ^{131}Te isotope, the SN100PN interaction locates the $23/2_1^+$ state at 1870 keV, close to the experimental value of 1941 keV. Here, the dominant configuration is 69% $\nu(h_{11/2}^{-2}d_{3/2}^{-1}) \otimes \pi g_{7/2}^2$. The stretched $\nu 23/2 \otimes \pi 0^+$ character in the decomposition of the $23/2_1^+$ state strongly hinders a decay to the other states whose neutron configurations involve an $I_\nu = 11/2$ spin. The SN100PN interaction computes the $B(E2; 19/2_1^- \rightarrow 15/2_1^-)$ value to be

$154 e^2\text{fm}^4$ in ^{131}Te and reproduces the experimental transition strength of $B(E2; 19/2_1^- \rightarrow 15/2_1^-) = 139_{-30}^{+54} e^2\text{fm}^4$ employing standard effective charges of $e_\pi = 1.5e$ and $e_\nu = 0.5e$. However, the small experimental $B(M2; 23/2^+ \rightarrow 19/2_1^-)$ value of 1.9×10^{-6} W.u. in ^{131}Te is overpredicted by two orders of magnitude (8.8×10^{-4} W.u.) considering free nuclear g factors. A similar calculation for ^{133}Xe yields a branching ratio of 81.2% for the $23/2_1^+ \rightarrow 19/2_1^-$ decay. The corresponding theoretical $M2$ transition strength is 3.4×10^{-3} W.u. Moreover, the transition strength to the $19/2_2^-$ state, predicted to be 54 keV higher in energy than the calculated $19/2_1^-$ state, is computed to be 1.8×10^{-3} W.u.

Similar to the $N = 78$ chain, Fig. 9(c) presents the evolution of several excited states along the $N = 79$ isotones. The novel $23/2_1^+$ candidate fits well into the isotone systematics. As yet, no $19/2^+$ and $21/2^+$ states have been observed in ^{131}Te , supporting the validity of both shell-model calculations, which locate these levels above the $23/2_1^+$ state. The presence of isomeric ($23/2^+$) states in the energy regime below 2.5 MeV is discontinued in ^{135}Ba and ^{137}Ce , before emerging again in ^{139}Nd . However, the 2389-keV state in ^{135}Ba , which was assigned with spin $J = (21/2)$ by both Che *et al.* [72] and Cluff [70], later revised to spin $J = (23/2)$ by Kumar *et al.* [38], could be an isomer candidate. Higher-lying (first excited) $23/2^+$ states are known in ^{135}Ba and ^{137}Ce which do not fit the $N = 79$ systematics. Besides, the recent discovery of the 277(2)-ns $J^\pi = 23/2^+$ isomer in ^{139}Nd [30] results in a smooth onset of $23/2^+$ states along the isotone chain from the high- Z side. Therefore, the existence of a lower-lying first $23/2^+$ state, possibly isomeric, might be anticipated at approximately 2.6 MeV in ^{137}Ce .

V. CONCLUSIONS

In summary, the high-spin level schemes of ^{132}Xe and ^{133}Xe were extended to excitation energies of 5665 and $4293 + x$ keV, respectively. The observation of a band unconnected to any known γ -ray cascade corroborates the existence of a long-lived isomer in ^{133}Xe . Based on isotonic systematics, shell-model calculations, and comparisons of in-beam and stopped-beam experiments, a minimum excitation energy of $E = 2107 + x$ keV is deduced for this state, and a spin-parity assignment of $J^\pi = (23/2^+)$ is suggested. The half-life is estimated to be $T_{1/2} \gg 1 \mu\text{s}$. This observation of a $(23/2^+)$

isomer fills in a missing cornerstone along the $N = 79$ isotones between ^{129}Sn , ^{131}Te , and ^{139}Nd . Future conversion-electron measurements will identify and resolve the multipole character of the isomer decay in ^{133}Xe . The well-established structure for the $N = 79$ isotonic chain still lacks some information. Specifically, detailed high-spin studies need to be pursued in forthcoming work, with due attention to the onset of $J^\pi = 23/2^+$ isomerism as a function of proton filling in the $gdsh$ orbitals. Thus far, there are no experimentally observed states which populate the $23/2^+$ isomer in the hard-to-reach nucleus ^{131}Te . Although studies of ^{135}Ba and ^{137}Ce were performed up to highest spins and excitation energies, no isomer candidates below 3 MeV were found yet. The observation of a $(23/2^+)$ isomer in this work and the recent observation of a 277(2)-ns isomer in ^{139}Nd corroborate the existence of $J^\pi = 23/2^+$ isomers also in the aforementioned two nuclei. Hence, thorough searches for isomers in ^{135}Ba and ^{137}Ce should be performed in the future to shed light on the onset of isomerism in this region.

ACKNOWLEDGMENTS

We would like to cordially thank Dr. G. J. Lane (Australian National University) for valuable discussions. Furthermore, we thank the IKP FN Tandem accelerator team for the professional support during the experiment. The research leading to these results has received funding from the German BMBF under Contract No. 05P12PKFNE TP4, from the European Union Seventh Framework Programme FP7/2007-2013 under Grant Agreement No. 262010 - ENSAR, from the Spanish Ministerio de Ciencia e Innovación under Contract No. FPA2011-29854-C04, from the Spanish Ministerio de Economía y Competitividad under Contract No. FPA2014-57196-C5, from the UK Science and Technology Facilities Council (STFC), and from the US National Science Foundation (NSF). E.T. and N.Y. were supported by a Grant-in-Aid for Japan Society for the Promotion of Science (JSPS) Fellows (Grant No. 26.10429). A.V. and L.K. thank the Bonn-Cologne Graduate School of Physics and Astronomy (BCGS) for financial support. One of the authors (A. Gadea) has been supported by the Generalitat Valenciana, Spain, under the grant PROMETEOII/2014/019 and by the EU under the FEDER program.

-
- [1] H. Morinaga and N. L. Lark, Collective excited states in even xenon isotopes, *Nucl. Phys.* **67**, 315 (1965).
 - [2] B. A. Brown, N. J. Stone, J. R. Stone, I. S. Towner, and M. Hjorth-Jensen, Magnetic moments of the 2_1^+ states around ^{132}Sn , *Phys. Rev. C* **71**, 044317 (2005).
 - [3] K. Higashiyama and N. Yoshinaga, Pair-truncated shell-model analysis of nuclei around mass 130, *Phys. Rev. C* **83**, 034321 (2011).
 - [4] E. Teruya, N. Yoshinaga, K. Higashiyama, and A. Odahara, Shell-model calculations of nuclei around mass 130, *Phys. Rev. C* **92**, 034320 (2015).
 - [5] L. Coraggio, A. Covello, A. Gargano, N. Itaco, and T. T. S. Kuo, Shell-model study of the $N = 82$ isotonic chain with a realistic effective Hamiltonian, *Phys. Rev. C* **80**, 044320 (2009).
 - [6] E. Caurier, F. Nowacki, A. Poves, and K. Sieja, Collectivity in the light xenon isotopes: A shell model study, *Phys. Rev. C* **82**, 064304 (2010).
 - [7] Y. Utsuno, T. Otsuka, N. Shimizu, M. Honma, T. Mizusaki, Y. Tsunoda, and T. Abe, Recent shell-model results for exotic nuclei, *EPJ Web Conf.* **66**, 02106 (2014).
 - [8] Y. Khazov, A. A. Rodionov, S. Sakharov, and B. Singh, Nuclear data sheets for $A = 132$, *Nucl. Data Sheets* **104**, 497 (2005).

- [9] Y. Khazov, A. Rodionov, and F. G. Kondev, Nuclear data sheets for $A = 133$, Nucl. Data Sheets **112**, 855 (2011).
- [10] L. Coquard, N. Pietralla, G. Rainovski, T. Ahn, L. Bettermann, M. P. Carpenter, R. V. F. Janssens, J. Leske, C. J. Lister, O. Möller, W. Rother, V. Werner, and S. Zhu, Evolution of the mixed-symmetry $2^+_{1,ms}$ quadrupole-phonon excitation from spherical to γ -soft Xe nuclei, Phys. Rev. C **82**, 024317 (2010).
- [11] E. E. Peters, T. J. Ross, S. F. Ashley, A. Chakraborty, B. P. Crider, M. D. Hennek, S. H. Liu, M. T. McEllistrem, S. Mukhopadhyay, F. M. Prados-Estévez, A. P. D. Ramirez, J. S. Thrasher, and S. W. Yates, 0^+ states in $^{130,132}\text{Xe}$: A search for E(5) behavior, Phys. Rev. C **94**, 024313 (2016).
- [12] A. Kerek, A. Luukko, M. Grecescu, and J. Sztarkier, Two- and three-quasiparticle states in ^{132}Xe and ^{131}Xe , Nucl. Phys. A **172**, 603 (1971).
- [13] T. Lönnroth and J. Kumpulainen and C. Tuokko, One- and three-quasiparticle states in $^{127,129,131,133}\text{Xe}$ and their coexistence with band structures, Phys. Scr. **27**, 228 (1983).
- [14] R. Broda, Spectroscopic studies with the use of deep-inelastic heavy-ion reactions, J. Phys. G **32**, R151 (2006).
- [15] A. Vogt, B. Birkenbach, P. Reiter, L. Corradi, T. Mijatović, D. Montanari, S. Szilner, D. Bazzacco, M. Bowry, A. Bracco, B. Bruyneel, F. C. L. Crespi, G. de Angelis, P. Désesquelles, J. Eberth, E. Farnea, E. Fioretto, A. Gadea, K. Geibel, A. Gengelbach, A. Giaz, A. Görgen, A. Gottardo, J. Grebosz, H. Hess, P. R. John, J. Jolie, D. S. Judson, A. Jungclaus, W. Korten, S. Leoni, S. Lunardi, R. Menegazzo, D. Mengoni, C. Michelagnoli, G. Montagnoli, D. Napoli, L. Pellegrini, G. Pollaro, A. Pullia, B. Quintana, F. Radeck, F. Recchia, D. Rosso, E. Şahin, M. D. Salsac, F. Scarlassara, P.-A. Söderström, A. M. Stefanini, T. Steinbach, O. Stezowski, B. Szpak, Ch. Theisen, C. Ur, J. J. Valiente-Dobón, V. Vandone, and A. Wiens, Light and heavy transfer products in $^{136}\text{Xe} + ^{238}\text{U}$ multinucleon transfer reactions, Phys. Rev. C **92**, 024619 (2015).
- [16] L. Atanasova, D. L. Balabanski, S. K. Chamoli, M. Hass, G. S. Simpson, D. Bazzacco, F. Becker, P. Bednarczyk, G. Benzoni, N. Blasi, A. Blazhev, A. Bracco, C. Brandau, L. Cáceres, F. Camera, F. C. L. Crespi, P. Detistov, P. Doornenbal, C. Fahlander, E. Farnea, G. Georgiev, J. Gerl, K. A. Gladnishki, M. Górska, J. Grebosz, R. Hoischen, G. Ilie, M. Ionescu-Bujor, A. Iordachescu, A. Jungclaus, G. Lo Bianco, M. Kmiecik, I. Kojouharov, N. Kurz, S. Lakshmi, R. Lozeva, A. Maj, D. Montanari, G. Neyens, M. Pfützner, S. Pietri, Zs. Podolyák, W. Prokopowicz, D. Rudolph, G. Rusev, T. R. Saito, A. Saltarelli, H. Schaffner, R. Schwengner, S. Tashenov, J. J. Valiente-Dobón, N. Vermeulen, J. Walker, E. Werner-Malento, O. Wieland, H. J. Wollersheim, H. Grawe, and M. Hjorth-Jensen, g -factor measurements at RISING: The cases of ^{127}Sn and ^{128}Sn , Europhys. Lett. **91**, 42001 (2010).
- [17] J. Genevey, J. A. Pinston, C. Foin, M. Rejmund, R. F. Casten, H. Faust, and S. Oberstedt, Conversion electron measurements of isomeric transitions in $^{130,132}\text{Te}$ and ^{134}Xe , Phys. Rev. C **63**, 054315 (2001).
- [18] M. v. Hartrott, J. Hadijuana, K. Nishiyama, D. Quitmann, D. Riegel, and H. Schweickert, Nuclear spin relaxation of Xe in liquid Te, Z. Phys. A **278**, 303 (1976).
- [19] T. Morek, H. Beuscher, B. Bochev, D. R. Haenni, R. M. Lieder, T. Kutsarova, M. Müller-Veggian, and A. Neskakis, Isomeric states in ^{134}Ba , Z. Phys. A **298**, 267 (1980).
- [20] M. Müller-Veggian, H. Beuscher, R. M. Lieder, Y. Gono, D. R. Haenni, A. Neskakis, and C. Mayer-Böricke, 10^+ isomers observed in even-even 78-neutron nuclei, Z. Phys. A **290**, 43 (1979).
- [21] W. Starzecki, G. De Angelis, B. Rubio, J. Styczen, K. Zuber, H. Güven, W. Urban, W. Gast, P. Kleinheinz, S. Lunardi, F. Soramel, A. Facco, C. Signorini, M. Morando, W. Meczynski, A. M. Stefanini, and G. Fortuna, Prolate and oblate 10^+ isomers in $^{140}\text{Sm}_{78}$ and $^{142}\text{Gd}_{78}$, Phys. Lett. B **200**, 419 (1988).
- [22] M. G. Procter, D. M. Cullen, C. Scholey, B. Niclasen, P. J. R. Mason, S. V. Rigby, J. A. Dare, A. Dewald, P. T. Greenlees, H. Iwasaki, U. Jakobsson, P. M. Jones, R. Julin, S. Juutinen, S. Ketelhut, M. Leino, N. M. Lumley, O. Möller, M. Nyman, P. Peura, T. Pissulla, A. Puurunen, P. Rakkila, W. Rother, P. Ruotsalainen, J. Sarén, J. Sorri, and J. Uusitalo, Lifetime measurements and shape coexistence in ^{144}Dy , Phys. Rev. C **81**, 054320 (2010).
- [23] H. F. Brinckmann, C. Heiser, and W. D. Fromm, Ein hochangeregter isomerer Kernzustand in ^{132}Xe , Nucl. Phys. A **96**, 318 (1967).
- [24] J. J. Valiente-Dobón, P. H. Regan, C. Wheldon, C. Y. Wu, N. Yoshinaga, K. Higashiyama, J. F. Smith, D. Cline, R. S. Chakrawarthy, R. Chapman, M. Cromaz, P. Fallon, S. J. Freeman, A. Görgen, W. Gelletly, A. Hayes, H. Hua, S. D. Langdown, I. Y. Lee, X. Liang, A. O. Macchiavelli, C. J. Pearson, Zs. Podolyák, G. Sletten, R. Teng, D. Ward, D. D. Warner, and A. D. Yamamoto, ^{136}Ba studied via deep-inelastic collisions: Identification of the $(\nu h_{11/2})^{-2}_{10+}$ isomer, Phys. Rev. C **69**, 024316 (2004).
- [25] J. Timar, Z. Elekes, and B. Singh, Nuclear data sheets for $A = 129$, Nucl. Data Sheets **121**, 143 (2014).
- [26] J. Genevey, J. A. Pinston, C. Foin, M. Rejmund, H. Faust, and B. Weiss, High spin isomers in ^{129}Sn and ^{130}Sb , Phys. Rev. C **65**, 034322 (2002).
- [27] Y. Khazov, I. Mitropolsky, and A. Rodionov, Nuclear data sheets for $A = 131$, Nucl. Data Sheets **107**, 2715 (2006).
- [28] P. K. Joshi, B. Singh, S. Singh, and A. K. Jain, Nuclear data sheets for $A = 139$, Nucl. Data Sheets **138**, 1 (2016).
- [29] A. Astier, M. G. Porquet, Ts. Venkova, Ch. Theisen, G. Duchêne, F. Azaiez, G. Barreau, D. Curien, I. Deloncle, O. Dorvaux, B. J. P. Gall, M. Houry, R. Lucas, N. Redon, M. Rousseau, and O. Stężowski, High-spin structures of $^{124-131}\text{Te}$: Competition of proton- and neutron-pair breakings, Eur. Phys. J. **50**, 1 (2014).
- [30] A. Vancraeynest, C. M. Petrache, D. Guinet, P. T. Greenlees, U. Jakobsson, R. Julin, S. Juutinen, S. Ketelhut, M. Leino, M. Nyman, P. Peura, P. Rakkila, P. Ruotsalainen, J. Saren, C. Scholey, J. Sorri, J. Uusitalo, P. Jones, C. Ducoin, P. Lautesse, C. Mancuso, N. Redon, O. Stezowski, P. Désesquelles, R. Leguillon, A. Korichi, T. Zerrouki, D. Curien, and A. Takashima, Identification of new transitions feeding the high-spin isomers in ^{139}Nd and ^{140}Nd nuclei, Phys. Rev. C **87**, 064303 (2013).
- [31] J. A. Pinston, C. Foin, J. Genevey, R. Béraud, E. Chabanat, H. Faust, S. Oberstedt, and B. Weiss, Microsecond isomers in $^{125,127,129}\text{Sn}$, Phys. Rev. C **61**, 024312 (2000).
- [32] R. L. Lozeva, G. S. Simpson, H. Grawe, G. Neyens, L. A. Atanasova, D. L. Balabanski, D. Bazzacco, F. Becker, P. Bednarczyk, G. Benzoni, N. Blasi, A. Blazhev, A. Bracco, C. Brandau, L. Cáceres, F. Camera, S. K. Chamoli, F. C. L. Crespi, J.-M. Daugas, P. Detistov, M. De Rydt, P. Doornenbal, C. Fahlander, E. Farnea, G. Georgiev, J. Gerl, K. A. Gladnishki, M. Górska, J. Grebosz, M. Hass, R. Hoischen, G. Ilie, M. Ionescu-Bujor, A. Iordachescu, J. Jolie, A. Jungclaus, M. Kmiecik, I. Kojouharov, N. Kurz, S. P. Lakshmi, G. Lo Bianco, S. Mallion,

- A. Maj, D. Montanari, O. Perru, M. Pfützner, S. Pietri, J. A. Pinston, Zs. Podolyák, W. Prokopowicz, D. Rudolph, G. Rusev, T. R. Saitoh, A. Saltarelli, H. Schaffner, R. Schwengner, S. Tashenov, K. Turzó, J. J. Valiente-Dobón, N. Vermeulen, J. Walker, E. Werner-Malento, O. Wieland, and H.-J. Wollersheim, New sub- μs isomers in $^{125,127,129}\text{Sn}$ and isomer systematics of $^{124-130}\text{Sn}$, *Phys. Rev. C* **77**, 064313 (2008).
- [33] C. T. Zhang, P. Bhattacharyya, P. J. Daly, Z. W. Grabowski, R. H. Mayer, M. Sferrazza, R. Broda, B. Fornal, W. Królas, T. Pawlat, D. Bazzacco, S. Lunardi, C. Rossi Alvarez, and G. de Angelis, Yrast excitations in $A = 126-131$ Te nuclei from deep inelastic $^{130}\text{Te} + ^{64}\text{Ni}$ reactions, *Nucl. Phys. A* **628**, 386 (1998).
- [34] B. Fogelberg, H. Mach, H. Gausemel, J. P. Omtvedt, and K. A. Mezilev, New high spin isomers obtained in thermal fission, in *The Second International Workshop on Nuclear Fission and Fission-Product Spectroscopy, April 1998, Seyssins, France*, edited by G. Fioni, H. Faust, S. Oberstedt, and F.-J. Hambsch, AIP Conf. Proc. No. 447 (AIP, New York, 1998), p. 191.
- [35] M. Müller-Veggian, H. Beuscher, D. R. Haenni, R. M. Lieder, A. Neskakis, and C. Mayer-Böricke, Investigation of high-spin states in $^{138,139}\text{Nd}$, *Nucl. Phys. A* **344**, 89 (1980).
- [36] M. Ferraton, R. Bourgain, C. M. Petrache, D. Verney, F. Ibrahim, N. de Séréville, S. Franchoo, M. Lebois, C. Phan Viet, L. Sagui, I. Stefan, J. F. Clavelin, and M. Vilmay, Lifetime measurement of the six-quasiparticle isomer in ^{140}Nd and evidence for an isomer above the $19/2^+$ state in ^{139}Nd , *Eur. Phys. J. A* **35**, 167 (2008).
- [37] M. Müller-Veggian, Y. Gono, R. M. Lieder, A. Neskakis, and C. Mayer-Böricke, High-spin states and isomers in $^{136,137,138}\text{Ce}$, *Nucl. Phys. A* **304**, 1 (1978).
- [38] S. Kumar, A. K. Jain, Alpina Goel, S. S. Malik, R. Palit, H. C. Jain, I. Mazumdar, P. K. Joshi, Z. Naik, A. Dhal, T. Trivedi, I. Mehrotra, S. Appannababu, L. Chaturvedi, V. Kumar, R. Kumar, D. Negi, R. P. Singh, S. Muralithar, R. K. Bhowmik, and S. C. Pancholi, Band structure and shape coexistence in $^{135}_{56}\text{Ba}_{79}$, *Phys. Rev. C* **81**, 067304 (2010).
- [39] T. Bhattacharjee, S. Chanda, A. Mukherjee, S. Bhattacharyya, S. K. Basu, S. S. Ghugre, U. D. Pramanik, R. P. Singh, S. Muralithar, N. Madhavan, J. J. Das, and R. K. Bhowmik, Multi-quasiparticle bands in ^{137}Ce , *Phys. Rev. C* **78**, 024304 (2008).
- [40] Evaluated Nuclear Structure Data File (ENSDF), <http://www.nndc.bnl.gov/ensdf/>
- [41] S. Akkoyun *et al.*, AGATA – Advanced GAMMA Tracking Array, *Nucl. Instrum. Methods Phys. Res. A* **668**, 26 (2012).
- [42] A. M. Stefanini, L. Corradi, G. Maron, A. Pisent, M. Trotta, A. M. Vinodkumar, S. Beghini, G. Montagnoli, F. Scarlassara, G. F. Segato, A. De Rosa, G. Inglima, D. Pierrooutsakou, M. Romoli, M. Sandoli, G. Pollaro, and A. Latina, The heavy-ion magnetic spectrometer PRISMA, *Nucl. Phys. A* **701**, 217 (2002).
- [43] S. Szilner, C. A. Ur, L. Corradi, N. Marginean, G. Pollaro, A. M. Stefanini, S. Beghini, B. R. Behera, E. Fioretto, A. Gadea, B. Guiot, A. Latina, P. Mason, G. Montagnoli, F. Scarlassara, M. Trotta, G. de Angelis, F. Della Vedova, E. Farnea, F. Haas, S. Lenzi, S. Lunardi, R. Marginean, R. Menegazzo, D. R. Napoli, M. Nespolo, I. V. Pokrovsky, F. Recchia, M. Romoli, M.-D. Salsac, N. Soić, and J. J. Valiente-Dobón, Multinucleon transfer reactions in closed-shell nuclei, *Phys. Rev. C* **76**, 024604 (2007).
- [44] L. Corradi, S. Szilner, G. Pollaro, D. Montanari, E. Fioretto, A. M. Stefanini, J. J. Valiente-Dobón, E. Farnea, C. Michelagnoli, G. Montagnoli, F. Scarlassara, C. A. Ur, T. Mijatović, D. Jelavić Malenica, N. Soić, and F. Haas, Multinucleon transfer reactions: Present status and perspectives, *Nucl. Instrum. Methods Phys. Res. B* **317, Part B**, 743 (2013).
- [45] I.-Y. Lee, The GAMMASPHERE, *Nucl. Phys. A* **520**, c641 (1990).
- [46] M. W. Simon, D. Cline, C. Y. Wu, R. W. Gray, R. Teng, and C. Long, CHICO, a heavy ion detector for Gammasphere, *Nucl. Instrum. Methods Phys. Res. A* **452**, 205 (2000).
- [47] L. Netterdon, V. Derya, J. Endres, C. Fransen, A. Hennig, J. Mayer, C. Müller-Gatermann, A. Sauerwein, P. Scholz, M. Spieker, and A. Zilges, The γ -ray spectrometer HORUS and its applications for nuclear astrophysics, *Nucl. Instrum. Methods Phys. Res. A* **754**, 94 (2014).
- [48] M. W. Reed, G. J. Lane, G. D. Dracoulis, F. G. Kondev, A. E. Stuchbery, A. P. Byrne, M. P. Carpenter, P. Chowdhury, S. S. Hota, R. O. Hughes, R. V. F. Janssens, T. Lauritsen, C. J. Lister, D. Seweryniak, E. C. Simpson, H. Watanabe, and S. Zhu, High-spin and delayed structure of ^{133}Xe (unpublished).
- [49] A. Gadea, E. Farnea, J. J. Valiente-Dobón, B. Million, D. Mengoni, D. Bazzacco, F. Recchia, A. Dewald, Th. Pissulla, W. Rother, G. de Angelis *et al.*, Conceptual design and infrastructure for the installation of the first AGATA sub-array at LNL, *Nucl. Instrum. Methods Phys. Res. A* **654**, 88 (2011).
- [50] A. Wiens, H. Hess, B. Birkenbach, B. Bruyneel, J. Eberth, D. Lersch, G. Pascovici, P. Reiter, and H.-G. Thomas, The AGATA triple cluster detector, *Nucl. Instrum. Methods Phys. Res. A* **618**, 223 (2010).
- [51] B. Bruyneel, B. Birkenbach, and P. Reiter, Pulse shape analysis and position determination in segmented HPGe detectors: The AGATA detector library, *Eur. Phys. J. A* **52**, 70 (2016).
- [52] A. Lopez-Martens, K. Hauschild, A. Korichi, J. Roccaz, and J.-P. Thibaud, γ -ray tracking algorithms: A comparison, *Nucl. Instrum. Methods Phys. Res. A* **533**, 454 (2004).
- [53] A. B. Brown, C. W. Snyder, W. A. Fowler, and C. C. Lauritsen, Excited States of the Mirror Nuclei, ^7Li and ^7Be , *Phys. Rev.* **82**, 159 (1951).
- [54] D. C. Radford, ESCL8R and LEVIT8R: Software for interactive graphical analysis of HPGe coincidence data sets, *Nucl. Instrum. Methods Phys. Res. A* **361**, 297 (1995).
- [55] N. Saed-Samii, Lifetime measurements using the FATIMA array in combination with EXOGAM@ILL, Diplomarbeit, Universität zu Köln, 2013 (unpublished).
- [56] N. Saed-Samii, computer code SOCO-v2, 2017, <https://gitlab.ikp.uni-koeln.de/nima/soco-v2>.
- [57] J. Theuerkauf, Die Analyse von zwei- und mehrdimensionalen $\gamma\gamma$ -Koinzidenzspektren an Beispielen aus Hochspinexperimenten in der Massengegend um ^{146}Gd , Ph.D. thesis, Universität zu Köln, 1994.
- [58] A. Linnemann, Das HORUS-Würfelspektrometer und Multiphononanregungen in ^{106}Cd , Ph.D. thesis, Universität zu Köln, 2006.
- [59] I. Wiedenhöver, computer code CORLEONE, 1997.
- [60] I. Wiedenhöver, O. Vogel, H. Klein, A. Dewald, P. von Brentano, J. Gableske, R. Krücken, N. Nicolay, A. Gelberg, P. Petkov, A. Gizon, J. Gizon, D. Bazzacco, C. Rossi Alvarez, G. de Angelis, S. Lunardi, P. Pavan, D. R. Napoli, S. Frauendorf, F. Döna, R. V. F. Janssens, and M. P. Carpenter, Detailed angular correlation analysis with 4π spectrometers: Spin determinations and multipolarity mixing measurements in ^{128}Ba , *Phys. Rev. C* **58**, 721 (1998).

- [61] K. S. Krane and R. M. Steffen, Determination of the $E2/M1$ multipole mixing ratios of the gamma transitions in ^{110}Cd , *Phys. Rev. C* **2**, 724 (1970).
- [62] K. S. Krane, R. M. Steffen, and R. M. Wheeler, Directional correlations of gamma radiations emitted from nuclear states oriented by nuclear reactions or cryogenic methods, *At. Data Nucl. Data Tables* **11**, 351 (1973).
- [63] L. Bettermann, C. Fransen, S. Heinze, J. Jolie, A. Linnemann, D. M\"ucher, W. Rother, T. Ahn, A. Costin, N. Pietralla, and Y. Luo, Candidates for the one-phonon mixed-symmetry state in ^{130}Xe , *Phys. Rev. C* **79**, 034315 (2009).
- [64] M. Dikšić, L. Yaffe, and D. G. Sarantites, Identification and decay characteristics of $^{132}\text{I}^m$, *Phys. Rev. C* **10**, 1172 (1974).
- [65] B. A. Brown and W. D. M. Rae, The shell-model code NuShellX@MSU, *Nucl. Data Sheets* **120**, 115 (2014).
- [66] R. Machleidt, F. Sammarruca, and Y. Song, Nonlocal nature of the nuclear force and its impact on nuclear structure, *Phys. Rev. C* **53**, R1483 (1996).
- [67] K. Higashiyama, N. Yoshinaga, and K. Tanabe, Shell model study of backbending phenomena in Xe isotopes, *Phys. Rev. C* **65**, 054317 (2002).
- [68] H. Kusakari, K. Kitao, K. Sato, M. Sugawara, and H. Katsuragawa, High-spin states in even-mass Xe nuclei and backbending phenomena, *Nucl. Phys. A* **401**, 445 (1983).
- [69] A. Vogt, B. Birkenbach, P. Reiter, A. Blazhev, M. Siciliano, J. J. Valiente-Dobón, C. Wheldon, D. Bazzacco, M. Bowry, A. Bracco, B. Bruyneel, R. S. Chakrawarthy, R. Chapman, D. Cline, L. Corradi, F. C. L. Crespi, M. Cromaz, G. de Angelis, J. Eberth, P. Fallon, E. Farnea, E. Fioretto, S. J. Freeman, A. Gadea, K. Geibel, W. Gelletly, A. Gengelbach, A. Giaz, A. G\"orgen, A. Gottardo, A. B. Hayes, H. Hess, H. Hua, P. R. John, J. Jolie, A. Jungclaus, W. Korten, I. Y. Lee, S. Leoni, X. Liang, S. Lunardi, A. O. Macchiavelli, R. Menegazzo, D. Mengoni, C. Michelagnoli, T. Mijatović, G. Montagnoli, D. Montanari, D. Napoli, C. J. Pearson, L. Pellegri, Zs. Podolyák, G. Pollarolo, A. Pullia, F. Radeck, F. Recchia, P. H. Regan, E. Şahin, F. Scarlassara, G. Sletten, J. F. Smith, P.-A. S\"oderstr\"om, A. M. Stefanini, T. Steinbach, O. Stezowski, S. Szilner, B. Szpak, R. Teng, C. Ur, V. Vandone, D. Ward, D. D. Warner, A. Wiens, and C. Y. Wu, High-spin structure of ^{134}Xe , *Phys. Rev. C* **93**, 054325 (2016).
- [70] W. T. Cluff, The High-Spin Structure of $^{134,135}\text{Ba}$ and ^{120}Te , Ph.D. thesis, Florida State University, 2008.
- [71] A. Astier, M.-G. Porquet, Ts. Venkova, D. Verney, Ch. Theisen, G. Duchêne, F. Azaiez, G. Barreau, D. Curien, I. Deloncle, O. Dorvaux, B. J. P. Gall, M. Houry, R. Lucas, N. Redon, M. Rousseau, and O. St\'ezowski, High-spin structures of five $N = 82$ isotopes: ^{136}Xe , ^{137}Cs , ^{138}Ba , ^{139}La , and ^{140}Ce , *Phys. Rev. C* **85**, 064316 (2012).
- [72] X. L. Che, S. J. Zhu, M. L. Li, Y. J. Chen, Y. N. U, H. B. Ding, L. H. Zhu, X. G. Wu, G. S. Li, C. Y. He, and Y. Liu, High-spin levels based on the $11/2^-$ isomer in ^{135}Ba , *Eur. Phys. J. A* **30**, 347 (2006).

Summary and conclusions

In the first part of this thesis, a complete and detailed detection of all reaction products, separation of fission products, and determination of the total kinetic energy loss for the $^{136}\text{Xe} + ^{238}\text{U}$ reaction is presented in the publication “*Light and heavy transfer products in $^{136}\text{Xe} + ^{238}\text{U}$ multinucleon-transfer reactions*”. A sophisticated analysis of the mass spectrometer yielded the nuclear charge Z , the atomic charge q and the mass A . In order to obtain correct mass yields and to extract cross sections from the mass-yield distributions, a detailed study of the mass-spectrometer transmission and efficiency was performed. An event distribution uniform in energy and entrance coordinates was transported through the spectrometer employing a Monte-Carlo simulation. Applied to the measured mass yield, the resulting response function $f(E, \theta, \phi)$ gave efficiency-corrected yields. The magnetic fields and the gas pressures in the focal plane detectors had to be tuned carefully in the same way as in the real experiment. Events were then transported event-by-event with a simulation based on the PRISMA ray-tracing code. The nuclear charge of the Xe-like ejectiles is at the limits of PRISMA’s specifications. Therefore, the Xe main channel is severely contaminated by the neighboring iodine and cesium channels. Likewise, the extent of xenon contaminations in the $\pm 1p$ reaction channels were identified by fitting characteristic Xe γ -ray signatures in the ejectile Doppler-corrected γ -ray spectra of isobaric mass channels. The contaminations were subsequently subtracted from the raw mass yields. Moreover, actinide fission strongly affects the multinucleon-transfer yield. Kinematic coincidences between PRISMA and the particle-tagging DANTE detector were used to discriminate both transfer and fission. In addition, transfer and fission contributions were identified and selected in matrices of the nuclear charge plotted against the time difference between PRISMA and DANTE.

After all corrections were applied, the yields were compared to calculated cross sections using the semi-empirical GRAZING multinucleon-transfer model. The experimental data were normalized to the usually well-reproduced $+1n$ channel, here ^{137}Xe . Experiment and theory are in good agreement for the neutron-transfer modes as well for neutron-rich nuclei in one-proton transfer channels. AGATA served as a complementary tool to investigate the population of actinide nuclei by comparing the X-ray yields in recoil Doppler-corrected γ -ray spectra. X-ray contributions are observed for actinide nuclei ranging from thorium to neptunium. The X-ray yields, scaled and normalized to the plutonium channel, are in a good agreement with the yields obtained by the kinematic coincidences between PRISMA and DANTE. This demonstrates the feasibility of binary-partner coincidences in in-beam γ -ray spectroscopy of heavy actinides. However, the population of heavier actinide nuclei beyond uranium is highly suppressed, thus, yields beyond plutonium are not observed at all.

The second publication of this thesis, “*Spectroscopy of the neutron-rich actinide nucleus ^{240}U following multinucleon-transfer reactions*”, presents results on the collective properties of ^{240}U . The spectroscopy of ^{240}U was performed in kinematic coincidence, i.e. the binary partner channel ^{134}Xe was selected with PRISMA. The Doppler correction was calculated assuming binary-partner kinematics. Time differences between PRISMA and DANTE were exploited to cope with the background and to suppress

the overwhelming fission events. The ground-state band of ^{240}U was extended up to the 24^+ state. Kinetic and dynamic moments of inertia were compared to theoretical predictions. An upbend at rotational frequencies of $\hbar\omega = 0.2$ MeV could be observed for the first time. Despite the experimental challenges, the $K = 0^-$ negative-parity band was extended up to a tentatively assigned 21^- state. The parity-splitting, defined as the ratio of rotational frequencies of yrast and first negative-parity band, and the staggering parameter $S(I)$ are good indicators for the collective features and octupole correlations. For higher spins, ^{240}U is best interpreted as an aligned octupole vibrator - similar to the neighboring ^{236}U and ^{238}U isotopes. Recent cranked relativistic Hartree-Bogoliubov (CRHB) calculations within the relativistic covariant density-functional theory (CDFT) framework [135, 136] show the best agreement with the experimental data.

The publications “*High-spin structure of ^{134}Xe* ” and “*High-spin structures and isomers in the $N = 81$ isotones ^{135}Xe and ^{137}Ba* ” comprise results on various intermediate-mass nuclei in the vicinity of the $Z = 50$ and $N = 82$ closed shells. The synergies of four different experiments employing the $^{136}\text{Xe} + ^{198}\text{Pt}$, $^{136}\text{Xe} + ^{208}\text{Pb}$, and $^{136}\text{Xe} + ^{238}\text{U}$ multinucleon-transfer reactions as well as the $^{11}\text{B} + ^{130}\text{Te}$ fusion-evaporation reaction were required to perform detailed γ -ray spectroscopy of these nuclei. The $^{136}\text{Xe} + ^{238}\text{U}$ AGATA experiment allowed for a discrimination of the two different population paths, multinucleon transfer and fission. In ^{134}Xe , several new high-spin states were discovered on top of the two long-lived 10^+ and 7^- isomers. The high-spin structure above the 10^+ isomer could be unambiguously identified for the first time by delayed-prompt $\gamma\gamma$ coincidences solving a “puzzle” of two former contradicting publications [126, 137]. The results are supported by prompt $\gamma\gamma$ -coincidence relations, γ -ray angular distributions, and detailed investigations of the total kinetic energy loss from the $^{136}\text{Xe} + ^{208}\text{Pb}$ experiment.

The identification and characterization of isomers near magic numbers are important for establishing the two-body matrix elements for modern-day shell-model interactions. High-spin isomerism has been well established in the $N = 81$ isotones ranging from $Z = 50$ (Sn) to $Z = 64$ (Gd), where the neutron $h_{11/2}$ orbital plays a crucial role. In ^{137}Ba , spins and parities of the ground state and the $11/2^-$ isomeric state at 661.659(3) keV were already well established. The $11/2^- \rightarrow 3/2^+$ $M4$ γ -ray transition is even one of the best known energy calibration standards [138–140]. However, the available data concern either low-spin levels observed in the single-nucleon transfer reaction or levels with spin values limited by the β -decay selection rules [113, 141, 142]. The existing data on the states above the isomer were rather scarce. Moreover, important experimental details on higher-spin isomers were missing in ^{135}Xe , i.e. the lifetime of the purported $19/2^-$ isomer in ^{135}Xe was still unknown. In the present thesis, the high-spin regimes of ^{135}Xe and ^{137}Ba could be significantly extended to higher excitation energies. Data from the $^{136}\text{Xe} + ^{198}\text{Pt}$ GAMMASPHERE+CHICO experiment gave not only detailed $\gamma\gamma$ - but also γ -time coincidences. A new 9.0(9)-ns isomer was identified in ^{135}Xe , finally closing a gap in the systematics of the $N = 81$ isotonic chain.

The experimental findings were confronted with modern large-scale shell-model interactions considering both neutrons and protons in the full *gds*h model space. The calculations perform generally well in reproducing the energies of the Xe- and Ba level schemes and corroborate most of the sug-

gested assignments. The novel PQM130 (Pairing+Quadrupole-Quadrupole+Multipole for the mass region 130) interaction by Teruya *et al.* [124] predicts the electromagnetic transition probabilities of $(19/2^-)$ isomer decays in ^{133}Te , ^{135}Xe , and ^{137}Ba with a remarkable accuracy. However, the well-established SN100PN interaction [117, 119] partially fails in reproducing the experimental $B(E2; 19/2^- \rightarrow 15/2^-)$ values for ^{135}Xe and ^{137}Ba . A comparison with the structure of ^{133}Te guides the interpretation of the more complex high-spin structures in ^{135}Xe and ^{137}Ba that are farther apart from the ^{132}Sn double-magic nucleus. The short-lived $J^\pi = (19/2^-)$ high-spin isomers above the $11/2^-$ states exhibit a strong proton component that is parallel to the yrast 6^+ isomers observed in the $N = 82$ isotones. The calculated proton configurations follow the nuclear-structure features of the adjacent isotopes in the closed $N = 82$ shell, validating at least the proton-proton part of the SN100PN interaction. Most probably, the monopole-part of the proton-neutron interaction may be responsible for not reproducing the nuclear structure in the higher-mass $N = 81$ isotones.

In the manuscript “*High-spin structures in ^{132}Xe and ^{133}Xe and evidence for isomers along the $N = 79$ isotones*” the high-spin level schemes were considerably extended above the $J^\pi = (7^-)$ and (10^+) isomers in ^{132}Xe and above the $11/2^-$ isomer in ^{133}Xe . Besides the AGATA and GAMMASPHERE data, ^{133}Xe was also studied as an evaporation residue after a $^{130}\text{Te}(\alpha, xn)^{134-xn}\text{Xe}$ fusion-evaporation reaction employing the HORUS γ -ray array at the University of Cologne. Evidence was found for a long-lived ($T_{1/2} \gg 1 \mu\text{s}$) isomer in ^{133}Xe , possibly of spin $23/2^+$, which fills in a missing corner stone along the $N = 79$ isotones between $^{129}_{50}\text{Sn}$, $^{131}_{52}\text{Te}$, and $^{139}_{60}\text{Nd}$. The experimental results were compared to the high-spin systematics of the $Z = 54$ as well as the $N = 78$ and $N = 79$ chains and confronted with shell-model calculations employing the SN100PN and PQM130 effective interactions.

Dedicated fusion-evaporation experiments in the $50 < Z, N < 82$ region require clean particle triggers to detect the elusive charged-particle evaporation channels. Tools of choice are double-sided silicon strip detectors (DSSSD) which were already in use in in-beam experiments at the tandem accelerator at the University of Cologne. In order to achieve the necessary readiness and the full level of performance, extensive tests of the detectors were carried out by irradiation with mixed triple- α sources. Results of the characterization are presented in the publication “*Characterization and calibration of radiation-damaged double-sided silicon strip detectors*”. The study showed that different parts of the detector were exposed non-homogeneously to varying accumulated doses in previous experiments. The also non-homogeneous radiation damage yields a position-dependent incomplete charge collection and varying responses along single detector segments. A newly-developed position-resolved calibration method based on the mutual consistency of p- and n-side segments allows for a significant enhancement of the energy resolution of radiation-damaged parts of the DSSSD.

Further experiments in the $N < 82$ region

Despite some limitations outlined in this thesis, multinucleon transfer proves to be an excellent tool for the spectroscopic study of many nuclei that can only be scarcely populated by means of other production methods, for example due to a lack of stable beam-target combinations. Notable cases are especially nuclei along the $N = 82$ closed shells. Similar to the cases of $^{132-135}\text{Xe}$ and ^{137}Ba presented

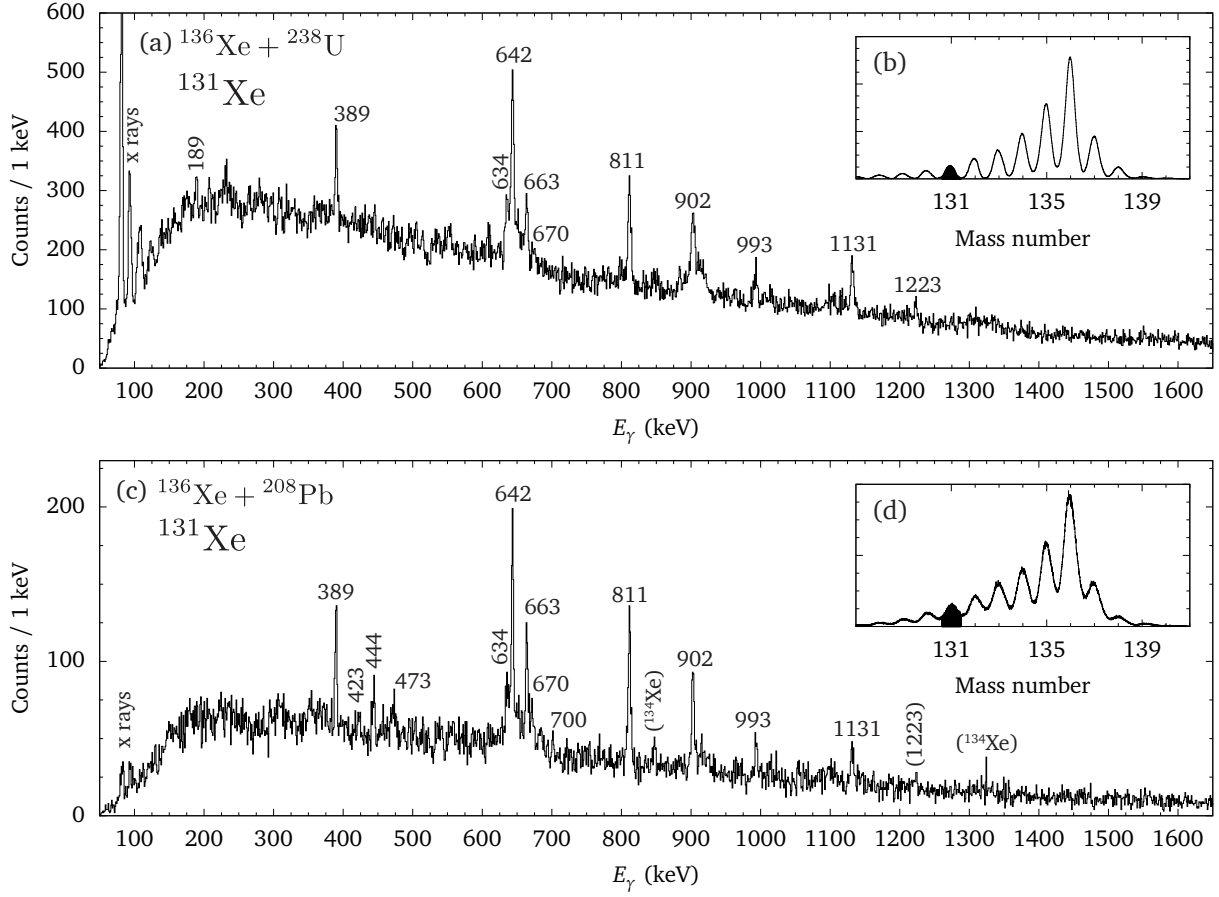


Figure 14: (a) Doppler-corrected γ -ray spectrum gated on ^{131}Xe identified in PRISMA in the $^{136}\text{Xe} + ^{238}\text{U}$ experiment. (b) Mass spectrum of the Xe isotopes obtained with PRISMA. The mass gate is marked in black. (c) Similar data from the $^{136}\text{Xe} + ^{208}\text{Pb}$ experiment; (d) mass spectrum with gate in black. Random background is subtracted with a gate on the prompt peak in the spectrum of time differences between AGATA and PRISMA. Remaining contaminations are marked in the spectrum.

in this thesis, further experiments focusing on other $Z > 50$, $N < 82$ nuclei are either planned or already in analysis.

Only the combination of several experimental approaches including multinucleon transfer provides the necessary experimental information to extend our knowledge on high-spin structures in the $N < 82$ region around xenon and barium. For instance, the high-spin regime of the (stable) $N = 77$ isotone ^{131}Xe is yet unknown. Most of the nuclear-structure information originates from β decay, Coulomb excitation, and (γ, γ') experiments [143]. Data on intermediate spins are only available from $^{128}\text{Te}(\alpha, n\gamma)$ and $^{130}\text{Te}(\alpha, 3n\gamma)$ experiments up to an excitation energy of 3.2 MeV and spin $J = (21/2)$ [110, 112, 144]. Like in the other even-odd Xe isotopes discussed in this work, a characteristic $\nu h_{11/2}^{-1}$ neutron-hole isomer with spin $J^\pi = 11/2^-$ at 163.930(8) keV, decaying via an $M4$ γ -ray transition to the $3/2^+$ ground state, is present in ^{131}Xe . The adopted half-life is $T_{1/2} = 11.84(4)$ d. A $(21/2)^- \xrightarrow{902 \text{ keV}} 19/2^- \xrightarrow{810 \text{ keV}} 15/2^- \xrightarrow{642 \text{ keV}} 11/2^-$ negative-parity band feeds the isomer. Furthermore, a $(19/2^+)$ isomer at 1805 keV was reported with a half-life of 14 ns,

comparable to a corresponding state in the +2p isotope ^{133}Ba with a half-life of 3.5 ns. This isomer decays predominantly via a 189.1-keV γ -ray to the $19/2^-$ state. Only two excited states of unknown spin and parity are known above the $(19/2^+)$ isomer [143].

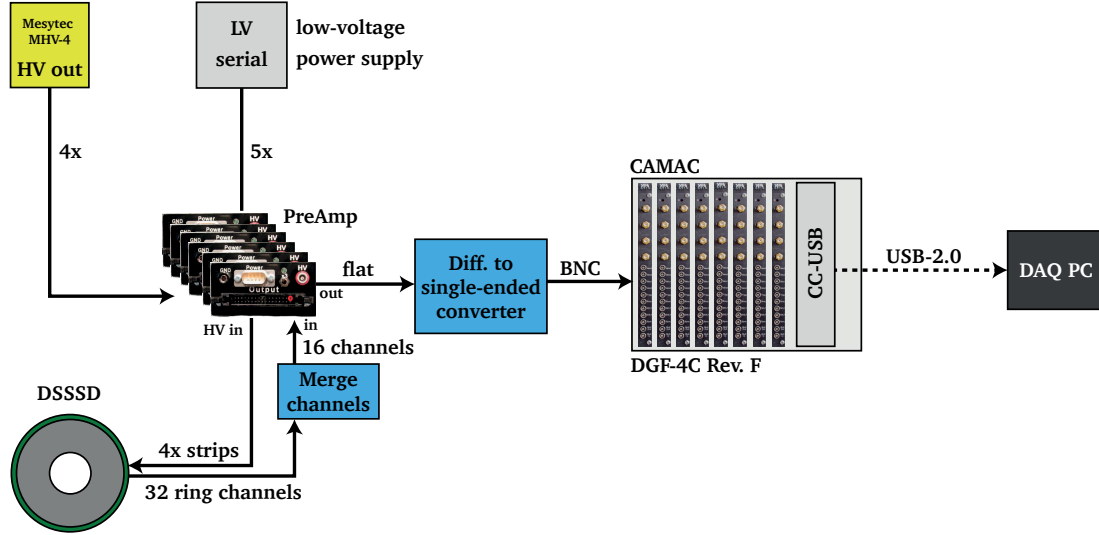


Figure 15: Block diagram of the employed electronics in the HORUS+DSSSD experiments. The DSSSD ring signals are merged pairwise, pre-amplified, converted to single-ended signals, and subsequently digitized by DGF-4C modules.

^{131}Xe was populated in both $^{136}\text{Xe} + ^{208}\text{Pb}$ and $^{136}\text{Xe} + ^{238}\text{U}$ AGATA+PRISMA experiments. Singles γ -ray spectra are shown in Fig. 14, corresponding mass gates are depicted in insets. In order to overcome the limited statistics in the available AGATA data, ^{131}Xe was also populated in an experiment via a $^{124}\text{Sn}(^{11}\text{B}, \text{p}3\text{n})$ fusion-evaporation reaction at the HORUS γ -ray array at the University of Cologne. The beam was provided by the tandem accelerator with an energy of 56 MeV. The $3.0\text{-mg}/\text{cm}^2$ ^{124}Sn target was enriched to 95.3% and evaporated onto a $2.7\text{ mg}/\text{cm}^2$ thick Ta foil. All evaporation residues were stopped within the target. Since the population cross section in the p3n evaporation channel is lower than 1% of the total fusion cross section, but approx. 30% of the corresponding charged-particle evaporation cross section, a clean and selective trigger was crucial. Therefore, a double-sided silicon strip detector (DSSSD) as presented in paper IV was employed as a particle trigger. Inner and outer diameter of the active silicon area are 32 and 85 mm, respectively; the silicon disk has a thickness of $\sim 310(10)\text{ }\mu\text{m}$. The active area is divided into 64 radial segments (sectors) on the p-type junction side and into 32 annular segments (rings) on the ohmic n-side. The pixels cover areas from (innermost) 5.3 to (outermost) 13.7 mm^2 . Adjacent sectors and rings are isolated against each other by an inter-sector or inter-ring area of $110\text{ }\mu\text{m}$ width.

Figure 15 shows a block diagram of the employed data-acquisition system. Photographs and a sketch of the experimental setup are depicted in Figs. 16(a) to (c). The DSSSD was biased by a Mesytec™ MHV-4 quad-channel module; the applied voltage was chosen to be 70 V. Full depletion is

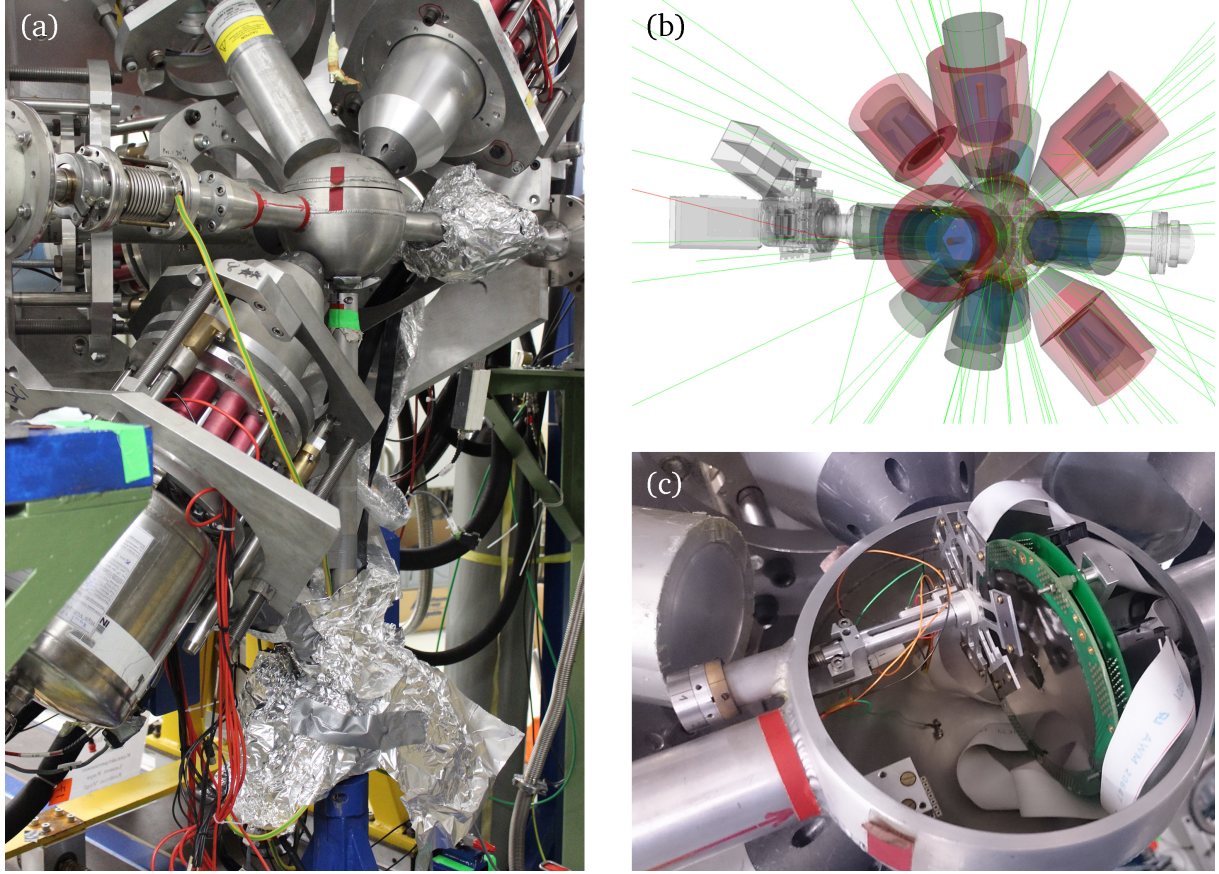


Figure 16: Experimental setup at HORUS, employed for the measurement of high-spin structures in ^{131}Xe and ^{137}Ba (see Paper V for details). (a) Photography of the DSSSD+HORUS setup. Vacuum feedthroughs are located next to the scattering chamber on the right side. Note the shielding against external electronic noise with aluminum foil around the feedthroughs and the preamplifier setup in the bottom part. (b) GEANT4 simulation of the experimental setup. (c) Detailed view into the scattering chamber with the DSSSD. A tantalum foil was mounted in front of the detector to stop all scattered beam particles. The thickness was chosen in such a way that only evaporated protons could reach the Si detector disk.

typically reached at 50 V. Due to the limited number of digital data-acquisition channels, only ring-side segments were read out. Each two neighboring ring channels are merged using a custom-made connector mounted on a PCB board next to the vacuum feedthrough. These pooled raw signals of the DSSSD are then amplified by charge-sensitive preamplifiers built by the electronics workshop of the IKP Cologne. Thereafter, the differential preamplifier signals are transmitted to a NIM converter module in which a circuit converts the differential input to a single-ended output. Finally, the signals are digitized by XIA™ DGF-4C Rev. F modules and written to disk. A global first-level trigger (GFLT) was set up, requiring at least two DGF channels to fire. Prior to the experiment, the employed DSSSD was thoroughly investigated in a dedicated analog experimental setup employing the GSI Multi-Branch System (MBS) software [145] in combination with the data-acquisition software MAR_aBQ_U [146]. Details of the tests and the detector performance, leakage currents, and energy resolutions are given in Paper V and in Ref. [147].

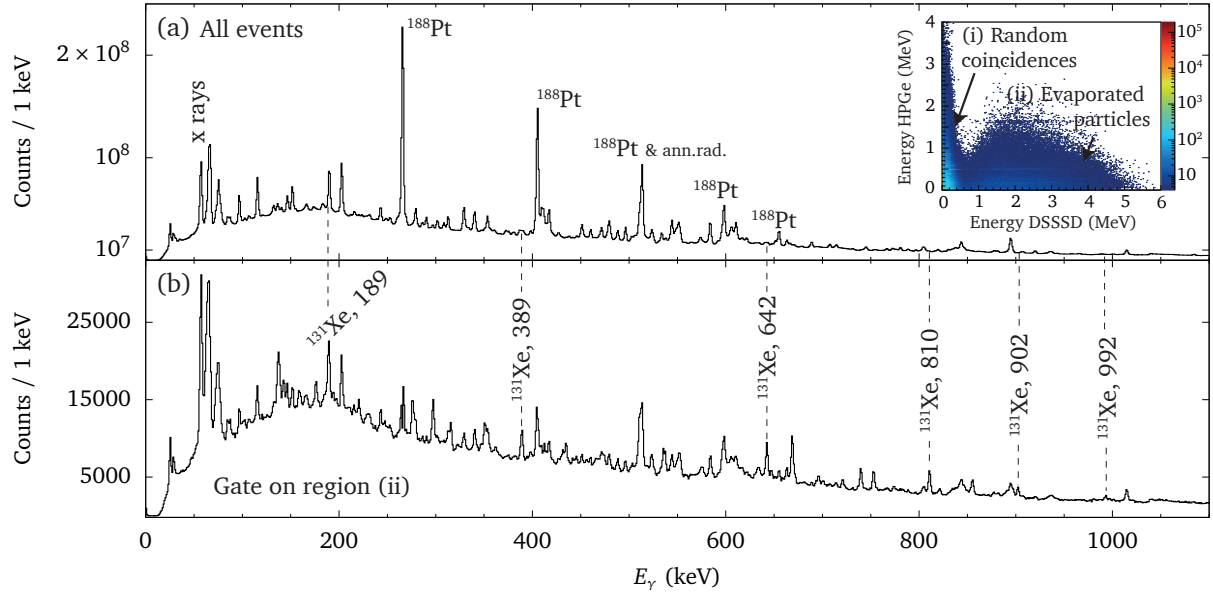


Figure 17: First preliminary results of the ^{131}Xe experiment at the HORUS+DSSSD setup. (a) γ -ray spectrum of all recorded events. The spectrum is severely contaminated by the $^{181}\text{Ta}(^{11}\text{B},4n)^{188}\text{Pt}$ reaction channel, γ -ray transitions of the elusive ^{131}Xe channel cannot be observed. (Inset) Evaporation residues are identified in the matrix of the energy detected by the DSSSD versus the HORUS γ -ray energy. Evaporated protons are expected in an energy range from approx. 1 to 6 MeV. Random coincidences are mainly caused by the detection of low-energy δ electrons and β particles. (b) HORUS γ -ray spectrum with a gate on evaporated particles; several yrast transitions are now prominently visible and marked in the spectrum.

First preliminary spectra are displayed in Fig. 17. Subfigure (a) shows a γ -ray spectrum of all recorded events. Apparently, the tin target formed an alloy with the tantalum backing, yielding a significant contribution of a $^{181}\text{Ta}(^{11}\text{B},4n)^{188}\text{Pt}$ reaction channel. The γ -ray transitions of ^{188}Pt and the 4n and 5n neutron-evaporation channels $^{130,131}\text{Cs}$ dominate the spectrum. Transitions of the elusive ^{131}Xe proton-evaporation channel cannot be observed. Evaporation residues are selected in matrices of the energy detected by the DSSSD plotted against the HORUS γ -ray energy. The evaporated protons are expected in an energy range from approx. 1 to 6 MeV. Random coincidences are mainly caused by the detection of low-energy δ electrons and electrons from β decay. A gated γ -ray spectrum is presented in Fig. 17(b). Several ^{131}Xe γ -ray transitions are now prominently visible and marked in the spectrum. Further details of the data analysis of the $^{11}\text{B} + ^{124}\text{Sn}$ experiment, final results on particle- $\gamma\gamma$ coincidences in ^{131}Xe , and detailed comparisons to modern shell-model calculations are presented in Ref. [148].

Further and complementary experiments in the Xe-Ba region could be performed in upcoming beam times at the Grand Accélérateur National d'Ions Lourds (GANIL) [149] employing $^{132,134,136}\text{Xe}$ beams. The extended AGATA spectrometer coupled to the Variable Mode Spectrometer (VAMOS) will allow for a more detailed spectroscopy of many $N < 82$ nuclei with small or medium effort. In particular, detailed angular-correlation and polarization measurements are needed to determine proper spin,

parity, and multipolarity assignments. More specifically, upcoming AGATA campaigns with ^{136}Xe will allow to study the onset of isomerism as function of proton number above the $Z = 50$ shell closure along the $N = 79$ chain. Even though studies of ^{135}Ba and ^{137}Ce were performed up to highest spins and excitation energies, no candidates for isomers below 3 MeV were found to date. The new discovery of a $(23/2^+)$ isomer in ^{133}Xe and the recent observation of a 277(2)-ns isomer in ^{139}Nd affirm the existence of $J^\pi = 23/2^+$ isomers also in these two nuclei. Both ^{135}Ba and ^{137}Ce are accessible in suitable multinucleon-transfer reactions. Furthermore, conversion-electron measurements are in order to resolve the multipole character of the isomer decay in ^{133}Xe .

Future experiments in the actinide region

The study of nuclear-structure features in neutron-rich actinides remains of utmost interest. Various theoretical predictions await experimental verification in the actinide region. Excitation energies and collective properties are predicted by studies employing mean-field and beyond mean-field, microscopic-macroscopic, and cluster-model approaches. Recent studies employing state-of-the-art complex density functionals [135, 136] predict sharp upbends in the kinetic moments of inertia along neutron-rich Th and U nuclei. From the experimental point of view, there is still scarce information on high-spin excitations beyond ^{240}U and ^{234}Th . The spectroscopy work of neutron-rich ^{240}U presented in this thesis paves the way for the spectroscopy of the collective properties of even heavier actinides and transactinide nuclei which will become feasible at next-generation facilities. Future experiments employing multinucleon-transfer reactions will require the same dedicated triggers and synergies of γ -ray-tracking spectrometers in combination with mass spectrometers and other sophisticated ancillary detectors to suppress the large fission background.

It has to be noted that the production yield of neutron-rich actinides is not necessarily favored at the reaction's grazing angle. Instead, optimum cross sections may be achieved under forward direction. Meanwhile, corresponding theoretical predictions for energies slightly above the Coulomb barrier are convincingly backed by several experimental results, especially from reaction studies performed at GSI [150, 151]. However, the small cross-sections down to the sub- μb region require a clean separation and possibly a single-event detection with refined detector systems.

New experimental studies and relevant improvements to previous experiments go hand in hand with refined detection capabilities. AGATA as a 1π tracking array with more than fifteen triple cryostats or 45 high-volume, high-efficiency, position-sensitive HPGe detectors will be an ideal setup and a unique opportunity for a comprehensive investigation of not only the reaction mechanisms, but also for the nuclear structure of several hard-to-reach isotopes, among them neutron-rich actinides. Future experiments will take advantage of an unprecedented high count-rate capability of the AGATA electronics and data-acquisition system which was successfully demonstrated in the Legnaro, GSI, and GANIL campaigns. Single AGATA crystals were running with a count rate of more than 50 kHz.

AGATA in combination with VAMOS at GANIL equipped with a Gas-Filled Separator (GFS) mode [153, 154] under zero degrees will offer a novel approach to measure elusive reaction channels not only

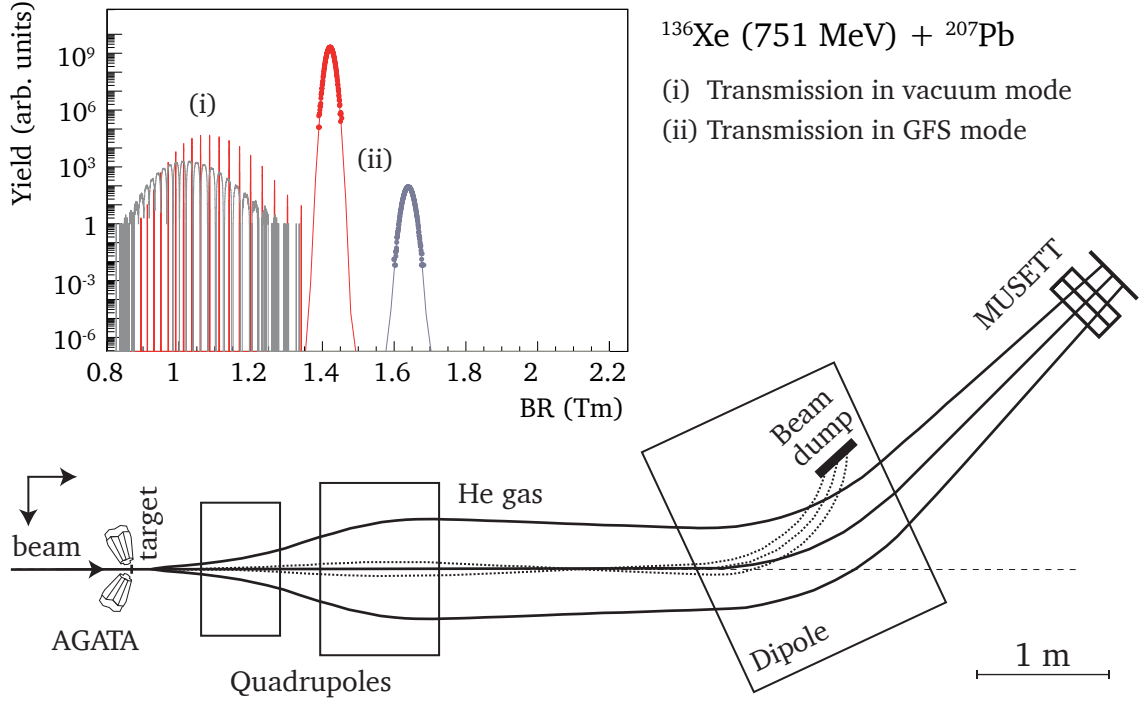


Figure 18: VAMOS mass spectrometer in the gas-filled mode. Red: Beam-like fragments. Grey: Target-like reaction products. Simulated transmission yields of a $^{136}\text{Xe} + ^{207}\text{Pb}$ multinucleon transfer reaction are shown in the top-left inset. At 0° , the reaction products can only be separated in the GFS mode [152]. VAMOS sketch adapted from Ref. [153].

via fusion-evaporation reactions, but also via multinucleon transfer. Like PRISMA, VAMOS is a large-solid-angle mass spectrometer employing numerical methods for the reconstruction of the particle trajectory and a complete identification of reaction products. In the standard vacuum mode, the ions are selected depending on their magnetic rigidity, equivalent to the momentum over charge state ratio, $BR = p/q$. Contrarily, in the GFS mode, the reaction products travel through a gas at low pressure. The concept is illustrated in Fig. 18. In the case of multinucleon transfer, the beam- and target-like fragments reach different mean charge states \bar{q} along their transport trajectory in the spectrometer. Thus, the magnetic rigidity is, to the first order, proportional to the mass. Undesirable ion species are directed into a beam dump. Beam rejection factors greater than 10^{10} are possible to be achieved with the GFS setup [153]. As shown in the top-left inset of Fig. 18, a separation of the reaction products after an example $^{136}\text{Xe} + ^{207}\text{Pb}$ multinucleon-transfer reaction cannot be achieved in the standard vacuum mode (cf. region (i)). Contrarily, beam and target-like species are separated in the GFS mode, as seen in region (ii). However, the ion transmission through the gas volume highly deteriorates the mass resolution. Therefore, it is necessary to isotopically identify the reaction products by their characteristic decay in a detector at the focal plane. The recoil nuclei are implanted into the highly-segmented window-less Si array MUSETT [155]. In case the nuclei decay via α , β or delayed fission in a suitable time window, the recoil-decay tagging technique is employed. Both position of the recoil and energy of the decay are measured and correlated with prompt γ -rays at the target position.

Clean trigger conditions and the high count-rate capability of AGATA will allow to address the nuclear structure of various heavy nuclei. Interesting physics cases are for example nuclei in the $84 < Z < 92$ region. In addition, the γ -ray spectroscopy will contribute via the measurements of X-ray yields, survival probabilities, maximum excitation-energies, and spin distributions to a better understanding of the actual reaction and will help to further explore the possibilities of multinucleon-transfer reactions for the population of heavy and superheavy systems.

Detailed studies on the formation of neutron-rich nuclei in the $N = 82$ Xe-Ba and $N > 144$ actinide regions via $^{136}\text{Xe} + ^{238}\text{U}$ multinucleon transfer could be addressed with the stand-alone magnetic spectrometer PRISMA in conjunction with its new *second-arm* detector array. This detector system consists of a position-sensitive Parallel-Plate Avalanche Counter (PPAC) followed by an axial-field ionization chamber (Bragg chamber), mounted at the kinematically correlated angles of the binary reaction, enabling the coincident detection of the complementary light and heavy MNT fragments [156]. First kinematic-coincidence experiments with the new PRISMA setup were performed for the $^{136}\text{Xe} + ^{208}\text{Pb}$ systems close to the Coulomb barrier at 6.4 MeV/nucleon [157]. A recent experiment focused on the $^{197}\text{Au} + ^{130}\text{Te}$ system at 1070 MeV to study projectile-like cross sections in the Pt-Os region [158]. In this reaction, also target-like yields around mass $A = 130$ are of high interest since nuclei in the vicinity of ^{132}Sn may be accessible by few-proton stripping and neutron pick-up.

It would be desirable to remeasure mass and charge yields, differential and total cross sections, and total kinetic energy distributions of the different multinucleon transfer channels in the $^{136}\text{Xe} + ^{238}\text{U}$ reaction with the sensitivity of the enhanced PRISMA plus second-arm setup. Such a setup would overcome the shortcomings due to the missing position information of DANTE in the present experiments. Furthermore, it is of great interest to continue the study of the fission part in the $^{136}\text{Xe} + ^{238}\text{U}$ reaction. In general, different kinds of fission processes may generate the final fission yields: (i) quasi-fission (QF), with masses located in between deep-inelastic transfer and symmetric fission from compound nuclei, (ii) fission after Coulomb excitation, and (iii) transfer-induced symmetric or asymmetric fission from the target. Each of these processes will be differently selected by the spectrometer and by the adjusted magnetic fields. Moreover, each of the processes will yield different Δt_{ToF} structures. A dedicated study would especially clarify the nature of the two different peaks in the Δt_{ToF} spectrum observed in paper I.

A detailed study of nucleon-nucleon correlation and channel-coupling effects in the heavy $^{136}\text{Xe} + ^{238}\text{U}$ system would be of high interest. However, within the present experimental setup angular distributions and TKEL spectra are very broad, mainly due to the employed thick target. Thus, the angular distributions and TKEL spectra are integrated over a large range of effective bombarding energies. The computer code GRAZING estimates the transfer cross section for a small range of impact parameters that are close to the grazing one, so all transfer channels have very similar angular distributions. Moreover, the corresponding energy spectra are also bell-shaped, centered at the optimum Q -value [159]. As a consequence, thick-target experiments cannot yield any selectivity on impact parameters. A given channel, normally selected by angles and Q -values, may be populated by far more complicated

mechanisms; measured angular and energy distributions do not necessarily reflect the original reaction mechanism. Consequently, the main challenge of such an experiment would be the production of a sufficiently thin ^{238}U target. If available, applicable and permitted, analog experiments could be envisaged employing ^{232}Th , ^{234}U , ^{235}U or even Pu targets.

From the theoretical point of view, it might be worth the effort to review the multinucleon-transfer reaction dynamics in terms of explicitly calculating the angular-momentum distributions for the projectile-like and target-like fragments in dependence of the nuclear deformation. A large nuclear deformation of the target can be associated with a larger angular-momentum transfer. The reaction partners may collide at a larger impact parameter because of the deformation, leading to differences in the entrance population and feeding of high-spin states. In the experiments reported in this thesis, ^{136}Xe impinged onto three targets with various nuclear shapes: the doubly-magical nucleus ^{208}Pb is spherical, ^{198}Pt is oblately deformed [160], and ^{238}U exhibits most likely an prolate deformation [161]. The microscopic framework of the time-dependent Hartree-Fock (TDHF) theory is continuously developed further and may shed light to this issue. Employing the particle-number projection technique that was proposed in Ref. [28], the average angular momentum could be computed for each of the reaction products in the near future [162].

Bibliography

- [1] K. Alder and A. Winther. “The Theory of Coulomb Excitation of Nuclei.” *Phys. Rev.* 91 (6 Sept. 1953), pp. 1578–1579 (cit. on p. 7).
- [2] M. Zielińska, L. P. Gaffney, K. Wrzosek-Lipska, E. Clément, T. Grahn, N. Kesteloot, P. Napiorkowski, J. Pakarinen, P. Van Duppen and N. Warr. “Analysis methods of safe Coulomb-excitation experiments with radioactive ion beams using the GOSIA code.” *EPJ A* 52.4 (2016), p. 99 (cit. on p. 7).
- [3] W. Królas. “Heavy-ion deep-inelastic collisions studied by discrete gamma-ray spectroscopy.” PhD thesis. University of Kraków, 1996 (cit. on p. 7).
- [4] N. V. Antonenko, E. A. Cherepanov, A. K. Nasirov, V. P. Permjakov and V. V. Volkov. “Compound nucleus formation in reactions between massive nuclei: Fusion barrier.” *Phys. Rev. C* 51 (5 May 1995), pp. 2635–2645 (cit. on p. 7).
- [5] G. Adamian, N. Antonenko, R. Jolos and W. Scheid. “Neck dynamics at the approach stage of heavy ion collisions.” *Nucl. Phys. A* 619.1 (1997), pp. 241–260 (cit. on p. 7).
- [6] R. Bass. *Nuclear Reactions with Heavy Ions. Theoretical and Mathematical Physics*. Springer Berlin Heidelberg, 1980 (cit. on pp. 7, 9).
- [7] J. Töke, R. Bock, G. Dai, A. Gobbi, S. Gralla, K. Hildenbrand, J. Kuzminski, W. Müller, A. Olmi, H. Stelzer, B. Back and S. Bjørnholm. “Quasi-fission – The mass-drift mode in heavy-ion reactions.” *Nucl. Phys. A* 440.2 (1985), pp. 327–365 (cit. on p. 8).
- [8] L. Corradi, G. Pollarolo and S. Szilner. “Multinucleon transfer processes in heavy-ion reactions.” *J. Phys. G* 36.11 (2009), p. 113101 (cit. on pp. 8–9, 13, 15).
- [9] K. E. Rehm, A. M. van den Berg, J. J. Kolata, D. G. Kovar, W. Kutschera, G. Rosner, G. S. F. Stephans and J. L. Yntema. “Transition from quasi-elastic to deep-inelastic reactions in the $^{48}\text{Ti}+^{208}\text{Pb}$ system.” *Phys. Rev. C* 37 (6 June 1988), pp. 2629–2646 (cit. on p. 8).
- [10] H. Takai, C. N. Knott, D. F. Winchell, J. X. Saladin, M. S. Kaplan, L. de Faro, R. Aryaeinejad, R. A. Blue, R. M. Ronningen, D. J. Morrissey, I. Y. Lee and O. Dietzsch. “Population of high spin states by quasi-elastic and deep inelastic collisions.” *Phys. Rev. C* 38 (3 Sept. 1988), pp. 1247–1261 (cit. on p. 8).
- [11] K. Rehm. “Quasi-elastic heavy-ion collisions.” *Annu. Rev. Nucl. Part. Sci.* 41.1 (1991), pp. 429–468 (cit. on p. 8).
- [12] L. Corradi, A. M. Stefanini, C. J. Lin, S. Beghini, G. Montagnoli, F. Scarlassara, G. Pollarolo and A. Winther. “Multinucleon transfer processes in $^{64}\text{Ni}+^{238}\text{U}$.” *Phys. Rev. C* 59 (1 Jan. 1999), pp. 261–268 (cit. on p. 8).
- [13] S. Szilner, C. A. Ur, L. Corradi, N. Marginean, G. Pollarolo, A. M. Stefanini, S. Beghini, B. R. Behera, E. Fioretto, A. Gadea, B. Guiot, A. Latina, P. Mason, G. Montagnoli, F. Scarlassara, M. Trotta, G. de Angelis, F. Della Vedova, E. Farnea, F. Haas, S. Lenzi, S. Lunardi, R. Marginean, R. Menegazzo, D. R. Napoli, M. Nespolo, I. V. Pokrovsky, F. Recchia, M. Romoli, M.-D. Salsac, N. Soić and J. J. Valiente-Dobón. “Multinucleon transfer reactions in closed-shell nuclei.” *Phys. Rev. C* 76 (2 Aug. 2007), p. 024604 (cit. on p. 9).
- [14] T. Mijatović, S. Szilner, L. Corradi, D. Montanari, G. Pollarolo, E. Fioretto, A. Gadea, A. Goasduff, D. J. Malenica, N. Mărginean, M. Milin, G. Montagnoli, F. Scarlassara, N. Soić,

- A. M. Stefanini, C. A. Ur and J. J. Valiente-Dobón. “Multinucleon transfer reactions in the $^{40}\text{Ar} + ^{208}\text{Pb}$ system.” *Phys. Rev. C* 94 (6 Dec. 2016), p. 064616 (cit. on pp. 9, 13).
- [15] T. Mijatović. “Study of heavy-ion reactions with large solid angle magnetic spectrometers.” PhD thesis. University of Zagreb, 2015 (cit. on p. 9).
- [16] L. Corradi, A. M. Vinodkumar, A. M. Stefanini, E. Fioretto, G. Prete, S. Beghini, G. Montagnoli, F. Scarlassara, G. Pollarolo, F. Cerutti and A. Winther. “Light and heavy transfer products in $^{58}\text{Ni} + ^{208}\text{Pb}$ at the Coulomb barrier.” *Phys. Rev. C* 66 (2 Aug. 2002), p. 024606 (cit. on pp. 10, 13).
- [17] J.-J. Gaimard and K.-H. Schmidt. “A reexamination of the abrasion-ablation model for the description of the nuclear fragmentation reaction.” *Nucl. Phys. A* 531.3-4 (1991), pp. 709–745 (cit. on p. 10).
- [18] Y. Blumenfeld, T. Nilsson and P. V. Duppen. “Facilities and methods for radioactive ion beam production.” *Phys. Scripta* 2013.T152 (2013), p. 014023 (cit. on pp. 10, 14).
- [19] N. Fukuda, T. Kubo, T. Ohnishi, N. Inabe, H. Takeda, D. Kameda and H. Suzuki. “Identification and separation of radioactive isotope beams by the BigRIPS separator at the RIKEN RI Beam Factory.” *Nucl. Instr. Meth. Phys. Res. B* 317, Part B (2013). XVIth International Conference on ElectroMagnetic Isotope Separators and Techniques Related to their Applications, December 2-7, 2012 at Matsue, Japan, pp. 323–332 (cit. on p. 10).
- [20] P. Spiller and G. Franchetti. “The FAIR accelerator project at GSI.” *Nucl. Instr. Meth. Phys. Res. A* 561.2 (2006). Proceedings of the Workshop on High Intensity Beam Dynamics, pp. 305–309 (cit. on p. 10).
- [21] E. Vigezzi and A. Winther. “On the application of complex trajectories to direct heavy-ion reactions.” *Ann. Phys. (N.Y.)* 192.2 (1989), pp. 432–486 (cit. on p. 10).
- [22] W. Nörenberg. “Transport phenomena in multi-nucleon transfer reactions.” *Phys. Lett. B* 52.3 (1974), pp. 289–292 (cit. on p. 10).
- [23] L. Moretto and J. Sventek. “A theoretical approach to the problem of partial equilibration in heavy ion reactions.” *Phys. Lett. B* 58.1 (1975), pp. 26–30 (cit. on p. 10).
- [24] C. Li, F. Zhang, J. Li, L. Zhu, J. Tian, N. Wang and F.-S. Zhang. “Multinucleon transfer in the $^{136}\text{Xe} + ^{208}\text{Pb}$ reaction.” *Phys. Rev. C* 93 (1 Jan. 2016), p. 014618 (cit. on p. 10).
- [25] K. Sekizawa and K. Yabana. “Time-dependent Hartree-Fock calculations for multinucleon transfer processes in $^{40,48}\text{Ca} + ^{124}\text{Sn}$, $^{40}\text{Ca} + ^{208}\text{Pb}$, and $^{58}\text{Ni} + ^{208}\text{Pb}$ reactions.” *Phys. Rev. C* 88 (1 July 2013), p. 014614 (cit. on p. 10).
- [26] K. Sekizawa and K. Yabana. “Time-dependent Hartree-Fock calculations for multinucleon transfer and quasifission processes in the $^{64}\text{Ni} + ^{238}\text{U}$ reaction.” *Phys. Rev. C* 93 (5 May 2016), p. 054616 (cit. on p. 10).
- [27] C. Simenel. “Particle Transfer Reactions with the Time-Dependent Hartree-Fock Theory Using a Particle Number Projection Technique.” *Phys. Rev. Lett.* 105 (19 Nov. 2010), p. 192701 (cit. on p. 10).
- [28] K. Sekizawa and K. Yabana. “Particle-number projection method in time-dependent Hartree-Fock theory: Properties of reaction products.” *Phys. Rev. C* 90 (6 Dec. 2014), p. 064614 (cit. on pp. 10, 131).

- [29] V. Zagrebaev and W. Greiner. “Low-energy collisions of heavy nuclei: dynamics of sticking, mass transfer and fusion.” *J. Phys. G* 34.1 (2007), p. 1 (cit. on p. 11).
- [30] V. Zagrebaev and W. Greiner. “Shell effects in damped collisions: a new way to superheavies.” *J. Phys. G* 34.11 (2007), p. 2265 (cit. on p. 11).
- [31] V. I. Zagrebaev, Y. T. Oganessian, M. G. Itkis and W. Greiner. “Superheavy nuclei and quasi-atoms produced in collisions of transuranium ions.” *Phys. Rev. C* 73 (3 Mar. 2006), p. 031602 (cit. on p. 11).
- [32] V. Zagrebaev and W. Greiner. “Synthesis of superheavy nuclei: A search for new production reactions.” *Phys. Rev. C* 78 (3 Sept. 2008), p. 034610 (cit. on p. 11).
- [33] V. Zagrebaev and W. Greiner. “Production of New Heavy Isotopes in Low-Energy Multinucleon Transfer Reactions.” *Phys. Rev. Lett.* 101 (12 Sept. 2008), p. 122701 (cit. on p. 11).
- [34] V. I. Zagrebaev and W. Greiner. “Production of heavy and superheavy neutron-rich nuclei in transfer reactions.” *Phys. Rev. C* 83 (4 Apr. 2011), p. 044618 (cit. on p. 11).
- [35] V. I. Zagrebaev and W. Greiner. “Production of heavy trans-target nuclei in multinucleon transfer reactions.” *Phys. Rev. C* 87 (3 Mar. 2013), p. 034608 (cit. on p. 11).
- [36] A. Winther. “Grazing reactions in collisions between heavy nuclei.” *Nucl. Phys. A* 572.1 (1994), pp. 191–235 (cit. on p. 11).
- [37] A. Winther. “Dissipation, polarization and fluctuation in grazing heavy-ion collisions and the boundary to the chaotic regime.” *Nucl. Phys. A* 594.2 (1995), pp. 203–245 (cit. on p. 11).
- [38] G. Pollaro and A. Winther. “Fusion excitation functions and barrier distributions: A semiclassical approach.” *Phys. Rev. C* 62 (5 Oct. 2000), p. 054611 (cit. on pp. 11–12).
- [39] G. Pollaro. Computer code GRAZING. 2006. URL: <http://www.to.infn.it/~nanni/grazing> (cit. on p. 11).
- [40] W. Nörenberg and H. Weidemüller. Introduction to the Theory of Heavy-Ion Collisions. Lecture Notes in Physics. Springer Berlin Heidelberg, 2013 (cit. on p. 11).
- [41] G. Pollaro. “Quasielastic Barrier Distributions: Role of Particle Transfer Channels.” *Phys. Rev. Lett.* 100 (25 June 2008), p. 252701 (cit. on pp. 11–12).
- [42] G. Pollaro. “Fusion Reactions as a Probe of the Nucleus-Nucleus Potential at Short Distances.” *Prog. Theor. Phys. Supp.* 154 (2004), pp. 201–208 (cit. on p. 12).
- [43] M. Dasgupta, A. Navin, Y. Agarwal, C. Baba, H. Jain, M. Jhingan and A. Roy. “Fusion of $^{28}\text{Si} + ^{68}\text{Zn}$, $^{32}\text{S} + ^{64}\text{Ni}$, $^{37}\text{Cl} + ^{59}\text{Co}$ and $^{45}\text{Sc} + ^{51}\text{V}$ in the vicinity of the Coulomb barrier.” *Nucl. Phys. A* 539.2 (1992), pp. 351–369 (cit. on p. 12).
- [44] S. Bottoni, G. Benzoni, S. Leoni, D. Montanari, A. Bracco, F. Azaiez, S. Franchoo, I. Stefan, N. Blasi, F. Camera, F. C. L. Crespi, A. Corsi, B. Million, R. Nicolini, E. Vigezzi, O. Wieland, F. Zocca, L. Corradi, G. De Angelis, E. Fioretto, B. Guiot, N. Marginean, D. R. Napoli, R. Orlandi, E. Sahin, A. M. Stefanini, J. J. Valiente-Dobon, S. Aydin, D. Bazzacco, E. Farnea, S. Lenzi, S. Lunardi, P. Mason, D. Mengoni, G. Montagnoli, F. Recchia, C. Ur, F. Scarlassara, A. Gadea, A. Maj, J. Wrzesinski, K. Zuber, Z. Dombradi, S. Szilner, A. Saltarelli and G. Pollaro. “Reaction dynamics and nuclear structure of moderately neutron-rich Ne isotopes by heavy-ion reactions.” *Phys. Rev. C* 85 (6 June 2012), p. 064621 (cit. on p. 13).

- [45] C. L. Jiang, K. E. Rehm, H. Esbensen, D. J. Blumenthal, B. Crowell, J. Gehring, B. Glagola, J. P. Schiffer and A. H. Wuosmaa. “Multineutron transfer in $^{58}\text{Ni}+^{124}\text{Sn}$ collisions at sub-barrier energies.” *Phys. Rev. C* 57 (5 May 1998), pp. 2393–2400 (cit. on p. 13).
- [46] G. Montagnoli, S. Beghini, F. Scarlassara, A. Stefanini, L. Corradi, C. Lin, G. Pollarolo and A. Winther. “Transfer reactions and sub-barrier fusion in $^{40}\text{Ca} + ^{90,96}\text{Zr}$.” *EPJ A* 15.3 (2002), pp. 351–356 (cit. on p. 13).
- [47] S. Szilner, L. Corradi, G. Pollarolo, S. Beghini, B. R. Behera, E. Fioretto, A. Gadea, F. Haas, A. Latina, G. Montagnoli, F. Scarlassara, A. M. Stefanini, M. Trotta, A. M. Vinodkumar and Y. Wu. “Multinucleon transfer processes in $^{40}\text{Ca} + ^{208}\text{Pb}$.” *Phys. Rev. C* 71 (4 Apr. 2005), p. 044610 (cit. on p. 13).
- [48] D. Montanari, L. Corradi, S. Szilner, G. Pollarolo, E. Fioretto, G. Montagnoli, F. Scarlassara, A. M. Stefanini, S. Courtin, A. Goasduff, F. Haas, D. Jelavić Malenica, C. Michelagnoli, T. Mijatović, N. Soić, C. A. Ur and M. Varga Pajtler. “Neutron Pair Transfer in $^{60}\text{Ni} + ^{116}\text{Sn}$ Far below the Coulomb Barrier.” *Phys. Rev. Lett.* 113 (5 July 2014), p. 052501 (cit. on p. 13).
- [49] M. Thoennessen. “Reaching the limits of nuclear stability.” *Rep. Prog. Phys.* 67.7 (2004), p. 1187 (cit. on p. 13).
- [50] A. Mueller and B. Sherrill. “Nuclei at the limits of particle stability.” *Annu. Rev. Nucl. Part. Sci.* 43.1 (1993), pp. 529–583 (cit. on p. 13).
- [51] P. Woods and C. Davids. “Nuclei beyond the proton drip-line.” *Annu. Rev. Nucl. Part. Sci.* 47.1 (1997), pp. 541–590 (cit. on p. 13).
- [52] J. Hamilton, A. Ramayya, J. Hwang, X. Luo, J. Rasmussen, E. Jones, X. Zhang, S. Zhu, P. Gore, T. Ginter, I. Lee, R. Janssens, I. Ahmed, J. Cole, W. Greiner, G. Ter-Akopian and Y. Oganessian. “New insights into neutron-rich nuclei at high spin.” *EPJ A* 15.1 (2002), pp. 175–179 (cit. on p. 13).
- [53] A. Gade and S. N. Liddick. “Shape coexistence in neutron-rich nuclei.” *J. Phys. G Nucl. Part. Phys.* 43.2 (2016), p. 024001 (cit. on p. 13).
- [54] J. K. Hwang, A. V. Ramayya, J. H. Hamilton, C. J. Beyer, X. Q. Zhang, J. O. Rasmussen, Y. X. Luo, S. C. Wu, T. N. Ginter, I. Y. Lee, C. M. Folden, P. Fallon, P. Zielinski, K. E. Gregorich, A. O. Macchiavelli, M. A. Stoyer and S. J. Asztalos. “ $\pi/2[413]$ rotational band and high spin states in odd-mass $^{115,117}\text{Ag}$.” *Phys. Rev. C* 65 (5 May 2002), p. 054314 (cit. on p. 13).
- [55] Y. X. Luo, J. O. Rasmussen, J. H. Hamilton, A. V. Ramayya, J. K. Hwang, C. J. Beyer, S. J. Zhu, J. Kormicki, X. Q. Zhang, E. F. Jones, P. M. Gore, T. N. Ginter, K. E. Gregorich, I.-Y. Lee, A. O. Macchiavelli, P. Zielinski, C. M. Folden, P. Fallon, G. M. Ter-Akopian, Y. T. Oganessian, A. V. Daniel, M. A. Stoyer, J. D. Cole, R. Donangelo, S. C. Wu and S. J. Asztalos. “Level structure of ^{141}Ba and ^{139}Xe and the level systematics of $N = 85$ even-odd isotones.” *Phys. Rev. C* 66 (1 July 2002), p. 014305 (cit. on p. 13).
- [56] R. Page. Private communication. Physics Department, University of Liverpool, 2017 (cit. on p. 14).
- [57] S. Agbemava, A. Afanasjev, D. Ray and P. Ring. “Global performance of covariant energy density functionals: Ground state observables of even-even nuclei and the estimate of theoretical uncertainties.” *Phys. Rev. C* 89 (5 May 2014), p. 054320 (cit. on p. 14).

- [58] A. M. Nathan, J. W. Olness, E. K. Warburton and J. B. McGrory. “Yrast decay schemes from heavy ion + ^{48}Ca fusion-evaporation reactions. I. $^{54-56}\text{Mn}$, ^{56}Cr , and $^{52-53}\text{V}$.” *Phys. Rev. C* 16 (1 July 1977), pp. 192–214 (cit. on p. 13).
- [59] E. K. Warburton, J. W. Olness, A. M. Nathan, J. J. Kolata and J. B. McGrory. “Yrast decay schemes from heavy-ion + ^{48}Ca fusion-evaporation reactions. II. $^{59-60}\text{Fe}$ and $^{59-60}\text{Co}$.” *Phys. Rev. C* 16 (3 Sept. 1977), pp. 1027–1039 (cit. on p. 13).
- [60] A. M. Nathan, J. W. Olness, E. K. Warburton and J. B. McGrory. “Yrast decay schemes from heavy-ion + ^{48}Ca fusion-evaporation reactions. III. $^{57,58}\text{Fe}$, $^{54,55}\text{Cr}$, and $^{57,58}\text{Mn}$.” *Phys. Rev. C* 17 (3 Mar. 1978), pp. 1008–1025 (cit. on p. 13).
- [61] E. K. Warburton, J. W. Olness, A. M. Nathan and A. R. Poletti. “Yrast decay schemes from heavy-ion + ^{48}Ca fusion-evaporation reactions: IV: ^{53}Cr , ^{54}V , ^{62}Co , and $^{61-63}\text{Ni}$.” *Phys. Rev. C* 18 (4 Oct. 1978), pp. 1637–1650 (cit. on p. 13).
- [62] P. H. Regan, J. W. Arrison, U. J. Hüttmeier and D. P. Balamuth. “Yrast γ -ray spectroscopy of the neutron rich isotopes $^{61,63}\text{Co}$.” *Phys. Rev. C* 54 (3 Sept. 1996), pp. 1084–1097 (cit. on p. 13).
- [63] D. Steppenbeck, A. N. Deacon, S. J. Freeman, R. V. F. Janssens, S. Zhu, M. P. Carpenter, P. Chowdhury, M. Honma, T. Lauritsen, C. J. Lister, D. Seweryniak, J. F. Smith, S. L. Tabor and B. J. Varley. “High-spin structures in the neutron-rich isotopes $^{57-60}\text{Mn}$.” *Phys. Rev. C* 81 (1 Jan. 2010), p. 014305 (cit. on p. 13).
- [64] H. Nishibata, R. Leguillon, A. Odahara, T. Shimoda, C. M. Petrache, Y. Ito, J. Takatsu, K. Tajiri, N. Hamatani, R. Yokoyama, E. Ideguchi, H. Watanabe, Y. Wakabayashi, K. Yoshinaga, T. Suzuki, S. Nishimura, D. Beaumel, G. Lehaut, D. Guinet, P. Desesquelles, D. Curien, K. Higashiyama and N. Yoshinaga. “High-spin states in ^{136}La and possible structure change in the $N = 79$ region.” *Phys. Rev. C* 91 (5 May 2015), p. 054305 (cit. on p. 15).
- [65] J. Hamilton, A. Ramayya, S. Zhu, G. Ter-Akopian, Y. Oganessian, J. Cole, J. Rasmussen and M. Stoyer. “New insights from studies of spontaneous fission with large detector arrays.” *Prog. Part. Nucl. Phys.* 35 (1995), pp. 635–704 (cit. on p. 15).
- [66] I.-Y. Lee. “The GAMMASPHERE.” *Nucl. Phys. A* 520 (1990), pp. c641–c655 (cit. on p. 15).
- [67] J. Simpson. “The Euroball Spectrometer.” *Z. Phys. A* 358.2 (1997), pp. 139–143 (cit. on p. 15).
- [68] P. Nolan. “EUROGAM: a high efficiency multidetector array for gamma-ray spectroscopy.” *Endeavour* 15.1 (1991), pp. 22–25 (cit. on p. 15).
- [69] W. Urban, M. Jones, J. Durell, M. Leddy, W. Phillips, A. Smith, B. Varley, I. Ahmad, L. Morss, M. Bentalab, E. Lubkiewicz and N. Schulz. “Octupole correlations in neutron-rich, even-even barium isotopes.” *Nucl. Phys. A* 613.1-2 (1997), pp. 107–131 (cit. on p. 15).
- [70] S. Zhu, J. Hamilton, A. Ramayya, E. Jones, J. Hwang, M. Wang, X. Zhang, P. Gore, L. Peker, G. Drafta, et al. “Octupole correlations in neutron-rich $^{143,145}\text{Ba}$ and a type of superdeformed band in ^{145}Ba .” *Phys. Rev. C* 60 (5 Oct. 1999), p. 051304 (cit. on p. 15).
- [71] J. G. Wang, S. J. Zhu, J. H. Hamilton, A. V. Ramayya, J. K. Hwang, Y. X. Luo, Y. J. Chen, J. O. Rasmussen, I. Y. Lee, X. L. Che, H. B. Ding, K. Li, C. T. Goodin and Q. Xu. “First identification of collective bands and octupole correlations in the neutron-rich ^{143}La nucleus.” *Phys. Rev. C* 75 (6 June 2007), p. 064301 (cit. on p. 15).

- [72] S.-C. Wu, R. Donangelo, J. O. Rasmussen, A. V. Daniel, J. K. Hwang, A. V. Ramayya and J. H. Hamilton. “New determination of the Ba-Mo yield matrix for ^{252}Cf .” *Phys. Rev. C* 62 (4 Aug. 2000), p. 041601 (cit. on p. 15).
- [73] C. Goodin, D. Fong, J. K. Hwang, A. V. Ramayya, J. H. Hamilton, K. Li, Y. X. Luo, J. O. Rasmussen, S. C. Wu, M. A. Stoyer, T. N. Ginter, S. J. Zhu, R. Donangelo, G. M. Ter-Akopian, A. V. Daniel, G. S. Popeko, A. M. Rodin and A. S. Fomichev. “New results for the intensity of bimodal fission in barium channels of the spontaneous fission of ^{252}Cf .” *Phys. Rev. C* 74 (1 July 2006), p. 017309 (cit. on p. 15).
- [74] F. Beck. “EUROBALL: Large gamma ray spectrometers through european collaborations.” *Prog. Part. Nucl. Phys.* 28 (1992), pp. 443–461 (cit. on p. 15).
- [75] A. Astier, M.-G. Porquet, T. Venkova, D. Verney, C. Theisen, G. Duchêne, F. Azaiez, G. Barreau, D. Curien, I. Deloncle, O. Dorvaux, B. J. P. Gall, M. Houry, R. Lucas, N. Redon, M. Rousseau and O. Stézowski. “High-spin structures of five $N = 82$ isotopes: ^{136}Xe , ^{137}Cs , ^{138}Ba , ^{139}La , and ^{140}Ce .” *Phys. Rev. C* 85 (6 June 2012), p. 064316 (cit. on pp. 15, 19, 23).
- [76] A. Astier, M.-G. Porquet, G. Duchêne, F. Azaiez, D. Curien, I. Deloncle, O. Dorvaux, B. J. P. Gall, M. Houry, R. Lucas, P. C. Srivastava, N. Redon, M. Rousseau, O. Stézowski and C. Theisen. “High-spin structures of $^{136}\text{Cs}_{81}$.” *Phys. Rev. C* 87 (5 May 2013), p. 054316 (cit. on pp. 15, 23).
- [77] A. Astier, T. Konstantinopoulos, M.-G. Porquet, M. Houry, R. Lucas and C. Theisen. “High-spin structures of $^{138}\text{La}_{81}$.” *Phys. Rev. C* 89 (3 Mar. 2014), p. 034310 (cit. on pp. 15, 23).
- [78] A. Astier, M.-G. Porquet, C. Theisen, D. Verney, I. Deloncle, M. Houry, R. Lucas, F. Azaiez, G. Barreau, D. Curien, O. Dorvaux, G. Duchêne, B. J. P. Gall, N. Redon, M. Rousseau and O. Stézowski. “High-spin states with seniority $\nu = 4, 5$, and 6 in $^{119-126}\text{Sn}$.” *Phys. Rev. C* 85 (5 May 2012), p. 054316 (cit. on pp. 15, 17, 23).
- [79] A. Astier, M.-G. Porquet, T. Venkova, C. Theisen, G. Duchêne, F. Azaiez, G. Barreau, D. Curien, I. Deloncle, O. Dorvaux, B. J. P. Gall, M. Houry, R. Lucas, N. Redon, M. Rousseau and O. Stézowski. “High-spin structures of $^{124-131}\text{Te}$: Competition of proton- and neutron-pair breakings.” *EPJ A* 50.1 (2014), p. 2 (cit. on pp. 15, 17, 23).
- [80] L. Corradi, S. Szilner, G. Pollarolo, D. Montanari, E. Fioretto, A. Stefanini, J. Valiente-Dobón, E. Farnea, C. Michelagnoli, G. Montagnoli, F. Scarlassara, C. Ur, T. Mijatović, D. J. Malenica, N. Soić and F. Haas. “Multinucleon transfer reactions: Present status and perspectives.” *Nucl. Instr. Meth. Phys. Res. B* 317, Part B.0 (2013), pp. 743–751 (cit. on p. 15).
- [81] R. Broda, M. Quader, P. Daly, R. Janssens, T. Khoo, W. Ma and M. Drigert. “Inelastic and transfer reactions in $^{92}\text{Mo} + 255 \text{ MeV } ^{60}\text{Ni}$ collisions studied by $\gamma\gamma$ coincidences.” *Phys. Lett. B* 251.2 (1990), pp. 245–249 (cit. on p. 15).
- [82] R. Broda. “Spectroscopic studies with the use of deep-inelastic heavy-ion reactions.” *J. Phys. G* 32.6 (2006), R151 (cit. on p. 15).
- [83] J. Cocks, P. Butler, K. Cann, P. Greenlees, G. Jones, J. Smith, P. Jones, R. Julin, S. Juutinen, D. Müller, M. Piiparinen, A. Savelius, R. Broda, B. Fornal, I. Ahmad, D. Blumenthal, M. Carpenter, B. Crowell, R. Janssens, T. Khoo, T. Lauritsen, D. Nisius, S. Asztalos, R. Clark, M. Deleplanque, R. Diamond, P. Fallon, I. Lee, A. Macchiavelli, R. MacLeod, F. Stephens, P. Bhattacharyya and C. Zhang. “Multi-nucleon transfer reactions as a tool for spectroscopy of heavy nuclei.” *J. Phys. G* 26.1 (2000), p. 23 (cit. on p. 15).

- [84] S. Akkoyun et al. “AGATA–Advanced GAMMA Tracking Array.” *Nucl. Instr. Meth. Phys. Res. A* 668 (2012), p. 26 (cit. on p. 15).
- [85] A. Gadea, E. Farnea, J. Valiente-Dobón, B. Million, D. Mengoni, D. Bazzacco, F. Recchia, A. Dewald, T. Pissulla, W. Rother, G. de Angelis, et al. “Conceptual design and infrastructure for the installation of the first AGATA sub-array at LNL.” *Nucl. Instr. Meth. Phys. Res. A* 654.1 (2011), pp. 88–96 (cit. on p. 16).
- [86] A. Wiens, H. Hess, B. Birkenbach, B. Bruyneel, J. Eberth, D. Lersch, G. Pascovici, P. Reiter and H.-G. Thomas. “The AGATA triple cluster detector.” *Nucl. Instr. Meth. Phys. Res. A* 618.1-3 (2010), pp. 223–233 (cit. on p. 16).
- [87] P.-A. Söderström, F. Recchia, J. Nyberg, A. Al-Adili, A. Atač, S. Aydin, D. Bazzacco, P. Bednarczyk, B. Birkenbach, D. Bortolato, A. Boston, H. Boston, B. Bruyneel, D. Bucurescu, E. Calore, S. Colosimo, F. Crespi, N. Dosme, J. Eberth, E. Farnea, F. Filmer, A. Gadea, A. Gottardo, X. Grave, J. Grebosz, R. Griffiths, M. Gulmini, T. Habermann, H. Hess, G. Jaworski, P. Jones, P. Joshi, D. Judson, R. Kempley, A. Khaplanov, E. Legay, D. Lersch, J. Ljungvall, A. Lopez-Martens, W. Meczynski, D. Mengoni, C. Michelagnoli, P. Molini, D. Napoli, R. Orlandi, G. Pascovici, A. Pullia, P. Reiter, E. Sahin, J. Smith, J. Strachan, D. Tonev, C. Unsworth, C. Ur, J. Valiente-Dobón, C. Veyssiere and A. Wiens. “Interaction position resolution simulations and in-beam measurements of the AGATA HPGe detectors.” *Nucl. Instr. Meth. Phys. Res. A* 638.1 (2011), pp. 96–109 (cit. on p. 16).
- [88] A. Stefanini, L. Corradi, G. Maron, A. Pisent, M. Trotta, A. Vinodkumar, S. Beghini, G. Montagnoli, F. Scarlassara, G. Segato, A. D. Rosa, G. Inglima, D. Pierroutsakou, M. Romoli, M. Sandoli, G. Pollarolo and A. Latina. “The heavy-ion magnetic spectrometer PRISMA.” *Nucl. Phys. A* 701.1-4 (2002), pp. 217–221 (cit. on p. 16).
- [89] P. R. John, V. Modamio, J. J. Valiente-Dobón, D. Mengoni, S. Lunardi, T. R. Rodríguez, D. Bazzacco, A. Gadea, C. Wheldon, T. Alexander, G. de Angelis, N. Ashwood, M. Barr, G. Benzoni, B. Birkenbach, P. G. Bizzeti, A. M. Bizzeti-Sona, S. Bottoni, M. Bowry, A. Bracco, F. Browne, M. Bunce, F. Camera, B. Cederwall, L. Corradi, F. C. L. Crespi, P. Désesquelles, J. Eberth, E. Farnea, E. Fioretto, A. Görgen, A. Gottardo, J. Grebosz, L. Grente, H. Hess, A. Jungclaus, T. Kokalova, A. Korichi, W. Korten, A. Kuşoğlu, S. Lenzi, S. Leoni, J. Ljungvall, G. Maron, W. Meczynski, B. Melon, R. Menegazzo, C. Michelagnoli, T. Mijatović, B. Million, P. Molini, G. Montagnoli, D. Montanari, D. R. Napoli, P. Nolan, C. Oziol, Z. Podolyák, G. Pollarolo, A. Pullia, B. Quintana, F. Recchia, P. Reiter, O. J. Roberts, D. Rosso, E. Şahin, M.-D. Salsac, F. Scarlassara, M. Sferrazza, J. Simpson, P.-A. Söderström, A. M. Stefanini, O. Stezowski, S. Szilner, C. Theisen, C. A. Ur and J. Walshe. “Shape evolution in the neutron-rich osmium isotopes: Prompt γ -ray spectroscopy of ^{196}Os .” *Phys. Rev. C* 90 (2 Aug. 2014), p. 021301 (cit. on p. 16).
- [90] P.-A. Söderström, J. Nyberg, P. H. Regan, A. Algora, G. de Angelis, S. F. Ashley, S. Aydin, D. Bazzacco, R. J. Casperson, W. N. Catford, J. Cederkäll, R. Chapman, L. Corradi, C. Fahlander, E. Farnea, E. Fioretto, S. J. Freeman, A. Gadea, W. Gelletly, A. Gottardo, E. Grodner, C. Y. He, G. A. Jones, K. Keyes, M. Labiche, X. Liang, Z. Liu, S. Lunardi, N. Mărginean, P. Mason, R. Menegazzo, D. Mengoni, G. Montagnoli, D. Napoli, J. Ollier, S. Pietri, Z. Podolyák, G. Pollarolo, F. Recchia, E. Şahin, F. Scarlassara, R. Silvestri, J. F. Smith, K.-M. Spohr, S. J. Steer, A. M. Stefanini, S. Szilner, N. J. Thompson, G. M. Tveten, C. A. Ur, J. J. Valiente-Dobón, V. Werner, S. J. Williams, F. R. Xu and J. Y. Zhu. “Spectroscopy of neutron-rich $^{168,170}\text{Dy}$: Yrast band evolution close to the $N_p N_n$ valence maximum.” *Phys. Rev. C* 81 (3 Mar. 2010), p. 034310 (cit. on p. 16).

- [91] P Walker and G. Dracoulis. “Energy traps in atomic nuclei.” *Nature* 399.6731 (May 1999), pp. 35–40 (cit. on p. 16).
- [92] R. L. Lozeva, G. S. Simpson, H. Grawe, G. Neyens, L. A. Atanasova, D. L. Balabanski, D. Bazzacco, F. Becker, P. Bednarczyk, G. Benzoni, N. Blasi, A. Blazhev, A. Bracco, C. Brandau, L. Cáceres, F. Camera, S. K. Chamoli, F. C. L. Crespi, J.-M. Daugas, P. Detistov, M. De Rydt, P. Doornenbal, C. Fahlander, E. Farnea, G. Georgiev, J. Gerl, K. A. Gladnishki, M. Górska, J. Grębosz, M. Hass, R. Hoischen, G. Ilie, M. Ionescu-Bujor, A. Iordachescu, J. Jolie, A. Jungclaus, M. Kmiecik, I. Kojouharov, N. Kurz, S. P. Lakshmi, G. L. Bianco, S. Mallion, A. Maj, D. Montanari, O. Perru, M. Pfützner, S. Pietri, J. A. Pinston, Z. Podolyák, W. Prokopowicz, D. Rudolph, G. Rusev, T. R. Saitoh, A. Saltarelli, H. Schaffner, R. Schwengner, S. Tashenov, K. Turzó, J. J. Valiente-Dobón, N. Vermeulen, J. Walker, E. Werner-Malento, O. Wieland and H.-J. Wollersheim. “New sub- μ s isomers in $^{125,127,129}\text{Sn}$ and isomer systematics of $^{124-130}\text{Sn}$.” *Phys. Rev. C* 77 (6 June 2008), p. 064313 (cit. on p. 17).
- [93] A. K. Jain, B. Maheshwari, S. Garg, M. Patial and B. Singh. “Atlas of Nuclear Isomers.” *Nucl. Data Sheets* 128 (2015), pp. 1–130 (cit. on p. 18).
- [94] J. Pinston and J. Genevey. “Microsecond isomers in the magic regions ^{78}Ni and ^{132}Sn .” *J. Phys. G* 30.2 (2004), R57 (cit. on p. 17).
- [95] T. Matsuzawa, H. Nakada, K. Ogawa and G. Momoki. “Seniority isomerism in proton-rich $N = 82$ isotones and its indication to stiffness of the $Z = 64$ core.” *Phys. Rev. C* 62 (5 Oct. 2000), p. 054304 (cit. on p. 18).
- [96] J. Genevey, J. A. Pinston, C. Foin, M. Rejmund, R. F. Casten, H. Faust and S. Oberstedt. “Conversion electron measurements of isomeric transitions in $^{130,132}\text{Te}$ and ^{134}Xe .” *Phys. Rev. C* 63 (5 Apr. 2001), p. 054315 (cit. on p. 19).
- [97] S. Pietri, A. Jungclaus, M. Górska, H. Grawe, M. Pfützner, L. Cáceres, P. Detistov, S. Lalkovski, V. Modamio, Z. Podolyák, P. H. Regan, D. Rudolph, J. Walker, E. Werner-Malento, P. Bednarczyk, P. Doornenbal, H. Geissel, J. Gerl, J. Grębosz, I. Kojouharov, N. Kurz, W. Prokopowicz, H. Schaffner, H. J. Wollersheim, K. Andgren, J. Benlliure, G. Benzoni, A. M. Bruce, E. Casarejos, B. Cederwall, F. C. L. Crespi, B. Hadinia, M. Hellström, R. Hoischen, G. Ilie, A. Khaplanov, M. Kmiecik, R. Kumar, A. Maj, S. Mandal, F. Montes, S. Myalski, G. Simpson, S. J. Steer, S. Tashenov and O. Wieland. “First observation of the decay of a 15^- seniority $\nu = 4$ isomer in ^{128}Sn .” *Phys. Rev. C* 83 (4 Apr. 2011), p. 044328 (cit. on p. 19).
- [98] Ł. W. Iskra, R. Broda, R. V. F. Janssens, J. Wrzesiński, B. Szpak, C. J. Chiara, M. P. Carpenter, B. Fornal, N. Hoteling, F. G. Kondev, W. Królas, T. Lauritsen, T. Pawłat, D. Seweryniak, I. Stefanescu, W. B. Walters and S. Zhu. “Higher-seniority excitations in even neutron-rich Sn isotopes.” *Phys. Rev. C* 89 (4 Apr. 2014), p. 044324 (cit. on p. 19).
- [99] K. Li, Y. X. Luo, J. K. Hwang, A. V. Ramayya, J. H. Hamilton, S. J. Zhu, C. Goodin, H. L. Crowell, J. O. Rasmussen, I. Y. Lee, S. C. Wu, A. Covello, A. Gargano, R. Donangelo, G. M. Ter-Akopian, A. V. Daniel, J. D. Cole, W. C. Ma and M. A. Stoyer. “Identification and shell model calculation of high spin states in $^{137,138}\text{Cs}$ nuclei.” *Phys. Rev. C* 75 (4 Apr. 2007), p. 044314 (cit. on p. 19).
- [100] M. Górska, L. Cáceres, H. Grawe, M. Pfützner, A. Jungclaus, S. Pietri, E. Werner-Malento, Z. Podolyák, P. Regan, D. Rudolph, et al. “Evolution of the shell gap below ^{132}Sn inferred from core excited states in ^{131}In .” *Phys. Lett. B* 672.4-5 (2009), pp. 313–316 (cit. on p. 19).

- [101] J. Taprogge, A. Jungclaus, H. Grawe, S. Nishimura, P. Doornenbal, G. Lorusso, G. S. Simpson, P.-A. Söderström, T. Sumikama, Z. Y. Xu, H. Baba, F. Browne, N. Fukuda, R. Gernhäuser, G. Gey, N. Inabe, T. Isobe, H. S. Jung, D. Kameda, G. D. Kim, Y.-K. Kim, I. Kojouharov, T. Kubo, N. Kurz, Y. K. Kwon, Z. Li, H. Sakurai, H. Schaffner, K. Steiger, H. Suzuki, H. Takeda, Z. Vajta, H. Watanabe, J. Wu, A. Yagi, K. Yoshinaga, G. Benzoni, S. Bönig, K. Y. Chae, L. Coraggio, A. Covello, J.-M. Daugas, F. Drouet, A. Gadea, A. Gargano, S. Ilieva, F. G. Kondev, T. Kröll, G. J. Lane, A. Montaner-Pizá, K. Moschner, D. Mücher, F. Naqvi, M. Niikura, H. Nishibata, A. Odahara, R. Orlandi, Z. Patel, Z. Podolyák and A. Wendt. “ $1p_{3/2}$.” *Phys. Rev. Lett.* 112 (13 Apr. 2014), p. 132501 (cit. on p. 19).
- [102] J. Taprogge, A. Jungclaus, H. Grawe, S. Nishimura, Z. Xu, P. Doornenbal, G. Lorusso, E. Nácher, G. Simpson, P.-A. Söderström, et al. “Identification of a millisecond isomeric state in ^{129}Cd via the detection of internal conversion and Compton electrons.” *Phys. Lett. B* 738 (2014), pp. 223–227 (cit. on p. 19).
- [103] H. Watanabe, G. Lorusso, S. Nishimura, T. Otsuka, K. Ogawa, Z. Y. Xu, T. Sumikama, P.-A. Söderström, P. Doornenbal, Z. Li, F. Browne, G. Gey, H. S. Jung, J. Taprogge, Z. Vajta, J. Wu, A. Yagi, H. Baba, G. Benzoni, K. Y. Chae, F. C. L. Crespi, N. Fukuda, R. Gernhäuser, N. Inabe, T. Isobe, A. Jungclaus, D. Kameda, G. D. Kim, Y. K. Kim, I. Kojouharov, F. G. Kondev, T. Kubo, N. Kurz, Y. K. Kwon, G. J. Lane, C.-B. Moon, A. Montaner-Pizá, K. Moschner, F. Naqvi, M. Niikura, H. Nishibata, D. Nishimura, A. Odahara, R. Orlandi, Z. Patel, Z. Podolyák, H. Sakurai, H. Schaffner, G. S. Simpson, K. Steiger, H. Suzuki, H. Takeda, A. Wendt and K. Yoshinaga. “Monopole-Driven Shell Evolution below the Doubly Magic Nucleus ^{132}Sn Explored with the Long-Lived Isomer in ^{126}Pd .” *Phys. Rev. Lett.* 113 (4 July 2014), p. 042502 (cit. on p. 19).
- [104] J. Taprogge, A. Jungclaus, H. Grawe, A. Gadea, A. Gargano, S. Ilieva, F. Kondev, T. Kröll, G. Lane, A. Montaner-Pizá, et al. “New decay scheme of the $^{136}_{51}\text{Sb}_{85}$ 6^- isomer.” *Phys. Rev. C* 92 (2 Aug. 2015), p. 024304 (cit. on p. 19).
- [105] A. Jungclaus, A. Gargano, H. Grawe, J. Taprogge, S. Nishimura, P. Doornenbal, G. Lorusso, Y. Shimizu, G. Simpson, P.-A. Söderström, et al. “First observation of γ rays emitted from excited states south-east of ^{132}Sn : The $\pi g_{9/2}^{-1} \otimes \nu f_{7/2}$ multiplet of $^{132}\text{In}_{83}$.” *Phys. Rev. C* 93 (4 Apr. 2016), p. 041301 (cit. on p. 19).
- [106] K. Alfonso et al., CUORE collaboration. “Search for Neutrinoless Double-Beta Decay of ^{130}Te with CUORE-0.” *Phys. Rev. Lett.* 115 (10 Sept. 2015), p. 102502 (cit. on p. 19).
- [107] M. Auger et al., EXO-200 collaboration. “Search for Neutrinoless Double-Beta Decay in ^{136}Xe with EXO-200.” *Phys. Rev. Lett.* 109 (3 July 2012), p. 032505 (cit. on p. 19).
- [108] R. Wadsworth, E. S. Paul, A. Astier, D. Bazzacco, A. J. Boston, N. Buorn, C. J. Chiara, D. B. Fossan, C. Fox, J. Gizon, D. G. Jenkins, N. S. Kelsall, T. Koike, D. R. LaFosse, S. Lunardi, P. J. Nolan, B. M. Nyakó, C. M. Petrache, H. Scraggs, K. Starosta, J. Timár, A. Walker, A. N. Wilson, L. Zolnai, B. G. Dong and I. Ragnarsson. “Smooth band termination in odd mass La nuclei: $^{127,129,131}\text{La}$.” *Phys. Rev. C* 62 (3 Aug. 2000), p. 034315 (cit. on p. 20).
- [109] E. S. Paul, P. T. W. Choy, C. Andreoiu, A. J. Boston, A. O. Evans, C. Fox, S. Gros, P. J. Nolan, G. Rainovski, J. A. Sampson, H. C. Scraggs, A. Walker, D. E. Appelbe, D. T. Joss, J. Simpson, J. Gizon, A. Astier, N. Buorn, A. Prévost, N. Redon, O. Stézowski, B. M. Nyakó, D. Sohler, J. Timár, L. Zolnai, D. Bazzacco, S. Lunardi, C. M. Petrache, P. Bednarczyk, D. Curien, N. Kintz and I. Ragnarsson. “Highest spin discrete levels in $^{131,132}\text{Ce}$: Spin generation near the mesoscopic limit.” *Phys. Rev. C* 71 (5 May 2005), p. 054309 (cit. on p. 20).

- [110] A. Kerek, A. Luukko, M. Grecescu and J. Sztarkier. “Two- and three-quasiparticle states in ^{132}Xe and ^{131}Xe .” *Nucl. Phys. A* 172.3 (1971), pp. 603–617 (cit. on pp. 20, 124).
- [111] J. Genevey, J. A. Pinston, C. Foin, M. Rejmund, R. F. Casten, H. Faust and S. Oberstedt. “Conversion electron measurements of isomeric transitions in $^{130,132}\text{Te}$ and ^{134}Xe .” *Phys. Rev. C* 63 (5 Apr. 2001), p. 054315 (cit. on p. 20).
- [112] T. Lönnroth, J. Kumpulainen and C. Tuokko. “One- and Three-Quasiparticle States in $^{127,129,131,133}\text{Xe}$ and Their Coexistence With Band Structures.” *Phys. Scripta* 27.4 (1983), p. 228 (cit. on pp. 20, 124).
- [113] A. Kerek and J. Kownacki. “The level structure of the $N = 81$ and 82 nucleides $^{137,138}\text{Ba}$ as investigated in $^{136}\text{Xe}(\alpha, xn)$ reactions.” *Nucl. Phys. A* 206.2 (1973), pp. 245–272 (cit. on pp. 20, 122).
- [114] Evaluated Nuclear Structure Data File (ENSDF). [<http://www.nndc.bnl.gov/ensdf/>]. 2015–2017 (cit. on p. 21).
- [115] B. A. Brown and W. D. M. Rae. “The Shell-Model Code NuShellX@MSU.” *Nucl. Data Sheets* 120 (2014), pp. 115–118 (cit. on p. 21).
- [116] N. Shimizu. “Nuclear shell-model code for massive parallel computation, KSHELL.” (2013) (cit. on p. 21).
- [117] B. A. Brown, N. J. Stone, J. R. Stone, I. S. Towner and M. Hjorth-Jensen. “Magnetic moments of the 2_1^+ states around ^{132}Sn .” *Phys. Rev. C* 71 (4 Apr. 2005), p. 044317 (cit. on pp. 22–23, 123).
- [118] H. G. Kruse and B. H. Wildenthal. *Bull. Am. Phys. Soc.* 27 (1982), p. 533 (cit. on p. 22).
- [119] R. Machleidt, F. Sammarruca and Y. Song. “Nonlocal nature of the nuclear force and its impact on nuclear structure.” *Phys. Rev. C* 53 (4 Apr. 1996), R1483–R1487 (cit. on pp. 23, 123).
- [120] S. Biswas, R. Palit, A. Navin, M. Rejmund, A. Bisoi, M. S. Sarkar, S. Sarkar, S. Bhattacharyya, D. C. Biswas, M. Caamaño, M. P. Carpenter, D. Choudhury, E. Clément, L. S. Danu, O. Delaune, F. Farget, G. de France, S. S. Hota, B. Jacquot, A. Lemasson, S. Mukhopadhyay, V. Nanal, R. G. Pillay, S. Saha, J. Sethi, P. Singh, P. C. Srivastava and S. K. Tandel. “Structure of $^{132}_{52}\text{Te}_{80}$: The two-particle and two-hole spectrum of $^{132}_{50}\text{Sn}_{82}$.” *Phys. Rev. C* 93 (3 Mar. 2016), p. 034324 (cit. on p. 23).
- [121] K. Higashiyama, N. Yoshinaga and K. Tanabe. “Shell model study of backbending phenomena in Xe isotopes.” *Phys. Rev. C* 65 (5 May 2002), p. 054317 (cit. on p. 23).
- [122] N. Yoshinaga and K. Higashiyama. “Systematic studies of nuclei around mass 130 in the pair-truncated shell model.” *Phys. Rev. C* 69 (5 May 2004), p. 054309 (cit. on p. 23).
- [123] K. Higashiyama and N. Yoshinaga. “Pair-truncated shell-model analysis of nuclei around mass 130.” *Phys. Rev. C* 83 (3 Mar. 2011), p. 034321 (cit. on p. 23).
- [124] E. Teruya, N. Yoshinaga, K. Higashiyama and A. Odahara. “Shell-model calculations of nuclei around mass 130.” *Phys. Rev. C* 92 (3 Sept. 2015), p. 034320 (cit. on pp. 23, 123).
- [125] K. Sieja, G. Martínez-Pinedo, L. Coquard and N. Pietralla. “Description of proton-neutron mixed-symmetry states near ^{132}Sn within a realistic large scale shell model.” *Phys. Rev. C* 80 (5 Nov. 2009), p. 054311 (cit. on p. 24).

- [126] A. Shrivastava, M. Caamaño, M. Rejmund, A. Navin, F. Rejmund, K.-H. Schmidt, A. Lemasson, C. Schmitt, L. Gaudefroy, K. Sieja, L. Audouin, C. O. Bacri, G. Barreau, J. Benlliure, E. Casarejos, X. Derkx, B. Fernández-Domínguez, C. Golabek, B. Jurado, T. Roger and J. Taieb. “Prompt γ -ray spectroscopy of isotopically identified fission fragments.” *Phys. Rev. C* 80 (5 Nov. 2009), p. 051305 (cit. on pp. 24, 122).
- [127] E. Caurier, F. Nowacki, A. Poves and K. Sieja. “Collectivity in the light xenon isotopes: A shell model study.” *Phys. Rev. C* 82 (6 Dec. 2010), p. 064304 (cit. on p. 24).
- [128] J. Menéndez, A. Poves, E. Caurier and F. Nowacki. “Disassembling the nuclear matrix elements of the neutrinoless $\beta\beta$ decay.” *Nucl. Phys. A* 818.3 (2009), pp. 139–151 (cit. on p. 24).
- [129] L. Vietze, P. Klos, J. Menéndez, W. C. Haxton and A. Schwenk. “Nuclear structure aspects of spin-independent WIMP scattering off xenon.” *Phys. Rev. D* 91 (4 Feb. 2015), p. 043520 (cit. on p. 24).
- [130] A. Vogt. “In-Beam Gamma-Ray Spectroscopy of Neutron-Rich Actinides after Multi-Nucleon Transfer Reactions.” Masterarbeit. Institut für Kernphysik, Universität zu Köln, 2014 (cit. on pp. 41–42).
- [131] D. Montanari, E. Farnea, S. Leoni, G. Pollarolo, L. Corradi, G. Benzoni, A. Gadea, E. Fioretto, A. Latina, G. Montagnoli, F. Scarlassara, A. Stefanini and S. Szilner. “Response function of the magnetic spectrometer PRISMA.” *EPJ A* 47.1 (2011), p. 4 (cit. on p. 42).
- [132] D. Montanari. “Reaction Dynamics of Neutron Rich Nuclei in Ca Isotopes with Heavy Ions and Gamma Spectroscopy.” PhD thesis. Università degli Studi di Milano, 2009 (cit. on p. 42).
- [133] R. Sayer. “Semi-empirical formulas for heavy-ion stripping data.” *Rev. Phys. Appl.* 12.10 (1977), pp. 1543–1546 (cit. on p. 42).
- [134] K. Shima, T. Mikumo and H. Tawara. “Equilibrium charge state distributions of ions ($Z_1 \geq 4$) after passage through foils: Compilation of data after 1972.” *At. Data Nucl. Data Tables* 34.3 (1986), pp. 357–391 (cit. on p. 42).
- [135] A. V. Afanasjev and O. Abdurazakov. “Pairing and rotational properties of actinides and superheavy nuclei in covariant density functional theory.” *Phys. Rev. C* 88 (1 July 2013), p. 014320 (cit. on pp. 122, 128).
- [136] A. V. Afanasjev. “Microscopic description of rotation: from ground states to the extremes of ultra-high spin.” *Phys. Scripta* 89.5 (2014), p. 054001 (cit. on pp. 122, 128).
- [137] N. Fotiades, R. O. Nelson, M. Devlin, J. A. Cizewski, J. A. Becker, W. Younes, R. Krücken, R. M. Clark, P. Fallon, I. Y. Lee, A. O. Macchiavelli, T. Ethvignot and T. Granier. “High-spin states in ^{135}Xe .” *Phys. Rev. C* 75 (5 May 2007), p. 054322 (cit. on p. 122).
- [138] E. Browne and J. Tuli. “Nuclear Data Sheets for $A = 137$.” *Nuclear Data Sheets* 108.10 (2007), pp. 2173–2318 (cit. on p. 122).
- [139] K. Moran, E. A. McCutchan, C. J. Lister, S. Zhu, M. P. Carpenter, P. Chowdhury, J. P. Greene, T. Lauritsen, E. Merchan and R. Shearman. “ $E5$ decay from the $J^\pi = 11/2^-$ isomer in ^{137}Ba .” *Phys. Rev. C* 90 (4 Oct. 2014), p. 041303 (cit. on p. 122).
- [140] C. Walz, H. Scheit, N. Pietralla, T. Aumann, R. Lefol and V. Y. Ponomarev. “Observation of the competitive double-gamma nuclear decay.” *Nature* 526.7573 (2015), pp. 406–409 (cit. on p. 122).

- [141] V. A. Bondarenko, I. L. Kuvaga, P. T. Prokofjev, A. M. Sukhovoij, V. A. Khitrov, Y. P. Popov, S. Brant and V. Paar. “Levels of ^{137}Ba studied with neutron-induced reactions.” *Nucl. Phys. A* 582.1-2 (1995), pp. 1–22 (cit. on p. 122).
- [142] I. Bikit, I. Aničin, J. Slivka, M. Krmar, J. Puzović and L. Čonkić. “Population of the 283 keV level of ^{137}Ba by the β decay of ^{137}Cs .” *Phys. Rev. C* 54 (6 Dec. 1996), pp. 3270–3272 (cit. on p. 122).
- [143] Y. Khazov, I. Mitropolsky and A. Rodionov. “Nuclear Data Sheets for $A = 131$.” *Nucl. Data Sheets* 107.11 (2006), pp. 2715–2930 (cit. on pp. 124–125).
- [144] A. Irving, P. Forsyth, I. Hall and D. Martin. “The properties of low-lying levels of ^{129}Xe and ^{131}Xe .” *J. Phys. G* 5.11 (1979), p. 1595 (cit. on p. 124).
- [145] H. G. Essel and N. Kurz. “The general purpose data acquisition system MBS.” *IEEE Trans. Nucl. Sci* 47.2 (Apr. 2000), pp. 337–339 (cit. on p. 126).
- [146] R. Lutter et al. “MARaBOOU - a MBS and ROOT based online/offline utility.” *IEEE Trans. Nucl. Sci* 47.2 (Apr. 2000), pp. 280–283 (cit. on p. 126).
- [147] L. Kaya. “Inbetriebnahme und Optimierung doppelseitig segmentierter Silizium-Detektoren für Gamma-Teilchen-Koinzidenzexperimente.” B.Sc. Thesis. 2015 (cit. on p. 126).
- [148] L. Kaya. “High-spin spectroscopy at the HORUS γ -ray spectrometer (*preliminary title*).” M.Sc. Thesis, in preparation. 2017 (cit. on p. 127).
- [149] E. Clément, C. Michelagnoli, G. de France, H. Li, A. Lemasson, C. B. Dejean, M. Beuzard, P. Bougault, J. Cacitti, J.-L. Foucher, G. Fremont, P. Gangnant, J. Goupil, C. Houarner, M. Jean, A. Lefevre, L. Legeard, F. Legruel, C. Maugeais, L. Ménager, N. Ménard, H. Munoz, M. Ozille, B. Raine, J. Ropert, F. Saillant, C. Spitaels, M. Tripon, P. Vallerand, G. Voltolini, W. Korten, M.-D. Salsac, C. Theisen, M. Zielińska, T. Joannem, M. Karolak, M. Kebbiri, A. Lotode, R. Touzery, C. Walter, A. Korichi, J. Ljungvall, A. Lopez-Martens, D. Ralet, N. Dosme, X. Grave, N. Karkour, X. Lafay, E. Legay, I. Kojouharov, C. Domingo-Pardo, A. Gadea, R. Pérez-Vidal, J. Civera, B. Birkenbach, J. Eberth, H. Hess, L. Lewandowski, P. Reiter, A. Nannini, G. D. Angelis, G. Jaworski, P. John, D. Napoli, J. Valiente-Dobón, D. Barrientos, D. Bortolato, G. Benzoni, A. Bracco, S. Brambilla, F. Camera, F. Crespi, S. Leoni, B. Million, A. Pullia, O. Wieland, D. Bazzacco, S. Lenzi, S. Lunardi, R. Menegazzo, D. Mengoni, F. Recchia, M. Bellato, R. Isocrate, F. E. Canet, F. Didierjean, G. Duchêne, R. Baumann, M. Brucker, E. Dangelser, M. Filliger, H. Friedmann, G. Gaudiot, J.-N. Grapton, H. Kocher, C. Mathieu, M.-H. Sigward, D. Thomas, S. Veeramootoo, J. Dudouet, O. Stézowski, C. Aufranc, Y. Aubert, M. Labiche, J. Simpson, I. Burrows, P. Coleman-Smith, A. Grant, I. Lazarus, P. Morrall, V. Pucknell, A. Boston, D. Judson, N. Lalović, J. Nyberg, J. Collado, V. González, I. Kuti, B. Nyakó, A. Maj and M. Rudigier. “Conceptual design of the AGATA array at GANIL.” *Nucl. Instr. Meth. Phys. Res. A* 855 (2017), pp. 1–12 (cit. on p. 127).
- [150] V. F. Comas, S. Heinz, S. Hofmann, D. Ackermann, J. A. Heredia, F. P. Heßberger, J. Khuyagbaatar, B. Kindler, B. Lommel and R. Mann. “Study of multi-nucleon transfer reactions in $^{58,64}\text{Ni} + ^{207}\text{Pb}$ collisions at the velocity filter SHIP.” *EPJ A* 49.9 (2013), p. 112 (cit. on p. 128).
- [151] H. Devaraja, S. Heinz, O. Beliuskina, V. Comas, S. Hofmann, C. Hornung, G. Münzenberg, K. Nishio, D. Ackermann, Y. Gambhir, M. Gupta, R. Henderson, F. Heßberger, J. Khuyagbaatar, B. Kindler, B. Lommel, K. Moody, J. Maurer, R. Mann, A. Popeko, D. Shaughnessy, M. Stoyer

- and A. Yeremin. “Observation of new neutron-deficient isotopes with in multinucleon transfer reactions.” *Phys. Lett. B* 748 (2015), pp. 199–203 (cit. on p. 128).
- [152] C. Theisen. Private communication. 2015 (cit. on p. 129).
- [153] C. Schmitt, M. Rejmund, A. Navin, B. Lecornu, B. Jacquot, G. de France, A. Lemasson, A. Shrivastava, P. Greenlees, J. Uusitalo, K. Subotic, L. Gaudefroy, C. Theisen, B. Sulignano, O. Dorvaux and L. Stuttgé. “New gas-filled mode of the large-acceptance spectrometer VAMOS.” *Nucl. Instr. Meth. Phys. Res. A* 621.1-3 (2010), pp. 558–565 (cit. on pp. 128–129).
- [154] S. Pullanhiotan, M. Rejmund, A. Navin, W. Mittig and S. Bhattacharyya. “Performance of VAMOS for reactions near the Coulomb barrier.” *Nucl. Instr. Meth. Phys. Res. A* 593.3 (2008), pp. 343–352 (cit. on p. 128).
- [155] C. Theisen, F. Jeanneau, B. Sulignano, F. Druillolle, J. Ljungvall, B. Paul, E. Virique, P. Baron, H. Bervas, E. Clément, E. Delagnes, A. Dijon, E. Dossat, A. Drouart, F. Farget, C. Flouzat, G. D. France, A. Görgen, C. Houarner, B. Jacquot, W. Korten, G. Lebertre, B. Lecornu, L. Legeard, A. Lermite, S. Lhenoret, C. Marry, C. Maugeais, L. Menager, O. Meunier, A. Navin, F. Nizery, A. Obertelli, E. Raully, B. Raine, M. Rejmund, J. Ropert, F. Saillant, H. Savajols, C. Schmitt, M. Tripon, E. Wanlin and G. Wittwer. “Musett: A segmented Si array for Recoil-Decay-Tagging studies at VAMOS.” *Nucl. Instr. Meth. Phys. Res. A* 747 (2014), pp. 69–80 (cit. on p. 129).
- [156] E. Fioretto, L. Corradi, S. Szilner, D. Montanari, C. Michelagnoli, T. Mijatović, G. Montagnoli, F. Scarlassara, A. Stefanini, C. Ur, G. Pollarolo and N. Soić. “Sub-barrier transfer reactions studied with the magnetic spectrometer PRISMA.” *JPCS* 533.1 (2014), p. 012006 (cit. on p. 130).
- [157] K. Novikov, I. Harca, E. Kozulin, S. Dmitriev, J. Itkis, G. Knyazheva, T. Loktev, L. Corradi, J. Valiente-Dobón, E. Fioretto, D. Montanari, A. Stefanini, E. Vardaci, D. Quero, G. Montagnoli, F. Scarlassara, E. Strano, G. Pollarolo, J. Piot, T. Mijatović, S. Szilner, D. Ackermann, G. Chubarian and W. Trzaska. “The study of neutron-rich nuclei production in the region of the closed shell $N = 126$ in the multi-nucleon transfer reaction $^{136}\text{Xe} + ^{208}\text{Pb}$.” *JPCS* 703.1 (2016), p. 012020 (cit. on p. 130).
- [158] L. Corradi. “Transfer reaction studies in inverse kinematics with the magnetic spectrometer PRISMA.” *EPJ Web of Conferences* 86 (2015), p. 00007 (cit. on p. 130).
- [159] G. Pollarollo. Private communication. 2016 (cit. on p. 130).
- [160] H. Xiaolong. “Nuclear Data Sheets for $A = 198$.” *Nucl. Data Sheets* 110.10 (2009), pp. 2533–2688 (cit. on p. 131).
- [161] D. L. Hendrie, B. G. Harvey, J. R. Meriwether, J. Mahoney, J.-C. Faivre and D. G. Kovar. “Multipole Deformation of ^{238}U .” *Phys. Rev. Lett.* 30 (12 Mar. 1973), pp. 571–574 (cit. on p. 131).
- [162] K. Sekizawa. Private communication. 2016 (cit. on p. 131).

List of figures

1	Reaction channels depending on the impact parameter.	7
2	Regimes of nuclear reactions between heavy ions.	8
4	Compound nuclei accessible via stable beam/target combinations.	14
5	Single-particle orbitals in the nuclear shell model.	17
6	Simplified Segrè charts showing all known 6^+ , 7^- , 10^+ , and $11/2^-$ isomers.	18
7	Maximum excitation energies in nuclei northwest of ^{132}Sn	20
8	Evolution of yrast states along the $Z = 54$ chain.	21
9	m -scheme dimensions in the $50 \leq Z, N \leq 82$ region.	22
10	Simulation of the PRISMA mass spectrometer.	41
11	Tuning of the magnetic fields in the PRISMA simulation.	43
12	PRISMA response function.	44
13	Contamination correction of Xe, I, and Cs mass distributions.	45
14	AGATA+PRISMA γ -ray spectra of ^{131}Xe	124
15	Block diagram of the employed electronics in the HORUS+DSSSD experiments.	125
16	Experimental setup of the DSSSD detector at the HORUS γ -ray spectrometer.	126
17	First γ -ray spectra of the ^{131}Xe experiment at the HORUS+DSSSD setup.	127
18	VAMOS mass spectrometer in the gas-filled mode.	129

List of publications

Publications in refereed journals

- [1] A. Vogt, B. Birkenbach, P. Reiter, L. Corradi, T. Mijatović, D. Montanari, S. Szilner, D. Bazzacco, M. Bowry, A. Bracco, B. Bruyneel, F. C. L. Crespi, G. de Angelis, P. Désesquelles, J. Eberth, E. Farnea, E. Fioretto, A. Gadea, K. Geibel, A. Gengelbach, A. Giaz, A. Görgen, A. Gottardo, J. Grebosz, H. Hess, P. R. John, J. Jolie, D. S. Judson, A. Jungclaus, W. Korten, S. Leoni, S. Lunardi, R. Menegazzo, D. Mengoni, C. Michelagnoli, G. Montagnoli, D. Napoli, L. Pellegri, G. Pollarolo, A. Pullia, B. Quintana, F. Radeck, F. Recchia, D. Rosso, E. Şahin, M. D. Salsac, F. Scarlassara, P.-A. Söderström, A. M. Stefanini, T. Steinbach, O. Stezowski, B. Szpak, C. Theisen, C. Ur, J. J. Valiente-Dobón, V. Vandone and A. Wiens.
Light and heavy transfer products in $^{136}\text{Xe} + ^{238}\text{U}$ multinucleon transfer reactions.
Phys. Rev. C 92 (2015), p. 024619.
- [2] B. Birkenbach, A. Vogt, K. Geibel, F. Recchia, P. Reiter, J. J. Valiente-Dobón, D. Bazzacco, M. Bowry, A. Bracco, B. Bruyneel, L. Corradi, F. C. L. Crespi, G. de Angelis, P. Désesquelles, J. Eberth, E. Farnea, E. Fioretto, A. Gadea, A. Gengelbach, A. Giaz, A. Görgen, A. Gottardo, J. Grebosz, H. Hess, P. R. John, J. Jolie, D. S. Judson, A. Jungclaus, W. Korten, S. Lenzi, S. Leoni, S. Lunardi, R. Menegazzo, D. Mengoni, C. Michelagnoli, T. Mijatović, G. Montagnoli, D. Montanari, D. Napoli, L. Pellegri, G. Pollarolo, A. Pullia, B. Quintana, F. Radeck, D. Rosso, E. Şahin, M. D. Salsac, F. Scarlassara, P.-A. Söderström, A. M. Stefanini, T. Steinbach, O. Stezowski, S. Szilner, B. Szpak, C. Theisen, C. Ur, V. Vandone and A. Wiens.
Spectroscopy of the neutron-rich actinide nucleus ^{240}U following multinucleon-transfer reactions.
Phys. Rev. C 92 (2015), p. 044319.
- [3] J. Litzinger, A. Blazhev, A. Dewald, F. Didierjean, G. Duchêne, C. Fransen, R. Lozeva, K. Sieja, D. Verney, G. de Angelis, D. Bazzacco, B. Birkenbach, S. Bottoni, A. Bracco, T. Braunroth, B. Cederwall, L. Corradi, F. C. L. Crespi, P. Désesquelles, J. Eberth, E. Ellinger, E. Farnea, E. Fioretto, R. Gernhäuser, A. Goasduff, A. Görgen, A. Gottardo, J. Grebosz, M. Hackstein, H. Hess, F. Ibrahim, J. Jolie, A. Jungclaus, K. Kolos, W. Korten, S. Leoni, S. Lunardi, A. Maj, R. Menegazzo, D. Mengoni, C. Michelagnoli, T. Mijatović, B. Million, O. Möller, V. Modamio, G. Montagnoli, D. Montanari, A. I. Morales, D. R. Napoli, M. Niikura, G. Pollarolo, A. Pullia, B. Quintana, F. Recchia, P. Reiter, D. Rosso, E. Sahin, M. D. Salsac, F. Scarlassara, P.-A. Söderström, A. M. Stefanini, O. Stezowski, S. Szilner, C. Theisen, J. J. Valiente Dobón, V. Vandone and A. Vogt.
Transition probabilities in neutron-rich $^{84,86}\text{Se}$.
Phys. Rev. C 92 (2015), p. 064322.
- [4] A. Vogt, B. Birkenbach, P. Reiter, A. Blazhev, M. Siciliano, J. J. Valiente-Dobón, C. Wheldon, D. Bazzacco, M. Bowry, A. Bracco, B. Bruyneel, R. S. Chakrawarthy, R. Chapman, D. Cline, L. Corradi, F. C. L. Crespi, M. Cromaz, G. de Angelis, J. Eberth, P. Fallon, E. Farnea, E. Fioretto, S. J. Freeman, A. Gadea, K. Geibel, W. Gelletly, A. Gengelbach, A. Giaz, A. Görgen, A. Gottardo, A. B. Hayes, H. Hess, H. Hua, P. R. John, J. Jolie, A. Jungclaus, W. Korten, I. Y. Lee, S. Leoni, X. Liang, S. Lunardi, A. O. Macchiavelli, R. Menegazzo, D. Mengoni, C. Michelagnoli, T. Mijatović, G. Montagnoli, D. Montanari, D. Napoli, C. J. Pearson, L. Pellegri, Z. Podolyák, G. Pollarolo, A. Pullia, F. Radeck, F. Recchia, P. H. Regan, E. Şahin, F. Scarlassara, G. Sletten, J. F. Smith, P.-A. Söderström, A. M. Stefanini, T. Steinbach, O. Stezowski, S. Szilner, B. Szpak, R. Teng,

- C. Ur, V. Vandone, D. Ward, D. D. Warner, A. Wiens and C. Y. Wu.
High-spin structure of ^{134}Xe .
Phys. Rev. C 93 (2016), p. 054325.
- [5] B. Fu, M. Seidlitz, A. Blazhev, M. Bouhelal, F. Haas, P. Reiter, K. Arnsward, B. Birkenbach, C. Fransen, G. Friessner, A. Hennig, H. Hess, R. Hirsch, L. Lewandowski, D. Schneiders, B. Siebeck, T. Steinbach, T. Thomas, A. Vogt, A. Wendt, K. Wolf and K. O. Zell.
 γ -ray spectroscopy of ^{33}P and ^{33}S after fusion-evaporation reactions.
Phys. Rev. C 94 (2016), p. 034318.
- [6] T. Grahn, J. Pakarinen, L. Jokiniemi, M. Albers, K. Auranen, C. Bauer, C. Bernards, A. Blazhev, P. A. Butler, S. Bönig, A. Damyanova, T. De Coster, H. De Witte, J. Elseviers, L. P. Gaffney, M. Huyse, A. Herzán, U. Jakobsson, R. Julin, N. Kesteloot, J. Konki, T. Kröll, L. Lewandowski, K. Moschner, P. Peura, M. Pfeiffer, D. Radeck, P. Rahkila, E. Rapisarda, P. Reiter, K. Reynders, M. Rudiger, M.-D. Salsac, S. Sambhi, M. Scheck, M. Seidlitz, B. Siebeck, T. Steinbach, S. Stolze, J. Suhonen, P. Thoele, M. Thürauf, N. Warr, P. Van Duppen, M. Venhart, M. J. Vermeulen, V. Werner, M. Veselsky, A. Vogt, K. Wrzosek-Lipska and M. Zielińska.
Collective 2_1^+ excitations in ^{206}Po and $^{208,210}\text{Rn}$.
EPJ A 52.11 (2016), p. 340.
- [7] A. Vogt, B. Birkenbach, P. Reiter, A. Blazhev, M. Siciliano, K. Hadyńska-Klęk, J. J. Valiente-Dobón, C. Wheldon, E. Teruya, N. Yoshinaga, K. Arnsward, D. Bazzacco, M. Bowry, A. Bracco, B. Bruyneel, R. S. Chakrawarthy, R. Chapman, D. Cline, L. Corradi, F. C. L. Crespi, M. Cromaz, G. de Angelis, J. Eberth, P. Fallon, E. Farnea, E. Fioretto, S. J. Freeman, B. Fu, A. Gadea, K. Geibel, W. Gelletly, A. Gengelbach, A. Giaz, A. Görgen, A. Gottardo, A. B. Hayes, H. Hess, R. Hirsch, H. Hua, P. R. John, J. Jolie, A. Jungclaus, L. Kaya, W. Korten, I. Y. Lee, S. Leoni, L. Lewandowski, X. Liang, S. Lunardi, A. O. Macchiavelli, R. Menegazzo, D. Mengoni, C. Michelagnoli, T. Mijatović, G. Montagnoli, D. Montanari, C. Müller-Gatermann, D. Napoli, C. J. Pearson, L. Pellegrini, Z. Podolyák, G. Pollarolo, A. Pullia, M. Queiser, F. Radeck, F. Recchia, P. H. Regan, D. Rosiak, N. Saed-Samii, E. Şahin, F. Scarlassara, D. Schneiders, M. Seidlitz, B. Siebeck, G. Sletten, J. F. Smith, P.-A. Söderström, A. M. Stefanini, T. Steinbach, O. Stezowski, S. Szilner, B. Szpak, R. Teng, C. Ur, V. Vandone, D. D. Warner, A. Wiens, C. Y. Wu and K. O. Zell.
Isomers and high-spin structures in the $N = 81$ isotones ^{135}Xe and ^{137}Ba .
Phys. Rev. C 95 (2017), p. 024316.
- [8] P. R. John, J. J. Valiente-Dobón, D. Mengoni, V. Modamio, S. Lunardi, D. Bazzacco, A. Gadea, C. Wheldon, T. R. Rodríguez, T. Alexander, G. de Angelis, N. Ashwood, M. Barr, G. Benzoni, B. Birkenbach, P. G. Bizzeti, A. M. Bizzeti-Sona, S. Bottoni, M. Bowry, A. Bracco, F. Browne, M. Bunce, F. Camera, L. Corradi, F. C. L. Crespi, B. Melon, E. Farnea, E. Fioretto, A. Gottardo, L. Grente, H. Hess, T. Kokalova, W. Korten, A. Kuşoğlu, S. Lenzi, S. Leoni, J. Ljungvall, R. Menegazzo, C. Michelagnoli, T. Mijatović, G. Montagnoli, D. Montanari, D. R. Napoli, Z. Podolyák, G. Pollarolo, F. Recchia, P. Reiter, O. J. Roberts, E. Şahin, M.-D. Salsac, F. Scarlassara, M. Sferrazza, P.-A. Söderström, A. M. Stefanini, S. Szilner, C. A. Ur, A. Vogt and J. Walshe.
In-beam γ -ray spectroscopy of the neutron-rich platinum isotope ^{200}Pt toward the $N = 126$ shell gap.
Phys. Rev. C 95 (2017), p. 064321.
- [9] L. Kaya, A. Vogt, P. Reiter, B. Birkenbach, R. Hirsch, K. Arnsward, H. Hess, M. Seidlitz, T. Steinbach, N. Warr, K. Wolf, C. Stahl, N. Pietralla, T. Limböck, K. Meerholz and R. Lutter.
Characterization and calibration of radiation-damaged

double-sided silicon strip detectors.

Nucl. Instr. Meth. Phys. Res. A 855 (2017), pp. 109–117.

- [10] K. Arnsward, T. Braunroth, M. Seidlitz, L. Coraggio, P. Reiter, B. Birkenbach, A. Blazhev, A. Dewald, C. Fransen, B. Fu, A. Gargano, H. Hess, R. Hirsch, N. Itaco, S. Lenzi, L. Lewandowski, J. Litzinger, C. Müller-Gatermann, M. Queiser, D. Rosiak, D. Schneiders, B. Siebeck, T. Steinbach, A. Vogt, K. Wolf and K. Zell.

Enhanced collectivity along the $N = Z$ line: Lifetime measurements in ^{44}Ti , ^{48}Cr , and ^{52}Fe .

Phys. Lett. B 772 (2017), pp. 599–606.

- [11] A. Vogt, M. Siciliano, B. Birkenbach, P. Reiter, K. Hadyńska-Klęk, C. Wheldon, J. J. Valiente-Dobón, E. Teruya, N. Yoshinaga, K. Arnsward, D. Bazzacco, A. Blazhev, A. Bracco, B. Bruyneel, R. S. Chakrawarthy, R. Chapman, D. Cline, L. Corradi, F. C. L. Crespi, M. Cromaz, G. de Angelis, J. Eberth, P. Fallon, E. Farnea, E. Fioretto, C. Fransen, S. J. Freeman, B. Fu, A. Gadea, W. Gelletly, A. Giaz, A. Görgen, A. Gottardo, A. B. Hayes, H. Hess, R. Hetzenegger, R. Hirsch, H. Hua, P. R. John, J. Jolie, A. Jungclaus, V. Karayonchev, L. Kaya, W. Korten, I. Y. Lee, S. Leoni, X. Liang, S. Lunardi, A. O. Macchiavelli, R. Menegazzo, D. Mengoni, C. Michelagnoli, T. Mijatović, G. Montagnoli, D. Montanari, C. Müller-Gatermann, D. Napoli, C. J. Pearson, Z. Podolyák, G. Pollarolo, A. Pullia, M. Queiser, F. Recchia, P. H. Regan, J.-M. Régis, N. Saed-Samii, E. Şahin, F. Scarlassara, M. Seidlitz, B. Siebeck, G. Sletten, J. F. Smith, P.-A. Söderström, A. M. Stefanini, O. Stezowski, S. Szilner, B. Szpak, R. Teng, C. Ur, D. D. Warner, K. Wolf, C. Y. Wu and K. O. Zell.

High-spin structures in ^{132}Xe and ^{133}Xe and evidence for isomers along the $N = 79$ isotones.

Phys. Rev. C 96 (2017), p. 024321.

Publications in conference proceedings

- [12] T. Grahn, M. Albers, K. Auranen, C. Bauer, C. Bernards, A. Blazhev, P. Butler, S. Bönig, A. Damyanova, T. De Coster, H. De Witte, J. Elseviers, L. P. Gaffney, M. Huyse, A. Herzán, U. Jakobsson, N. Kesteloot, J. Konki, T. Kröll, L. Lewandowski, K. Moschner, J. Pakarinen, P. Peura, M. Pfeiffer, D. Radeck, P. Rahkila, E. Rapisarda, P. Reiter, K. Reynders, M. Rudiger, M.-D. Salsac, S. Sambi, M. Scheck, B. Siebeck, M. Seidlitz, T. Steinbach, S. Stolze, P. Thoele, M. Thürauf, N. Warr, P. Van Duppen, M. Venhart, M. J. Vermeulen, V. Werner, M. Veselsky, A. Vogt, F. Wenander, K. Wrzosek-Lipska and M. Zielinska.

Coulomb excitation of re-accelerated ^{208}Rn and ^{206}Po beams.

EPJ Web of Conferences 63 (2013), p. 01009.

Publications in annual reports

- [13] A. Vogt et al.
In-Beam Gamma-Ray Spectroscopy of Neutron-Rich Actinides after Multi-Nucleon Transfer Reactions.
LNL Annual Report 2014 241 (2015), pp. 79–80.
- [14] A. Vogt et al.
High-spin spectroscopy of ^{134}Xe .
LNL Annual Report 2015 242 (2016), pp. 80–81.

- [15] B. Birkenbach, A. Vogt, et al.
Spectroscopy of ^{240}U after Multinucleon-Transfer Reactions.
LNL Annual Report 2015 242 (2016), pp. 33–64.

Acknowledgements – Danksagung

Ich danke Herrn Prof. Dr. Peter Reiter für die Vergabe des vielseitigen und interessanten Promotions-themas und für die Möglichkeit diese Arbeit in seiner Arbeitsgruppe am Institut für Kernphysik durchführen zu können. Ich bedanke mich für die vielfältige wissenschaftliche und methodische Unterstützung während der gesamten Bearbeitungsphase meiner Dissertation.

Ich danke weiterhin herzlich Herrn Prof. Dr. Andreas Zilges für die Übernahme des Koreferats sowie Herrn Prof. Dr. Joachim Krug für die Übernahme des Vorsitzes der Prüfungskommission. Ich danke herzlich Herrn Prof. Dr. Rolf-Dietmar Herzberg für die Übernahme des Drittgutachtens.

Mein besonderer Dank geht an Herrn Dr. Benedikt Birkenbach, der mir stets mit Tatkraft und Fachwissen zur Seite stand. Ich danke für die gemeinsame Arbeit und die vielen Diskussionen zur Interpretation der erzielten Ergebnisse.

I owe special thanks to Prof. Dr. Carl Wheldon from the University of Birmingham for providing the GAMMASPHERE dataset and the great collaboration.

I also wish to thank Marco Siciliano from the Laboratori Nazionali di Legnaro for providing the $^{136}\text{Xe} + ^{208}\text{Pb}$ dataset and all the discussions on the Xe and Ba papers.

Furthermore, I would like to thank Ms. Eri Teruya and Prof. Dr. Naotaka Yoshinaga from Saitama University, Japan for providing the results of their shell-model calculation. Thank you for the great collaboration.

I wish to thank Dr. Lorenzo Corradi, Dr. Jose-Javier Valiente-Dobón, and Dr. Kasia Hadyńska-Klęk from the Laboratori Nazionali di Legnaro, Italy, Prof. Dr. Suzanna Szilner and Dr. Tea Mijatović from the University of Zagreb, Croatia and Dr. Philipp John from the University of Padua, Italy (now TU Darmstadt), for their great and constructive collaborations. I am also grateful to Dr. Daniele Montanari from Laboratori Nazionali di Legnaro, Italy for the help with the PRISMA simulation code.

Ich danke herzlich Herrn Levent Kaya für die konstruktive und erfolgreiche Zusammenarbeit bei der Inbetriebnahme unserer DSSSD-Detektoren und der gemeinsam durchgeführten Experimente. Mein Dank geht an Herrn Dr. Nigel Warr für die viele Hilfe beim Aufbau unseres Marabou-Teststands. Ebenso danke ich Herrn Dr. Christian Stahl von der Technischen Universität Darmstadt für die Bereitstellung von AGATA-Daten und Herrn Rudi Lutter von der Ludwig-Maximilians-Universität München für die Hilfestellungen bei der Implementierung unserer Marabou-User-Codes. Ich danke Herrn Professor Klaus Meerholz und Herrn Thorsten Limböck für die fruchtbare Kollaboration.

Meiner gesamten Arbeitsgruppe gilt Dank für die zahlreichen fachlichen Gespräche, Ratschläge und Anmerkungen und für die freundliche und angenehme Arbeitsatmosphäre.

Ganz besonders danke ich Herrn Dr. Herbert Hess, Herrn Dr. Michael Seidlitz, Herrn Dr. Jürgen Eberth, Herrn Claus Müller-Gattermann, Herrn Dr. Andrey Blazhev, Herrn Dr. Christoph Fransen, Herrn Nima Saed-Samii und Herrn Dr. Jean-Marc Régis für viele anregende Diskussionen und konstruktive

Hilfestellungen. Ich danke auch insbesondere Herrn Konrad Arnswald, Herrn Thomas Braunroth, Herrn Mario Cappellazzo, Herrn Bo Fu, Herrn Rouven Hirsch, Herrn Robert Hetzenegger, Herrn Vasil Karayonchev, Herrn Levent Kaya, Herrn Lars Lewandowski, Herrn Jan Mayer, Herrn Simon Pickstone, Herrn Michael Queiser, Herrn Dawid Rosiak, Herrn David Schneiders und Herrn Tim Steinbach, Herrn Michael Weinert und Herrn Kai Wolf für die enge Zusammenarbeit, Hilfe und Unterstützung in vielen Projekten und Experimenten.

Ein großer Dank geht an die Operateure des Tandembeschleunigers des IKP, Herrn Frank Bielau, Herrn Victor Rehl, Herrn Otto Rudolph und Herrn Albert Wedel, die für einen reibungslosen Strahlbetrieb bei unseren Experimenten am IKP sorgten. Ich danke weiterhin Herrn Dr. Andrey Blazhev und Herrn Dr. Karl-Oskar Zell für die Herstellung der Targets für die von mir durchgeführten Experimente am Tandem-Beschleuniger des IKP. Ich danke der Feinmechanikwerkstatt des IKP unter der Leitung von Herrn Stefan Thiel und der Elektronikwerkstatt des IKP unter der Leitung von Herrn Christoph Görden für die großartige Zusammenarbeit.

In ganz besonderem Maße danke ich der Bonn-Cologne Graduate School für die Gewährung der finanziellen Mittel bzw. für das Honor's-Branch-Stipendium über die zweite Hälfte meiner Promotion.

Ich danke vielmals meiner Lerngruppe, Herrn Jan Gelhausen, Herrn David Koser, Herrn Manuel Pietsch, Herrn Philipp Schreier und Herrn Stefan Wolff für die treue Begleitung und Freundschaft durch das Studium.

Meinen Freunden Christian und Lisa Remmert, Christian Reifferscheid, Dr. Norman Mellein und Klaus Trimborn danke ich herzlich für ihre treue und fortwährende Unterstützung und ihr Interesse an meiner Arbeit.

Ein ganz besonderer Dank gilt meinen Eltern und Großeltern sowie meiner Schwester, die mich auf meinem Weg durch das Studium begleitet und unterstützt haben.

Contribution to publications essential for this thesis

Publication I:

Light and heavy transfer products in $^{136}\text{Xe} + ^{238}\text{U}$ multinucleon transfer reactions

- A. Vogt participated in the experiment which was conceived and carried out by P. Reiter, B. Birkenbach, K. Geibel, and the LNL 11.22 collaboration
- A. Vogt carried out the channel selection of the Te, I, Cs, and Ba channels
- B. Birkenbach carried out the channel selection of the Xe channel
- A. Vogt performed the data analysis
- A. Vogt carried out the model calculation with S. Szilner and T. Mijatović
- A. Vogt wrote the paper, P. Reiter, B. Birkenbach, and L. Corradi co-wrote the paper.

Publication II:

Spectroscopy of the neutron-rich actinide nucleus ^{240}U

- A. Vogt participated in the experiment which was conceived and carried out by P. Reiter, B. Birkenbach, K. Geibel, and the LNL 11.22 collaboration
- A. Vogt participated in the data analysis and channel selection of ^{240}U
- A. Vogt conceived the theoretical part of the paper and confronted the experimental observables with theory
- B. Birkenbach wrote the paper, A. Vogt co-wrote the paper

Publication III:

High-spin structure of ^{134}Xe

- A. Vogt participated in the LNL 11.22 experiment which was conceived and carried out by P. Reiter, B. Birkenbach, K. Geibel, and the LNL 11.22 collaboration
- B. Birkenbach carried out the channel selection of the Xe channel
- M. Siciliano and K. Hadyńska-Klęk carried out the data analysis of experiment LNL 10.26
- J.J. Valiente-Dobón and C. Wheldon carried out the sorting and channel selection of the LBNL dataset, C. Wheldon provided the data
- A. Vogt carried out the refined data analysis of the three experiments
- A. Vogt and A. Blazhev carried out the SN100PN shell-model calculations; pair-truncated shell-model calculations were provided by E. Teruya and N. Yoshinaga
- A. Vogt wrote the paper, P. Reiter and B. Birkenbach co-wrote the paper

Publication IV:

High-spin structures and isomers in the $N = 81$ isotones ^{135}Xe and ^{137}Ba

- A. Vogt participated in the experiment which was conceived and carried out by P. Reiter, B. Birkenbach, K. Geibel, and the LNL 11.22 collaboration
- B. Birkenbach and A. Vogt carried out the data analysis of the LNL 11.22 experiment
- M. Siciliano and K. Hadyńska-Klęk carried out the channel selection of experiment LNL 10.26; A. Vogt performed the post-analysis
- J.J. Valiente-Dobón and C. Wheldon carried out the sorting and channel selection of the LBNL dataset, A. Vogt carried out the refined data analysis
- A. Vogt performed the SN100PN shell-model calculations; pair-truncated shell-model calculations were provided by E. Teruya and N. Yoshinaga
- A. Vogt wrote the paper, A. Blazhev co-wrote the paper

Publication V:

Characterization and calibration of radiation-damaged double-sided silicon strip detectors

- A. Vogt conceived the Cologne experiment
- A. Vogt and L. Kaya constructed and carried out the Cologne experiment
- T. Limböck performed the atomic-force microscopy
- C. Stahl performed the data analysis of the AGATA data
- A. Vogt and L. Kaya post-analyzed the AGATA data
- A. Vogt wrote the paper, L. Kaya co-wrote the paper

High-spin structures in ^{132}Xe and ^{133}Xe and evidence for isomers along the $N = 79$ isotones

- A. Vogt conceived and carried out the Cologne experiment
- M. Siciliano and K. Hadyńska-Klęk carried out the channel selection of experiment LNL 10.26; A. Vogt performed the post-analysis
- J.J. Valiente-Dobón and C. Wheldon carried out the sorting and channel selection of the LBNL dataset, A. Vogt carried out the refined data analysis
- A. Vogt performed the SN100PN shell-model calculations; pair-truncated shell-model calculations were provided by E. Teruya and N. Yoshinaga
- A. Vogt wrote the paper

Curriculum vitae

Persönliche Daten

Name: Andreas Günter Heinz Vogt
Anschrift: Eckewartstr. 20, 50739 Köln
Geburtsdatum: 27. September 1988
Geburtsort: Köln
Nationalität: deutsch
Konfession: evangelisch
Eltern: Heinz-Dieter Vogt, Apotheker
Dr. Claudia Vogt, geb. Schölzel, Apothekerin

Hochschulstudium und Promotion

2014-2017 Promotion an der Universität zu Köln
im Fach Experimentalphysik
2012-2014 Studium der Physik an der Universität zu Köln
(M.Sc. Physik)
2009-2012 Studium der Physik an der Universität zu Köln
(B.Sc. Physik)

Arbeitsverhältnisse

seit 2014 Wissenschaftlicher Mitarbeiter am Institut für Kernphysik
der Universität zu Köln
2011-2014 Studentische Hilfskraft am Institut für Kernphysik
der Universität zu Köln

Wehrdienst

seit 2010 Beorderung beim Taktischen Luftwaffengeschwader 31
„Boelcke“, letzter Dienstgrad Stabsgefreiter d.R.
2008-2009 Instandsetzungs- und Elektronikstaffel
Jagdbombergeschwader 31 „Boelcke“,
heute Taktisches Luftwaffengeschwader 31 „Boelcke“,
letzter Dienstgrad Obergefreiter d.R.
2008 10./Luftwaffenausbildungsregiment

Schulbildung

1999-2008 Erich Kästner-Gymnasium, Köln
1995-1999 Katholische Grundschule Bülowstraße, Köln

Erklärung zur Dissertation

Ich versichere, dass ich die von mir vorgelegte Dissertation selbständig angefertigt, die benutzten Quellen und Hilfsmittel vollständig angegeben und die Stellen der Arbeit – einschließlich Tabellen, Karten und Abbildungen –, die anderen Werken im Wortlaut oder dem Sinn nach entnommen sind, in jedem Einzelfall als Entlehnung kenntlich gemacht habe; dass diese Dissertation noch keiner anderen Fakultät oder Universität zur Prüfung vorgelegen hat; dass sie – abgesehen von unten angegebenen Teilpublikationen – noch nicht veröffentlicht worden ist, sowie, dass ich eine solche Veröffentlichung vor Abschluss des Promotionsverfahrens nicht vornehmen werde. Die Bestimmungen der Promotionsordnung sind mir bekannt. Die von mir vorgelegte Dissertation ist von Prof. Dr. Peter Reiter betreut worden.

Teilpublikationen

- A. Vogt *et al.* “Light and heavy transfer products in $^{136}\text{Xe}+^{238}\text{U}$ multinucleon transfer reactions”. *Phys. Rev. C* 92 024619 (2015)
- B. Birkenbach, A. Vogt *et al.* “Spectroscopy of the neutron-rich actinide nucleus ^{240}U following multinucleon-transfer reactions”. *Phys. Rev. C* 92 044319 (2015)
- A. Vogt *et al.* “High-spin structure of ^{134}Xe ”. *Phys. Rev. C* 93 054325 (2016)
- A. Vogt *et al.* “Isomers and high-spin structures in the $N = 81$ isotones ^{135}Xe and ^{137}Ba ”. *Phys. Rev. C* 95 024316 (2017)
- L. Kaya, A. Vogt *et al.* “Characterization and calibration of radiation-damaged double-sided silicon strip detectors”. *Nucl. Instr. Meth. Phys. Res. A*, 855 109–117 (2017)
- A. Vogt *et al.* “High-spin structures in ^{132}Xe and ^{133}Xe and evidence for isomers along the $N = 79$ isotones”. *Phys. Rev. C* 96 024321 (2017)

Köln, den 4. September 2017

(Andreas Vogt)